Genesis of BIF-hosted iron ore deposits in the Carajás mineral province, Brazil: constraints from in-situ Fe isotope analysis and whole-rock geochemistry

Doctoral Thesis

(Dissertation)

to be awarded the degree of

Doctor rerum naturalium (Dr. rer. nat.)

submitted by

Stefan Halder

from Lindenberg im Allgäu, Germany

approved by the Faculty of Energy and Management Science,

Clausthal University of Technology

Date of oral examination

17.02.2017

Dean

Prof. Dr. Inge Wulf

Chairperson of the Board of Examiners

Prof. Dr. Hans-Jürgen Gursky

Supervising Tutor

Prof. Dr. Bernd Lehmann

Reviewer

Prof. Dr. Kurt Mengel

This dissertation was undertaken at the Mineral Resources Department of the Institute of Disposal Research of the Clausthal University of Technology.

For my family

Acknowledgments

This thesis would not have been possible without the help and contribution of many people, who supported me both personally and academically during my graduate studies.

First and foremost, I would like to express my sincere gratitude to my supervisor Prof. Bernd Lehmann. His continuous support, advice and guidance throughout the four years of writing this thesis was quite extraordinary and is deeply appreciated.

Prof. Kurt Mengel is sincerely thanked for accepting to be the reviewer of this dissertation.

I am very grateful to Dr. Alexandre Raphael Cabral, for collecting the samples from the Carajás region and countless conversations at the coffee table that led to improvements in this thesis.

My gratitude goes to Prof. Stefan Weyer for the opportunity to carry out iron isotope measurements at the Leibniz Universität Hannover and his thorough reviews of my manuscripts. I also thank Dr. Ingo Horn, Dr. Stephan Schuth and the other staff members of the Institute for Mineralogy of the Leibniz Universität Hannover, who helped me with the iron isotope analyses.

Special thanks is due to my colleagues Ulf Hemmerling for the preparation of polished thin sections, Fred Türck for technical support and Elvira Schulze for her assistance. I would like to thank the entire staff of the Institute of Disposal Research of the Clausthal University of Technology for their friendliness and assistance. I enjoyed working with you very much.

I thank the mining company Vale S.A. for providing the sample material for this study. This thesis was funded by the "Geofluxes" graduate school of the Braunschweig-Clausthal-Hannover university consortium (Niedersächsische Technische Hochschule).

Words cannot express how grateful I am to my parents, siblings and friends for their unending support and encouragement during my academic career. I am especially grateful to my mother for her great and selfless love. Lastly, I would like to thank my loving girlfriend Naghmeh Fannipour, who stood by my side and supported me during the last two years of this thesis.

Ich danke euch allen.

Abstract

The Carajás mineral province, located in northern Brazil, hosts the largest high-grade iron ore resource in the world (18 Gt @ 66 wt.% Fe). The iron ore deposits formed from banded iron formation (BIF) units of the Neoarchean Carajás Formation, and are situated on the northern (Serra Norte) and southern (Serra Sul) limbs of the WNW-striking Carajás fold.

Unweathered BIF samples from two Serra Norte ore bodies (N7, N8) and an ore body from the Serra Sul (S11D), have a simple mineralogy, consisting of alternating magnetite and quartz-rich bands. This mineral assemblage is characteristic for oxide facies BIF. Sedimentation of the BIF units occurred in distal basin parts, as shown by low abundances of Al_2O_3, TiO_2 and high field strength elements (HFSE). Seawater-like rare-earth element (REE) distribution patterns indicate a formation by marine chemical sedimentation. The absence of true Ce anomalies shows that suboxic to anoxic conditions were prevalent in the Carajás basin, at the time of BIF deposition. Unusually strong positive Eu anomalies were detected in all BIF samples. These anomalies record a high hydrothermal flux to the Carajás basin. The strictly positive Fe isotope composition of magnetite in BIF samples indicates derivation from Archean seawater by partial oxidation of aqueous Fe(II). The low variability between the Fe isotope composition of iron-rich bands at the 10-cm scale demonstrates that BIF formation took place with remarkable consistency over several thousand years. Rayleigh modeling of Fe isotope fractionation during Fe(II) oxidation suggests that BIF sedimentation occurred at low ocean temperatures.

The iron ore deposits consist mainly of friable hematite–goethite ore (so-called "soft ore"). Martite, i.e. hematite pseudomorphic after magnetite, is the main constituent of soft ore. The homogenous Fe isotope composition of martite in individual samples strongly resembles the invariable Fe isotope composition of magnetite, which suggests that iron remained immobile during geological history. This argues against proposed models of hypogene iron ore formation, since hydrothermal overprint would have introduced a large scatter in the Fe isotope composition of magnetite and martite, combined with a considerable shift towards a more positive Fe isotope composition. Microplaty hematite is a minor constituent of soft ore and often occurs as crystals nucleating on martite. This observation and the homogenous Fe isotope composition of microplaty hematite and martite, detected in samples of BIF and soft ore, indicate that microplaty hematite formed by recrystallization of pre-existing martite. Pressure and temperature conditions during weathering should not allow this degree of recrystallization. Thus, martitization and microplaty hematite formation must have occurred earlier, possibly during retrograde metamorphism, when the prevalent P-T conditions shifted the stability of magnetite towards hematite. By contrast, goethite, formed in an open system during subrecent/recent weathering, has a more variable Fe isotope composition. Consequently, martitization and microplaty hematite formation must have taken place during retrograde metamorphism, while leaching of silica and residual high-grade iron ore formation occurred over the last 70 Ma by intense weathering under essentially bulk iron-immobile conditions.

Kurzfassung

In der Carajás Lagerstättenprovinz in Nordbrasilien treten die weltweit größten Ressourcen an high-grade Eisenerz auf (18 Gt @ 66 wt.% Fe). Die Eisenerzlagerstätten bildeten sich aus Bändereisenerz (BIF) der neoarchaischen Carajás Formation. Die Lagerstätten befinden sich auf den nördlichen (Serra Norte) und südlichen (Serra Sul) Faltenschenkeln der WNW-streichenden Carajás Falte.

Unverwitterte BIF-Proben aus zwei Erzkörpern der Serra Norte (N7, N8) und eines Erzkörpers der Serra Sul (S11D), weisen eine einfache Mineralogie auf, welche aus wechselgelagerten Magnetit- und Quarz-reichen Bändern besteht. Diese Mineralzusammensetzung ist charakteristisch für Oxidfazies BIF. Niedrige Gehalte an Al_2O_3, TiO_2 und "high field strength elements" (HFSE) deuten an, dass die BIF-Ablagerung in distalen Beckenbereichen erfolgte. Meerwasserähnliche Verteilungsmuster von Seltenen Erdmetallen (REE), weisen auf eine Bildung durch marine chemische Sedimentation hin. Das Fehlen echter Ce Anomalien zeigt an, dass zum Zeitpunkt der BIF-Ablagerung suboxische bis anoxische Bedingungen im Carajás Becken vorherrschten. Ungewöhnlich starke positive Eu Anomalien wurden in allen BIF-Proben nachgewiesen. Diese Anomalien dokumentieren einen hohen hydrothermalen Flux in das Carajás Becken. Die ausschließlich positive Fe Isotopenzusammensetzung von Magnetit in BIF-Proben deutet auf eine Bildung aus archaischem Meerwasser durch partielle Oxidation von gelöstem Fe(II) hin. Die geringe Variation zwischen der Fe Isotopenzusammensetzung der eisenreichen Bänder im 10-cm Maßstab zeigt, dass BIF-Ablagerung bemerkenswert gleichmäßig über mehrere tausend Jahre ablief. Rayleigh-Modellierung der Fe Isotopenfraktionierung während der Fe(II) Oxidation legt nahe, dass die Bildung der BIFs bei relativ niedrigen Ozeantemperaturen erfolgte.

Die Eisenerzlagerstätten bestehen hauptsächlich aus pulverigem Hämatit-Goethit Erz (sogenanntes "Soft ore"). Martit, eine Pseudomorphose von Hämatit nach Magnetit, bildet den Hauptbestandteil des Soft ore. Die homogene Fe Isotopenzusammensetzung des Martits in einzelnen Proben ähnelt der gleichartigen Fe Isotopenzusammensetzung von Magnetit, was nahelegt, dass sich Eisen über geologische Zeiträume hinweg immobil verhielt. Dies spricht gegen Modelle einer hypogenen Eisenerzbildung, da hydrothermale Überprägung eine große Streuung in die Fe Isotopenzusammensetzung von Magnetit und Martit eingebracht hätte, in Kombination mit einer beträchtlichen Verschiebung hin zu einer positiveren Fe-Isotopenzusammensetzung. "Microplaty hematite" ist ein geringer Bestandteil des Soft ores und tritt häufig in Form von Kristallen auf, welche auf Martit wachsen. Sowohl diese Beobachtung, als auch die festgestellte homogene Fe-Isotopenzusammensetzung von Microplaty hematite und Martit in BIF und Soft ore Proben deuten darauf hin, dass die Bildung von Microplaty hematite durch Rekristallisation bereits vorhandenen Martits erfolgte. Da die Druck- und Temperaturbedingungen während der Verwitterung nicht einen solchen Grad der Rekristallisation ermöglichen sollten, muss Martitisierung und die Bildung von Microplaty hematite bereits früher erfolgt sein. Möglicherweise während retrograden Metamorphismus, als vorherrschende P-T

Bedingungen die Stabilität des Magnetits zu Gunsten des Hämatits verschoben. Im Gegensatz hierzu zeigt Goethit, dessen Bildung in einem offenen System während subrezenter/rezenter Verwitterung erfolgte, eine deutlich unregelmäßigere Fe Isotopenzusammensetzung. Folglich muss die Martitisierung und Bildung von Microplaty hematite bereits während der retrograden Metamorphose erfolgt sein. Die Auslaugung von Quarz und die residuale Eisenerzbildung erfolgte hingegen in den vergangenen 70 Ma durch intensive Verwitterung unter Bedingungen in denen sich Eisen im Wesentlichen immobil verhielt.

List of Contents

List of Figures

Chapter 1

Chapter 2

Chapter 3

Chapter 4

Chapter 5

List of Tables

Chapter 1

Chapter 2

Chapter 3

Chapter 4

Chapter 5

Appendix

Chapter 1 Introduction

Banded iron formation or "BIF" are chemical sedimentary rocks that formed in a marine environment during the Precambrian. They occur in metavolcano-sedimentary successions on cratons and shields of every continent. In general, BIFs consist of two main components (Fig. 1.1A), chert (43 to 56 wt.% SiO_2) and iron oxides (20 to 40 wt.% Fe), which make up the characteristic banding of these rocks (KLEIN, 2005). Removal of chert by hydrothermal or weathering processes generates high-grade iron ore, often reaching grades ≥60 wt.% Fe. Because of their high iron content and typically vast resources of several billion tonnes of ore (Fig. 1.2), BIF-hosted iron ore deposits are of immeasurable importance for the global steel industry. At present, Australia and Brazil contribute about two thirds of the world's iron ore exports (USGS, 2016). The ore stems from mining of giant Paleoproterozoic BIF-hosted iron ore deposits of the Hamersley basin in Australia, and Neoarchean deposits of the Quadrilátero Ferrífero and Carajás region in Brazil.

Besides their economic significance, BIFs are also of great scientific interest, since they provide a "window" into the early geological history of our planet. Their study allows us to explore the conditions prevalent in the Precambrian, when magmatism formed the first continents and Earth developed its atmosphere. Ultimately, BIFs offer insights into the evolution of life itself on our planet. The involvement of bacteria in the genesis of these fascinating rocks that only formed in the Precambrian, is indicated by direct and indirect geochemical evidence (e.g. CLOUD, 1968; JOHNSON et al., 2008). The following sections address the tectonic setting, temporal distribution, facies types and genesis of BIFs. The likely origin of dissolved iron in the Precambrian ocean and the conceptual models for high-grade iron ore formation are shortly presented and discussed in two sections.

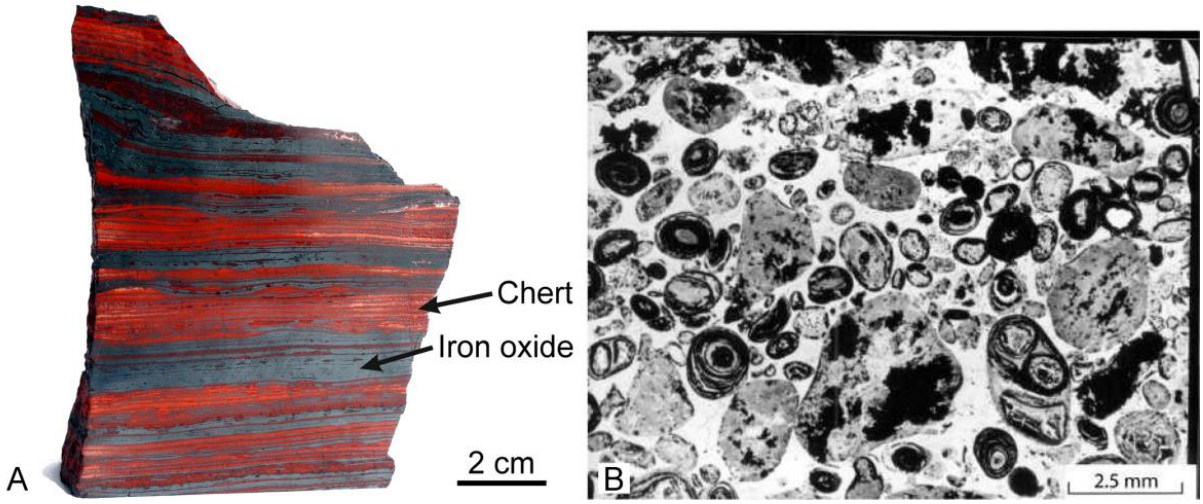

Fig. 1.1 (**A**) Oxide facies BIF hand specimen (Carajás, Brazil), showing the typical alternation of chert (transparent-reddish) and iron oxide-rich bands (black). This banding is a characteristic feature of BIF. (**B**) In contrast, Paleoproterozoic granular iron formations (GIFs) have a granular and in part oolitic texture (modified after KLEIN, 2005).

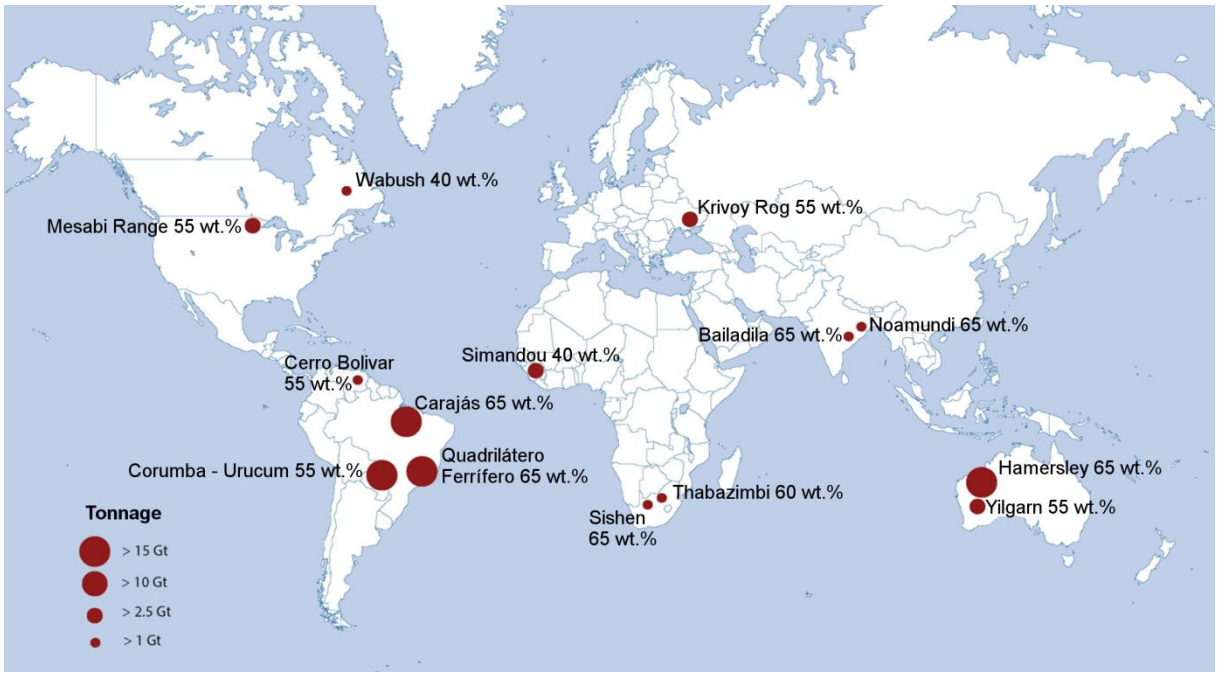

Fig. 1.2 Global map showing the distribution of major BIF-hosted iron ore deposits. Circle size indicates tonnage, ore grade is given in wt.% (modified after HAGEMANN et al., 2016).

1.1 Tectonic setting

In the classic scheme of GROSS (1980), BIFs are categorized into so-called Algoma and Lake Superior types, based on their associated lithologies (Fig. 1.3). Algoma type-BIFs occur together with volcanic rocks and greywacke and likely formed in volcanic arc or rift settings. BIFs belonging to this type exhibit a fine, undisturbed banding, indicative of sedimentation below the storm wave base, i.e. ≥200 m water depth. Lake Superior-type BIFs are associated with dolomite and black shale and were deposited on continental shelfs. Depending on the water depth, they occur as BIFs or in shallow water as reworked GIFs (BEUKES & KLEIN, 1990), with a granular or oolitic texture (Fig. 1.1B). So-called Rapitan-type BIFs represent a third category. This type formed in the Neoproterozoic between ca. 0.8 to 0.6 Ga. Rapitan-type BIFs are associated with glaciomarine sequences (YOUNG, 1976), indicating that their genesis is related to the large-scale glaciations in the Neoproterozoic ("Snowball Earth").

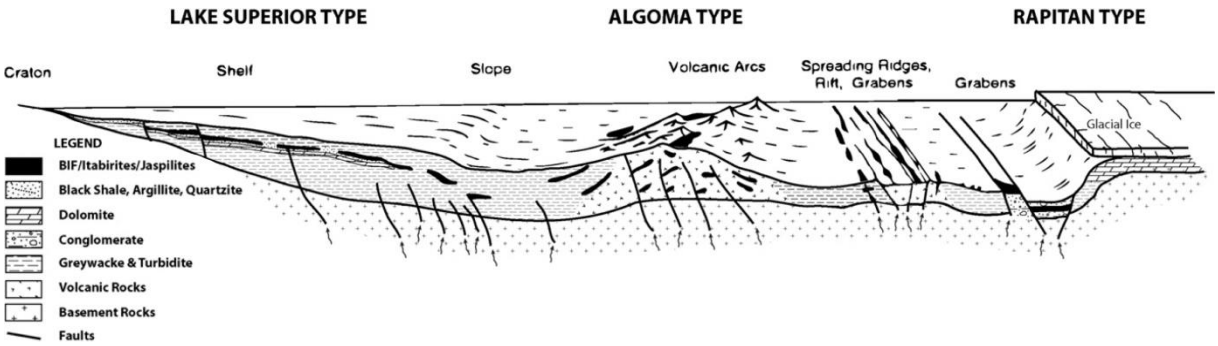

Fig. 1.3 Tectonic setting of Algoma, Lake Superior and Rapitan-type BIFs (modified after HAGEMANN et al., 2016).

1.2 Size and temporal distribution

BIFs only formed in the Precambrian. The oldest known occurrences have an age of 3.76 Ga and are part of the Isua Greenstone Belt in Greenland (SHIMIZU et al., 1990). These BIFs belong to the Algoma type, which formed throughout the Archean and Paleoproterozoic. In contrast, Lake Superior-type BIFs only occur in the Paleoproterozoic, while the Rapitan type is temporally confined to the Neoproterozoic. BIF sedimentation reached its peak in the early Paleoproterozoic (Fig. 1.4). This coincides with the timing of the Great Oxidation Event (GOE) at about 2.45 Ga, during which free oxygen first attained significant atmospheric levels (BEKKER et al., 2004). Due to this temporal overlap, it is possible that BIF genesis is directly linked to the emergence and evolution of oxygen-producing bacteria (CLOUD, 1968). However, the apparent peak of BIF sedimentation in the early Paleoproterozoic might in part result from inaccurate size estimates. Lake Superior-type BIFs, e.g. the Australian Hamersley and South African Transvaal sequences, are usually undeformed and cover large areal extents. In contrast, Algoma-type BIFs occur in deformed greenstone belt sequences. Consequently, adequate size estimates for Lake Superior-type BIFs can be carried out easily, but are considerably more difficult for Algoma-type BIFs. It is likely that the true extent/volume of Algoma-type BIFs is greatly underestimated (GOLE & KLEIN, 1981).

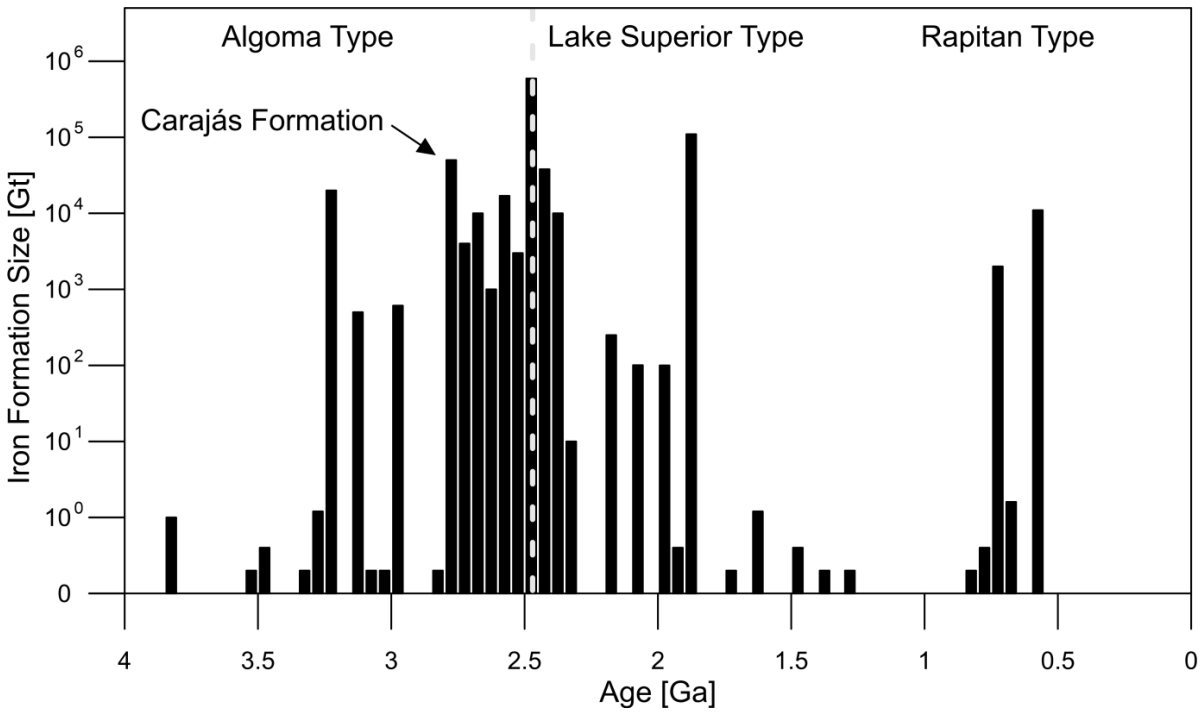

Fig. 1.4 Estimated size and age of Precambrian iron formations (BIFs & GIFs, n = 91; modified after BEKKER et al., 2010, 2014; HUSTON & LOGAN, 2004). A single bar represents a period of 50 Ma. For iron formations with uncertain dimensions, a tonnage of 0.2 Gt is assumed. The position of the Carajás Formation is indicated in the diagram. The dashed line marks the timing of the Great Oxidation Event. Algoma-type BIFs are predominant in the Archean, while Lake Superior-type BIFs are confined to the Paleoproterozoic. The Rapitan type only occurs in the Neoproterozoic.

Large BIF occurrences disappear from the rock record around 1.8 Ga. The reason for this is not yet understood. Some researchers argue that at this time, the deep sea became oxygenated enough to prevent ferruginous conditions (e.g. HOLLAND, 2005), while others invoke sulfidic conditions in the Mesoproterozoic ocean to explain the absence of large BIFs (CANFIELD, 1998; POULTON et al., 2004). The latter would prompt the precipitation of iron as sulfides, preventing the deep ocean from attaining the high iron concentrations necessary for BIF genesis. More recently, it was shown that ferruginous conditions could have been widespread in the Mesoproterozoic (PLANAVSKY et al., 2011). This notion is in accordance with current reports of some BIFs with ages in the range of 1.5 to 1.23 Ga (DUDLEY, 2010; YANG et al., 2016), and shows that BIFs did not disappear completely from the geologic record in the Mesoproterozoic. In light of these findings, ocean-models invoking sulfidic or oxygenated conditions in the period from 1.8 to 0.8 Ga, should be re-evaluated. In the Neoproterozoic, BIFs return in larger numbers. Their reappearance coincides with the 710 Ma Stuartian, 635 Ma Marinoan and 580 Ma Ediacaran glaciations. HOFFMAN (2005) proposed that the deep ocean returned to anoxic conditions during this period, which allowed iron to accumulate again in seawater. However, the earliest known Neoproterozoic BIF, the ca. 840 Ma Aok Formation (RAINBIRD et al., 1996), predates the Stuartian glaciation by more than 100 Ma and is unassociated with glacial sediments. Thus, the recurrence of BIFs in the Neoproterozoic might be unrelated to the glaciations. In fact, periods of BIF deposition correlate well with superplume activity in the Precambrian (Fig. 1.5). During these periods of enhanced magmatism, the iron flux to the ocean could have been many times greater than under normal circumstances, thus triggering BIF deposition (ISLEY & ABBOTT, 1999).

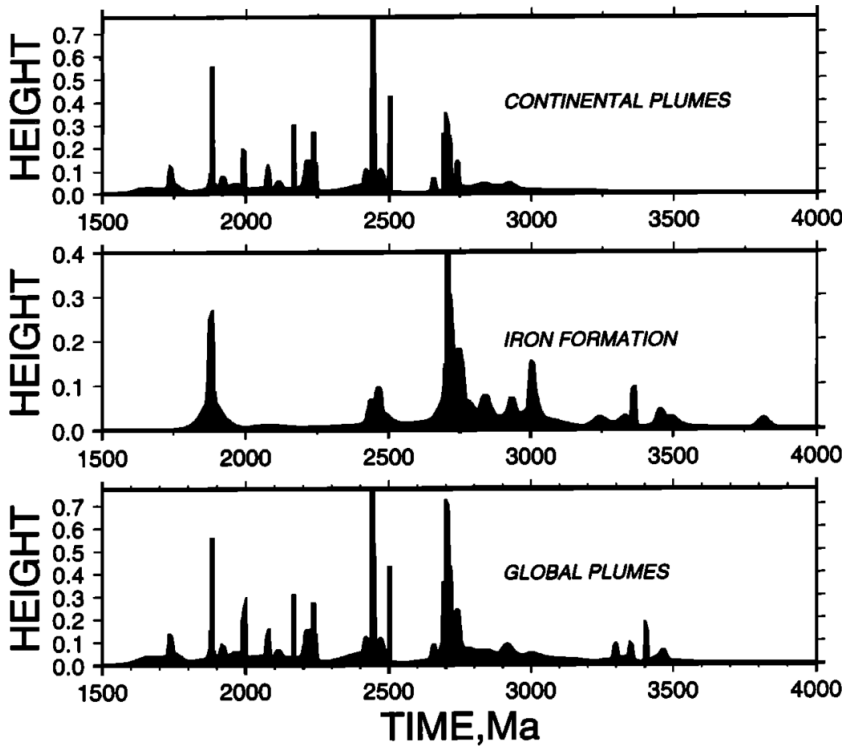

Fig. 1.5 Gaussian distribution plots illustrating the correlation between plume activity and periods of BIF sedimentation (ISLEY & ABBOTT, 1999).

1.3 BIF facies types

JAMES (1954) identified four different facies types, based on the observed mineral assemblages of BIFs in the Lake Superior region (Table 1.1). Today, the pyritic carbonaceous slate termed "sulfide facies" by JAMES (1954), is usually classified as black shale.

Table 1.1 BIF facies types of JAMES (1954).

Facies	Main iron minerals	Subordinate iron minerals
Sulfide	Pyrite	Siderite, ankerite, greenalite
Carbonate	Siderite, ankerite, ferroan dolomite	Pyrite, stilpnomelane, minnesotaite, magnetite, hematite
Silicate	Greenalite, minnesotaite, stilpnomelane, chlorite,	Magnetite, siderite, ankerite, hematite
Oxide	Magnetite, hematite	Siderite, ankerite, greenalite, minnesotaite, stilpnomelane, pyrite

While the carbonate and oxide facies are easily divisible, the exact position of the silicate facies is problematic, since it does not occur as a single unit, but instead appears interlayered within both oxide and carbonate facies BIFs. A proposal by KRAPEŽ et al. (2003) that BIFs might be the product of density currents, would in part solve this dilemma. In this model, the silicate facies would represent turbidites of smectite-rich volcaniclastic mud, remobilized from the flanks of submarine volcanoes. The failing of this model is that it does not explain the spatial division of the sulfide/black shale, carbonate and oxide facies (JAMES, 1954; KLEIN & BEUKES, 1989).

A detailed drill core study of the 2.3 Ga Kuruman Iron Formation and the underlying Campbellrand carbonate sequence by KLEIN & BEUKES (1989) revealed the lateral changes in the depositional environment of BIFs. In the analyzed drill cores, black shale overlies shallow water cryptalgal limestone. The black shale is followed by carbonate facies BIF, which in turn is succeeded by oxide facies BIF. The high Al_2O_3 and trace element content of black shale indicates clastic contamination from a continental source. In contrast, carbonate and oxide facies BIF units represent almost pure chemical sediments. KLEIN & BEUKES (1989) conclude that the studied drill cores record a marine transgression. By applying Walther's law of facies (e.g. MIDDLETON, 1973), the oxide facies must have formed in distal parts of a marine basin, followed by carbonate facies BIF and black shale, which were deposited in the proximal part of the basin (Fig. 1.6).

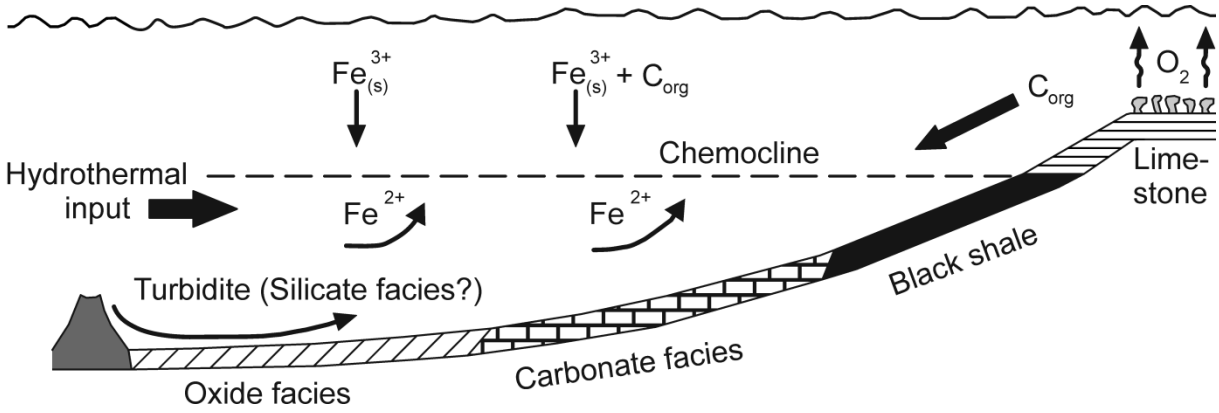

Fig. 1.6 Reconstruction of the depositional environment of BIFs, based on the observations of KLEIN & BEUKES (1989).

1.4 BIF genesis

To understand the genesis of BIF, it is necessary to determine the underlying process causing the oxidation and precipitation of billions of tonnes of iron from ferruginous seawater. This endeavour is complicated by the fact that the atmosphere was anoxic over long periods when BIF sedimentation took place. CLOUD (1968) proposed that early cyanobacterial life could have triggered iron oxidation by releasing oxygen into the ocean as a waste product of photosynthesis. The reaction can be summarized as:

$$2\ Fe^{2+} + 0.5\ O_2 + 5\ H_2O \rightarrow 2\ Fe(OH)_3\downarrow + 4\ H^+ \quad (1)$$

It is possible that early cyanobacteria did not possess an efficient protection against elevated oxygen levels. Thus, if the concentration of ferrous iron in seawater sunk below a critical level, the bacteria would have "poisoned" themselves. In the ensuing period of low bacterial activity, chert formation would be the dominant sediment-forming process. Such a cycle of bacterial blooms and extinctions could explain the characteristic banding of BIFs (Fig. 1.1A).

Another approach invokes iron oxidation by microaerophilic bacteria like *Gallionella ferruginea*. Such bacteria could have utilized traces of oxygen produced by early cyanobacteria (HOLM, 1989):

$$6\ Fe^{2+} + 0.5\ O_2 + CO_2 + 16\ H_2O \rightarrow CH_2O + 6\ Fe(OH)_3\downarrow + 12\ H^+ \quad (2)$$

This reaction proceeds about sixty times faster than abiotic iron oxidation (SØGAARD et al., 2000), and could have easily precipitated large amounts of iron-oxyhydroxide minerals over short periods of time.

A mechanism that does not require any free oxygen, is the direct oxidation of ferrous iron by anoxygenic phototrophic bacteria (GARRELS et al., 1973):

$$4\ Fe^{2+} + HCO_3^- + 10\ H_2O + light \rightarrow 4\ Fe(OH)_3\downarrow + CH_2O + 7\ H^+ \quad (3)$$

This type of metabolism is deeply seated in the phylogenetic tree of life and appears to predate the emergence of oxygenic photosynthesis (MULKIDJANIAN & GALPERIN, 2013; XIONG, 2006). Laboratory experiments, model calculations and studies of modern ferruginous basins indicate that photoferrotrophy could easily account for the iron accumulated in Precambrian BIFs (CROWE et al., 2008; KAPPLER et al., 2005; KONHAUSER et al., 2002; LLIRÓS et al., 2015).

UV photooxidation was first proposed by CAIRNS-SMITH (1978) as an entirely abiotic process for BIF genesis. Prior to the existence of an oxygenated atmosphere, Earth lacked an ozone layer and was virtually unprotected against solar radiation. Ultraviolet light with wavelengths between 200 to 300 nm could have generated short-lived free radicals in the upper ocean with the potential to oxidize ferrous iron:

$$2\ Fe^{2+} + 2\ H^{+} + h\nu \rightarrow 2\ Fe^{3+}\downarrow + H_2\uparrow \quad (4)$$

However, laboratory experiments conducted by KONHAUSER et al. (2007) show that UV photooxidation is not a viable pathway for BIF sedimentation. In their experiments, simulating seamount-type vent systems in a relatively shallow marine environment, the contribution of photooxidation is negligible in comparison to the precipitation of siderite and an amorphous silicate phase. The chemical composition of the siliceous precipitate matches the composition of greenalite.

An alternative abiotic mechanism was first proposed by KRAPEŽ et al. (2003) and later adopted by LASCELLES (2007). This approach is based on sedimentological features of BIF from the Hamersley basin, Australia. Both studies suggest that BIFs formed by resedimentation of hydrothermal muds, which were initially deposited on the flanks of submarine volcanoes. The results of KONHAUSER et al. (2007) give weight to this hypothesis. Their experiments show that siderite and a greenalite-precursor, both the main iron minerals of two BIF facies types, easily form under the conditions prevalent in the Precambrian ocean without the assistance of bacterial life. An abiotic origin would also explain the typically low content of organic carbon in BIF (KLEIN, 2005). As mentioned in section 1.3, the flaw of this model is that it fails to explain the clearly recognizable spatial division between the different BIF facies types.

1.5 Origin of dissolved iron in the Precambrian ocean

The primary source of the iron contained in BIFs has been disputed for decades. It is possible that iron was mobilized during weathering of continental crust and transported into the Precambrian oceans. Alternatively, submarine hydrothermal vent systems could have released ferrous iron into the deep ocean. A recent study by PONS et al. (2013) focussing on the Zn isotope composition of BIFs with ages between 3.8 to 1.5 Ga, indicates that continental runoff was predominantly alkaline prior to 2.7 Ga. If this observation is correct, continental weathering could be excluded as a primary source to the pre-2.7 Ga ocean, since ferrous iron has a low solubility at higher pH values. This suggests that submarine hydrothermal vent systems likely represent the primary iron supplier of Archean BIFs, like the 2.75 Ga Carajás Formation studied in this thesis.

If the exposed upper part of the juvenile continental crust was mostly comprised of mafic rocks, e.g. basalt or komatiite, weathering should have increased the pH of continental surface waters. A number of geochemical and geological observations support this assumption. Archean shales generally have low Th and high Cr, Ni and Sc contents. This "komatiite effect" is interpreted as evidence for subaerial weathering of extensive areas of komatiite (CONDIE, 1993). Relatively undeformed supracrustal sequences of the Kaapvaal and Pilbara Cratons show that in the Archean, mafic rocks made up a significant portion of the upper continental crust. Examples are the 2.98 to 2.97 Ga Nsuze Group of the Kaapvaal Craton (MUKASA et al., 2013), and the 2.77 to 2.71 Ga Nullagine and Mount Jope Supersequences of the Pilbara Craton (BLAKE et al., 2004). Archean paleoweathering profiles like the 2.78 to 2.76 Ga Mt. Roe #2 paleosol (YANG et al., 2002), the 2.72 Ga paleoweathering profile of the Paulson Lake sequence (DRIESE et al., 2011), and the 2.95 Ga Denny Dalton paleosol (DELVIGNE et al., 2016), provide further evidence for the widespread subaerial weathering of basalt. Weathering of komatiite and basalt mobilizes Mg^{2+}, Ca^{2+}, Na^{+} and K^{+}. These cations would have shifted the pH of Archean continental runoff into the alkaline range. Hydrogeochemical studies show that modern surface- and groundwaters in regions with large basalt exposures possess a weak to medium alkaline pH (Fig. 1.7; GISLASON & EUGSTER, 1987; FRIDRIKSSON et al., 2009; FLAATHEN et al., 2009; KAASALAINEN & STEFÁNSSON, 2012).

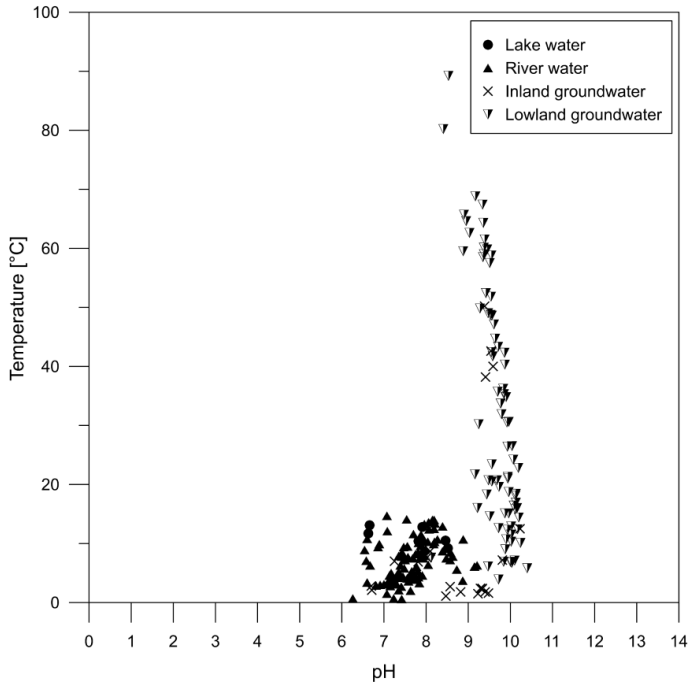

Fig. 1.7 Temperature and pH of natural waters from the tertiary flood basalt region Skagafjördur in northern Iceland (data from FRIDRIKSSON et al., 2009).

In the alkaline pH range, the solubility of Fe^{2+} decreases rapidly (Fig. 1.8). Under standard conditions, Fe^{2+} with a concentration of 10^{-6} mol/l is soluble up to a maximum pH of 9. At a higher concentration of 10^{-4} mol/l, the maximum pH is lowered to 8. Higher temperatures also negatively impact the solubility of Fe^{2+} in alkaline solutions (Fig. 1.9). At a temperature of 60°C, Fe^{2+} with a concentration of 10^{-6} mol/l is soluble up to a maximum pH of 8 and with

a concentration of 10^{-4} mol/l only up to a pH of 7. So far, it is still uncertain whether the temperature of the Archean atmosphere and hydrosphere was higher compared to modern times (DE WIT & FURNES, 2016). Temperature estimates for the Archean ocean range from 26 to 85°C (KNAUTH & EPSTEIN, 1976; KNAUTH & LOWE, 2003; ROBERT & CHAUSSIDON, 2006; HREN et al., 2009; BLAKE et al., 2010). Modeling of the subaerial weathering of basalt, based on the mineral assemblages of Neoarchean and Paleoproterozoic paleosols, indicates that pedogenesis occurred under moderate climates in a pH range of 6.2 to 9.2 (ALFIMOVA et al., 2014). Today, in regions with widespread basalt-weathering, pH increases significantly from surface- to groundwaters (Fig. 1.7). If this feature also applies to the Archean, meteoric fluids would have mobilized traces of iron and transported it downward. At depth, the higher pH of groundwater would then have immobilized the iron. Thus, Archean weathering profiles should be depleted in iron near the paleosurface and enriched in iron in deeper levels. Studies of the Mt. Roe #2 paleosol and the Denny Dalton paleosol show that this is actually the case (YANG et al., 2002; DELVIGNE et al., 2016). It follows that aqueous iron was not transported into the ocean during continental weathering. Instead, iron was immobilized on site during supracrustal weathering. Although it cannot be excluded that iron-bearing minerals arrived in the ocean by riverine or aeolian transport, it is unlikely that continental weathering played a major role in BIF genesis, since BIFs first appear around 3.76 Ga, at a time when large continental landmasses had not yet developed.

Alternatively, submarine hydrothermal vent fields could have been the primary iron supplier to the Archean ocean. Models of the thermal evolution of our planet point to a much hotter mantle and a higher mantle heat-flux during the Precambrian (BICKLE, 1986; DAVIES, 2009; HÖINK et al., 2013). The more frequent occurrences of komatiite (GROVE & PARMAN, 2004), and the higher emplacement temperatures of non-arc basalts in the Precambrian (HERZBERG et al., 2010), support this hypothesis. ISLEY & ABBOTT (1999) showed that periods of BIF sedimentation often occur contemporaneously with superplume events (Fig. 1.5). The higher mantle heat-flux during these events likely lead to an increase in oceanic crust generation (BURKE & KIDD, 1978; BICKLE, 1986; LENARDIC, 1998), and thus a higher activity of submarine hydrothermal vent fields. Modern submarine hydrothermal systems represent poor iron suppliers. Due to the high sulfur concentration of vent fluids, most of the dissolved iron precipitates as sulfides directly after the fluids are emitted into the ocean. The elevated sulfur content is owed to the high sulfate concentration of seawater, which in turn results from oxidative weathering of continental crust. Prior to the GOE, the atmosphere was anoxic and the sulfate concentration of seawater was low (CROWE et al., 2014). Calculations by KUMP & SEYFRIED (2005) show that vent fluids with low sulfur levels would release significantly higher amounts of iron into the ocean. Experiments carried out by SEYFRIED & JANECKY (1985) demonstrate that lower pressure, as well as higher temperatures promote the solubility of iron. A change from 400 to 425°C at 400 bar would increase the iron content of the fluid by four to ten times. Considering the higher mantle heat-flux in the Precambrian, it is likely that vent fluids also had higher temperatures. In the sulfate-poor pre-GOE ocean, submarine hydrothermal systems must have been major iron suppliers.

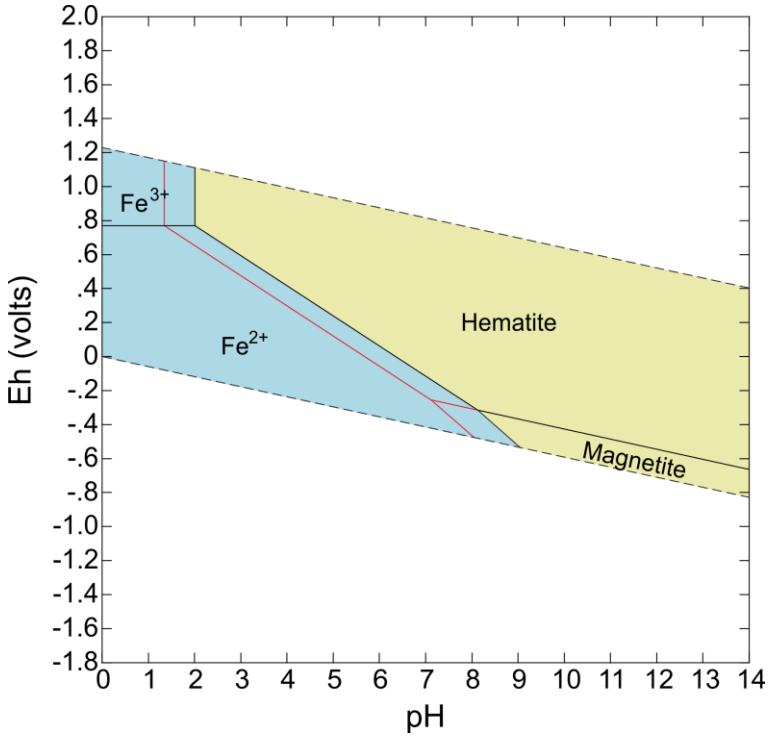

Fig. 1.8 Eh-pH diagram for the Fe-O-water system under standard conditions (25°C, 1.013 bar). The activity of Fe^{2+} is 10^{-6}. The red lines indicate the position of the stability fields at an activity of 10^{-4} (calculated with The Geochemist's Workbench).

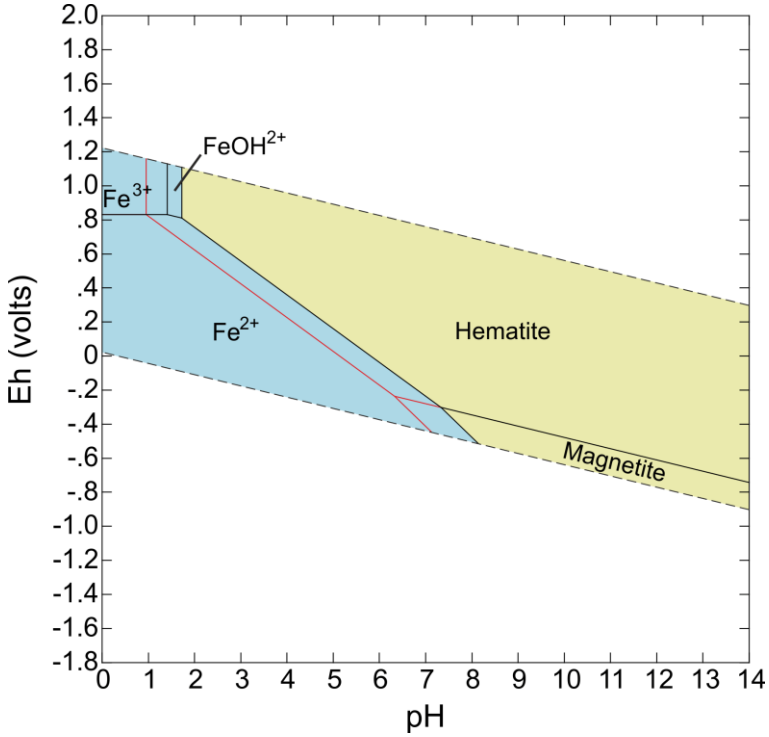

Fig. 1.9 Eh-pH diagram for the Fe-O-water system at 60°C and 1.013 bar. The activity of Fe^{2+} is 10^{-6}. The red lines indicate the position of the stability fields at an activity of 10^{-4}. The $FeOH^{2+}$ species is absent at an activity of 10^{-4} (calculated with The Geochemist's Workbench).

1.7 High-grade iron ore formation

Genetic models for BIF-hosted iron ore deposits invoke supergene or hypogene processes to account for the extensive removal of chert, which is required for the generation of the typically high iron contents of this deposit type. In addition, a number of studies propose a combination of both processes, i.e. a hypogene stage of ore formation preceding supergene enrichment or vice versa.

An alternative approach put forward by LASCELLES (2002) postulates ore formation from chert-free BIF. LASCELLES (2002, 2007, 2012) suggests that prior to lithification, the hydrostatic pressure of the overlying sediment caused the removal of silica gel through fractures in the BIF precursor. The assumed product of this process, chert-free BIF, has only been reported for the Mt Gibson deposit in the Yilgarn Craton. If silica removal took place during dewatering of the sedimentary BIF precursor, as envisaged by LASCELLES (2002, 2007, 2012), then the question arises why the BIF units surrounding the chert-free BIF in the Mt Gibson deposit were unaffected by this process. Furthermore, fragments and lenses of BIF are common components of BIF-hosted iron ore bodies and the duricrusts that developed above them (SHUSTER et al., 2012). The occurrence of BIF fragments within the ore itself is incompatible with the concept of LASCELLES (2002) and provides a strong argument against the notion that early diagenetic desilicification represents a typical step, necessary for the formation of BIF-hosted iron ore deposits. Instead, the chert-free BIF of the Mt Gibson deposit might be the product of hypogene processes or could have formed by submarine slumping, similar to the magnetite-rich breccia in the basal part of the Carajás Formation (see chapter 2, section 2.2.5; CABRAL et al., 2013).

Supergene models of ore formation assume that meteoric waters are responsible for the removal of chert and the oxidation of the iron-bearing minerals contained in the protore BIF (e.g. LEITH, 1903; MACLEOD, 1966; RAMANAIDOU, 2009). The dissolution of quartz in water can be summarized as:

$$SiO_2 + 2\ H_2O \rightarrow H_4SiO_4 \quad (5)$$

The oxidation of magnetite by meteoric fluids is shown in the following reactions:

$$4\ Fe_3O_4 + O_2 \rightarrow 6\ Fe_2O_3 \quad (6)$$

or

$$2\ Fe_3O_4 + H_2O \rightarrow 3\ Fe_2O_3 + H_2 \quad (7)$$

Under oxygenated conditions and at neutral pH, the solubility of quartz is approximately 11 ppm (= 11 mg L^{-1}) at 25°C (RIMSTIDT, 1997), while ferric iron is practically insoluble (Figs. 1.8 and 1.9). Given long periods of weathering, e.g. several million years, meteoric fluids should be able to remove considerable quantities of silica. Available $^{40}Ar/^{39}Ar$ ages of manganese minerals from weathering profiles of the Carajás Mineral Province and the

Quadrilátero Ferrífero in Brazil, indicate that the BIF-hosted iron ore deposits of these regions have been affected by weathering since at least the Early Eocene to Late Cretaceous, i.e. for a duration of 50 to 70 Ma (RUFFET et al., 1996; SPIER et al., 2006; VASCONCELOS et al., 1994). Futhermore, BELEVTSEV (1973) report on the existence of linear zones of oxidized BIF reaching depths of more than 2400 m within the Saksagan band of the Krivoyrog basin, in Ukraine. These deep oxidation zones are confined to fault zones and areas affected by cross folding. The observations mentioned above show that supergene processes operating over long periods of time could account for the formation of BIF-hosted iron ore deposits. In combination with deep-reaching faults, weathering can extend to great depths. However, reports of deep-seated iron ore bodies that appear to have been unaffected by weathering, e.g. the Thabazimbi deposit in South Africa (BEUKES et al., 2003), and also the common occurrence of microplaty hematite in iron ore bodies, suggests that BIF-hosted iron ore deposits are not the product of supergene enrichment alone.

The origin of microplaty hematite is controversial. It forms either by dehydration of goethite (MORRIS, 1985, 2012), or by recrystallization of pre-existing martite (HENSLER et al., 2015). Alternatively, it could also precipitate from oxidizing hydrothermal fluids (POWELL et al., 1999). The first two modes of formation require oxidation, possibly due to weathering, followed by burial and at least low-grade metamorphism. The supergene-metamorphic model of MORRIS (1980, 1985, 2012) for Australian BIF-hosted iron ore deposits, assumes that a first stage of lateritic weathering affected the protore in the Paleoproterozoic, on the basis of oxidized BIF and iron ore fragments present in conglomerates of the ca. 2.0 Ga Wyloo Group (MORRIS, 1980). Subsequent burial and metamorphism would then have transformed goethite into microplaty hematite. Exhumation of the deposits in the Late Cretaceous or Early Paleogene lead to a second stage of supergene enrichment. In order to explain the existence of isolated, deep-seated iron ore bodies, MORRIS et al. (1980) propose that electronic conduction through magnetite layers created electochemical cells between BIF at depth and its segments exposed at the surface. In this model, ionic exchange would have been controlled by downward groundwater flow.

Hypogene models assume that chert removal was controlled by hydrothermal systems. Proposed fluid sources include heated meteoric fluids (GRUNER, 1937; POWELL et al., 1999), magmatic fluids (DORR, 1965) and metamorphic solutions (BELEVTSEV, 1973). Some studies suggest that hypogene ore formation is a multistage process that involves varying fluid sources (FIGUEIREDO E SILVA et al., 2013; HENSLER et al., 2015, SÓSNICKA et al., 2016). At present, there appears to be no consensus, on whether chert dissolution is achieved by alkaline (BARLEY et al., 1999; Taylor et al., 2001), or acidic fluids (THORNE et al., 2004; FIGUEIREDO E SILVA et al., 2013).

Hypogene models gained popularity in the past ca. fifteen years due to an increasing number of studies focussing on so-called "hard ore" (see chapter 2, section 2.2.5). This ore type usually only makes up a fraction of BIF-hosted iron ore deposits and is closely associated with small meter-sized mafic dikes (FIGUEIREDO E SILVA et al., 2011; LOBATO et al., 2005). In the

vicinity of these dikes, textural evidence indicative of carbonate metasomatism is common. Consequently, the majority of recent hypogene models invoke hydrothermal desilicification and replacement of chert by carbonate, followed by carbonate removal during weathering (BEUKES et al., 2003; GUEDES et al., 2003; LOBATO et al., 2005). Evidence for widespread carbonate metasomatism, however, is absent in BIF-hosted iron ore deposits. Thus, it is more likely that carbonate metasomatism represents a localized feature, constrained to the periphery of mafic dikes. In fact, synmetamorphic carbonation of mafic sills and dikes is a well known and common phenomena under greenschist facies conditions that produces similar textures (GRAHAM et al., 1983; SKELTON, 2011).

Although hydrothermal fluids could have transported large amounts of silica, since quartz solubility is quite high at elevated temperatures, e.g. 715 ppm (= 715 mg L^{-1}) at 300°C (RIMSTIDT, 1997), the absence of silica enriched aureoles in country rocks surrounding BIF-hosted iron ore deposits argues strongly against the occurrence of such a process (MORRIS & KNEESHAW, 2011).

Chapter 2 Geological Setting

2.1 Regional geology

The Carajás Mineral Province is located in the eastern part of the Southern Amazon Craton (Fig. 2.1). The province is composed of two major tectonic segments, the 3.0 to 2.86 Ga Rio Maria Block in the south (ALMEIDA et al., 2011), and the 3.0 to 2.55 Ga Itacaiúnas Shear Belt in the north (MACHADO et al., 1991). Recently, FEIO et al. (2013) proposed the existence of a smaller third segment. This transitional sub-domain is situated in the southern part of the Itacaiúnas Shear Belt. U-Pb dating of zircon from granitic rocks of the Canaã dos Carajás area, suggests that a crustal terrane existed in this sub-domain at ca. 3.2 Ga, 200 Ma prior to the formation of the Rio Maria Block and the basement rocks of the Itacaiúnas Shear Belt. To the east, the Carajás Mineral Province is bordered by the Neoproterozoic Araguaia Belt, which formed during the Brasiliano/Pan-African orogeny (750 to 550 Ma). In the north, it is limited by the Trans-Amazonian (2.2 to 1.95 Ga) Maroni-Itacaiúnas province (TASSINARI & MACAMBIRA, 1999).

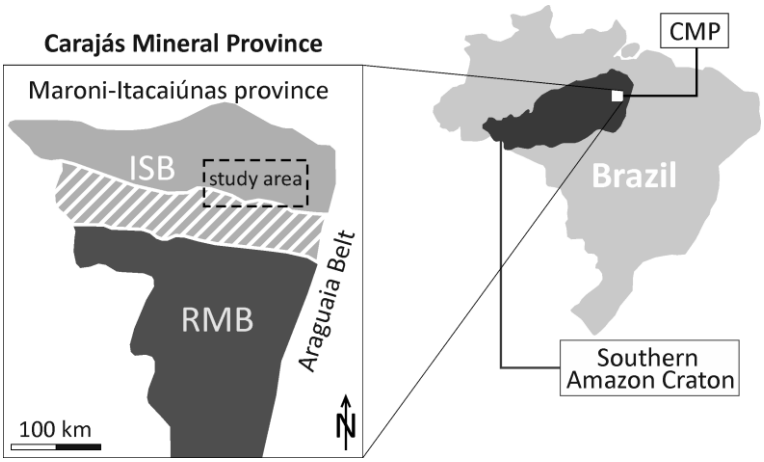

Fig. 2.1 Location of the Carajás Mineral Province (CMP) in Brazil (after GRAINGER et al., 2008; SIEPIERSKI & FILHO, 2016). The study area (Fig. 2.2) is located in the northern part of the CMP, in the Itacaiúnas Shear Belt (ISB). The southern part of the CMP is comprised of the Rio Maria Block (RMB). The dashed area represents the transitional sub-domain, proposed by FEIO et al. (2013). To the east, the CMP is bordered by the Araguaia Belt, and to the north by the Maroni-Itacaiúnas province.

The Rio Maria Block consists of metamorphosed greenstone sequences of the Andorinhas Supergroup. Bulk geochemical and neodymium isotope data suggest a formation in an island-arc setting (SOUZA et al., 2001). The Rio Maria Block was intruded various times, between 3.0 to 2.86 Ga, by ultramafic to felsic melts. In the period of 2.86 to 2.76 Ga, the island arcs were cratonized (amalgamation, uplift and crustal stabilization). Subsequent weathering and erosion of the craton provided material for the formation of the platform sediments of the <2.76 Ga Rio Fresco Group. Both the Rio Maria Block and the Itacaiúnas Shear Belt were affected by A-type granite magmatism between 1.9 to 1.8 Ga, which took place in an extensional tectonic setting. During this period, wide areas (ca. 1 500 000 km^2) of

the Amazon Craton were affected by the Uatumã magmatic event (KLEIN et al., 2012). A general overview of the tectonic evolution of the Rio Maria Block is given in Table 2.1.

Table 2.1 Tectonic evolution of the Rio Maria Block (modified after SOUZA et al., 2001).

Age [Ga]	Lithostratigraphy	Source	Tectonic Setting	Episode
3.04 - 2.94 (?)	**Andorinhas Supergroup**			
	Komatiite, tholeiitic basalts and gabbros	Depleted mantle	Island-arc (?)	
	Dacite	Oceanic crust	Island-arc	Juvenile accretion
2.97	**Serra Azul Complex**			
	Ultramafic and mafic layered intrusions	Depleted mantle (?)	?	
2.96	**Arco Verde Tonalite**	Oceanic crust	Island-arc	
		Unconformity		
2.87 - 2.86	**Intrusions** *(tonalite-trondhjemite-granite-granodiorite)*			
	Rio Maria granodiorite	Oceanic crust	Island-arc	Juvenile accretion
	Mogno Trondhjemite	Oceanic crust	Island-arc	
	Leucogranites	Contaminated oceanic crust	Island-arc	
	The Rio Maria Block stabilized at ca. 2.87 – 2.86 Ga by amalgamation of island arcs			
		Unconformity		
<2.76	**Rio Fresco Group**			
	Platform Sediments		Passive continental margin (?)	Regional extension
1.9 - 1.8	**Jamon Suite** *(A-type granites)**			
	Seringa Jamon Musa etc.			Regional extension

* DALL'AGNOL et al. (2005) and references therein.

The crystalline basement of the Itacaiúnas Shear Belt formed around 3.0 Ga (AVELAR et al., 1999; PIDGEON et al., 2000), similar to the oldest known units of the Rio Maria Block. It is unconformably overlain by metavolcano-sedimentary rocks of the Itacaiúnas Supergroup (DOCEGEO, 1988), deposited in the Neoarchean Carajás basin. The Itacaiúnas Shear Belt hosts a number of mafic to felsic intrusions with varying dimensions. Their emplacement is closely related to the tectonic evolution of the region (compression and shearing events). A detailed description of the geology and the development of the Itacaiúnas Shear Belt is given in the following section. The spatial distribution of the stratigraphic units is illustrated in the geological map of the study area (Fig. 2.2).

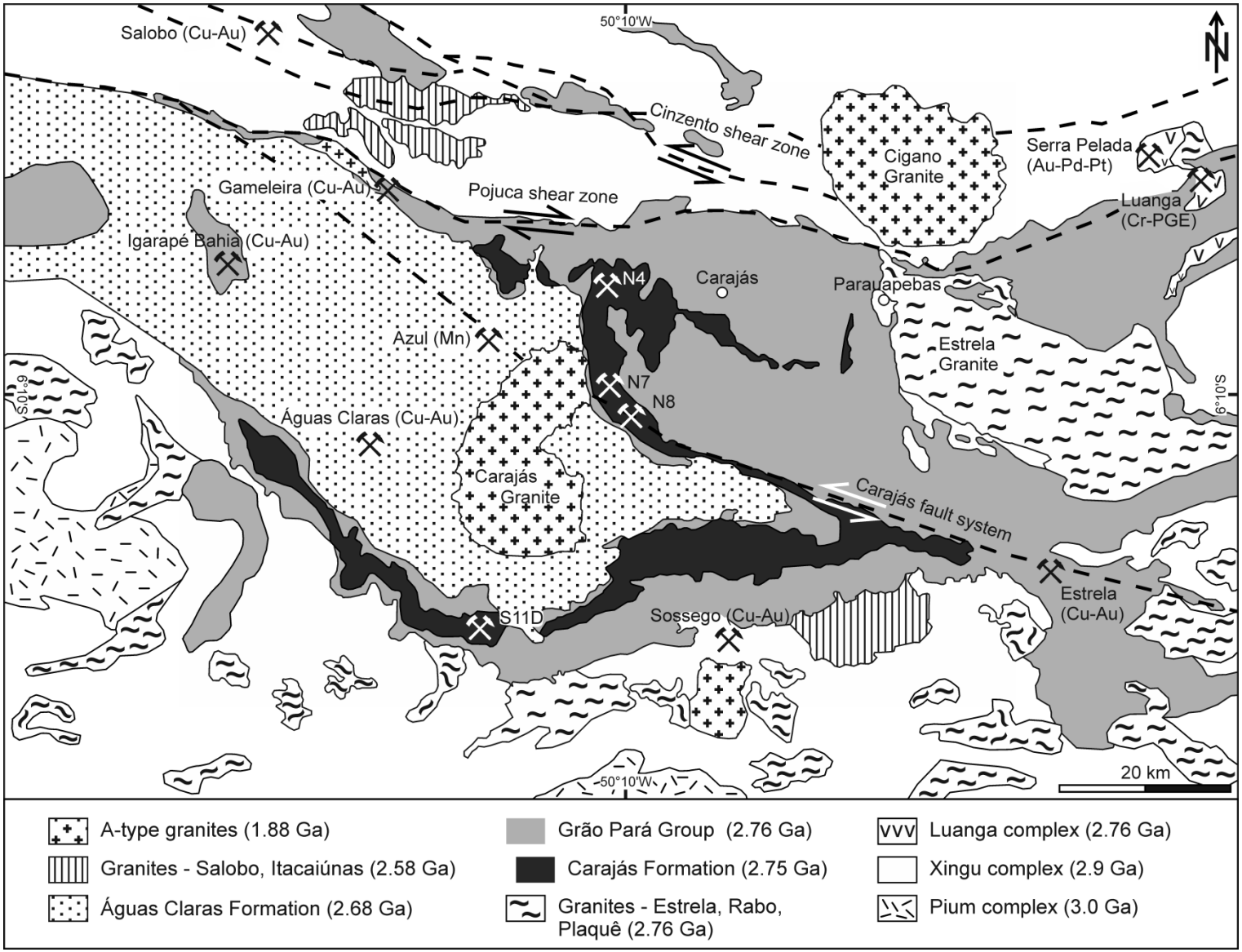

Fig. 2.2 Geological map of the study area, located in the northern part of the Carajás Mineral Province (after DOCEGEO, 1988; COSTA, 2007; ASSIS, 2013; Vale, unpublished data).

2.2 Local geology

2.2.1 Crystalline basement

The study area is located in the northern part of the Carajás Mineral Province, in the Itacaiúnas Shear Belt (Fig. 2.1). The crystalline basement of the region consists of the Pium and the Xingu complex. The Pium complex is made up of mafic (tholeiitic) and felsic (charnockite, enderbite) orthogranulites. Its parent rocks were initially emplaced at ca. 3.0 Ga and underwent granulite facies metamorphism around 2.86 Ga, based on U-Pb dating of oscillatory-zoned cores and rims of zircon, hosted in enderberite (PIDGEON et al., 2000). The ca. 2.9 Ga Xingu complex (AVELAR et al., 1999), consists of orthogneiss, metagranodiorite, trondjhemite, amphibolite and migmatite. The latest episode of migmatization affected the Xingu complex at 2.86 Ga (MACHADO et al., 1991), contemporaneous with the granulite facies metamorphism of the Pium complex.

2.2.2 Metavolcano-sedimentary successions

The crystalline basement is unconformably overlain by volcanic and sedimentary sequences, deposited in the Neoarchean Carajás basin. These rocks underwent varying degrees of metamorphism. DOCEGEO (1988) assign the stratigraphic units to the Itacaiúnas Supergroup (Table 2.2). These researchers propose that the Igarapé Pojuca Group formed coeval with the Igarapé Salobo Group.

The lithology and geochronological data presented in Table 2.2 shows that the stratigraphy of the Itacaiúnas Supergroup can be further simplified. The Igarapé Pojuca, Igarapé Salobo, Grão Pará and Igarapé Bahia Groups all consist of chemical and clastic metasedimentary rocks, which are intercalated with mafic and subordinate intermediate to felsic metavolcanic rocks. The available geochronological data indicates that they formed during the same period between ca. 2.76 to 2.75 Ga (GALARZA et al., 2001; KRYMSKY et al., 2007; MACHADO et al., 1991). In fact, the different groups only vary in the level of metamorphic overprint and the areas in which they are exposed. For example, the Igarapé Salobo Group is present in outcrops along the Cinzento Shear Zone and was affected by amphibolite facies metamorphism, while the Grão Pará Group rocks occur ca. 10 km south and underwent lower greenschist facies metamorphism. Hence, the above mentioned groups can be summarized into a single stratigraphic unit, which locally underwent varying degrees of metamorphism. Throughout the thesis, this unit will be referred to as Grão Pará Group.

The Buritirama and the Rio Fresco Group were also subjected to different levels of metamorphism. However, both groups share similarities in their lithology, e.g. they are made up of clastic and chemical metasediments, host manganese deposits and contain no metavolcanic rocks. This indicates that they form a single stratigraphic unit that locally underwent varying degrees of metamorphism (DARDENNE & SCHOBBENHAUS, 2001). Consequently, ARAÚJO et al. (1988) rearranged the two groups into the Águas Claras Formation.

This term has since then become established in the literature on the Itacaiúnas Shear Belt and will be used in the thesis instead of the Buritirama and Rio Fresco Groups of DOCEGEO (1988).

Table 2.2 Stratigraphy of the Itacaiúnas Supergroup after DOCEGEO (1988) with additional geochronological data.

Group	Lithology	Metamorphism	Age [Ma]	Reference
Rio Fresco	Clastic and chemical sediments hosting manganese deposits	None/very low grade	<2760 (assumed)	e.g. SOUZA et al. (2001)
Buritirama	Clastic and chemical metasediments (quartzite, mica schist) hosting manganese deposits	Medium grade	-	-
Igarapé Bahia	mafic metavolcanic rocks, oxide- and silicate facies BIF, clastic metasediments	Low grade	2747 ± 1	GALARZA et al. (2001)
Grão Pará	Mafic and minor intermediate to felsic metavolcanic rocks, oxide facies BIF, clastic metasediments (quartzite and meta-arkose)	Low grade	2751 ± 4	KRYMSKY et al. (2007)
			2759 ± 2	MACHADO et al. (1991)
Igarapé Pojuca & Igarapé Salobo	Mafic and minor intermediate metavolcanic rocks, oxide and silicate facies BIF, clastic metasediments (quartzite and meta-arkose)	Medium grade	2761 ± 3	MACHADO et al. (1991)

The Grão Pará Group is subdivided into the Parauapebas, Carajás and Igarapé Cigarra Formation (Table 2.3). The Parauapebas Formation is a 4 to 6 km thick metavolcanic sequence that forms the lower part of the Grão Pará Group. It consists predominantly of metabasalt and mafic agglomeratic breccias, which are intercalated with meter-scale units of metaryholite, -dacite and stratified felsic metatuffs. In outcrops on the Serra Norte mountain range, the felsic rocks account for ca. 10 to 15% of the exposed Parauapebas Formation (OLSZEWSKI et al., 1989). U-Pb dating of zircon from a rhyodacitic saprolite gave an age of ca. 2.76 Ga for the Parauapebas Formation (MACHADO et al., 1991).

The Carajás Formation conformably overlies the Parauapebas Formation (BEISIEGEL et al., 1973). It is made up of oxide facies BIF units, which host the giant high-grade iron ore deposits of the Carajás Mineral Province. The BIFs contain minor units of black shale (CABRAL et al., 2013), and are intruded by mafic sills and dikes. TRENDALL et al. (1998) obtained an U-Pb age of 2.74 Ga for zircon from a dolerite sill, hosted in the N4 deposit.

TEIXEIRA & EGGLER (1994) further report the existence of felsic dikes in the N4 deposit, a feature that has not been observed in any other BIF-hosted iron ore deposit of the Carajás region. These felsic dikes could be related to a nearby granite intrusion, which is located only 3 km north of the N4 deposit (PINHEIRO, 1997). In the Serra Sul mountain range, the BIF units are underlain by a >50 m thick magnetite-rich sedimentary breccia, which likely formed by submarine slumping of an unconsolidated BIF precursor sediment (CABRAL et al., 2013). The thickness of the Carajás Formation varies between 200 to 250 m in the Serra Norte and extends to more than 300 m in the Serra Sul (BEISIEGEL et al., 1973). U-Pb dating of zircon obtained from a trachyte at the base of the Carajás Formation provided a maximum age of ca. 2.75 Ga (KRYMSKY et al., 2007).

The Igarapé Cigarra Formation rests conformably on the Carajás Formation. In its basal part, it consists of metabasalt and mafic metatuff intercalated with subordinate BIF. These units are overlain by chemical and clastic sediments, mainly chert and quartz arenites (MACAMBIRA et al., 1990). At present, no geochronological data is available for the Igarapé Cigarra Formation. An attempt by TRENDALL et al. (1998) to date zircon from metabasalt of the lower Igarapé Cigarra Formation, produced a wide range of Pb/U ratios with no consistent age population. This could be the result of Pb-loss or late growth of new zircon.

Table 2.3 Simplified stratigraphy of the Itacaiúnas Supergroup with geochronological data.

Group	Formation	Lithology	Age [Ma]	Reference
-	Águas Claras	Clastic and chemical sediments hosting manganese deposits	2645 ± 12 2681 ± 5	DIAS et al. (1996) TRENDALL et al. (1998)
		Unconformity (?)		
Grão Pará	Igarapé Cigarra	Metabasalt, metatuff, subordinate BIF, clastic and chemical sediments	-	-
	Carajás	Oxide facies BIF	2751 ± 4	KRYMSKY et al. (2007)
	Parauapebas	Metabasalt with minor felsic metavolcanic rocks	2759 ± 2	MACHADO et al. (1991)

It is generally assumed that the Águas Claras Formation rests unconformably on the Grão Pará Group, although this contact has never been observed in the field (e.g. TOLBERT et al., 1971). Available geochronological data for the Águas Claras Formation, however, point to a formation between ca. 2.68 to 2.64 Ga, based on U-Pb dating of detrital zircon by TRENDALL et al. (1998) and zircon derived from a metagabbroic sill by DIAS et al. (1996). Due to the apparent 70 Ma gap between the deposition of the Grão Pará Group and the Águas Claras Formation, opinions differ on whether the Águas Claras Formation should be included in the Itacaiúnas Supergroup/Grão Pará Group, or if the terminology should be rearranged in a new

way. The Águas Claras Formation consists of sediments from two different depositional environments. First, arenites and conglomerates deposited in braided river systems, and second, sequences of mud- and siltstones, which formed in a continental shelf setting. The predominantly sericitic matrix of the sediments indicates that they underwent anchimetamorphism (ARAÚJO & MAIA, 1991). Locally, the mud- and siltstone sequences forming the top of the Águas Claras Formation are associated with manganese deposits, e.g. the Azul and Buritirama deposits.

2.2.3 Basin type models

Over the past 45 years a number of models emerged, concerning the origin and development of the Carajás basin in the Neoarchean. Based on lithological, structural and geochemical data, researchers reached different conclusions.

Geologists of DOCEGEO (1988) first proposed that the Carajás basin formed by continental rifting, due to the observed succession of lithological units in the area. In their reasoning, the bimodal volcanism of the Parauapebas Formation signals the opening of the basin, while the Carajás Formation is representative of sedimentation and volcanism in a fully developed rift. The deposition of the Igarapé Cigarra Formation took place at the time when the basin began to close. The marine shallow water and fluvial sediments of the Águas Claras Formation record the final stage of its closing.

The discovery of a large E-W trending fault system with sinistral strike-slip movement, located in the center of the Carajás Fold, by ARAÚJO et al. (1988), established the term Itacaiúnas Shear Belt for the northern part of the Carajás Mineral Province. It also inspired an alternative interpretation of the Carajás basin. In this model, the juxtaposed iron ore bodies, situated on the ridges of the Serra Norte mountain range, developed from BIF that was initially deposited not in a single, but in several isolated transtensional basins. These basins opened along faults of the Itacaiúnas Shear Belt. In order to explain the position of the iron ore deposits on the Serra Norte, a later transpressional event was invoked. This hypothetical event would have thrusted the BIFs upwards on the Serra Norte, thus generating a positive flower structure.

This idea was challenged by PINHEIRO & HOLDSWORTH (1997) with detailed structural data of the N4 iron ore deposit. Their results indicate that BIF deposition took place in a single, large intracratonic basin. Later fragmentation and uplift would then have produced the isolated iron ore deposits of the Serra Norte (Fig. 2.3).

The hypothesis of PINHEIRO & HOLDSWORTH (1997) was challenged in turn by ROSIÈRE et al. (2006) with regional structural data for the northern Carajás Mineral Province. These researchers suggest that the Carajás Fold and the Carajás Fault system represent superimposed events. They argue that the Carajás Fold is a synform-antiform pair, formed by N-S oriented compression. In this context, the NW-SE trending Carajás Fault system would represent a lateral escape structure, which developed in response to the N-S oriented

shortening. According to ROSIÈRE et al. (2006), the regional structure of the Carajás basin best fits a back-arc basin setting. This interpretation is in accordance with geochemical studies of the Grão Pará Group by DARDENNE et al. (1988) and ZUCCHETTI (2007). Metabasalts of the Grão Pará Group have a calc-alkaline affinity and further geochemical characteristics indicative of a formation in a continental arc (Fig. 2.4).

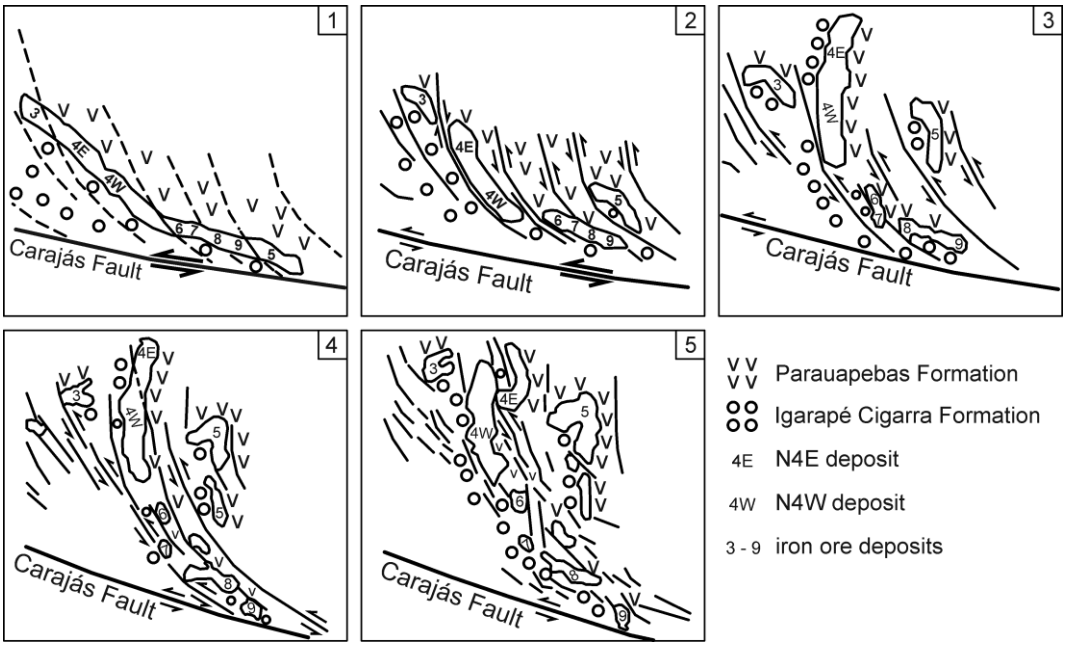

Fig. 2.3 Development of the Serra Norte iron ore deposits, based on the model of PINHEIRO & HOLDSWORTH (1997). Sinistral movement along the Carajás Fault system causes the fragmentation of the Carajás Formation and the uplifting of its segments on the Serra Norte (redrawn from MACAMBIRA, 2003).

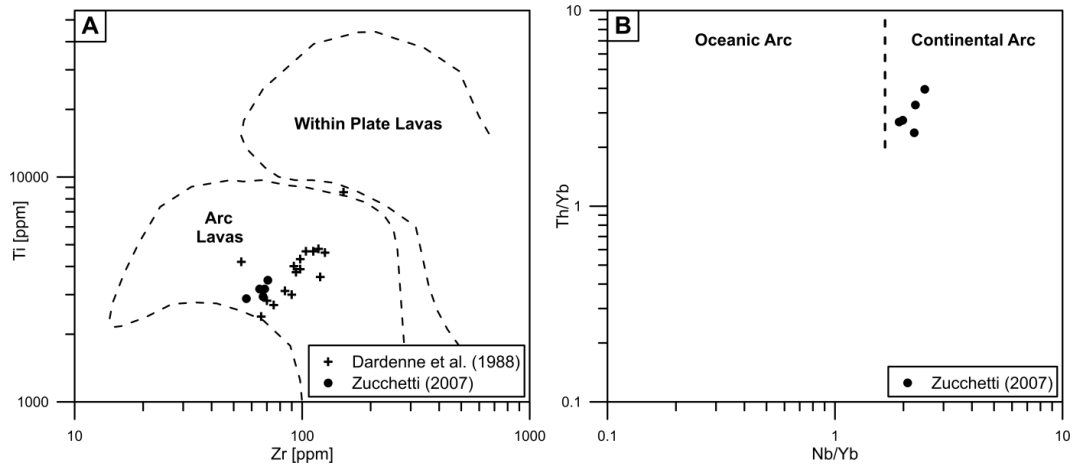

Fig. 2.4 (**A**) Ti vs. Zr and (**B**) Th/Yb vs. Nb/Yb covariation diagrams for metabasaltic rocks of the Grão Pará Group. (**A**) The analyses plot in the field of volcanic arc lavas (modified after DARDENNE et al., 1988). (**B**) The covariation diagram after PEARCE (1983) indicates that the metabasalts formed in a continental arc setting (redrawn from ZUCCHETTI, 2007).

2.2.4 Magmatism and tectonic evolution of the Itacaiúnas Shear Belt

The Itacaiúnas Shear Belt was intruded in the Neoarchean and Proterozoic by melts with varying compositions (Table 2.4). Magmatism in the Carajás region largely occurred during three episodes.

The first episode from 2.76 to 2.73 Ga is characterized by the emplacement of E-W elongated granitoid bodies of the Estrela complex, Serra do Rabo, Plaquê Suite and Igarapé Gelado granites. These intrusions likely formed in a continental margin orogeny, associated with weak and protracted N-S oriented shortening. This tectonic setting is indicated by structural data of the Estrela complex, Igarapé Gelado and Serra do Rabo granite, which point to a synkinematic emplacement (BARROS et al., 2009). The Luanga complex, a layered mafic-ultramafic intrusion, formed coeval to the granitoids, due to plume or rift magmatism. The Plaquê Suite granites have calc-alkaline affinities, which is in accordance with a synorogenic setting. The Igarapé Gelado granite has a more intermediate composition, while the granites of the Estrela complex and the Serra do Rabo derived from alkaline melts (A-type). Although A-type granites are often associated with rifting environments, they are also common in post-collisional settings, where they occur as intrusions along strike-slip faults (SYLVESTER, 1989). The geochemistry and structure of the Estrela complex and the Serra do Rabo granite shows that they formed in a post-collisional setting and were emplaced along E-W trending shear zones. As mentioned in section 2.2.3, the structural data for the northern Carajás Mineral Province points to a regional tectonic evolution in two stages, consisting of N-S oriented shortening, followed by lateral escape and the development of NW-SE trending strike-slip faults, i.e. the Itacaiúnas Shear Belt (ROSIÈRE et al., 2006). The A-type granites of the Estrela complex and the Serra do Rabo likely record the initial formation of the Itacaiúnas Shear Belt at ca. 2.76 Ga.

The strike-slip system was reactivated between 2.58 to 2.50 Ga, as indicated by overgrowths on zircon and newly formed monazite and titanite in plutonic and metavolcanic rocks (MACHADO et al., 1991). The reactivation was accompanied by a second episode of magmatism. The intrusion of granitoid bodies occurred predominantly along major shear zones, e.g. the Old Salobo granite was emplaced adjacent to the Cinzento shear zone.

The third major episode of magmatism took place in the Paleoproterozoic around 1.88 Ga and was characterized by the widespread emplacement of A-type granites in both the Itacaiúnas Shear Belt and the Rio Maria Block. In fact, large parts (ca. 1 500 000 km^2) of the Amazon Craton were affected by the so called Uatumã magmatic event (KLEIN et al., 2012). In the Itacaiúnas Shear Belt, this event is recorded by the emplacement of the Carajás, Cigano and Pojuca granites. The A-type Gameleira granite is likely also associated with this event, however, SHRIMP U–Pb dating produced a much younger age of ca. 1.6 Ga (PIMENTEL et al., 2003). All intrusions attributed to the third episode of magmatism are generally undeformed, which suggests that major movement along the strike-slip faults of the Itacaiúnas Shear Belt stopped prior to 1.9 Ga.

Table 2.4 Age and tectonic setting of intrusive rocks in the Itacaiúnas Shear Belt.

Intrusion	Lithology	Tectonic Setting	Age [Ma]	Reference
Gameleira granite	Syenogranite (A-type)	Anorogenic	1583 + 9/ - 7	PIMENTEL et al. (2003)
Pojuca granite	Rapakivi granites (A-type)	Anorogenic	1874 ± 2	MACHADO et al. (1991)
Carajás granite			1880 ± 2	MACHADO et al. (1991)
Cigano granite			1883 ± 2	MACHADO et al. (1991)
Itacaiúnas granite	Granite	Intracontinental (?)	2560 ± 37	SOUZA et al. (1996)
Old Salobo granite	Granite	Intracontinental (?)	2573 ± 2	MACHADO et al. (1991)
Mafic sill	Gabbro	Passive margin	2645 ± 12	DIAS et al. (1996)
Igarapé Gelado granite	Monzogranite, granodiorite	Synorogenic	2731 ± 26	BARROS et al. (2009)
Plaquê Suite	Calc-alkaline granite	Synorogenic	2736 ± 24	AVELAR et al. (1999)
Serra do Rabo granite	Granite, syenogranite (A-type)	Synorogenic	2743 ± 2	BARROS et al. (2009)
Luanga complex	Gabbro, norite, peridotite, dunite	Plume or rift magmatism (?)	2763 ± 6	MACHADO et al. (1991)
Estrela complex	Monzogranite, syenogranite (A-type)	Synorogenic	2763 ± 7	BARROS et al. (2009)

At present, the regional structure of the Itacaiúnas Shear Belt is dominated by the Serra dos Carajás range and the Carajás, Cinzento and Pojuca Shear Zones (Fig. 2.5). The Serra dos Carajás is an irregular, s-shaped mountain range consisting of several topographic plateaus, i.e. the BIF-hosted iron ore deposits (TOLBERT et al., 1971), which are part of a WNW-striking synform–antiform pair, termed the Carajás fold (ROSIÈRE et al., 2006). The Serra dos Carajás formed by N-S oriented compression, possibly related to the second episode of magmatism. The southern range, the so called Serra Sul is a synform and the northern range, the Serra Norte represents an antiform. During the compressional phase, the Pium complex acted as a buttress against the metavolcano-sedimentary units located to its north, which resulted in the NE oriented deformation of the western segment of the Serra Sul. In its core, the synform–antiform pair is truncated by the Carajás Shear Zone, a strike-slip fault system, which also strikes approximately WNW (PINHEIRO & HOLDSWORTH, 1997; ROSIÈRE et al., 2006). The 1.88 Ga Carajás granite, situated in the center of the the Carajás fold, is undeformed,

which shows that no major lateral movement occurred along the Carajás Shear Zone in the past 1.88 Ga. However, the presence of hot springs in the Cururú area, forming the middle part of the Cinzento strike-slip system (PINHEIRO, 1997), and the occurrence of minor earthquakes in the Carajás region, indicates that the faults are still active (COSTA et al., 1993). Thus, minor episodes of fault reactivation probably occurred in the past 1.88 Ga (HOLDSWORTH & PINHEIRO, 2000).

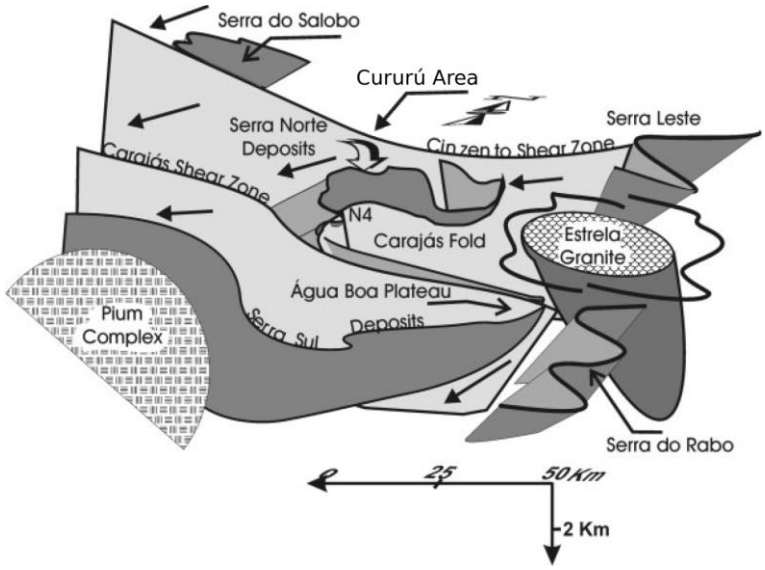

Fig. 2.5 Block model illustrating the regional structure of the Itacaiúnas Shear Belt (modified after ROSIÈRE et al., 2006).

2.2.4 Mineral deposits

The Carajás region hosts a variety of mineral deposits with Fe, Mn, Cu, Au, PGE and Cr mineralizations. Large BIF-hosted high-grade iron ore bodies are situated on the Serra Norte (N1 - N9) and the Serra Sul (S1 - S45), with probable and proven reserves of 7 Gt @ 66 wt.% Fe (Vale, 2014) and estimated resources of 18 Gt @ 66 wt.% Fe (BEISIEGEL et al., 1973). Additional iron ore deposits are located on the São Felix (W of the study area) and the Serra Leste (NE of the study area). A detailed description of the high-grade iron ore deposits of the Serra dos Carajás is provided in section 2.2.5.

Sediment-hosted manganese deposits, e.g. the Azul and Buritirama (N of the study area) deposits, are locally present in mud- and siltstone sequences of the 2.68 Ga Águas Claras Formation.

The gold mineralization of the Carajás Mineral Province includes base metal-poor orogenic lode-gold deposits, characteristic of the Rio Maria Block and IOCG (iron oxide-copper-gold) deposits, present in the Itacaiúnas Shear Belt (GRAINGER et al., 2008). The IOCG deposits are subdivided into two groups, according to their characteristic styles of mineralization. Deposits enriched in Cu, Au, W, Sn and Bi, e.g. the Águas Claras, Gameleira and Estrela

deposits, are linked to the regional 1.88 Ga episode of A-type magmatism (TALLARICO et al., 2004). IOCG deposits with Cu-Au (Mo-Ag-U-REE) mineralizations, e.g. the Igarapé Bahia, Salobo and Sossego deposits, are associated with the second episode of magmatism that affected the Carajás region earlier, between 2.58 to 2.50 Ga (TALLARICO et al., 2005).

In the NE part of the study area lie the Serra Pelada and Luanga deposits, which are both enriched in PGE. The Serra Pelada is a sediment-hosted, epigenetic Au-Pd-Pt deposit whose mineralization seems to be linked to the 1.88 Ga A-type magmatism (GRAINGER et al., 2008). The exact nature of the deposit, however, is still debated. The Luanga deposit is part of the 2.76 Ga Luanga complex, a mafic-ultramafic layered intrusion. The PGE mineralization is associated to chromite seams and layers (DIELLA et al., 1995).

2.2.5 BIF-hosted iron ore deposits

The high-grade iron ore deposits of the northern Carajás Mineral Province form large outcrops on the northern (Serra Norte) and southern (Serra Sul) ridges of the Serra dos Carajás, which stand out from the general morphology as topographic plateaus (TOLBERT et al., 1971).

The iron ore bodies consist mainly of friable material. This so-called "soft ore" is comprised of martite, i.e. hematite pseudomorphs after magnetite, microplaty hematite, goethite, chert fragments and minor pyrite, chalcopyrite and covellite. The ore bodies extend to depths of several hundred meters and host lenses of compact hematite ore, so-called "hard ore", and chunks of BIF (Fig. 2.6A). Hard ore occurs in the vicinity of mafic sills and dikes (Fig. 2.6B), and in hinge zones of large folds (FIGUEIREDO E SILVA et al., 2011; LOBATO et al., 2005). Hard ore is made up of anhedral and microplaty hematite, martite, carbonate, and minor pyrite, chalcopyrite and covellite. Oxygen isotope and fluid inclusion studies hint towards a hydrothermal origin (GUTZMER et al., 2006; FIGUEIREDO E SILVA et al., 2013). Hard ore formation likely represents a local feature associated with the emplacement of small, meter-sized mafic intrusions and enhanced fluid flow along faults.

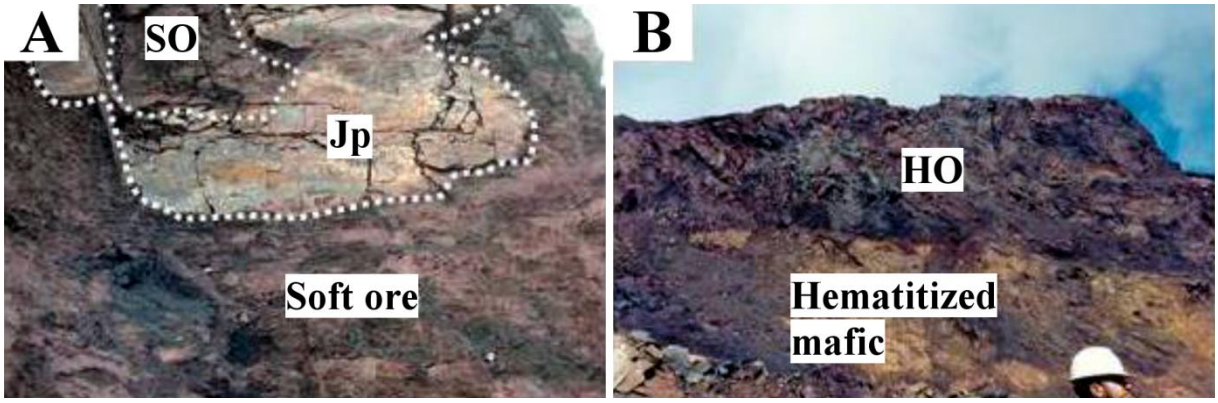

Fig. 2.6 (**A**) BIF fragment (Jp) embedded in soft ore (SO), N4W deposit. (**B**) Hard ore (HO) surrounding a hematitized mafic dike, N5E deposit (modified after FIGUEIREDO E SILVA et al., 2011).

The contact of the ore bodies to the underlying BIF is abrupt, typically within less than one meter (Fig. 2.7). Pristine BIF of the Carajás Formation consists of alternating chert and magnetite-rich layers. This mineral assemblage is characteristic for oxide facies BIF. Hydrothermal alteration in the vicinity of mafic dikes introduced carbonate, pyrite, chalcopyrite, stilpnomelane and chlorite (see chapter 3, section 3.2). Near the contact to the overlying ore bodies, magnetite is partially or completely martitized.

Fig. 2.7 Photograph of the transition from BIF to high-grade iron ore, i.e. soft ore (S11D deposit, drillhole S11D-330, 217 m depth).

Minor units of sulfidic black shale occur in the upper, middle and lower parts of BIF underlying the S11D iron ore deposit (CABRAL et al., 2013). Furthermore, drilling of this deposit intercepted a >50 m thick magnetite-rich breccia at the base of the Carajás Formation (CABRAL et al., 2013).

At the surface, the iron ore bodies are covered by "canga", an iron duricrust comprised of hematite and BIF fragments, which are cemented by iron oxyhydroxide minerals. Canga is extremely resistant to weathering. SHUSTER et al. (2012) estimate a rate of surface erosion between 0.13 to 0.46 m/Ma for canga from the Carajás region. Fig. 2.8 illustrates the typical build-up of BIF-hosted high-grade iron ore deposits in the Carajás Mineral Province.

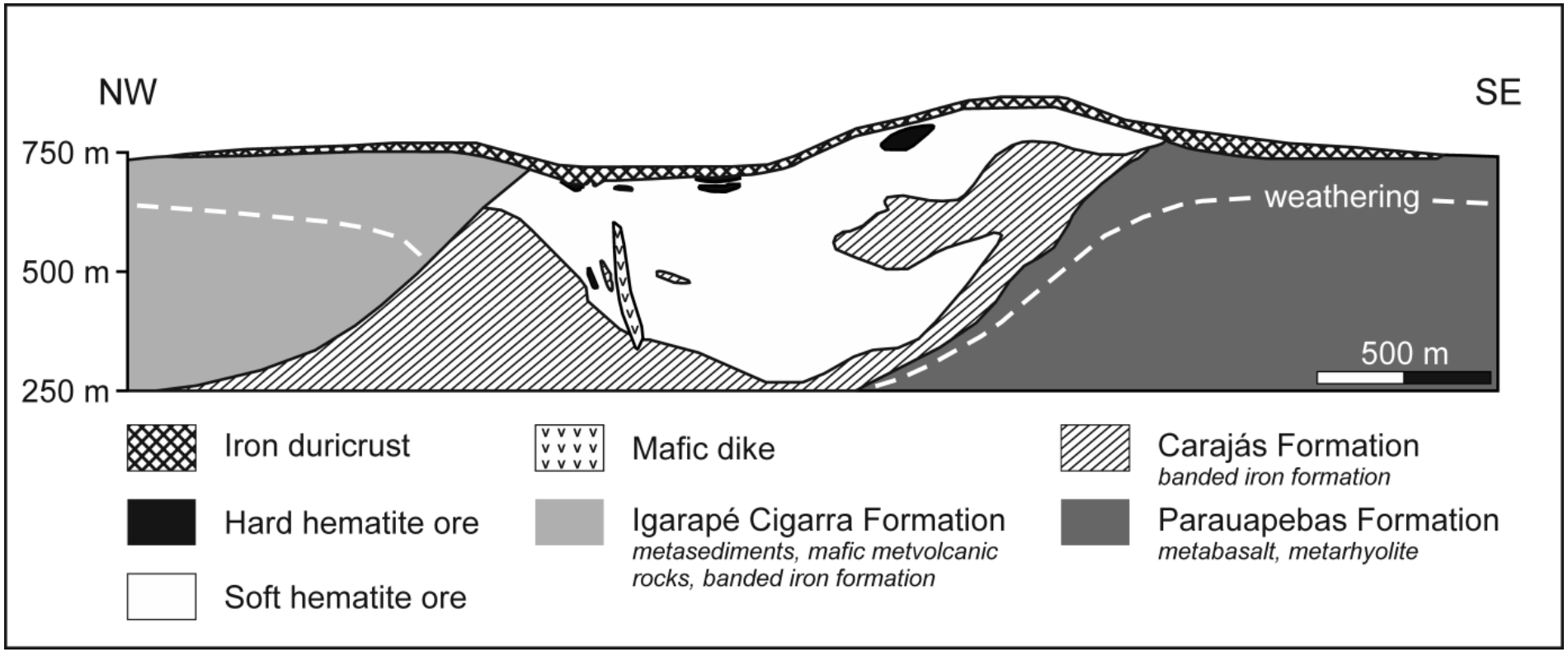

Fig. 2.8 Cross section of the S11D deposit, Serra Sul (modified after Vale, unpublished data).

Chapter 3 Samples

The samples used in this study were taken from drill cores provided by the mining company Vale during field work in 2010. In total, 46 core sections from five drill holes of the N7, N8 and S11D deposits were carefully selected after the inspection of over 2000 m of drill core. The locations of the drill holes are shown in Fig. 3.1. Their geographic coordinates are provided in Table 3.1. The sample set comprises drill cores of canga (n=1), soft ore (n=26), BIF (n=10), a magnetite-rich breccia (n=6) and intercalated volcanic units (n=3). A comprehensive list of all samples and the methods used for their analysis, is given in Table 3.2. The petrography of the samples was studied in 41 polished thin sections using transmitted and reflected light microscopy (section 3.2). In total, 47 samples were chosen for whole-rock geochemical analysis (see chapter 4). Ten representative thin sections were selected for in-situ Fe isotope measurements (see chapter 5).

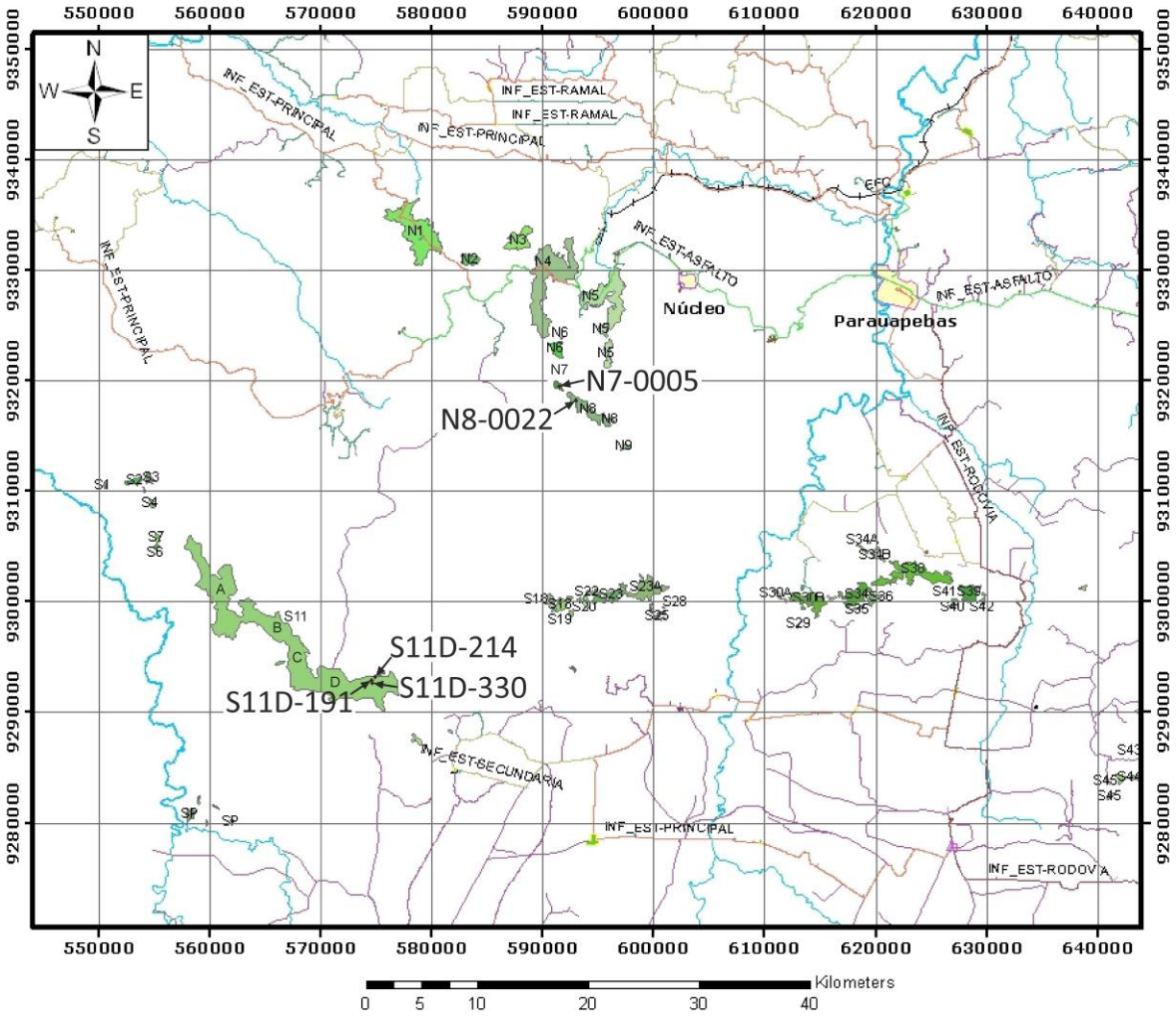

Fig. 3.1 Map of the northern Carajás region, showing the locations of the iron ore deposits (green). The sampled drill holes are indicated (modified after Vale, unpublished data).

Table 3.1 Geographic locations of the sampled drill holes.

Drill hole	Deposit	Coordinates (UTM)
S11D-330	S11D	574614.30 E / 9292634.55 S
S11D-191	S11D	574554.28 E / 9292889.28 S
S11D-214	S11D	574867.63 E / 9293194.47 S
N7-0005	N7	591494.78 E / 9319515.27 S
N8-0022	N8	592976.66 E / 9318234.46 S
UTM-zone 22, projection: WGS 84		

Table 3.2 Sample list and associated analytical work (bars indicate the number of samples).

Depth [m]	Type	Geochemistry	Microscopy	Fe isotope analysis
Drill hole S11D-330				
0.10 - 0.30	Canga			
06.00 - 06.20	Soft ore			
14.05 - 14.25	Soft ore			
24.40 - 24.60	Soft ore			
34.85 - 35.05	Soft ore			
45.15 - 45.35	Soft ore			
55.05 - 55.25	Soft ore			
65.35 - 65.55	Soft ore			
76.25 - 76.45	Soft ore			
87.85 - 88.05	Soft ore			
97.50 - 97.70	Soft ore			
107.40 - 107.60	Soft ore			
117.55 - 117.75	Soft ore			
132.65 - 132.85	Soft ore			
132.85 - 133.05	Soft ore			
142.70 - 142.90	Soft ore			
152.50 - 153.00	Soft ore			
162.80 - 163.00	Soft ore			
172.85 - 173.05	Soft ore			
182.75 - 182.95	Soft ore			
192.95 - 193.15	Soft ore			
203.30 - 203.50	Soft ore			
213.15 - 213.35	Soft ore			
217.50 - 217.70	Soft ore			
217.70 - 217.90	BIF			
219.61 - 219.70	BIF			
234.18 - 234.49	BIF			

Table 3.2 (*continued*).

Depth [m]	Type	Geochemistry	Microscopy	Fe isotope analysis
Drill hole S11D-191				
219.38 - 219.62	BIF			
251.41 - 251.83	BIF			
281.45 - 281.92	Magnetite-rich breccia			
Drill hole S11D-214				
105.15 - 106.05	Volcanic material			
361.36 -361.61	Magnetite-rich breccia			
397.11 - 397.36	Magnetite-rich breccia			
428.07 - 428.27	Magnetite-rich breccia			
434.52 -434.74	Magnetite-rich breccia			
495.40 - 495.55	Magnetite-rich breccia			
Drill hole N7-0005				
111.98 - 112.35	BIF			
391.02 - 391.39	Volcanic material			
Drill hole N8-0022				
11.30 - 11.50	Soft ore			
29.60 - 29.80	Soft ore			
48.46 - 48.66	Soft ore			
50.80 - 50.99	BIF			
84.36 - 84.52	BIF			
98.59 - 98.75	BIF			
127.73 - 128.19	Volcanic material			
135.50 - 135.60	BIF			

3.1 Macroscopic sample description

The studied BIF samples are comprised of micro- (0.3 to 1.7 mm) and mesobands (<2.54 cm) of chert and iron oxides (Fig. 3.2A). The banding is contorted and discontinuous due to crosscutting fractures. The appearance of the BIF samples reflects the long and complex tectonic history of the Carajás Mineral Province (see chapter 2, section 2.2.4). The chert bands have a grey to reddish color. The latter is the result of finely dispersed hematite. Soft ore has a reddish color, since it consists almost entirely of hematite (martite and minor microplaty hematite). With an increasing proportion of goethite, the color of soft ore shifts towards yellowish brown. The ore is comprised of millimeter to centimeter-sized clasts of hematite ± goethite/quartz embedded in a fine-grained groundmass (Fig. 3.2B). Canga is a compact iron duricrust made up of hematite and BIF fragments that are cemented by iron-oxyhydroxide minerals (Fig. 3.2C). The volcanic rocks studied here, are fine-grained, have a greenish color and an amygdaloidal texture. The infill of the vesicles consists of chlorite (Fig. 3.2D). Crosscutting veins are made up of quartz and goethite. The magnetite-rich breccia

consists of chert fragments floating in a matrix comprised almost entirely of magnetite (Fig. 3.2E, F). The presence of rounded, bent and tear-shaped chert fragments is suggestive of soft-sediment deformation (CABRAL et al., 2013; Fig. 3.2E). It is likely that the breccia formed by submarine slumping of an unconsolidated BIF precursor sediment. The magnetite-rich breccia shown in Fig. 3.2F is situated in the vicinity of a dolerite dike and was affected by hydrothermal alteration.

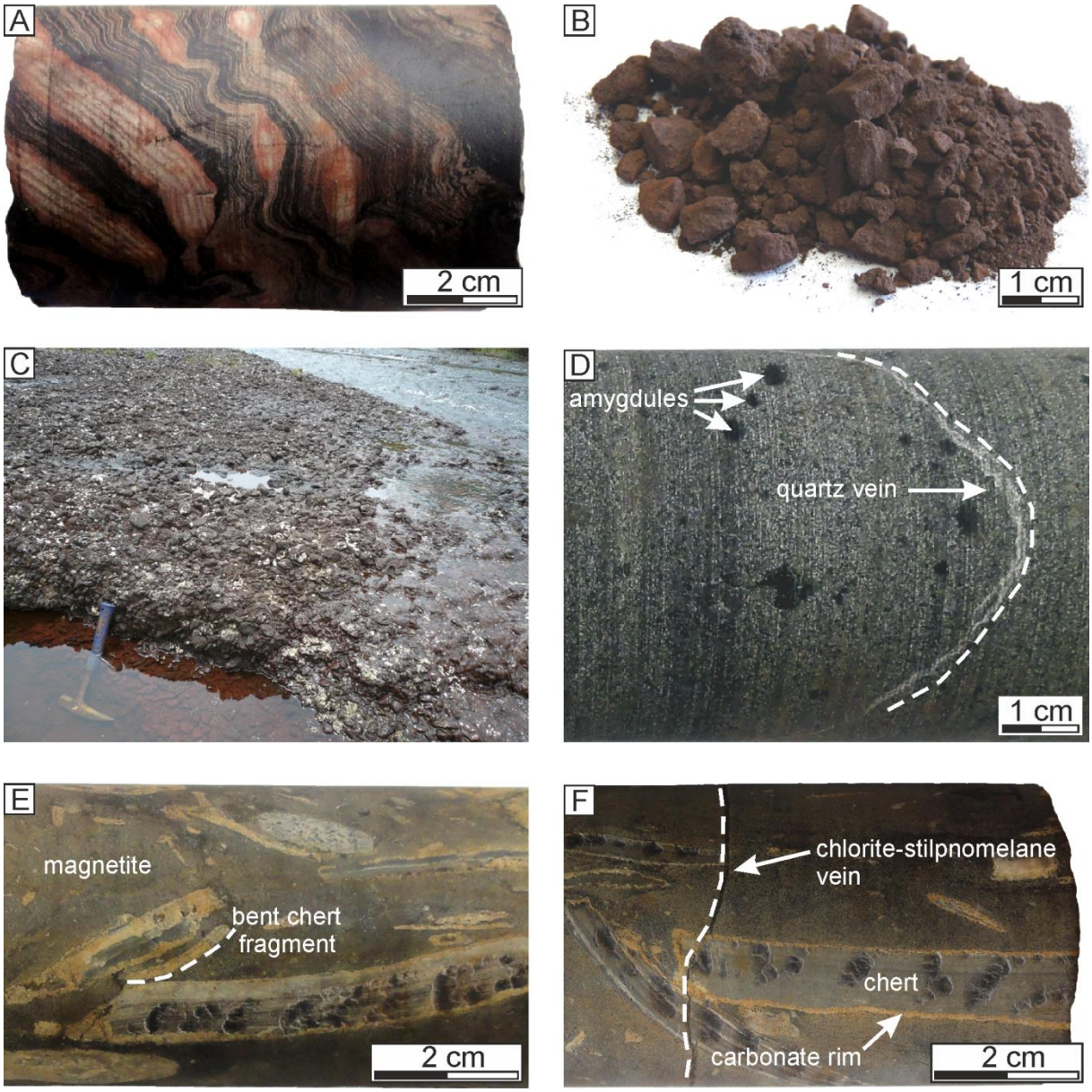

Fig. 3.2 Photographs of representative samples, illustrating the different rock units studied here. (**A**) Microbanded BIF (S11D-191, 251 m). (**B**) Soft ore comprised of reddish iron-oxyhydroxide minerals (S11D-330, 142 m). (**C**) Canga exposed along a riverbed (S11D deposit). (**D**) Aphanitic volcanic rock unit with an amygdaloidal texture. The drill core is truncated by a quartz vein (N7-0005, 391 m). (**E**) & (**F**) Magnetite-rich breccia hosting bent chert fragments (S11D-330, 361 m). Hydrothermal alteration associated with a nearby mafic dike emplaced chlorite-stilpnomelane veinlets and caused the formation of carbonate rims surrounding/replacing chert fragments.

3.2 Microscopic sample description

Polished thin sections (n=41) of BIF, soft ore, canga, magnetite-rich breccia and volcanic units were prepared by Ulf Hemmerling at the Clausthal University of Technology. The petrology and mineralization of the samples was studied under transmitted and reflected light using a Carl Zeiss Axio Scope.A1 binocular microscope. Pictures were taken with an Axiocam ICc 5 colour camera with a resolution of 5 megapixels.

Pristine BIF samples have a rather simple mineral assemblage comprised of magnetite and quartz (Fig. 3.3A, B, C). In addition, some samples, e.g. N8-0022, 98 m and N7-0005, 112.35 m, host spherulitic microstructures in chert bands (Fig. 3.3D). The occurrence of chert microspherulites has been reported before, for samples from the Serra Norte deposits (MACAMBIRA, 2003; LUZ & CROWLEY, 2012). Although chert microspherulites are a common component in BIFs worldwide, their origin is rather controversial. While some researchers propose a biogenic origin for these microstructures, supporting the role of microorganisms in BIF genesis (LABERGE, 1973; LUZ & CROWLEY, 2012), others suggest that they are the product of hydrothermal or diagenetic processes (HEANEY & VEBLEN, 1991; OEHLER, 1976).

In most of the studied BIF samples, the iron-rich bands consist mainly of magnetite, but minor martite and microplaty hematite are usually present, too. The proportion of the latter two minerals is significantly higher in the vicinity of the high-grade iron ore bodies (Fig. 3.3E, F). The optical examination of the polished thin sections under reflected light shows that magnetite is replaced by martite via an intermediate step of kenomagnetite formation. Kenomagnetite is an iron-deficient form of magnetite, and can be identified easily by its lower reflectivity in comparison to regular magnetite (KULLERUD et al., 1969). During the martitization process, part of the Fe(II) in magnetite diffuses through the crystal structure and reacts with oxygen to hematite (martite) along the rims of the now iron-deficient kenomagnetite crystal (DAVIS et al., 1968). This loss of Fe(II) causes a decrease in reflectivity, which gives kenomagnetite a brown color under reflected light (Fig. 3.3E, F). The pseudomorphic replacement of magnetite by martite is accompanied by a 2% increase in volume (MÜCKE & CABRAL, 2005), which generates small fractures, mostly along the grain boundaries of kenomagnetite and the newly formed martite. This allows meteoric fluids to enter and replace kenomagnetite cores with goethite (Fig. 3.3F).

Minor microplaty hematite is present in BIF and soft ore, as finely dispersed platelets and as crystals nucleating on martite (Figs. 3.3F and 3.4A, B). According to the conceptual model of MORRIS (1985; 2012), microplaty hematite forms by dehydration of goethite at temperatures in excess of 80°C (LANGMUIR, 1971). However, in the samples from the Carajás deposits, microplaty hematite crystals are often nucleating on martite, which suggests a formation by recrystallization from pre-existing martite (Fig. 3.4A, B). This observation is in accordance with recent geochemical evidence indicating that microplaty hematite forms by isochemical recrystallization of martite (HENSLER et al., 2015).

Hydrothermal alteration associated with mafic sills and dikes precipitated pyrite, chalcopyrite and carbonate in fractures crosscutting BIF and along the contact of chert and iron-rich bands (Fig. 3.4C, E, F). In some samples chalcopyrite is oxidized to covellite (Fig. 3.4D). Trace amounts of pyrite and/or chalcopyrite were observed in all thin sections, even in near-surface soft ore and canga (Fig. 3.5A). In the vicinity of dolerite dikes, hydrothermal fluids precipitated substantial amounts of chlorite and stilpnomelane (Figs. 3.4E and 3.5B), e.g. in the magnetite-rich breccia shown in Fig. 3.2E, F. In this sample, carbonate is present in rims surrounding and replacing chert fragments (Fig. 3.4E, F). Similar replacement textures have been observed in the N4 and N5 deposits and were interpreted as evidence for a hypogene stage of ore formation preceding supergene enrichment (BEUKES et al., 2003; GUEDES et al., 2003; LOBATO et al., 2005). The basic idea is that widespread hydrothermal carbonate metasomatism caused the replacement of chert by carbonate, which was later removed during weathering, thus producing friable soft ore. However, these replacement textures occur only locally, i.e. in the periphery of dolerite dikes, and are rarely observed in other iron ore deposits of the Carajás Mineral Province (FIGUEIREDO E SILVA et al., 2011). The hypogene model invoking widespread carbonate metasomatism is therefore highly unlikely. In contrast, localized synmetamorphic carbonation of marginal areas of mafic dikes under greenschist facies conditions, followed by postmetamorphic quartz-carbonate-sulfide veining is well documented in the literature (ANDERSON et al., 2004; GRAHAM et al., 1983; KLEINE, 2015; SKELTON, 2011; SKELTON et al., 1995; WHITE et al., 2003), and produces the same textures that were observed in the N4 and N5 deposits and in our sample set. This is in accordance with the observed mineral assemblage of metabasalts directly underlying the N4 deposit. The metabasalts are part of the Parauapebas Formation and are made up of actinolite, chlorite, calcite, epidote and quartz (TEIXEIRA & EGGLER, 1994). Such a mineral paragenesis is characteristic for greenschist facies metamorphism of basaltic rocks (e.g. BUCHER & FREY, 1994). Thus, carbonate metasomatism likely represents a localized phenomenon, which occurred during retrograde greenschist metamorphism (GRAHAM et al., 1983). According to SKELTON (2011), synmetamorphic carbonation of mafic dikes is best presented by the following bulk reaction:

$$3\ \text{amphibole} + 2\ \text{epidote} + 8\ H_2O + 10\ CO_2 \rightarrow 3\ \text{chlorite} + 10\ \text{calcite} + 21\ \text{quartz} \quad (1)$$

This reaction fits well with the observed mineral content of the volcanic units from the Carajás deposits studied here, which are made up of chlorite, plagioclase, quartz and carbonate (Fig. 3.5C).

Soft ore and canga consist predominantly of martite, goethite, minor microplaty hematite and relicts of kenomagnetite (Figs. 3.4A, B and 3.5A, D). Microbanding is usually destroyed or only recognizable in restricted areas within the thin sections. In some samples, martite exhibits a porous, skeletal microstructure, resulting from intense leaching of remaining kenomagnetite relicts (Fig. 3.5D). Chert fragments are rare and typically have a rounded shape. Meteoric fluids mobilized chert and reprecipitated quartz as fillings in fractures or pore space (Fig. 3.5E, F).

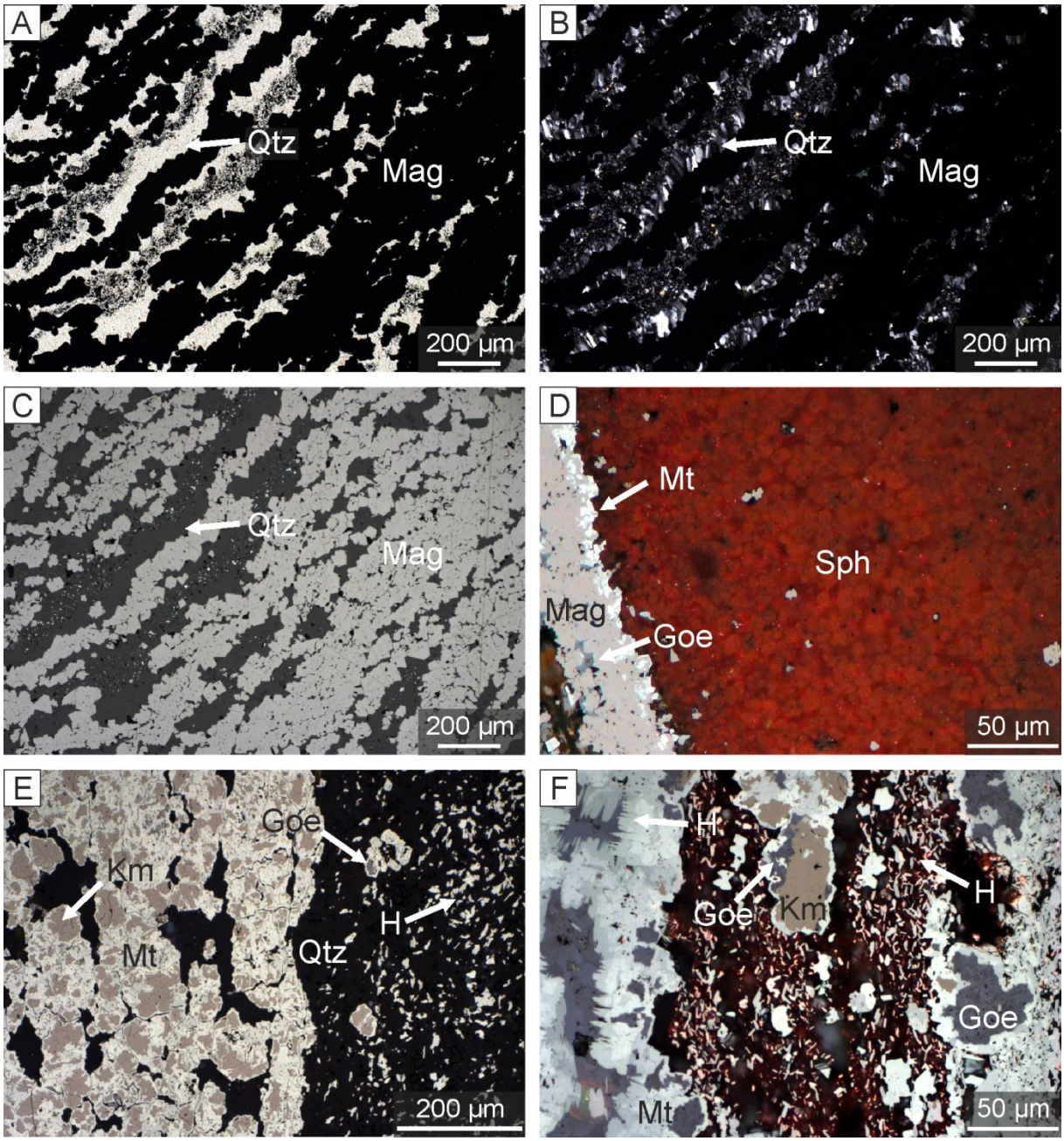

Fig. 3.3 Photomicrographs of typical BIF textures. (**A**) Pristine BIF, comprised of microbands of magnetite (Mag) and chert (Qtz) (S11D-191, 219 m, transmitted light). (**B**) Same as (A), with crossed nicols. (**C**) Same as (A) & (B), under reflected light. (**D**) Chert band with microspherulitic structures (Sph) next to a magnetite band that is affected by incipient martitization (Mt). Goethite (Goe) occurs along fractures (N7-0005, 112.35 m, reflected light, oil immersion). (**E**) Martitized kenomagnetite (Km) next to a chert band, hosting finely dispersed microplaty hematite (H). Goethite has replaced the kenomagnetite core of a martite grain (S11D-330, 217 m, reflected light). (**F**) Martite rims surrounding kenomagnetite that is being replaced by goethite. Microplaty hematite is present as small platelets and as crystals nucleating on martite (S11D-330, 219 m, reflected light, oil immersion).

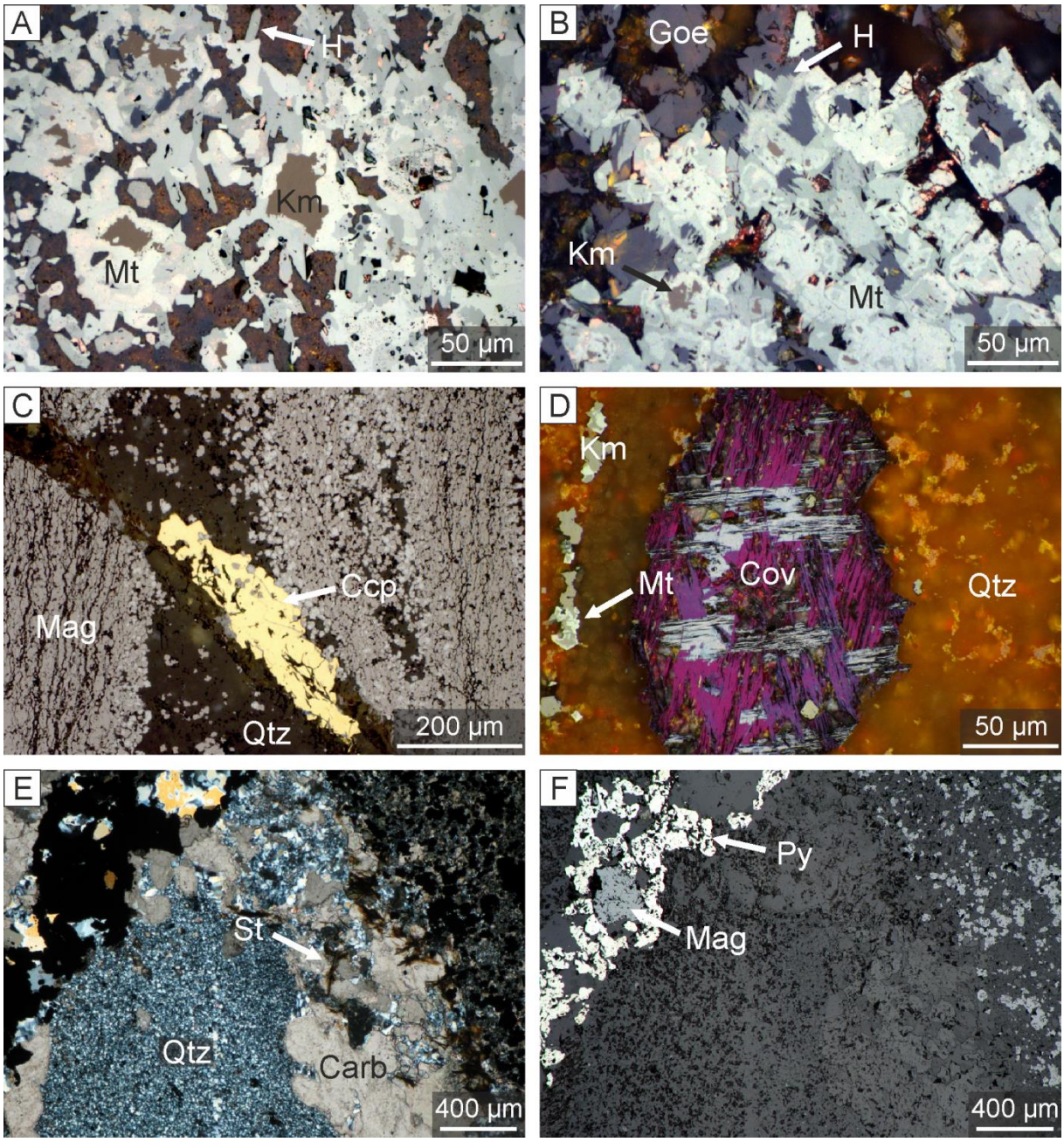

Fig. 3.4 Photomicrographs of typical BIF and ore textures. (**A**) Martite and kenomagnetite intergrown with microplaty hematite. Microplaty hematite nucleates on martite and appears to replace it (soft ore, S11D-330, 172 m, reflected light, oil immersion). (**B**) Microplaty hematite nucleating on martite, intergrown with goethite (soft ore, S11D-330, 97 m, reflected light, oil immersion). (**C**) Chalcopyrite (Ccp) in a fracture that truncates magnetite bands (BIF, N7-0005, 112.15 m, reflected light, oil immersion). (**D**) Covellite (Cov) formed by oxidation of chalcopyrite, next to kenomagnetite affected by incipient martitization (BIF, N7-0005, 112.35 m, reflected light, oil immersion). (**E**) Fibrous stilpnomelane (St) intergrown with carbonate surrounding and replacing a chert fragment (magnetite-rich breccia, S11D-330, 361 m, transmitted light with crossed nicols). (**F**) Same as (E), under reflected light. Pyrite (Py) formed coeval with carbonate and overgrows magnetite.

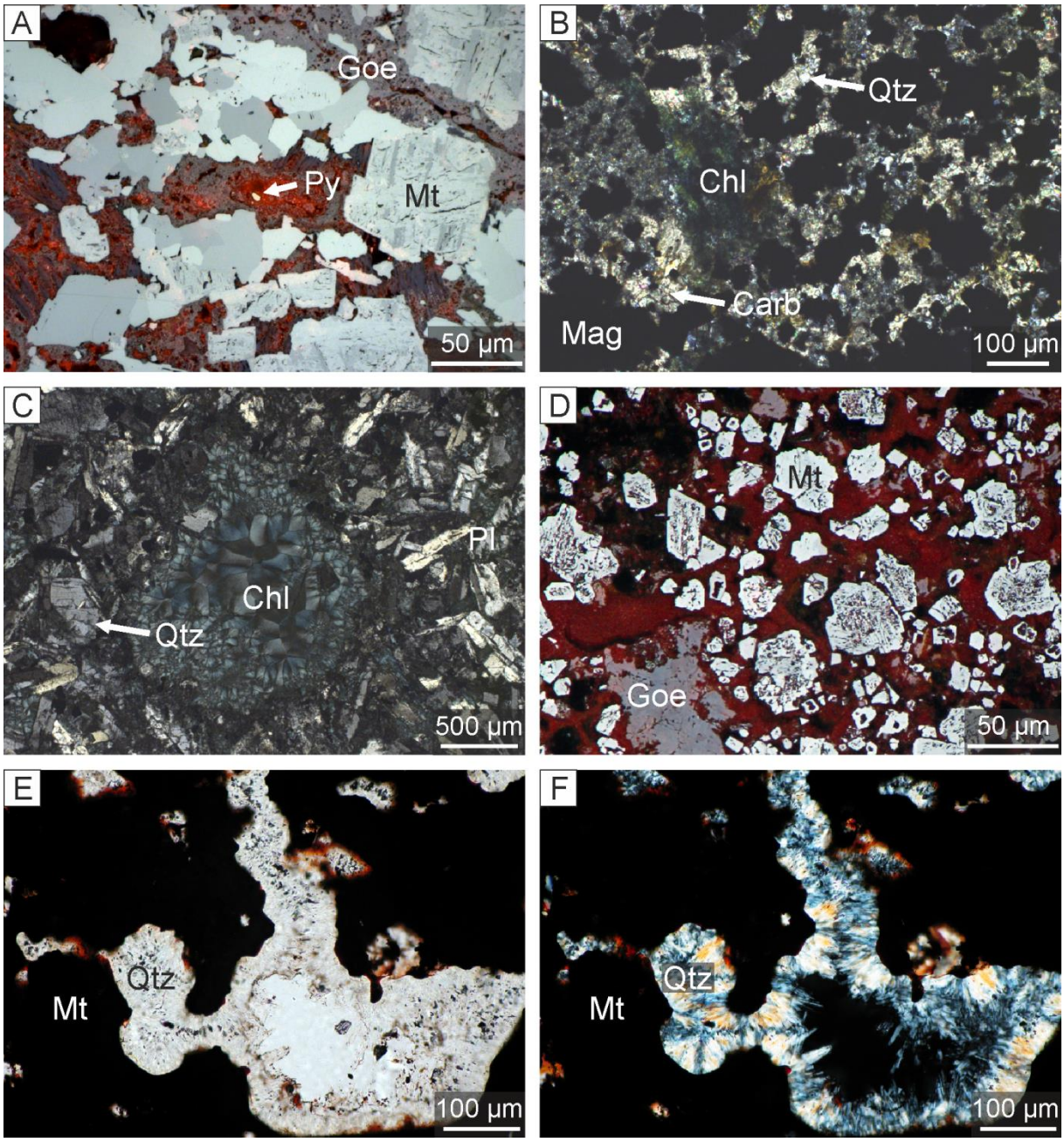

Fig. 3.5 Photomicrographs of typical textures of canga, magnetite-rich breccia, mafic volcanic units and soft ore. (**A**) Pyrite grain (Py) next to martite and goethite precipitated in a fracture (canga, S11D-330, 0.10 m, reflected light, oil immersion). (**B**) Groundmass of a hydrothermally altered magnetite-rich breccia, made up of chlorite (Chl), carbonate and quartz (magnetite-rich breccia, S11D-330, 361 m, transmitted light with crossed nicols). (**C**) Chlorite forming the infill of a vesicle, surrounded by quartz and altered plagioclase (Pl) (mafic volcanic unit, N7-0005, 391 m, transmitted light with crossed nicols). (**D**) Skeletal martite with interstitial goethite (soft ore, S11D-330, 34 m, reflected light, oil immersion). (**E**) Quartz forming the infill of a fracture and connected pore space (soft ore, S11D-330, 34 m, transmitted light). (**F**) Same as (E), with crossed nicols.

Chapter 4 Whole-rock Geochemistry

4.1 Introduction

Whole-rock major- and trace-element analysis is a classical and still powerful tool to constrain the depositional conditions of BIF formation. Whole-rock data also provide an insight in the processes operating during the alteration/weathering of BIF and the genesis of BIF-hosted iron ore.

In the past, geochemical studies led to important findings regarding this enigmatic rock type. Based on low abundances of HFSE (high field strength elements) and superchondritic Y/Ho ratios, it has been argued that BIFs generally represent pure marine chemical sediments. REEs (rare earth elements) have proven to be especially useful in unravelling the complex history of BIFs. The REE distribution patterns of BIFs closely resemble modern seawater, with the exception of the redox-sensitive elements Ce and Eu. Modern oxygenated seawater has a strong negative Ce anomaly and shows no Eu anomaly (GERMAN & ELDERFIELD, 1990). The absence of prominent negative Ce anomalies in BIFs older than 1.9 Ga indicates that the Precambrian oceans were predominantly suboxic to anoxic (PLANAVSKY et al., 2010). BIFs generally exhibit positive Eu anomalies indicative of a significant hydrothermal flux to the Precambrian oceans. Due to the low oceanic sulfate concentrations before the GOE (Great Oxidation Event) (CROWE et al., 2014), submarine hydrothermal vents would have emitted high amounts of iron into the ocean (KUMP & SEYFRIED, 2005). The positive Eu anomaly is therefore regarded as a key argument for the hydrothermal origin of iron in BIFs (BAU & MÖLLER, 1993; KLEIN, 2005).

For this thesis, 47 samples from the N7, N8 and S11D high-grade iron ore deposits were analyzed for their major- and trace-element abundances. The sample set is comprised of canga (n=1), soft ore (n=26), BIF (n=11), magnetite-rich breccia (n=6) and intercalated volcanic units (n=3). A brief description of the utilized analytical techniques is given in section 4.2. The results are presented in section 4.3 and discussed extensively in the following sections.

An evaluation of the effects of syndepositional addition of terrigenous material and later localized hydrothermal overprint on the major- and trace-element composition of the samples, is provided in section 4.4. Mass balance calculations regarding the ore forming process are presented in section 4.5. The REE geochemistry of the samples is discussed in section 4.6. The geochemistry of the sampled volcanic material is discussed separately in the last section.

4.2 Analytical methods

Sample preparation consisted of crushing, followed by grinding to a fine powder in an agate-lined shatter box. Analytical work was carried out by ACME Analytical Laboratories Ltd. in Vancouver, Canada. The major- and trace-element contents were analyzed with ICP-ES and ICP-MS techniques after lithium metaborate/tetraborate fusion and dilute nitric digestion. The equivalent of 0.2 g sample powder was analyzed with ICP-ES. The loss on ignition (LOI) was measured by calculating the weight difference after the ignition of the samples at 1000°C. The total carbon (TOT/C) and total sulfur (TOT/S) contents were determined by burning the samples in an induction furnace and measuring the CO_2 and SO_2 concentrations in the combustion gas with infrared radiation cells (Leco analysis).

Trace-element analysis was carried out with four different methods:

(1) The determination of Sc and Cr followed the same procedure used on the major elements, i.e. lithium metaborate/tetraborate fusion and dilute nitric digestion followed by analysis with ICP-ES. (2) 0.5 g of each sample was leached in aqua regia at 95°C and analyzed for Ni, Cu, Zn, As, Se, Mo, Ag, Cd, Sb, Au, Hg, Tl, Pb and Bi with ICP-MS. (3) Be, V, Co, Ga, Rb, Sr, Y, Zr, Nb, Sn, Cs, Ba, La, Ce, Pr, Nd, Sm, Eu, Gd, Tb, Dy, Ho, Er, Tm, Yb, Lu, Hf, Ta, W, Th, U were analyzed with ICP-MS after the same digestion that was used for the major element analysis. (4) Pd and Pt contents were determined via ICP-MS, following lead-collection fire-assay fusion and digestion of the Ag dore bead.

The Fe contents in soft ore were systematically too low, i.e. the sum of major elements was between 90 to 95 wt.%. Therefore, the soft ore and BIF samples were reanalyzed with fused disc (lithium tetraborate/metaborate flux) XRF, which produced correct sums of 99 to 100 wt.%. The disadvantage of this approach is that sodium nitrate is used during the production of the discs for XRF analysis. Because of the addition of sodium to the sample material, Na_2O was not measured by this method; neither was the total carbon content (TOT/C) determined.

The upper and lower detection limits of all measurement techniques are listed in Table 4.1.

As mentioned above, the major-element contents of the soft ore samples were first measured with ICP-ES and later reanalyzed with XRF. By comparing the collected data, it is possible to assess the reliability of the reported major-element contents. As shown in Fig. 4.1, both analytical techniques produced similar results (with the exception of iron), which indicates that the reported major-element contents are not affected by measurement errors.

Table 4.1 Detection and upper limits of the utilized measurement techniques.

ICP-ES

Analyte	Detection Limit	Upper Limit
SiO_2	0.01 wt.%	100 wt.%
TiO_2	0.01 wt.%	100 wt.%
Al_2O_3	0.01 wt.%	100 wt.%
Fe_2O_3	0.04 wt.%	100 wt.%
MnO	0.01 wt.%	100 wt.%
MgO	0.01 wt.%	100 wt.%
CaO	0.01 wt.%	100 wt.%
Na_2O	0.01 wt.%	100 wt.%
K_2O	0.01 wt.%	100 wt.%
P_2O_5	0.01 wt.%	100 wt.%
LOI	0.10 wt.%	100 wt.%
Cr	14 ppm	100 wt.%
Sc	1 ppm	10 000 ppm

ICP-MS

Analyte	Detection Limit	Upper Limit
Be	1 ppm	10 000 ppm
V	8 ppm	10 000 ppm
Co	0.2 ppm	10 000 ppm
Ga	0.5 ppm	10 000 ppm
Rb	0.1 ppm	10 000 ppm
Sr	0.5 ppm	50 000 ppm
Y	0.1 ppm	50 000 ppm
Zr	0.1 ppm	50 000 ppm
Nb	0.1 ppm	50 000 ppm
Sn	1 ppm	10 000 ppm
Cs	0.1 ppm	10 000 ppm
Ba	1 ppm	50 000 ppm
La	0.1 ppm	50 000 ppm
Ce	0.1 ppm	50 000 ppm
Pr	0.02 ppm	10 000 ppm
Nd	0.3 ppm	10 000 ppm
Sm	0.05 ppm	10 000 ppm
Eu	0.02 ppm	10 000 ppm
Gd	0.05 ppm	10 000 ppm
Tb	0.01 ppm	10 000 ppm
Dy	0.05 ppm	10 000 ppm
Ho	0.02 ppm	10 000 ppm
Er	0.03 ppm	10 000 ppm
Tm	0.01 ppm	10 000 ppm
Yb	0.05 ppm	10 000 ppm
Lu	0.01 ppm	10 000 ppm
Hf	0.1 ppm	10 000 ppm
Ta	0.1 ppm	50 000 ppm
W	0.5 ppm	10 000 ppm
Th	0.2 ppm	10 000 ppm
U	0.1 ppm	10 000 ppm

XRF

Analyte	Detection Limit	Upper Limit
SiO_2	0.01 wt.%	80.0 wt.%
TiO_2	0.01 wt.%	40.0 wt.%
Al_2O_3	0.01 wt.%	80.0 wt.%
Fe_2O_3	0.01 wt.%	100 wt.%
MnO	0.01 wt.%	80.0 wt.%
MgO	0.01 wt.%	80.0 wt.%
CaO	0.01 wt.%	40.0 wt.%
K_2O	0.01 wt.%	40.0 wt.%
P_2O_5	0.01 wt.%	40.0 wt.%
LOI	0.10 wt.%	100 wt.%
S	0.001 wt.%	4.0 wt.%
Cr	27 ppm	7.0 wt.%

Leco Analysis

Analyte	Detection Limit	Upper Limit
TOT/C	0.02%	100%
TOT/S	0.02%	100%

Aqua Regia + ICP-MS

Analyte	Detection Limit	Upper Limit
Ni	0.1 ppm	10 000 ppm
Cu	0.1 ppm	10 000 ppm
Zn	1 ppm	10 000 ppm
As	0.5 ppm	10 000 ppm
Se	0.5 ppm	100 ppm
Mo	0.1 ppm	2000 ppm
Ag	0.1 ppm	100 ppm
Cd	0.1 ppm	2000 ppm
Sb	0.1 ppm	2000 ppm
Au	0.5 ppb	100 ppm
Hg	0.01 ppm	50 ppm
Tl	0.1 ppm	1000 ppm
Pb	0.1 ppm	10 000 ppm
Bi	0.1 ppm	2000 ppm

Fire Assay + ICP-MS

Pd	0.5 ppb	1 ppm
Pt	0.1 ppb	1 ppm

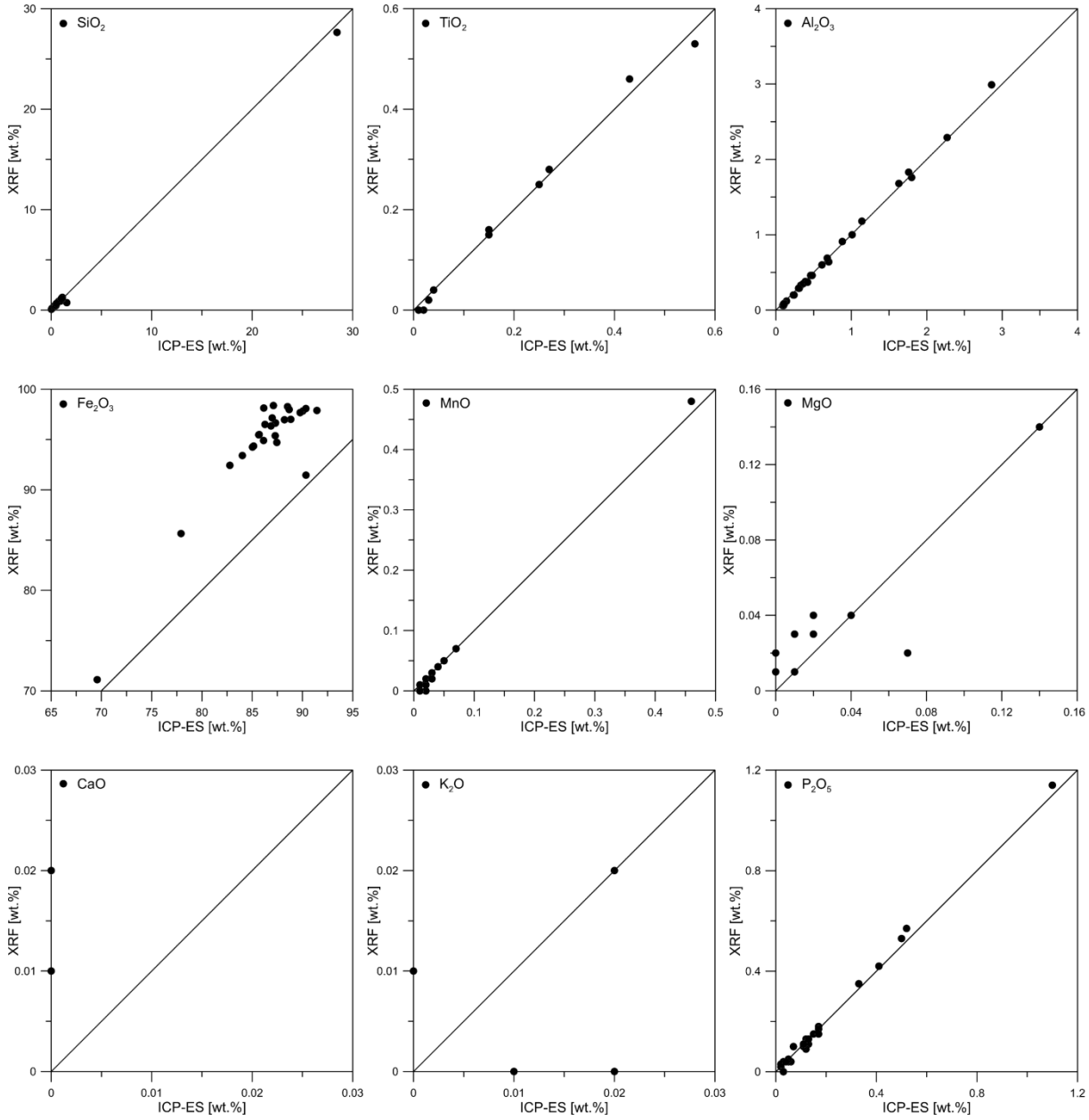

Fig. 4.1 Binary diagrams showing the major-element contents of the soft ore samples measured with XRF, plotted against the results obtained with ICP-ES. SiO_2, TiO_2, Al_2O_3, MnO and P_2O_5 plot along straight lines with gradients of 45°, showing that both analytical techniques produced similar and thus reliable results. High levels of Fe_2O_3 are systematically underestimated in the ICP-ES measurements. Consequently, high-grade ore samples deviate vertically from the 45° reference line, but still follow a well-defined linear trend. The scattered distribution of MgO, CaO and K_2O shows that both techniques are less reliable at low element contents approaching the detection limit.

The accuracy and precision of the utilized analytical techniques were evaluated by repeated measurements of in-house standards of ACME Analytical Laboratories Ltd. (4XlFe, DS10, GS311-1, Pd1 and SO-18), with known elemental compositions. A list of all analyzed major and trace elements and their respective accuracy and precision is given in Table 4.2. Accuracy was calculated as relative error and represents the bias between the measured and the expected composition of a standard. Precision was assessed by calculating the coefficient of variation (CV):

$$CV = \frac{1 \times \text{standard deviation}}{\text{arithmetic mean}} \times 100\ [\%] \quad (1)$$

The values listed in Table 4.2 should be regarded with caution, since they are based on a very limited number of analyses, often less than five measurements.

Table 4.2 Accuracy [%] and precision [%] for major- and trace-element analysis.

Element	Accuracy	Precision	Element	Accuracy	Precision
Major elements					
SiO_2	0.91	0.39	Na_2O	2.16	1.20
TiO_2	12.3	0	K_2O	5.26	0
Al_2O_3	6.89	0.28	P_2O_5	1.67	0.85
Fe_2O_3	0.46	0.19	LOI	1.83	0.41
MnO	2.27	2.22	TOT/C	4.90	1.96
MgO	6.67	6.67	S	5.77	5.89
CaO	1.37	0.15			
Trace elements					
Be	76.5	50.8	Ce	4.60	5.19
Sc	5.23	1.95	Pr	5.49	3.92
V	4.68	4.30	Nd	7.23	6.61
Cr	1.06	1.20	Sm	6.06	4.55
Co	3.97	4.62	Eu	6.15	3.85
Ni	6.12	6.29	Gd	3.87	4.36
Cu	5.93	6.74	Tb	10.4	5.27
Zn	6.53	5.88	Dy	6.35	7.20
Ga	5.31	4.99	Ho	7.50	7.23
As	7.48	5.65	Er	5.91	5.90
Se	13.0	13.6	Tm	3.70	3.82
Rb	4.30	2.39	Yb	7.99	9.26
Sr	3.45	4.06	Lu	3.92	5.68
Y	4.22	3.83	Hf	6.18	3.77
Zr	2.05	2.52	Ta	13.0	8.17
Nb	3.14	3.70	W	5.41	4.98
Mo	9.69	11.0	Pt	3.07	3.00
Pd	3.40	0.30	Au	41.4	36.7
Ag	9.18	10.3	Hg	16.3	17.2
Cd	6.99	6.28	Tl	11.9	8.59
Sn	6.27	6.04	Pb	8.09	8.24
Sb	14.5	5.10	Bi	5.87	6.77
Cs	4.89	5.35	Th	4.22	4.98
Ba	2.59	2.44	U	6.46	3.30
La	4.54	4.80			

4.3 Results

The major-element contents of the BIF samples from the Carajás Formation are inconspicuous and lie within the typical range of Archean to Paleoproterozoic BIFs (Table 4.3). In comparison to the studied BIF units, the soft ore samples have significantly lower SiO_2, MgO and CaO levels, but also elevated TiO_2, Al_2O_3, Fe_2O_3 and P_2O_5 contents (Fig. 4.2A, B). The major-element contents of the magnetite-rich breccia samples resemble the analyzed BIF units with the exception of MgO, CaO and K_2O, which are higher in the magnetite-rich breccia samples (Fig. 4.2C). The three analyzed samples of volcanic material exhibit similar abundances of SiO_2, Al_2O_3, MnO and MgO, but variable contents of TiO_2, Fe_2O_3, CaO, Na_2O, K_2O and P_2O_5 (Fig. 4.2D).

Trace-element abundances are variable in the studied lithologies. In comparison to the BIF samples, Y, Zr, REEs and Th are elevated in the soft ore samples, while Cu, Rb and Sr are depleted (Fig. 4.3A, B). Similar to the analyzed BIF units, the magnetite-rich breccia samples have elevated levels of Rb and Sr, but in contrast to the BIF units, the magnetite-rich breccia samples also show elevated abundances of Zr, Ba, REEs and Th (Fig. 4.3C). The samples of volcanic material have by far the highest trace-element contents, with the exception of Cu and Pb. The highest Cu levels were measured in BIF samples. The highest Pb content was detected in a canga sample. The REE+Y contents of all samples from the Carajás Formation are rather low. $\sum$REE+Y of BIF ranges from 5.13 to 24.6 ppm, 6.26 to 83.7 ppm for canga and soft ore, 13.9 to 28.7 ppm for magnetite-rich breccia and 47.1 to 415 ppm for volcanic material. The average REE+Y content (arithmetic mean) of soft ore and canga (25.9 ppm, n = 27) is higher compared to BIF (9.67 ppm, n = 11) and the magnetite-rich breccia (20.6 ppm, n = 6), but much smaller in comparison to the volcanic material (203 ppm, n = 3).

The major- and trace-element contents of all samples are provided in the appendix of the thesis (Table 1, 2, 3).

Table 4.3 Major-element content of the studied BIF samples and data from literature.

	BIF samples - Carajás Formation		BIF - 3.76 to 1.88 Ga (KLEIN, 2005)	
Element	Minimum [wt.%]	Maximum [wt.%]	Minimum [wt.%]	Maximum [wt.%]
SiO_2	33.6	62.5	34.0	56.0
TiO_2	<0.01	<0.01	-	-
Al_2O_3	<0.01	0.19	0.09	1.80
Fe_2O_3	37.4	66.3	28.6	57.2
MnO	0.01	0.18	0.10	1.15
MgO	<0.01	3.03	1.20	6.70
CaO	0.01	4.21	1.75	9.00
Na_2O	-	-	0	0.80
K_2O	<0.01	0.04	0	1.15
P_2O_5	<0.01	0.03	-	-

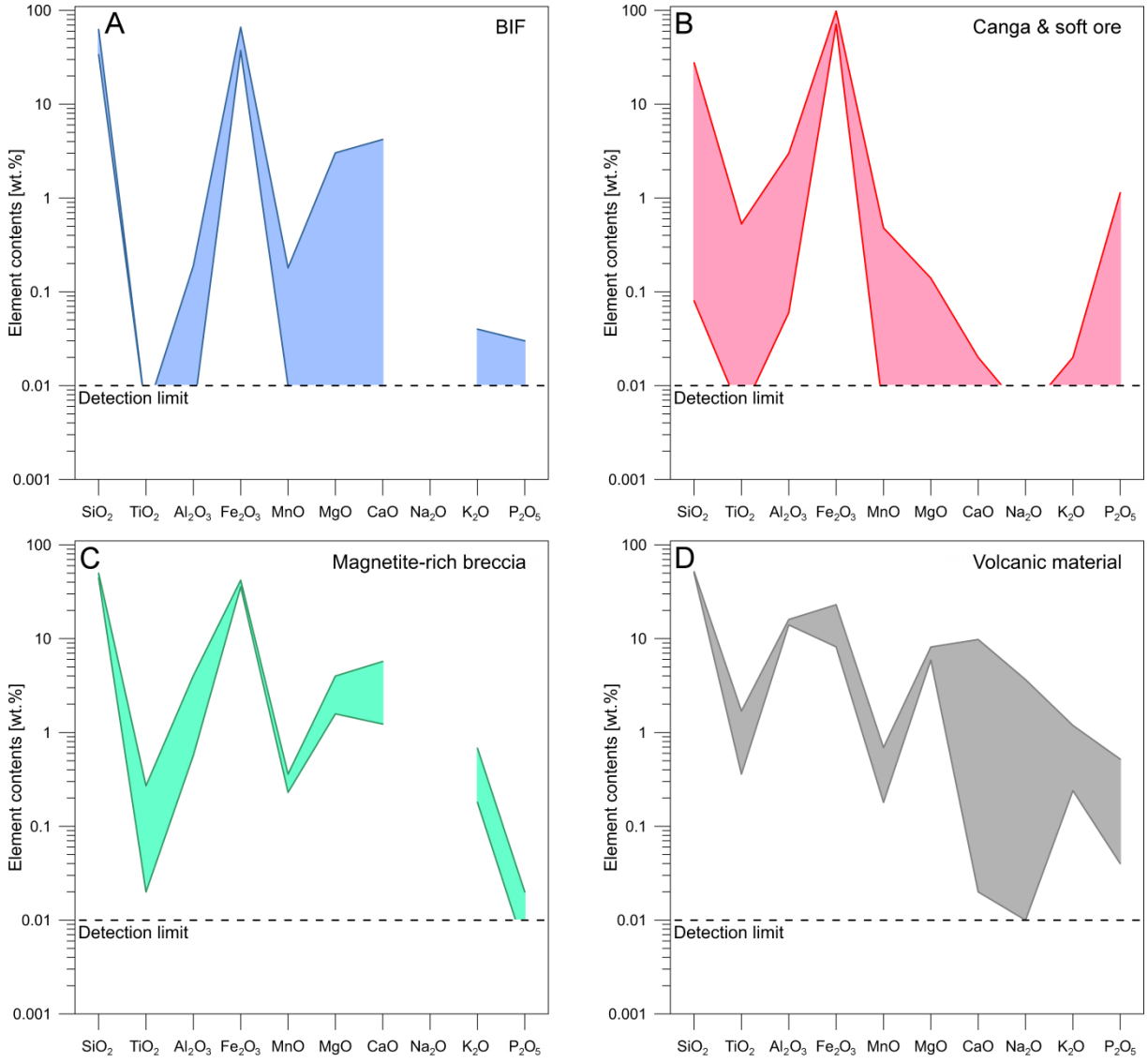

Fig. 4.2 Multi-element diagrams illustrating the compositional range of the studied lithologies, i.e. (**A**) BIF, (**B**) canga and soft ore, (**C**) magnetite-rich breccia and (**D**) volcanic material. Major-element contents are given in [wt.%].

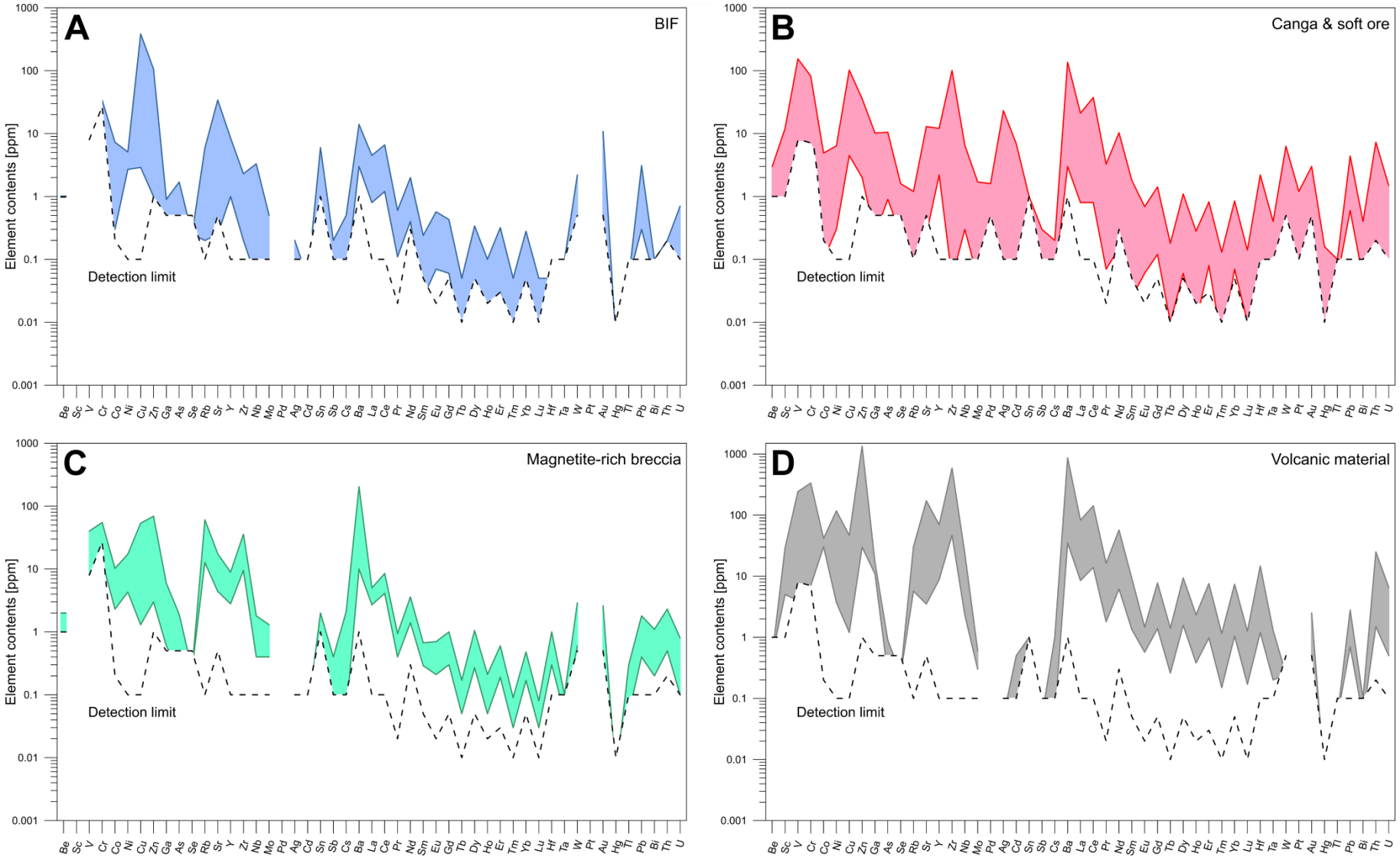

Fig. 4.3 Multi-element diagrams illustrating the compositional range of the studied lithologies, i.e. (**A**) BIF, (**B**) canga and soft ore, (**C**) magnetite-rich breccia and (**D**) volcanic material. Trace-element contents are given in [ppm], with the exception of Pd, Pt and Au, which are given in [ppb].

4.4 Detrital input and hydrothermal overprint

BIFs represent pure marine chemical sediments that reflect the prevalent chemical conditions of their depositional environments. In general, they contain only insignificant amounts of terrigenous material. In some cases, however, pelitic material derived from continental runoff, volcanic ash fall or density currents, can be a larger constituent (silicate facies; see chapter 1, section 1.3). Later events, like the emplacement of dikes and associated hydrothermal overprint, might add to this impurity.

Besides iron, oxygen and silica, pure BIF contains only small amounts of other elements. Thus, even minor additions of detrital material could have a serious impact on the interpretation of its geochemical composition. For example, samples contaminated with terrigenous sediments have elevated REE contents with flat shale-normalized distribution patterns, unlike the signature of pure BIF that mostly resembles modern seawater. Furthermore, detrital input masks the otherwise well recognizable positive Eu anomaly of BIFs. This anomaly is widely regarded as a key argument for the hydrothermal origin of REE, and by analogy also iron in BIF (BAU & MÖLLER, 1993; KLEIN, 2005). The importance of detecting impurities must therefore be stressed.

Indications for detrital input are elevated Al_2O_3 contents, since aluminosilicates are main components of pelitic material, increased levels of TiO_2 and higher abundances of incompatible elements. Both aluminium and titanium are immobile in most aqueous fluids. Thus, higher contents in BIF require detrital input. The upper continental crust is enriched in incompatible elements, i.e. LILE (large-ion lithophile elements) and HFSE (high field strength elements). Similar to aluminium and titanium, HFSE are relatively immobile. Therefore, elevated levels of HFSE in BIF indicate syndepositional addition of terrigenous sediments. HFSE commonly used in the literature as an index for detrital material are Zr, Hf, Th, REE and Y (BAU & DULSKI, 1996; LAN et al., 2014). HFSE contents can be used to construct a Y/Ho versus Zr/Hf diagram, in order to detect detrital contributions. With the exception of high-silica suites (>70 wt.% SiO_2), igneous rocks and epiclastic sediments have chondritic Y/Ho and Zr/Hf ratios, while chemical sediments formed from aqueous solutions exhibit non-chondritic ratios (BAU, 1996). Furthermore detritus-free BIF should exhibit chondrite-normalized $(La/Sm)_{CN}$ >1, shale-normalized $(Sm/Yb)_{SN}$ <1 and $(Eu/Sm)_{SN}$ >1, regardless of their age and metamorphic grade (BAU & DULSKI, 1996; BAU & MÖLLER, 1993).

LILE are unsuitable to assess detrital input. Their low ionic potential causes weak bonds, which means that they are easily mobilized in aqueous fluids during low-grade metamorphism (BREWER & ATKIN, 1989). However, they could be useful to evaluate hydrothermal overprint in samples devoid of detrital material. Detritus-free BIF should only contain low contents of LILE and HFSE. If a detritus-free sample shows elevated levels of LILE, e.g. K, Rb, Sr and Ba, it is likely that it was influenced by hydrothermal solutions. As mentioned before, the Carajás Formation was affected by localized hydrothermal overprint associated with mafic dikes, during retrograde greenschist metamorphism (see chapter 2, section 2.2.5; chapter 3, section 3.2). This overprint introduced chlorite, stilpnomelane,

carbonate and sulfide minerals into the host rock of the dikes. Based on the chemical composition of these minerals (Table 4.4), hydrothermal alteration should be recognizable by elevated contents of Mg, Al, S, K, Ca and Cu.

Table 4.4 Minerals associated with localized hydrothermal overprint in the Carajás deposits.

Mineral	Chemical formula
Pyrite	FeS_2
Calcite	$CaCO_3$
Dolomite	$CaMg(CO_3)_2$
Chalcopyrite	$CuFeS_2$
Stilpnomelane	$K(Fe^{2+}, Mg, Fe^{3+})_8(Si, Al)_{12}(O, OH)_{27}$
Chlorite	$(Mg,Fe)_3(Si,Al)_4O_{10}(OH)_2 \cdot (Mg,Fe)_3(OH)_6$

4.4.1 Detrital input

The aluminium contents are low in most samples and titanium levels lie predominantly below the detection limit. In a limited number of samples, including one canga, seven soft ore and all magnetite-rich breccia samples, both TiO_2 and Al_2O_3 levels are slightly elevated. The TiO_2 and Al_2O_3 contents of the magnetite-rich breccia samples correlate well ($R_{breccia}$= 0.97) and plot along a regression line (Fig. 4.4A). A magnetite-rich breccia sample from the S11D-deposit, analyzed by CABRAL et al. (2013), also follows this linear trend. The elevated TiO_2 and Al_2O_3 contents, and the good correlation between these elements, suggest that all magnetite-rich breccia samples contain terrigenous material. Two soft ore samples, from depths of 55 and 203 m, plot close to the regression line of the magnetite-rich breccia, indicating the presence of detrital material. In contrast, near-surface soft ore (<35 m depth) shows a scatter distribution and considerably higher TiO_2 and Al_2O_3 contents (Fig. 4.4A). It is notable that a single soft ore sample, from a depth of ca. 35 m, plots close to the regression line of the magnetite-rich breccia samples. The carbon content of this sample is more than ten times lower compared to the other near-surface samples. Since organic material is known to form complexes with multi-charged cations, i.e. Al^{3+} or Fe^{3+} (TIPPING, 2002), it is reasonable to assume that the observed scatter distribution of samples from 0 to 25 m depth results from variable removal of aluminium due to interactions with organic material. It follows that the two soft ore samples from 55 and 203 m depth record syndepositional addition of terrigenous sediments, while near-surface material was affected by recent weathering. A likely scenario is that meteoric waters washed in organic and detrital material and thus contaminated the upper parts of the high-grade iron ore deposits.

The binary diagrams of HFSE presented here, i.e. Th vs. Hf, Zr vs. Hf and Zr vs. Th (Fig. 4.4B, C, D), and the PAAS-normalized REE+Y diagram showing the average compositions of the studied lithologies (Fig. 4.4F; PAAS = post-Archean Australian shale), display a distinct and consistent order. Near-surface material is most enriched in HFSE, followed by the magnetite-rich breccia, soft ore from greater depths and finally BIF with HFSE concentrations generally below the detection limit.

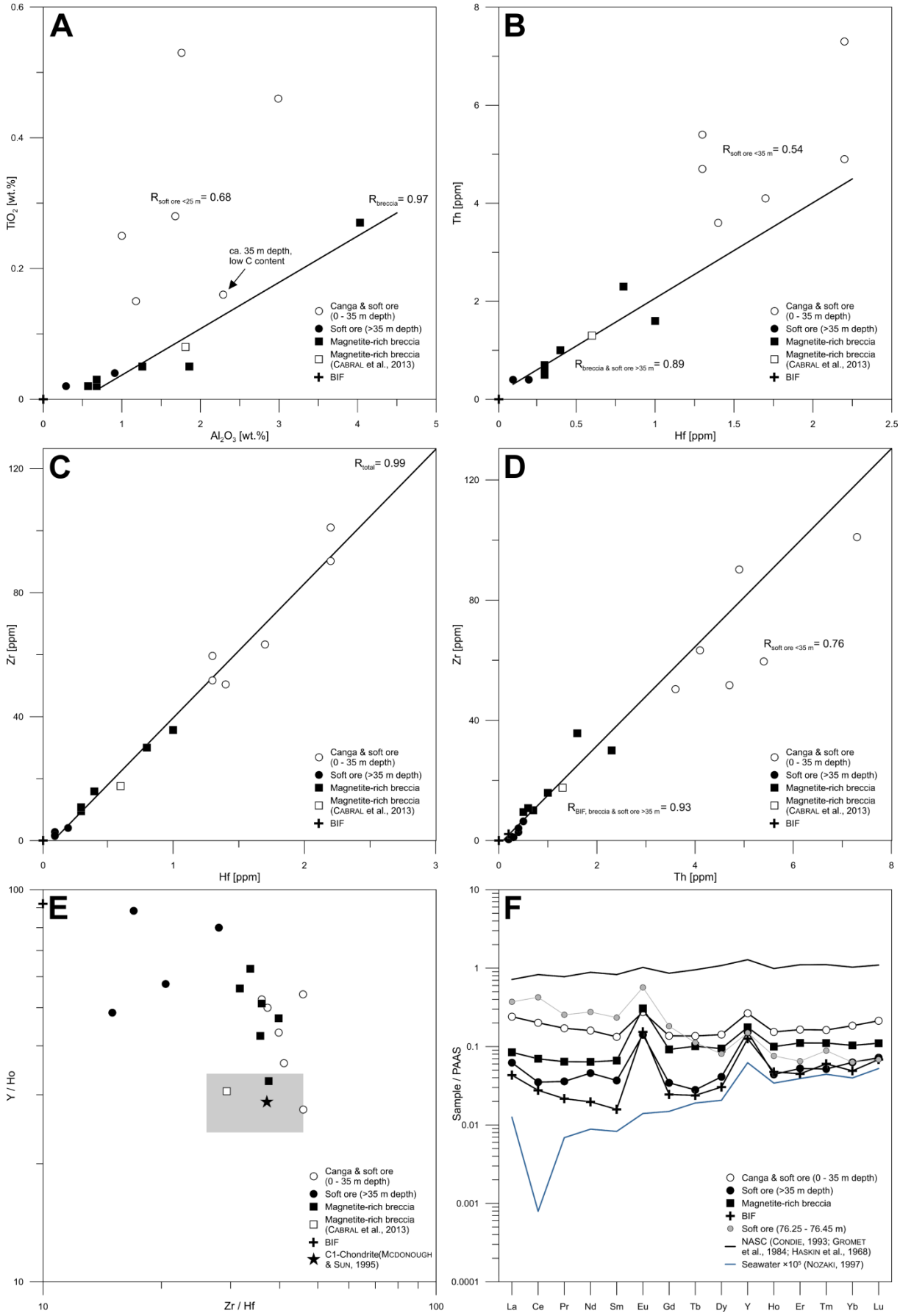

Fig. 4.4 Diagrams used to assess detrital contribution. (**A**) TiO_2 vs. Al_2O_3. (**B**) Th vs. Hf. (**C**) Zr vs. Hf. (**D**) Zr vs. Th. (**E**) Y/Ho vs. Zr/Hf. (**F**) PAAS-normalized REE+Y diagram.

There is some variation considering BIF and soft ore from >35 m depth, e.g. a soft ore sample at ca. 97 m depth has Zr and Th contents suggestive of detrital input, but Hf, Al_2O_3 and TiO_2 levels below the detection limit. A list of all samples that were potentially affected by detrital input is presented in Table 4.5.

In the REE+Y diagram (Fig. 4.4F), a single soft ore sample from ca. 76 m depth is selectively shown, because of its highly unusual signature. The sample is considerably enriched in LREE, even more than the near-surface soft ore, and depleted in HREE. Its Al_2O_3, TiO_2 and HFSE contents suggest that it represents detritus-free material. Low concentrations of MgO, CaO, K_2O, S, Cu and LILE indicate that the sample was unaffected by hydrothermal alteration. The REE+Y pattern of the soft ore sample does, however, closely resemble the signature of modern submarine vent-fluids, which also show enrichment in LREE and depletion in HREE in PAAS-normalized diagrams. This indicates that the BIF-precursor of the soft ore sample might have formed in close vicinity to a submarine hydrothermal vent. A more detailed discussion of the REE+Y patterns of all samples is provided in section 4.6.

In the Y/Ho vs. Zr/Hf diagram after BAU (1996), only three samples plot in the field indicative of epiclastic sediments (Fig. 4.4E). This illustrates well that detrital input affected several samples, but apparently this contribution was comparatively low and did not significantly change the non-chondritic behavior of Y/Ho and Zr/Hf.

Surprisingly, almost all samples fulfill the criteria of BAU & DULSKI (1996) and BAU & MÖLLER (1993) for detritus-free BIF, i.e. exhibit ratios of $(La/Sm)_{CN}$ >1, $(Sm/Yb)_{SN}$ <1 and $(Eu/Sm)_{SN}$ >1 (Table 4.6). This includes most of the samples presented in Table 4.5. However, a quick evaluation shows that this approach is seriously flawed. Black shale, a detrital sediment which generally formed in the proximal parts of marine basins in the Precambrian (KLEIN & BEUKES, 1989), exhibits similar ratios as "detritus-free BIF" (Table 4.7). Even the North American shale composite (NASC), a standard used as a proxy for the composition of the upper continental crust, has ratios of $(La/Sm)_{CN}$ >1, $(Sm/Yb)_{SN}$ <1 and $(Eu/Sm)_{SN}$ >1. Consequently, these ratios are not characteristic for detritus-free BIF and should not be used to assess syndepositional addition of detrital material.

Table 4.5 Samples and associated diagrams indicating the presence of detrital material.

Type	Depth [m]	Al_2O_3 *vs.* TiO_2	Zr *vs.* Hf	Zr *vs.* Th	Th *vs.* Hf	Y/Ho *vs.* Zr/Hf
Drill hole S11D-330						
Canga	0.10 - 0.30	▮	▮	▮	▮	
Soft ore	06.00 - 06.20	▮	▮	▮	▮	
Soft ore	14.05 - 14.25	▮	▮	▮	▮	
Soft ore	24.40 - 24.60	▮	▮	▮	▮	
Soft ore	34.85 - 35.05	▮	▮	▮	▮	
Soft ore	45.15 - 45.35		▮			
Soft ore	55.05 - 55.25	▮		▮		
Soft ore	87.85 - 88.05		▮	▮	▮	
Soft ore	97.50 - 97.70			▮		
Soft ore	117.55 - 117.75			▮		
Soft ore	132.85 - 133.05		▮			
Soft ore	142.70 - 142.90		▮	▮	▮	
Soft ore	203.30 - 203.50	▮				
Drill hole S11D-191						
BIF	251.41 - 251.83			▮		
Magnetite-rich breccia	281.45 - 281.92	▮	▮	▮	▮	
Drill hole S11D-214						
Magnetite-rich breccia	361.36 -361.61	▮	▮	▮	▮	
Magnetite-rich breccia	397.11 - 397.36	▮	▮	▮	▮	▮
Magnetite-rich breccia	428.07 - 428.27	▮	▮	▮	▮	
Magnetite-rich breccia	434.52 -434.74	▮	▮	▮	▮	
Magnetite-rich breccia	495.40 - 495.55	▮	▮	▮	▮	
Magnetite-rich breccia[1]	480	▮	▮	▮	▮	▮
Drill hole N8-0022						
Soft ore	11.30 - 11.50	▮	▮	▮	▮	▮

[1]Data from CABRAL et al. (2013)

▮ - Detrital input

Table 4.6 $(La/Sm)_{CN}$, $(Sm/Yb)_{SN}$ and $(Eu/Sm)_{SN}$ ratios of the studied samples.

Type	Depth [m]	$(La/Sm)_{CN}$	$(Sm/Yb)_{SN}$	$(Eu/Sm)_{SN}$
Drill hole S11D-330				
Canga	0.10 - 0.30	7.60	0.97	1.98
Soft ore	06.00 - 06.20	7.44	0.63	1.94
Soft ore	14.05 - 14.25	7.32	1.16	1.98
Soft ore	24.40 - 24.60	5.40	0.81	1.79
Soft ore	34.85 - 35.05	7.87	0.26	3.97
Soft ore	45.15 - 45.35	3.90	0.55	4.49
Soft ore	55.05 - 55.25	7.06	0.82	3.45
Soft ore	65.35 - 65.55	>1	<1	>1
Soft ore	76.25 - 76.45	6.44	3.71	2.43
Soft ore	87.85 - 88.05	6.80	0.94	3.53
Soft ore	97.50 - 97.70	12.3	1.57	3.90
Soft ore	107.40 - 107.60	>1	<1	>1
Soft ore	117.55 - 117.75	7.10	0.31	7.21
Soft ore	132.65 - 132.85	9.99	0.17	15.9
Soft ore	132.85 - 133.05	8.62	0.42	5.67
Soft ore	142.70 - 142.90	6.54	2.69	3.29
Soft ore	152.50 - 153.00	8.22	0.59	5.67
Soft ore	162.80 - 163.00	12.5	0.30	7.93
Soft ore	172.85 - 173.05	10.4	0.14	9.44
Soft ore	182.75 - 182.95	>1	<1	>1
Soft ore	192.95 - 193.15	11.9	0.34	7.01
Soft ore	203.30 - 203.50	12.5	0.39	9.44
Soft ore	213.15 - 213.35	5.41	0.39	4.15
Soft ore	217.50 - 217.70	6.24	0.68	4.45
BIF	217.70 - 217.90	6.24	0.68	4.67
BIF	219.61 - 219.70	>1	<1	>1
BIF	234.18 - 234.49	15.3	0.34	6.70
Drill hole S11D-191				
BIF	219.38 - 219.62	8.33	0.15	16.1
BIF	251.41 - 251.83	18.7	0.15	17.9
Magnetite-rich breccia	281.45 - 281.92	3.45	0.61	5.92
Drill hole S11D-214				
Magnetite-rich breccia	361.36 -361.61	5.44	0.80	4.20
Magnetite-rich breccia	397.11 - 397.36	5.29	0.63	2.69
Magnetite-rich breccia	428.07 - 428.27	5.83	0.66	5.16
Magnetite-rich breccia	434.52 -434.74	5.95	0.75	5.27
Magnetite-rich breccia	495.40 - 495.55	6.24	0.49	4.10
Drill hole N7-0005				
BIF	111.98 - 112.35	9.65	0.21	17.5
BIF	111.98 - 112.35	11.7	0.38	13.5

Table 4.6 (*continued*).

Type	Depth [m]	$(La/Sm)_{CN}$	$(Sm/Yb)_{SN}$	$(Eu/Sm)_{SN}$
Drill hole N8-0022				
Soft ore	11.30 - 11.50	9.20	0.79	1.64
Soft ore	29.60 - 29.80	6.95	2.26	2.00
Soft ore	48.46 - 48.66	14.4	0.38	5.67
BIF	50.80 - 50.99	11.6	0.51	5.67
BIF	84.36 - 84.52	13.1	<1	7.93
BIF	98.59 - 98.75	>1	D.L.	D.L.
BIF	135.50 - 135.60	16.7	0.26	7.55

CN - Chondrite-normalized ratios; chondrite data from McDonough & Sun (1995)
SN - Shale-normalized ratios (PAAS); shale data from Pourmand et al. (2012)
D.L. - The values needed for calculation are below the detection limit

Table 4.7 $(La/Sm)_{CN}$, $(Sm/Yb)_{SN}$ and $(Eu/Sm)_{SN}$ ratios of detrital sediments.

Type	Depth [m]	$(La/Sm)_{CN}$	$(Sm/Yb)_{SN}$	$(Eu/Sm)_{SN}$
NASC	-	3.51	0.80	1.23
Drill hole S11D-214				
Black shale	310 m	4.76	0.88	1.22
Black shale	315 m	4.79	0.73	1.38
Black shale	316 m	5.18	0.77	1.41
Black shale	320 m	4.86	1.02	1.32
Breccia	480 m	5.00	0.50	3.85
Drill hole S11D-191				
Black shale	211.78 m	4.42	0.84	1.73
Black shale	211.81 m	4.20	0.74	1.54
Black shale	211.87 m	4.42	0.88	1.65
Black shale	211.90 m	4.46	0.77	1.70
Black shale	211.93 m	4.72	0.58	1.88
Black shale	211.96 m	4.96	0.66	1.72
Black shale	211.99 m	4.49	0.75	1.55
Black shale	301 m	4.40	0.72	1.73
Black shale	302 m	4.50	0.78	1.71
Black shale	304 m	3.96	0.66	1.72
Black shale	306 m	5.02	0.94	1.74

Black shale - Data from Cabral et al. (2013)
NASC - Data from Condie (1993); Gromet et al. (1984); Haskin et al. (1968)

4.4.2 Hydrothermal overprint

Hydrothermal alteration in the periphery of mafic dikes introduced calcite, chlorite, stilpnomelane, pyrite and chalcopyrite into the surrounding host rocks, i.e. BIF and the magnetite-rich breccia (see chapter 3, section 3.2). Distal alteration is characterized by quartz veins containing sulfide and carbonate minerals (FIGUEIREDO E SILVA et al., 2011; chapter 3, Fig. 3.4C), while the proximal alteration zone is recognizable through the presence of chlorite, stilpnomelane, carbonate and sulfides (FIGUEIREDO E SILVA et al., 2011; ZUCCHETTI, 2007; chapter 3, Fig. 3.4E, F).

Hydrothermal overprint in the proximal alteration zone should therefore be discernible through elevated levels of Mg, Al, S, K, Ca and Cu (Fig. 4.5). Samples from the distal alteration zone should exhibit relatively high base-metal and LILE contents, in combination with inconspicuous levels of major elements. However, these geochemical indications only apply to unweathered and detritus-free samples (Fig. 4.5A, B). It is also uncertain whether high abundances of Mg and Ca truly reflect hydrothermal alteration. At present, there is no consensus whether occurrences of dolomitized BIF formed by carbonate metasomatism (FIGUEIREDO E SILVA et al., 2008), or simply represent carbonate facies BIF (DALSTRA & GUEDES, 2004).

The recognition of hydrothermal overprint is less straightforward for samples containing detrital material, since it is unclear whether chlorite precipitated from hydrothermal fluids or replaced pre-exisiting clay minerals during greenschist facies metamorphism. Most of the samples affected by detrital input have super-chondritic Y/Ho ratios (Fig. 4.4E), which shows that the detrital contribution was comparatively low. Thus, it is likely that syndepositional addition of terrigenous material was limited to the sedimentation of suspended clay particles. The Al_2O_3 contents of samples affected by detrital input are therefore higher compared to detritus-free samples and do not necessarily reflect hydrothermal addition of stilpnomelane or chlorite. In contrast, some detritus-free BIF samples and the magnetite-rich breccia samples have similar CaO and MgO contents (Fig. 4.5A, C). In these samples, the CaO and MgO contents are significantly higher in comparison to samples from the distal alteration zone, which points to the presence of anomalous amounts of calcite and dolomite. Higher levels of CaO and MgO should be present in the vicinity of mafic dikes, since they underwent synmetamorphic carbonation. Given the additionally high Cu and S contents in several magnetite-rich breccia samples and the close vicinity of a mafic dike to the S11D-214 drill hole, it is very likely that they were affected by hydrothermal overprint in the proximal alteration zone.

Weathering removed most of the mobile elements, e.g. LILE, CaO, MgO, etc. from the soft ore. Thus, it is unclear whether soft ore samples were affected by hydrothermal fluids in the distal or proximal alteration zone. Nonetheless, hydrothermal overprint can be identified by elevated Cu and Zn contents (Fig. 4.5B, D). In total, 14 samples were likely affected by hydrothermal alteration. A list of these samples is provided in Table 4.8.

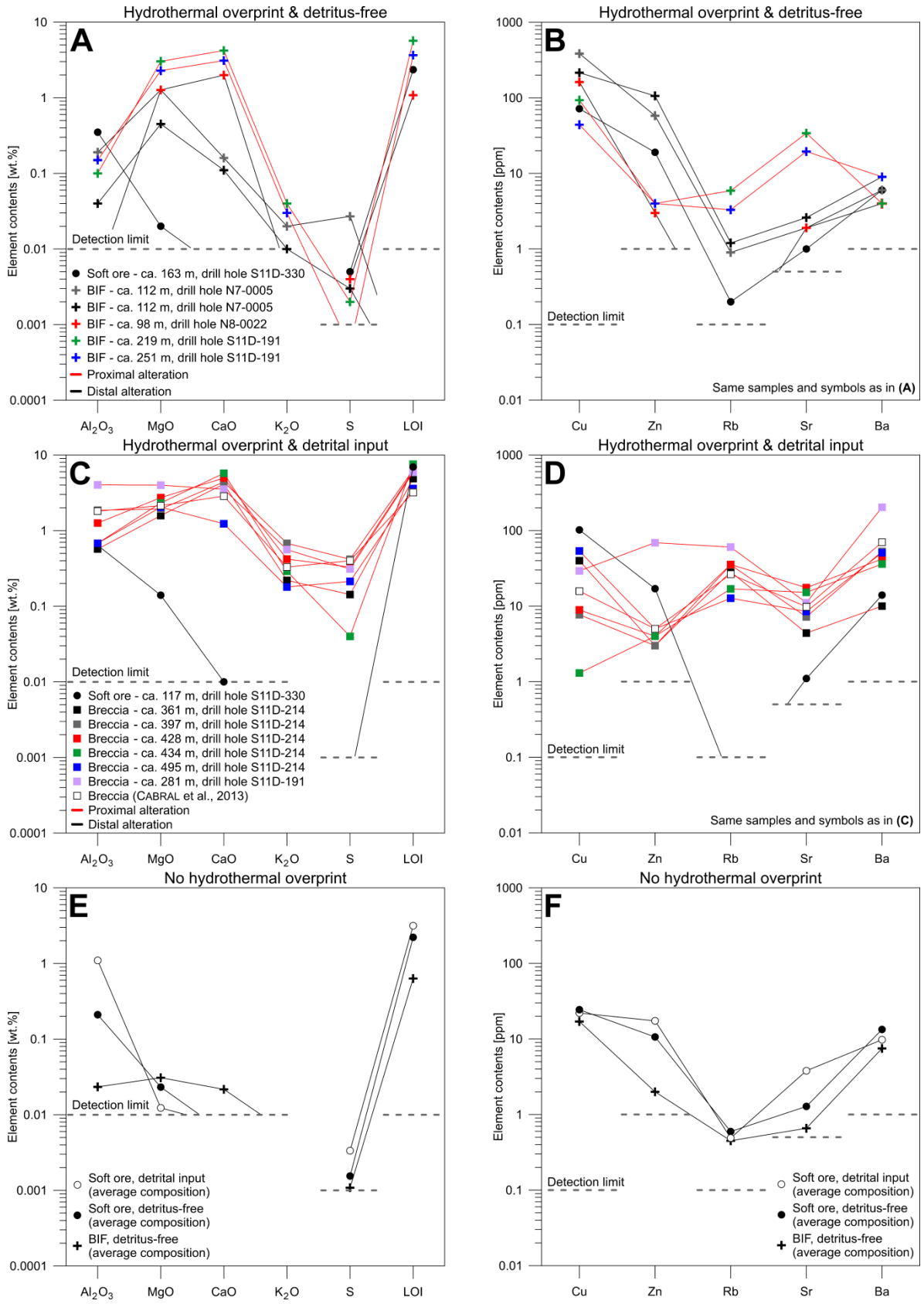

Fig. 4.5 Multi-element plots of samples affected by hydrothermal alteration associated to mafic dikes. (**A**) & (**B**) Detritus-free samples affected by hydrothermal alteration; (**C**) & (**D**) Samples affected by detrital input and hydrothermal alteration (Breccia = magnetite-rich breccia). (**E**) & (**F**) Average composition of samples unaffected by hydrothermal alteration.

Table 4.8 Samples affected by hydrothermal overprint.

Drillhole	Depth [m]	Type	Drillhole	Depth [m]	Type
Proximal			**Distal**		
S11D-191	219.38 - 219.62	BIF	S11D-330	117.55 - 117.75	Soft ore
S11D-191	251.41 - 251.83	BIF	S11D-330	162.80 - 163.00	Soft ore
S11D-191	281.45 - 281.92	Breccia	N7-0005	111.98 - 112.35	BIF
S11D-214	361.36 -361.61	Breccia	N7-0005	111.98 - 112.35	BIF
S11D-214	397.11 - 397.36	Breccia	N8-0022	98.59 - 98.75	BIF
S11D-214	428.07 - 428.27	Breccia			
S11D-214	434.52 -434.74	Breccia			
S11D-214	495.40 - 495.55	Breccia	[1] Data from CABRAL et al. (2013)		
S11D-214	480	Breccia[1]			

4.5 Mass balance considerations

In comparison to the studied BIF units, the soft ore samples have significantly lower SiO_2, MgO and CaO levels, indicating that these elements were removed during the ore-forming process. Since iron and silica are by far the most abundant components of the BIF units, silica-removal is always accompanied by residual enrichment of iron (Fig. 4.6).

The average composition of detritus-free BIF that was unaffected by hydrothermal alteration, corresponds to 46 wt.% SiO_2 and 54 wt.% Fe_2O_3. The BIF-hosted high-grade iron ore deposits situated on the Serra Norte and Serra Sul have estimated resources of 18 Gt @ 66 wt.% Fe (BEISIEGEL et al., 1973), i.e. 16.9 Gt of Fe_2O_3. Assuming that basically no iron was removed during the process of ore formation and that the protore BIF units had similar average contents of iron and silica like the BIF samples studied here, 14.4 Gt of SiO_2 must have been removed during the ore-forming process. Under standard conditions, the solubility of quartz is 11 mg/l (RIMSTIDT, 1997). The removal of 14.4 Gt of SiO_2 by meteoric waters would therefore require 1.31×10^{15} m^3 of water. If quartz was instead leached by hydrothermal fluids, as suggested by proponents of hypogene models of ore formation (e.g. BEUKES et al., 2003; GUEDES et al., 2003; LOBATO et al., 2005, 2008), a smaller volume of water would suffice. The trapping temperatures of fluid inclusions from the N4 and N5 deposits range from 210 to 320°C (FIGUEIREDO E SILVA et al., 2013). At 320°C, the calculated solubility of quartz is 0.77 g/l and the dissolution of 14.4 Gt of SiO_2 would require 1.87 10^{13} m^3 of water. The influence of salinity on silica dissolution (EVANS et al., 2013), is not considered in these calculations. Since both hypogene and supergene-metamorphic models assume that ore formation occurs at shallow depths (FIGUEIREDO E SILVA et al., 2013; MORRIS 1985), the calculated solubilities of quartz do not need to be corrected for higher pressures.

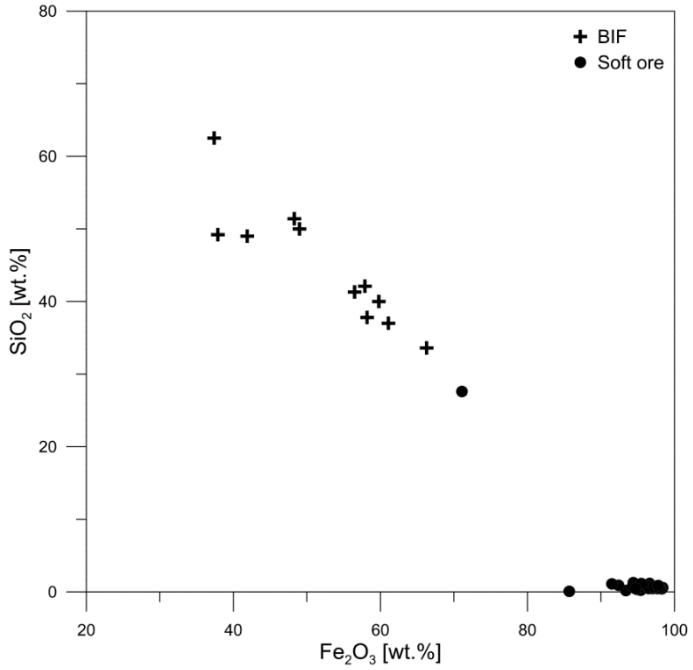

Fig. 4.6 Binary diagram of SiO_2 vs. Fe_2O_3 illustrating the linear correlation between silica and iron in the analyzed BIF and soft ore samples.

4.6 Rare earth element geochemistry

4.6.1 Secondary element mobility

The average ∑REE+Y of canga and soft ore (25.9 ppm) is significantly higher compared to BIF (9.67 ppm) and represents residual enrichment of REEs, caused by the removal of SiO_2 during the ore-forming process. The good correlation between Ce, Eu and their neighboring REEs shows that the REE content of the soft ore samples from the Carajás deposits was mostly unaffected by post-depositional mobilization, i.e. during diagenesis, metamorphism or weathering (Fig. 4.7). Unlike the other REEs which only form trivalent cations, Ce and Eu can reside in two oxidation states as Ce^{3+} or Ce^{4+} and as Eu^{2+} or Eu^{3+}, which makes them more redox-sensitive. Consequently, alteration processes should have the strongest effect on Ce and Eu (BOLHAR et al., 2015; WANG et al., 2017).

In the La vs. Ce diagram (Fig. 4.7A), three soft ore samples from depths of 35, 76 and 88 m deviate from the regression line and are enriched in Ce. The three samples are from the S11D deposit, drill hole S11D-330. As discussed in section 4.4.1, recent weathering contaminated near-surface soft ore with detrital material to a depth of 35 m. Percolating meteoric waters washed in organic and detrital material. Depending on the chemistry of the waters, Ce might have been mobilized and enriched in the soft ore sample at 35 m depth, which is situated at the lower boundary of the zone affected by near-surface contamination. The two soft ore samples at 76 and 88 m depth have anomalous PAAS-normalized REE+Y distribution patterns, showing LREE enrichment and HREE depletion (Fig. 4.12). BIFs and BIF-derived iron ores usually display exactly the opposite trend in PAAS-normalized diagrams (MENDES et al., 2016; PLANAVSKY et al., 2010), i.e. LREE depletion and HREE enrichment (Fig. 4.10A). Evidently, the deviation of the two soft ore samples from the regression line in the La vs. Ce diagram results from their anomalous REE+Y distribution patterns and does not represent redox-controlled decoupling of Ce from its neighboring REEs.

The Eu vs. Gd graph illustrates that the near-surface soft ore samples are variably depleted in Eu (Fig. 4.7B). Since weathering introduced organic material into the upper parts of the high-grade iron ore deposits (see section 4.4.1), it is likely that Eu was reduced to Eu^{2+} in the presence of organic carbon and decoupled from its neighboring trivalent REEs. This interpretation is in accordance with the apparent removal of Al_2O_3 relative to TiO_2, in the near-surface soft ore samples (Fig. 4.4A). The deviation of the soft ore sample at 88 m depth (drill hole S11D-330) from the regression line in the Eu vs. Gd diagram, is likely owed to its anomalous REE+Y pattern.

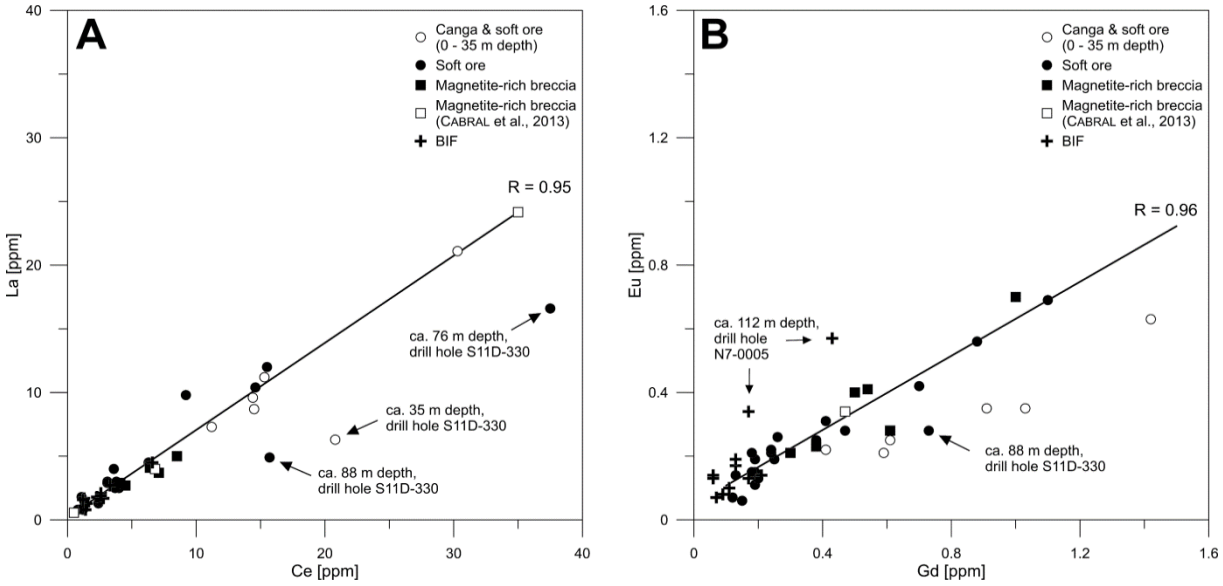

Fig. 4.7 Binary diagrams of (**A**) La vs. Ce & (**B**) Eu vs. Gd. The majority of the samples shows a good correlation and plots along regression lines with near-zero intercepts. Some samples deviate from this linear trend, indicating minor post-depositional mobilization, anomalous REE+Y patterns, or in the case of near-surface soft ore, introduction of organic and detrital material related to recent weathering (B).

4.6.2 Assessment of true Ce anomalies

The shale-normalized REE+Y distribution pattern of modern seawater exhibits a distinct negative Ce anomaly (Fig. 4.10A). This anomaly is caused by the oxidation of Ce^{3+} to less soluble Ce^{4+}. In contrast, suboxic to anoxic waters lack pronounced negative Ce anomalies (GERMAN & ELDERFIELD, 1990). The presence or absence of Ce anomalies in BIFs is therefore of great importance, since it provides information on the oxidation state of the ocean at the time of their deposition. However, in order to detect "true" Ce anomalies, potentially anomalous enrichment of La in seawater must be taken into consideration (BAU & DULSKY, 1996). Anomalously elevated levels of La could indicate a non-existent, i.e. false Ce anomaly if calculated only with the following formula (2):

$$(Ce/Ce^*)_{PAAS} = \frac{Ce_{PAAS}}{0.5La_{PAAS} + 0.5Pr_{PAAS}} \quad (2)$$

In order to avoid false Ce anomalies, $(Ce/Ce^*)_{PAAS}$ should be plotted against $(Pr/Pr^*)_{PAAS}$ (3).

$$(Pr/Pr^*)_{PAAS} = \frac{Pr_{PAAS}}{0.5Ce_{PAAS} + 0.5Nd_{PAAS}} \quad (3)$$

This approach after BAU & DULSKY (1996) should allow to discriminate between true Ce anomalies and false anomalies indicated by anomalous levels of La. As shown in Fig. 4.8, the BIF and magnetite-rich breccia samples from the Carajás Formation dominantly plot in the field of Archean to early Paleoproterozoic BIFs. A single BIF sample from drill hole S11D-330 exhibits a negative Ce anomaly. This sample is located at the contact with the ore body at ca. 217 m depth. A sample from the directly overlying soft ore exhibits a similar negative Ce

anomaly, while underlying BIF from ca. 219 m depth has no anomaly (Fig. 4.9A). The detected negative Ce anomaly likely results from weathering and does not reflect the prevalent oxidation state of the ocean at the time of the sedimentation of the BIF unit.

In the discriminative diagram after BAU & DULSKY (1996), a BIF sample from drill hole S11D-191, at ca. 219 m depth, plots in the field indicative of a positive Ce anomaly (Fig. 4.8). However, this apparent Ce anomaly is not detectable in the PAAS-normalized REE+Y distribution pattern of the sample (Fig. 4.9B). It appears that the sample exhibits a negative La anomaly in combination with low $(Pr/Pr^*)_{PAAS}$ ratios. Decreasing abundances of LREE, i.e. Ce >Pr >Nd, can produce $(Pr/Pr^*)_{PAAS}$ ratios <0.95. In fact, $(Pr/Pr^*)_{PAAS}$ ratios <0.95 appear to be rather common, as shown by the fields illustrating the range of $(Ce/Ce^*)_{PAAS}$ and $(Pr/Pr^*)_{PAAS}$ ratios of BIFs (Fig.4.8), and the $(Pr/Pr^*)_{PAAS}$ ratios of BIF and magnetite-rich breccia samples from the Carajás Formation. Consequently, anomalously low levels of La, in combination with decreasing abundances of LREE, might indicate positive Ce anomalies that are actually non-existent, as is the case for the BIF sample from drill hole S11D-191.

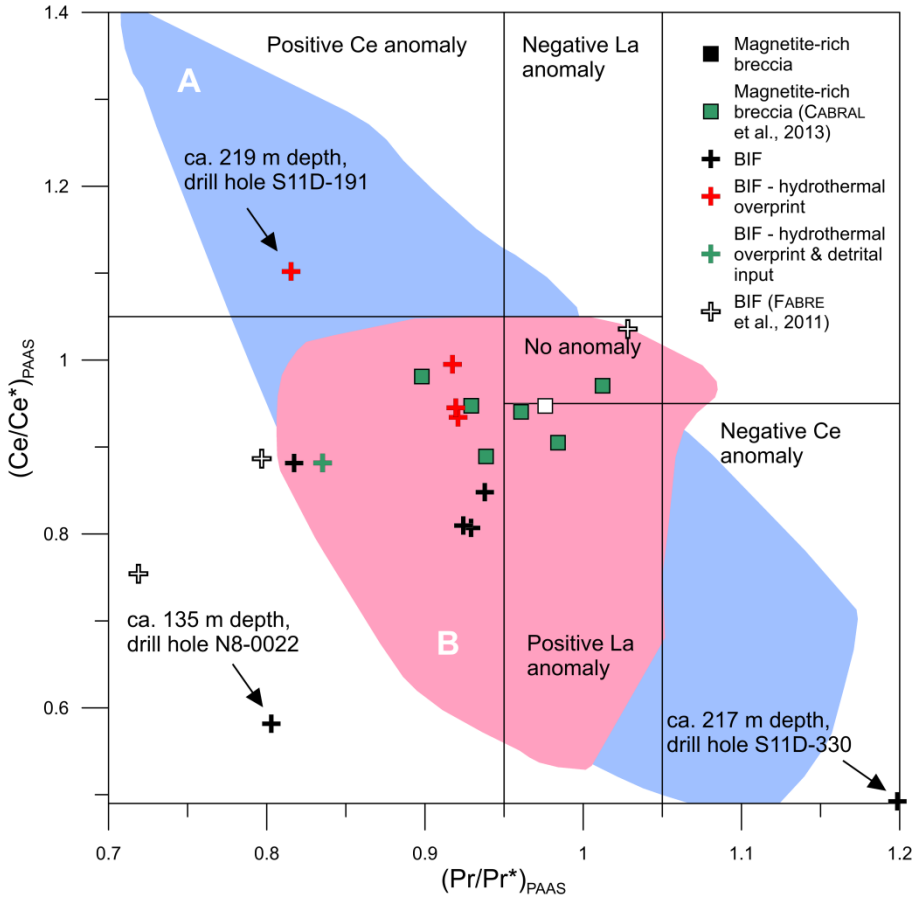

Fig. 4.8 Shale-normalized $(Ce/Ce^*)_{PAAS}$ and $(Pr/Pr^*)_{PAAS}$ ratios of BIF and magnetite-rich breccia samples from the Carajás Formation, including results from CABRAL et al. (2013) and FABRE et al. (2011). Most samples plot outside the fields indicative of positive or negative Ce anomalies (BAU & DULSKI, 1996). The range of $(Ce/Ce^*)_{PAAS}$ and $(Pr/Pr^*)_{PAAS}$ ratios of middle to late Paleoproterozoic BIFs (A, blue) and Archean to early Paleoproterozoic BIFs (B, red) are shown together with the data from the Carajás Formation (A and B redrawn from WANG et al., 2017).

In Fig. 4.8, a BIF sample from drill hole N8-0022, at ca. 135 m depth, and a BIF sample from FABRE et al. (2011) plot outside of any fields. The low $(Pr/Pr^*)_{PAAS}$ ratios of both samples are owed to anomalously high abundances of Nd.

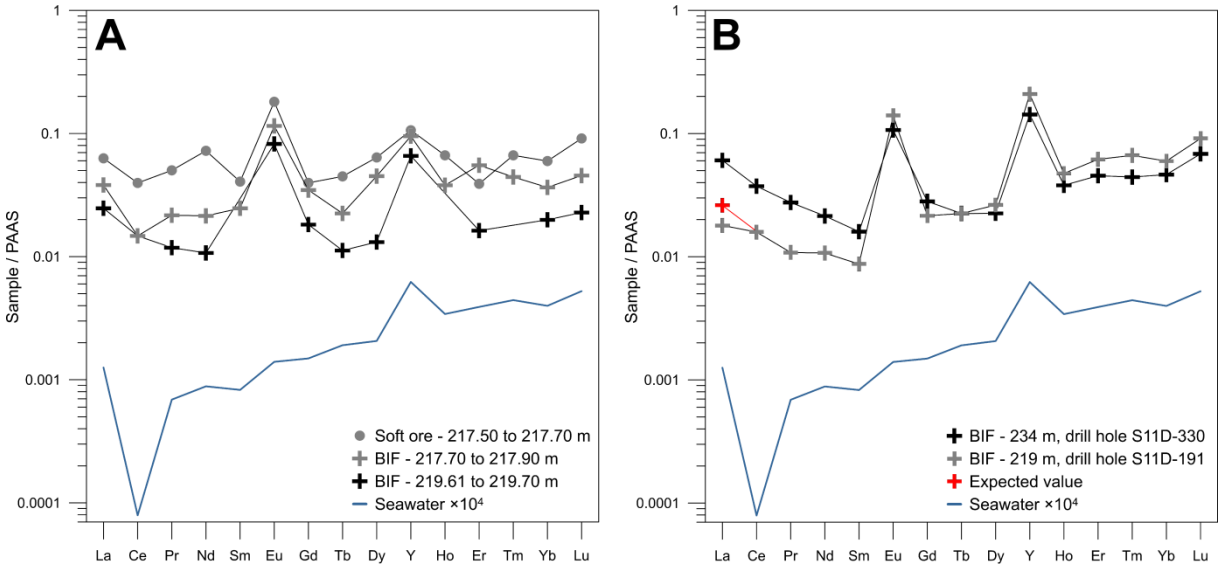

Fig. 4.9 PAAS-normalized REE+Y diagrams. (**A**) REE+Y patterns of soft ore and BIF from drill hole S11D-330. The samples are directly located at the contact of BIF to the overlying ore body. (**B**) REE+Y pattern of a BIF sample from drill hole S11D-191 showing an anomalously low abundance of La. The expected value for La, determined by back-extrapolation over Pr and Ce, and a BIF sample from drill hole S11D-330 were added for comparison.

4.6.3 Shale-normalized REE+Y signatures

Shale-normalized REE+Y distribution patterns of BIFs bear an obvious resemblance to modern seawater, i.e. LREE depletion, minor HREE enrichment and positive Y anomalies. This feature applies to all BIF-types, regardless of their depositional environment and age (PLANAVSKY et al., 2010), and provides a strong argument for the classification of BIFs as chemical sedimentary rocks that formed in a marine setting. In contrast to modern seawater, BIFs exhibit positive Eu anomalies indicative of a significant hydrothermal contribution to the dissolved REE content of the Precambrian ocean. The magnitude of the Eu anomaly decreases from Archean to Neoproterozoic BIFs (Fig. 4.10A). This could reflect a decline in the hydrothermal flux to the Precambrian ocean related to the thermal evolution of the mantle (DERRY & JACOBSEN, 1990), or it might signal an increasing REE-input from continental sources (KATO et al., 2006). A prominent negative Ce anomaly is characteristic for modern oxygenated seawater, but typically absent in BIFs older than 1.9 Ga (PLANAVSKY et al., 2010), although it has been occasionally observed in older BIFs (e.g. CABRAL et al., 2016; DELVIGNE et al., 2012).

The BIF samples from the Carajás Formation exhibit PAAS-normalized REE+Y distribution patterns that are typical for BIFs, i.e. LREE depletion, minor HREE enrichment and positive Y and Eu anomalies (Fig. 4.10B, C). As expected for Archean BIFs, the samples from the Carajás Formation exhibit distinct Eu anomalies. The magnitude of the detected Eu anomalies is, however, surprising. Shale-normalized $(Eu/Eu^*)_{PAAS}$ ratios of Archean BIFs typically range from 1.26 to 4.29 (PLANAVSKY et al., 2010). In contrast, the BIF samples from the N7, N8 and S11D deposits have high $(Eu/Eu^*)_{PAAS}$ ratios of 4.81 to 15.5 with an arithmetic mean of 9.32 (n = 7). As shown in Fig. 4.7B, the Eu content of two samples from the N7 deposit was affected by secondary element mobility, probably related to distal hydrothermal overprint. By excluding the two samples from the N7 deposit, the range of $(Eu/Eu^*)_{PAAS}$ ratios changes to 4.81 to 11.8 with an average of 7.71 (n = 5). FABRE et al. (2011) detected a similiar $(Eu/Eu^*)_{PAAS}$ ratio of 7.16 in a BIF sample from the N4 deposit. Such elevated $(Eu/Eu^*)_{PAAS}$ ratios indicate an unusually strong hydrothermal contribution to the Carajás basin at the time of the deposition of the BIF units. With the exception of a single weathering-related negative Ce anomaly in a BIF sample from drill hole S11D-330 (Fig. 4.9A), no Ce anomalies are detectable in the REE+Y distribution patterns of the BIF samples (Fig. 4.10B, C). It appears that post-depositional hydrothermal overprint, related to the emplacement of mafic dikes, was not severe enough to alter the REE contents (with the exception of Eu in two samples) or the REE+Y distribution patterns of the studied BIF samples (Fig. 4.10B, C).

The magnetite-rich breccia samples have rather flat REE+Y distribution patterns reflecting syndepositional addition of detrital material (Fig. 4.10D). However, detrital input was comparatively low (see section 4.4.1), and thus did not obscure their Eu and Y anomalies. The $(Eu/Eu^*)_{PAAS}$ ratios of the magnetite-rich breccia samples are lower in comparison to the analyzed BIF samples and range from 2.35 to 4.86 with an arithmetic mean of 3.94 (n = 6; Table 4.9). Similar to the BIF samples, no Ce anomalies are visible in the REE+Y distribution patterns of the magnetite-rich breccia samples (Fig. 4.10D).

Near-surface soft ore has elevated REE+Y levels and rather flat REE+Y distribution patterns comparable to the magnetite-rich breccia samples (Fig. 4.11A, F). These flat patterns are the result of near-surface contamination with detrital material during recent weathering. In contrast, soft ore samples from greater depths have REE+Y distribution patterns that closely resemble the studied BIF samples (Fig. 4.11B, C, D, E, F). Eu and Y anomalies are present in all samples. Near-surface soft ore is variably depleted in europium due to the reduction of Eu^{3+} in the presence of organic material and its removal as Eu^{2+} (see section 4.6.1). The $(Eu/Eu^*)_{PAAS}$ ratios of these samples are therefore rather low in comparison to soft ore from greater depths and the protore BIF. The $(Eu/Eu^*)_{PAAS}$ ratios of near-surface soft ore range from 1.81 to 2.67 and have an arithmetic mean of 2.04 (n = 6; Table 4.9). The $(Eu/Eu^*)_{PAAS}$ ratios of soft ore samples from greater depths are considerably higher and range from 2.45 to 9.39 with an arithmetic mean of 5.08 (n = 21; Table 4.9). Positive and negative Ce anomalies were observed in several soft ore samples. The magnitudes of the detected Ce anomalies are generally small. Since no soft ore samples show significant deviations from the

regression line in the La vs. Ce diagram (Fig. 4.7A), it is likely that the small Ce anomalies only represent insignificant mobilization of Ce during weathering.

Five soft ore samples exhibit anomalous REE+Y distribution patterns characterized by elevated LREE and depleted HREE contents (Fig. 4.12). The major and trace element levels of the samples suggest that they were unaffected by hydrothermal overprint, while HFSE diagrams indicate that three samples were affected by minor syndepositional addition of terrigenous sediments (Fig. 4.12B). However, considerable detrital addition should result in flat PAAS-normalized patterns. The observed LREE enrichment cannot be the product of detrital input. Furthermore, the REE+Y content of the soft ore sample at 76 m depth is extremely elevated, with $\sum$REE+Y = 76 ppm, compared to the average REE+Y content of soft ore with $\sum$REE+Y = 25.9 ppm. The anomalous REE+Y signatures of these five soft ore samples closely resemble the REE+Y distribution pattern of modern submarine vent-fluids (Fig. 4.12), which are characterized by remarkable LREE enrichment and high REE abundances that are two or three orders of magnitude higher in comparison to modern seawater (KATO et al., 2006). Given the unusually high $(Eu/Eu^*)_{PAAS}$ ratios in BIF and soft ore from the Carajás Formation (Table 4.9), indicative of a strong hydrothermal contribution to the Carajás basin at the time of the deposition of the BIF units, it is possible that the observed anomalous REE+Y distribution patterns reflect sedimentation in the direct vicinity of submarine hydrothermal vent fields. At present, this interpretation is only speculative and requires further investigation, since no anomalous REE+Y distribution patterns were observed in any of the BIF samples from the Carajás Formation studied here.

Alternatively, the anomalous REE+Y distribution patterns could reflect preferential mobilization of HREE during weathering. As shown by NELSON et al. (2003), carbonate, hydroxide, fluoride and organic anions preferentially form complexes with HREE in neutral to slightly alkaline waters, at ambient temperatures. HREE depletion has been reported for lateritic soils (BRAUN et al., 1990), and supergene BIF-hosted iron ores from the Maramane Dome and Urucum deposits (GUTZMER et al., 2008). However, this process fails to explain the extreme enrichment of LREE in the soft ore sample at 76 m depth, in comparison to the other soft ore samples. Furthermore, it seems unlikely that only five soft ore samples would be affected by weathering-related HREE depletion.

Table 4.9 Range of $(Eu/Eu^*)_{PAAS}$ ratios for different lithologies.

Lithology	Minimum	Maximum	Average
Near-surface soft ore	1.81	2.67	2.04
Soft ore	2.45	9.39	5.08
Magnetite-rich breccia	2.35	4.86	3.94
BIF (Carajás Formation)	4.81	11.8	7.71
Archean BIF[1]	1.26	4.29	2.33

[1] Data from PLANAVSKY et al. (2010)

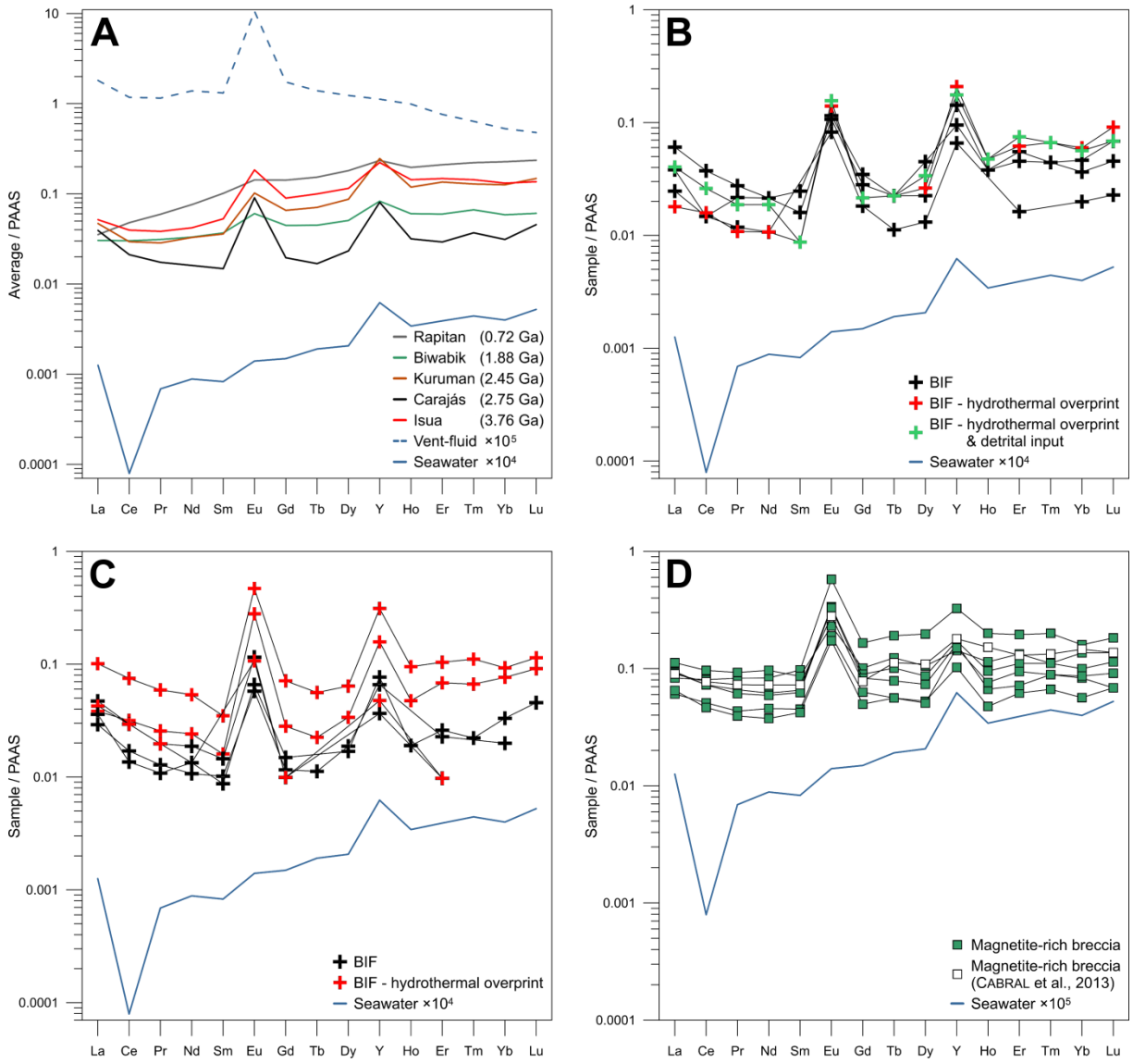

Fig. 4.10 PAAS-normalized REE+Y diagrams. (**A**) Average REE+Y pattern of hydrothermally unaltered and detritus-free BIF from the Carajás Formation, compared to Archean, Paleo- and Neoproterozoic iron formations (REE+Y data sources: Rapitan - HALVERSON et al., 2011; Biwabik - PLANAVSKY et al., 2010; Kuruman - BAU & DULKSI, 1996; Isua - BOLHAR et al., 2004; Vent-fluid - BAO et al., 2008; Seawater - NOZAKI, 1997). (**B**) REE+Y patterns of BIF from the Serra Sul, S11D-deposit. (**C**) REE+Y patterns of BIF from the Serra Norte, N7 and N8 deposits. (**D**) REE+Y patterns of Magnetite-rich breccia samples from the Serra Sul, S11D-deposit.

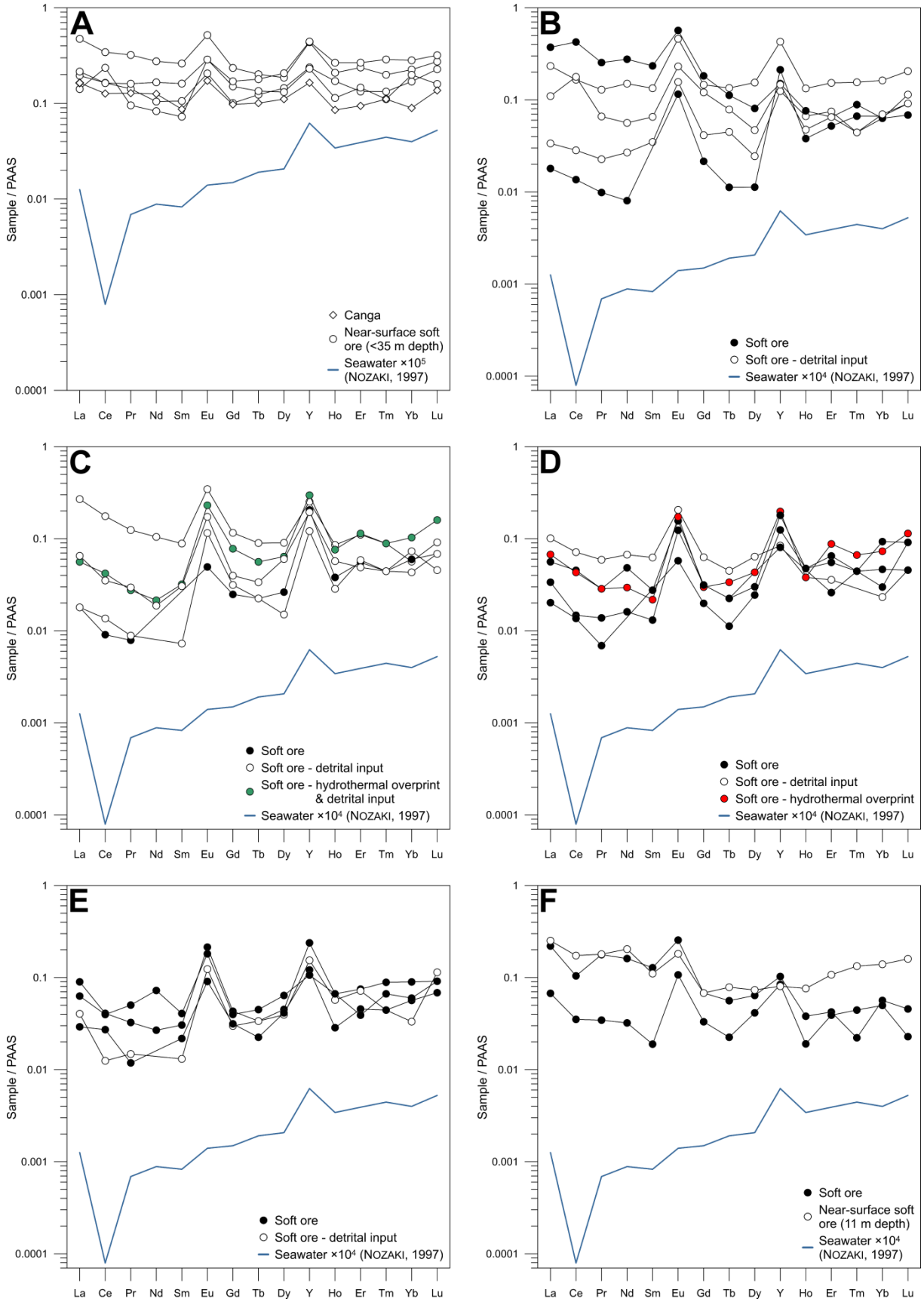

Fig. 4.11 PAAS-normalized REE+Y diagrams. (**A**) to (**E**) REE+Y patterns of soft ore from the S11D deposit, Serra Sul. (**F**) REE+Y patterns of soft ore from the N8 deposit, Serra Norte.

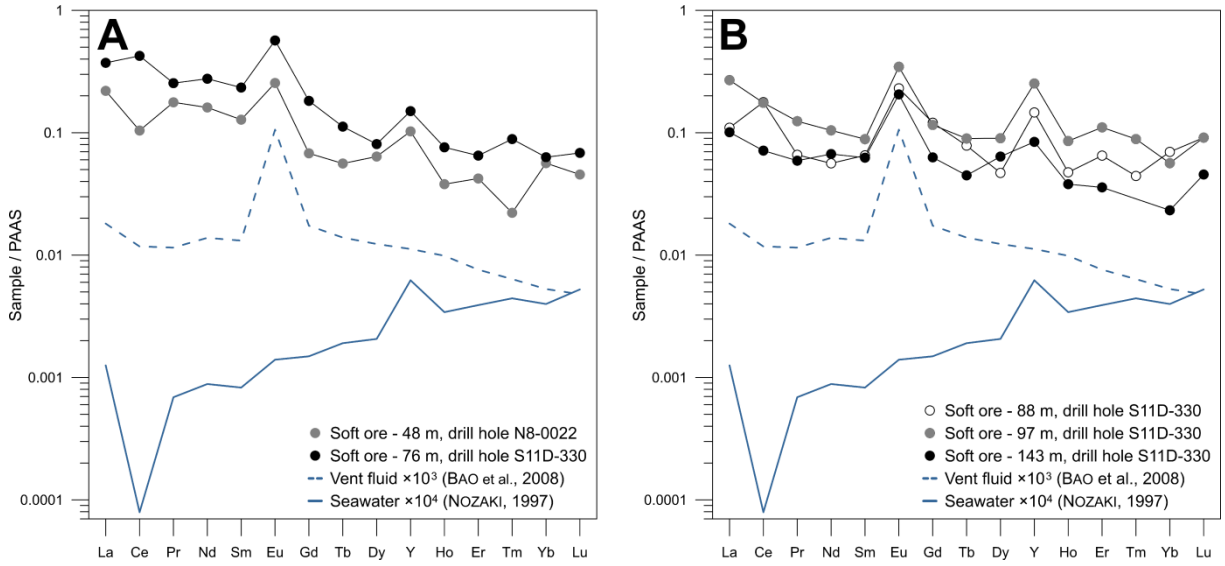

Fig. 4.12 PAAS-normalized REE+Y diagrams. (**A**) Anomalous REE+Y patterns of detritus-free soft ore. (**B**) Anomalous REE+Y patterns of soft ore affected by detrital input.

4.7 Volcanic material

Three units of fine-grained volcanic material were intercepted in the drill holes S11D-214, N7-0005 and N8-0022 at depths of ca. 105, 391 and 128 m, respectively (see chapter 3).

The Zr/TiO_2 vs. Nb/Y diagram after PEARCE (1996) was utilized for the discrimination of these volcanic rocks, since the likely mobile behavior of most major elements during hydrothermal overprint prevents the utilization of the TAS diagram. The two samples from the S11D and N7 deposits plot in the field of basalt, together with metabasalt samples of ZUCCHETTI (2007) from the N4 and N5 deposits (Fig. 4.13). In contrast, the sample from the N8 deposit plots in the field of rhyolite/dacite. Since the sample from the N8 deposit contains considerable amounts of chlorite (see chapter 3, section 3.1 and 3.2), this finding is quite surprising. Chlorite forms by replacement of pyroxene, amphibole or biotite, i.e. mafic minerals. Nonetheless, the sample has an elevated REE content (Fig. 4.14), is depleted in TiO_2 and considerably enriched in HFSE (Fig. 4.15), which supports the classification of the sample as rhyolite/dacite. Therefore, the large amount of chlorite in the sample from the N8 deposit did not form by replacement of pre-existing mafic minerals, but rather precipitated from a magnesium-bearing fluid that was channelled along the contact of the volcanic unit and its country rock.

It is unclear, whether the three volcanic units formed by synsedimentary volcanism or if they were emplaced later as sills or dikes in the Carajás Formation. The position of the basalt samples in the Th/Yb vs. Nb/Yb covariation diagram after PEARCE (1983) indicates that they formed in a continental arc (Fig. 4.16A). In the Ti vs. Zr diagram, the basalt sample from the S11D deposit plots in the field of arc lavas (Fig. 4.16B), together with metabasalt samples of ZUCCHETTI (2007) and DARDENNE et al. (1988) from the Grão Pará Group. In contrast, the basalt sample from the N7 deposit plots in the field of within plate lavas. ZUCCHETTI (2007) reports a poor correlation for Ti and Y with other HFSE in samples of metagabbro from the N4 deposit

and suggests that both elements were partially mobile during intense hydrothermal overprint. It is possible that the basalt sample from the N7 deposit became slightly enriched in Ti during hydrothermal alteration and thus plots in the field of within plate lavas.

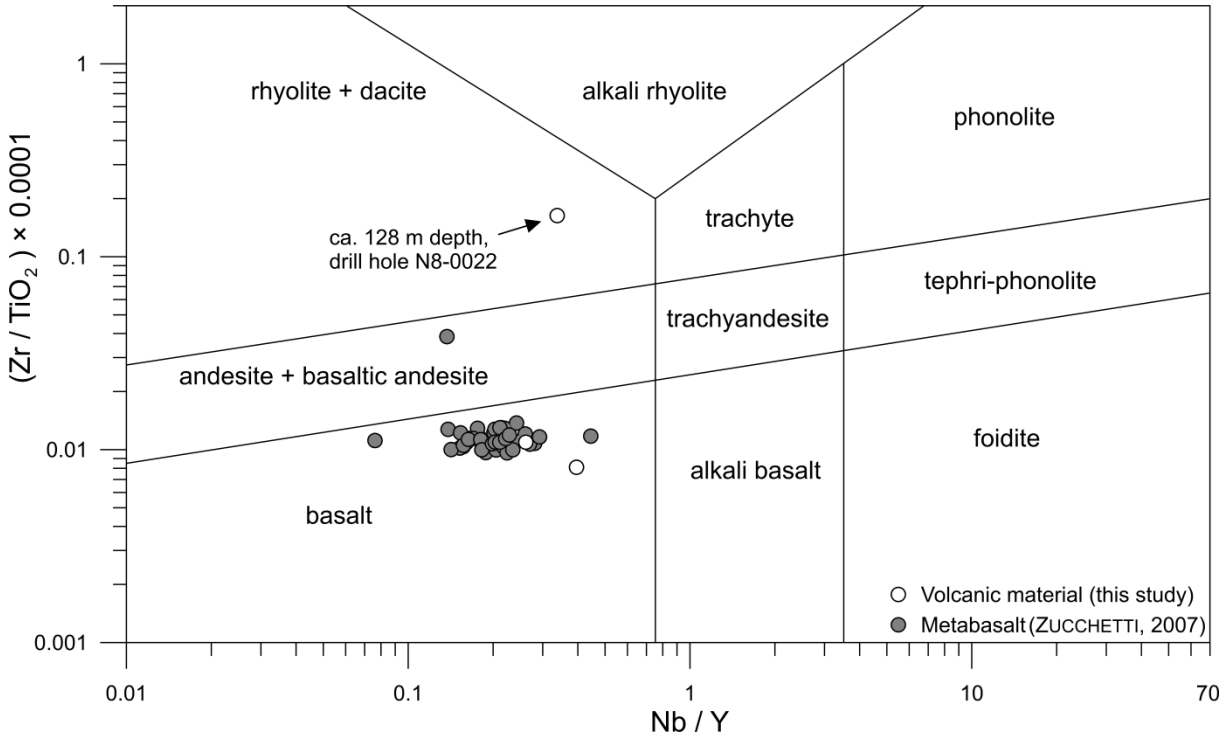

Fig. 4.13 Discriminative diagram for volcanic rocks after PEARCE (1996), redrawn from ZUCCHETTI (2007). Metabasalt samples of ZUCCHETTI (2007) from the N4 and N5 deposits were added for comparison.

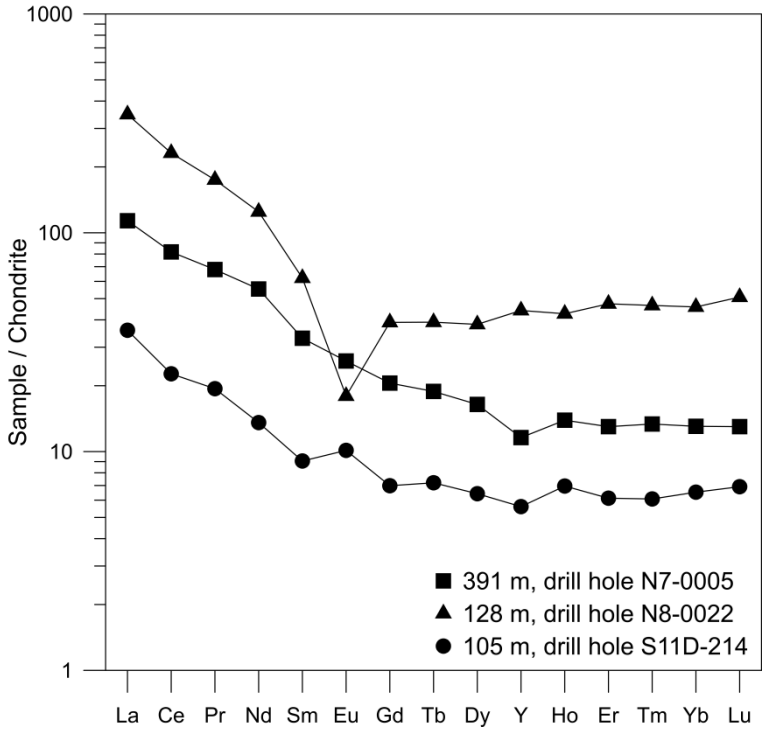

Fig. 4.14 Chondrite-normalized REE+Y distribution patterns of samples consisting of volcanic material. C1-chondrite data is from MCDONOUGH & SUN (1995).

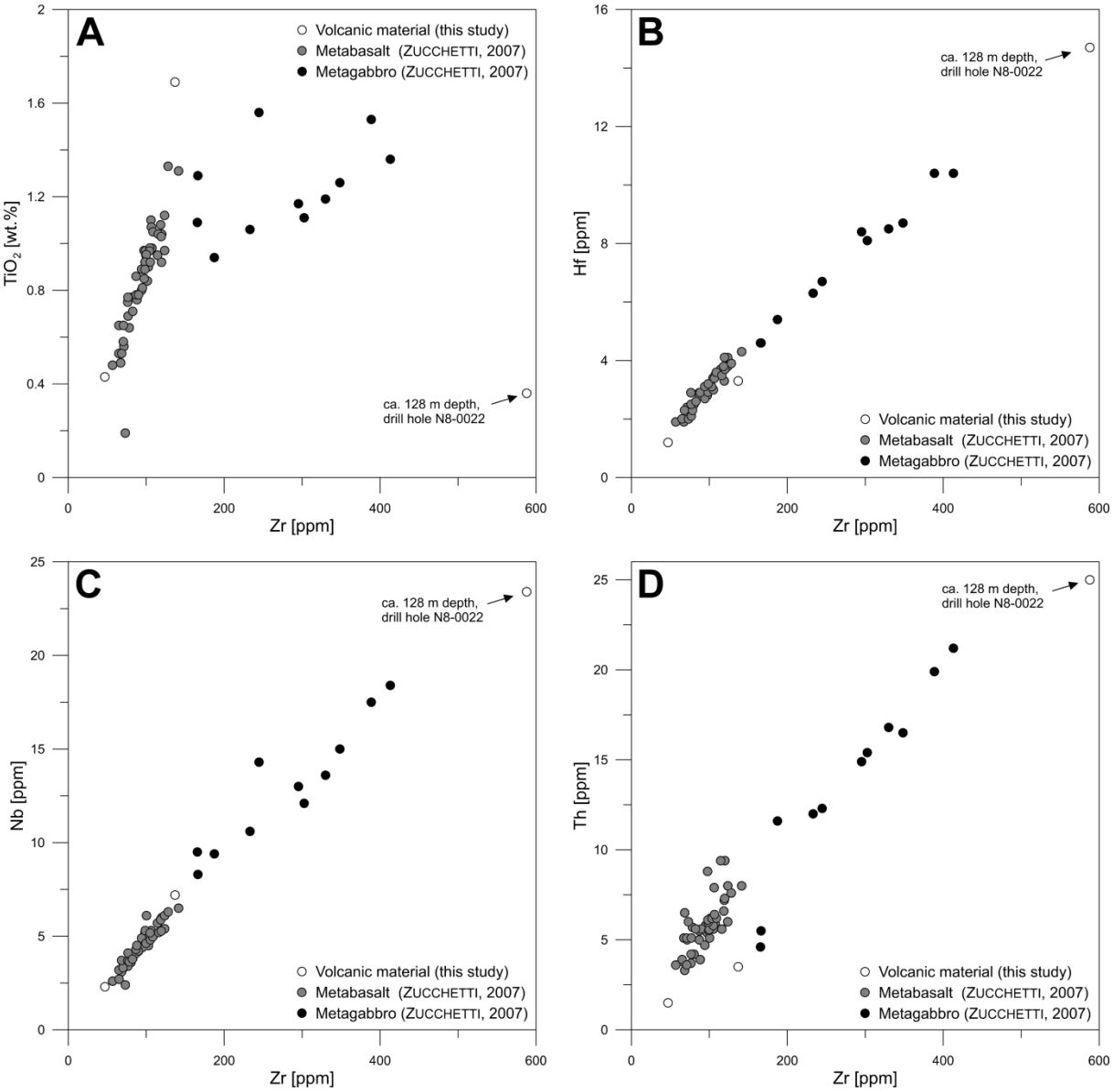

Fig. 4.15 Binary diagrams of (**A**) TiO_2 vs. Zr, (**B**) Hf vs. Zr, (**C**) Nb vs. Zr and (**D**) Th vs. Zr. Metabasalt and metagabbro samples of ZUCCHETTI (2007) from the N4 and N5 deposits were added for comparison.

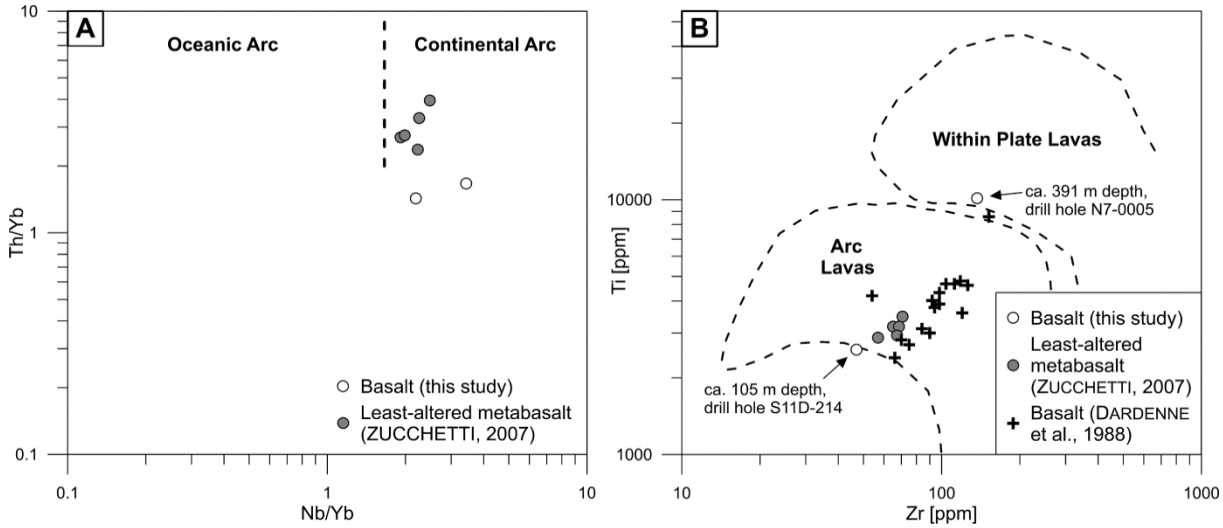

Fig. 4.16 (**A**) Th/Yb vs. Nb/Yb covariation and (**B**) Ti vs. Zr diagrams for basalts of the Grão Pará Group. (**A**) The covariation diagram after PEARCE (1983) indicates that the basalts formed in a continental arc setting (redrawn from ZUCCHETTI, 2007). (**B**) With the exception of the basalt sample from the N7 deposit, all analyses plot in the field of volcanic arc lavas (modified after DARDENNE et al., 1988).

Chapter 5 In-situ Fe Isotope Analysis

Naturally occurring iron has four stable isotopes (TAYLOR et al., 1992), ^{54}Fe (5.845 mol.%), ^{56}Fe (91.754 mol.%), ^{57}Fe (2.1191 mol.%) and ^{58}Fe (0.2819 mol.%). It has been shown that terrestrial and most extraterrestrial iron is only affected by isotope fractionation processes that are strictly mass-dependent (DAUPHAS et al., 2004). Mass-independent fractionation of iron was reported for pre-solar silicon carbide grains (TRIPA et al., 2002; DAVIS et al., 2002). However, these results obtained with TOF-RIMS (time-of-flight resonance ionization mass spectrometry) could not be reproduced with NanoSIMS (Nano secondary ion mass spectrometry; MARHAS et al., 2004), which indicates that the measurements of TRIPA et al. (2002) and DAVIS et al. (2002) were likely affected by analytical artifacts, e.g. isobaric interferences or contamination (DAUPHAS & ROUXEL, 2006).

Thus, it appears that the Fe isotope composition of iron-bearing minerals is only controlled by mass-dependent fractionation processes, i.e. equilibrium or kinetic fractionation.

At chemical equilibrium, the heavier isotope of an element becomes enriched in the phase or chemical compound that induces the largest reduction of its vibrational energy (mainly its zero-point energy). The vibrational energy is minimized in chemical compounds with high bond forces (BIGELEISEN, 1965). This process, called equilibrium fractionation, is temperature-dependent and strongest at low temperatures.

Kinetic fractionation takes place during unidirectional chemical reactions and also during reversible reactions that have not yet attained isotopic equilibrium. Light isotopes react slightly faster than their respective heavier isotopes due to their lower mass (HOEFS, 1987). Hence, the product of non-equilibrium reactions becomes enriched in the light isotope, i.e. ^{54}Fe in the case of iron.

Over the past two decades, Fe isotope fractionation factors were determined for a number of chemical reactions, both experimentally (α-factors) and through theoretical considerations (β-factors). A brief overview is given in Table 5.1.

The measurement of the Fe isotope composition of BIF and high-grade iron ore provides a valuable insight in the processes controlling BIF genesis and ore formation. Fe isotope studies represent a relatively new approach, which already led to important discoveries concerning the continuity of BIF sedimentation over varying timescales and the role of bacteria during early diagenesis (JOHNSON et al., 2008; LI et al., 2015).

Table 5.1 Fe isotope fractionation factors (modified after STEINHOEFEL et al., 2009b).

Reactant	Product	Condition	$\Delta^{56}Fe_{product-Reactant}$ [‰]		References
Experimental studies (α-factors)			*T = 22°C*	*T = 98°C*	
$Fe(II)_{aq}$	$Fe(III)_{aq}$	Equilibrium	2.8 to 3.0		JOHNSON et al. (2002), WELCH et al. (2003)
$Fe(II)_{aq}$	$Si_{0.67}$-$Fe(III)_{0.33}$	Equilibrium	3.5 ± 0.2		WU et al. (2012)
$Fe(II)_{aq}$	$Si_{0.25}$-$Fe(III)_{0.75}$	Equilibrium	4.0 ± 0.2		WU et al. (2012)
$Fe(OH)_3$	$Fe(II)_{aq}$	Anaerobic photosynthesis	-1.5 ± 0.2		CROAL et al. (2004)
$Fe(OH)_3$	$Fe(II)_{aq}$	Abiotic	-1.0		BULLEN et al. (2001)
Fe_2O_3, FeO(OH)	$Fe(II)_{aq}$	DIR, equilibrium	-3.0		CROSBY et al. (2007)
$Fe(II)_{aq}$	FeO(OH)	Equilibrium	1.05		BEARD et al. (2010)
$Fe(III)_{aq}$	Fe_2O_3	Equilibrium		+0.1 ± 0.2	SKULAN et al. (2002)
$Fe(III)_{aq}$	Fe_2O_3	Kinetic		-1.0 to -2.0	SKULAN et al. (2002)
				T = 200°C	
$Fe(III)_{aq}$	Fe_2O_3	Equilibrium		0	SAUNIER et al. (2011)
				T = 300°C	
$Fe(II)Cl_{2(aq)}$	Fe_2O_3	Equilibrium		0.36	SAUNIER et al. (2011)
$Fe(II)_{aq}$	Fe_3O_4	DIR, equilibrium	1.3 ± 0.1		JOHNSON et al. (2005)
$Fe(II)_{aq}$	Fe_3O_4	Magnetotactic bacteria	0		MANDERNACK et al. (1999)
$Fe(II)_{aq}$	$FeCO_3$	Abiotic	-0.5 ± 0.2		WIESLI et al. (2004)
$Fe(II)_{aq}$	$FeCO_3$	DIR, equilibrium	0		JOHNSON et al. (2005)
Fe_3O_4	$FeCO_3$	DIR, equilibrium	-1.3		JOHNSON et al. (2005)
Predictions by modelling (β-factors)[1]			*T = 22°C*	*T = 200°C*	
$Fe(II)_{aq}$	$Fe(III)_{aq}$	Equilibrium	2.5 to 3.0	1.1 to 1.2	ANBAR et al. (2005)
$Fe(II)_{aq}$	Fe_3O_4	Equilibrium	0.2 to 0.4	0.1	ANBAR et al. (2005), POLYAKOV et al. (2007)
$Fe(III)_{aq}$	Fe_3O_4	Equilibrium	-2.3	-1	ANBAR et al. (2005), POLYAKOV et al. (2007)
Fe_2O_3	Fe_3O_4	Equilibrium	-0.9	-0.3	POLYAKOV et al. (2007)
$Fe(II)_{aq}$	$FeCO_3$	Equilibrium	-2.5 to -2.7	-1.1	POLYAKOV & Mineev (2000), ANBAR et al. (2005)
Fe_3O_4	$FeCO_3$	Equilibrium	-2.9	-1.2	POLYAKOV & Mineev (2000), POLYAKOV et al. (2007)

[1]Calculations were carried out with estimates from DFT-PCM, DFT, Mössbauer and INRXS (see references)

In the past, stable isotope studies of transition metals were carried out by thermal ionisation mass spectrometry (TIMS). This method requires long measurement times and is limited by a time-dependent isotope fractionation effect (HIRATA & OHNO, 2001). However, over the last two decades, analytical improvements in the field of multiple collector inductively coupled plasma mass spectrometry (MC-ICP-MS), significantly advanced the applicability of heavy stable isotope analysis (HALLIDAY et al., 1995; HIRATA & OHNO, 2001). Today, Fe isotope measurements are usually carried out either with solution MC-ICP-MS, which provides information about the bulk isotope composition of the analyzed samples, or with laser-ablative MC-ICP-MS, which allows to study the isotope composition of individual mineral grains, in-situ.

For this thesis, ten representative polished thin sections were selected, including BIF, soft ore, canga and the magnetite-rich breccia from the basal part of the Carajás Formation. In-situ Fe isotope analyses of magnetite, martite, microplaty hematite, goethite, pyrite and chalcopyrite were carried out at the Institute for Mineralogy of the Leibniz Universität Hannover, using a deep UV (194 nm) femtosecond laser coupled to a MC-ICP-MS instrument. In contrast to conventional nanosecond laser ablation MC-ICP-MS, femtosecond laser ablation (fs-LA) MC-ICP-MS provides matrix-independent high precision Fe isotope data without requiring a matrix match between standards and samples (STEINHOEFEL et al., 2009a; OESER et al., 2014). Furthermore, fs-LA-MC-ICP-MS does not induce time-dependent isotope fractionation (HORN & VON BLANCKENBURG, 2007).

A detailed description of the instrumental setup and the studied samples is provided in the first two sections. The quality and reliability of the acquired data is assessed shortly. The results are presented in one section and discussed extensively in the last section and its subsections.

5.1 Instrumental setup and measurement procedure

High precision in-situ Fe isotope measurements were performed with a deep UV femtosecond laser coupled to a MC-ICP-MS instrument (Thermo Finnigan Neptune). A schematic sketch of the instrumental setup is given in Fig. 5.1.

The laser ablation system consists of a 100 femtosecond Ti:sapphire regenerative amplifier system (Spectra Physics Solstice™) with a pulse energy of 0.07 mJ. The fundamental wavelength of the femtosecond laser is 775 nm (OESER et al., 2014). A wavelength of 194 nm is achieved through frequency-quadrupling with harmonic generators (HORN et al., 2006).

Following ablation, the aerosol is transported to the MC-ICP-MS instrument, using helium as carrier gas. Prior to entering the torch, a nickel reference solution (NIST SRM 986) is added to the aerosol together with argon, via a quartz glass spray chamber equipped with an ESI PFA-ST nebuliser (OESER et al., 2014). The determination of the $^{60}Ni/^{58}Ni$ ratio, simultaneous to the measurement of ^{57}Fe, ^{56}Fe and ^{54}Fe, is needed for instrumental mass bias correction. By applying the standard-sample bracketing method, the influence of mass bias and instrumental drift is minimized.

The MC-ICP-MS instrument is equipped with nine Faraday detectors (cups) and is capable of high mass resolution measurements ($M/\Delta M \approx 9000$). A summary of the used cup configuration and further important instrumental parameters is given in Table 5.2. Measuring Fe isotopes in high mass resolution mode effectively eliminates molecular interferences. Using narrow entrance slits (high mass resolution) in combination with wide collector slits (low mass resolution), prevents polyatomic interferences from entering the detectors while simultaneously providing flat peaks (Fig. 5.2), which are a prerequisite for high precision isotope measurements (WEYER & SCHWIETERS, 2003). Common molecular interferences for Fe isotope measurements are argon nitrides, e.g. $^{40}Ar^{14}N$ on ^{54}Fe, and argon oxides, e.g. $^{40}Ar^{16}O$ on ^{56}Fe. Depending on the sample matrix, further chemical compounds, e.g. $^{40}Ca^{16}O$ or $^{44}Ca^{12}C$, might interfere with the measurements, if not carried out in high mass resolution mode (WEYER & SCHWIETERS, 2003). The isobaric interference of ^{54}Cr on ^{54}Fe is resolved by simultaneous monitoring of ^{52}Cr. Due to the mass-dependent fractionation of chromium, the influence of ^{54}Cr can be determined and subtracted from the attained results.

For the analyses presented in this study, a laser beam spot size of 40 to 50 µm was used, depending on the diameter of the mineral grains. The obtained Fe isotope data are reported relative to the IRMM-014 reference material (IRMM, 2008), in the standard $\delta^{56}Fe$ notation:

$$\delta^{56}Fe = \left(\frac{^{56}Fe/^{54}Fe_{sample}}{^{56}Fe/^{54}Fe_{IRMM\text{-}014}} - 1 \right) \times 1000\ [‰] \quad (1)$$

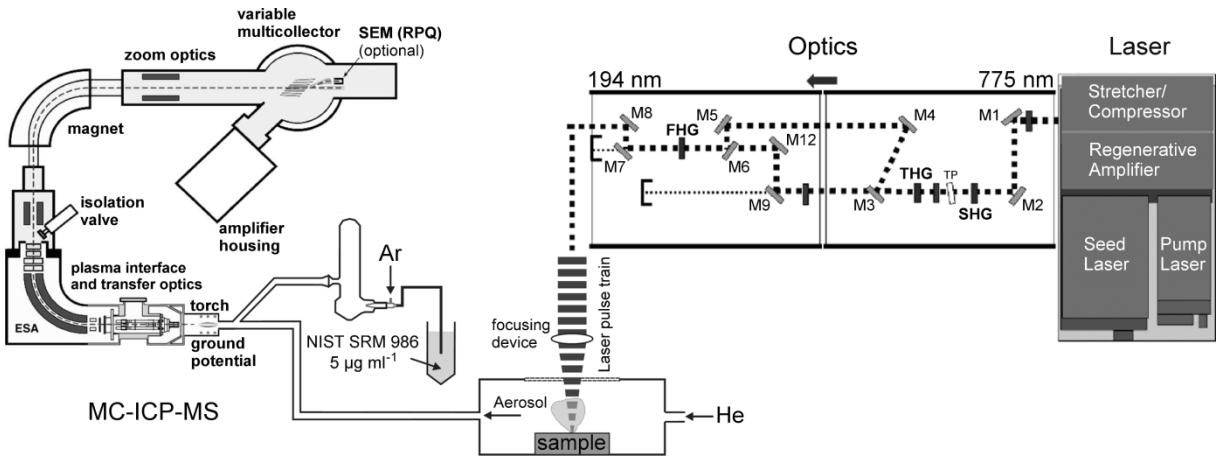

Fig. 5.1 Schematic representation of the instrumental setup. The diagram illustrates the wavelength conversion setup for the femtosecond laser (from 775 to 194 nm; M = mirror, SHG= second harmonic generator, THG = third harmonic generator, FHG = fourth harmonic generator). The build-up of the ablation cell/stage and introduction system is shown in the middle section of the picture (NIST SRM 986 = Ni reference solution). A cross-section of the ion optics of the MC-ICP-MS instrument is shown on the left (modified after HORN et al., 2006; OESER et al., 2014; WEYER & SCHWIETERS, 2003).

Table 5.2 Instrumental parameters for Fe isotope measurements with fs-LA-MC-ICP-MS (modified after OESER et al., 2014).

Fs-LA system	
Spot diameter [µm]	40 to 50
Repetition rate [Hz]	4 to 100
Pulse length [sec]	ca. 200 × 10^{-15}
Pulse energy output [mJ]	0.07
Pulse energy at sample [mJ]	0.015
Achievable energy density [J cm^{-2}]	ca. 2
Ablation cell volume [cm^3]	30
MC-ICP-MS (Thermo Finnigan Neptune)	
Cool gas: Ar [L min^{-1}]	14.6 to 15
Auxiliary gas: Ar [L min^{-1}]	0.7 to 0.9
Sample gas: Ar [L min^{-1}]	0.88 to 0.94
Carrier gas: He [L min^{-1}]	0.5 to 0.7
Nebulizer uptake rate [µL min^{-1}]	ca. 100
RF generator power [W]	1200 to 1240
Acceleration voltage [V]	-10 000
Extraction [V]	-1850 to -2000
Focus [V]	-590 to -680
Sample cone: Ni; Skimmer cone: Ni, X-type	
Faraday cup setup:	
^{52}Cr (L4), ^{54}Fe (L2), ^{56}Fe (Center), ^{57}Fe (H1), ^{58}Ni (H2), ^{60}Ni (H4)	

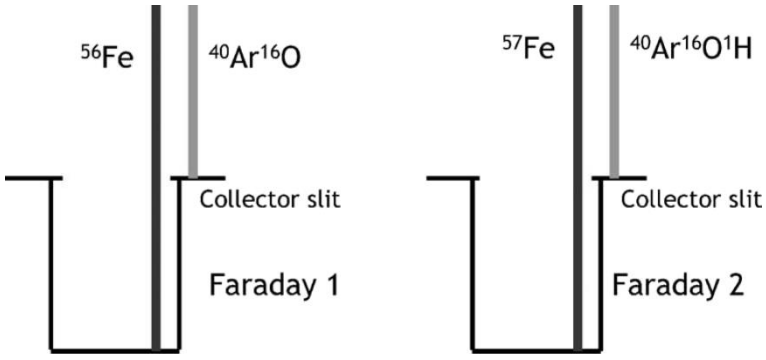

Fig. 5.2 Schematic sketch illustrating the collector setup used for high precision Fe isotope measurements. By utilizing narrow entrance slits in combination with wide collector slits, molecular interferences are eliminated, while still enabling accurate Fe isotope measurements (WEYER & SCHWIETERS, 2003).

5.2 Sample description

Ten polished thin sections were selected for in-situ Fe isotope measurements. The sample set includes one magnetite-rich breccia, one canga, three soft ore and five BIF sections. A brief description of the samples is provided in Table 5.3. The major element and copper contents of the drill cores, from which the thin sections were prepared, is listed in Table 5.4 (for detailed geochemical information, see chapter 4).

In the analyzed BIF samples and the magnetite-rich breccia, magnetite is the most abundant iron-bearing mineral, while hematite is prevalent as martite and microplaty hematite in soft ore and canga. The magnetite-rich breccia was affected by localized carbonate metasomatism and contains abundant chlorite, carbonate, pyrite and chalcopyrite (see chapter 3, section 3.2). Trace amounts of pyrite and chalcopyrite were observed in all thin sections. Goethite is interstitial in most samples and more abundant in the soft ore samples and the superficial canga. The three BIF samples from the N7 deposit are from a single 37 cm long drill core interval. They are weakly affected by incipient martitization. In contrast, the BIF sample from the N8 deposit is unaffected by martitization and hosts finely dispersed microplaty hematite and minor chalcopyrite. The BIF sample from the N8 deposit and one sample from the N7 deposit (112.35 m), both host chert microspherulites. Kenomagnetite and martite are abundant in the BIF sample from the S11D deposit (217 m), which is directly located at the contact with the overlying ore body. Microplaty hematite is a minor constituent in this sample, too. Microplaty hematite is abundant in the soft ore sample at 172 m depth, as finely dispersed platelets and also as larger crystals that nucleate on martite and replace it. In the soft ore sample at 97 m depth, microplaty hematite is a minor component, and absent in the near-surface soft ore sample at 34 m depth, which is mainly made up of martite with a skeletal microstructure. The canga sample consists predominantly of martite and goethite. Microplaty hematite is absent. It hosts numerous relicts of magnetite and quartz grains, which suggests that it formed mainly from weathering of BIF corestones that were preserved in soft ore, prior to exhumation.

Table 5.3 Sample description.

Drillhole	Depth	Type	Mineral content
S11D-330	0 m	Canga	Martite, goethite, chert, minor magnetite, traces of pyrite/chalcopyrite
S11D-330	34 m	Soft ore	Martite, goethite, chert, traces of pyrite/chalcopyrite
S11D-330	97 m	Soft ore	Martite, microplaty hematite, chert, traces of pyrite/chalcopyrite
S11D-330	172 m	Soft ore	Martite, microplaty hematite, magnetite, chert, traces of pyrite/chalcopyrite
S11D-330	217 m	BIF	Magnetite, chert, martite, microplaty hematite, traces of pyrite/chalcopyrite
S11D-214	361 m	Magnetite-rich breccia	Magnetite, chert, pyrite, stilpnomelane, chlorite, carbonate
N7-0005	111.98 m	BIF	Magnetite, chert, minor martite, traces of pyrite/chalcopyrite
N7-0005	112.15 m	BIF	Magnetite, chert, minor martite, traces of pyrite/chalcopyrite
N7-0005	112.35 m	BIF	Magnetite, chert, minor martite, traces of pyrite/chalcopyrite
N8-0022	98 m	BIF	Magnetite, chert, microplaty hematite, traces of pyrite/chalcopyrite

Table 5.4 Major element contents [wt.%] and Cu [ppm] of the studied samples.

Deposit	S11D	S11D	S11D	S11D	S11D	S11D	N7	N8
Type	Canga	Soft ore	Soft ore	Soft ore	BIF	Magnetite-rich breccia	BIF	BIF
Depth	0 m	34 m	97 m	172 m	217 m	361 m	112 m	98 m
SiO_2	1.27	0.22	0.53	0.45	40.0	47.8	50.0	37.8
TiO_2	0.25	0.16	<0.01	<0.01	<0.01	0.02	<0.01	<0.01
Al_2O_3	1.00	2.29	0.60	0.20	<0.01	0.57	0.19	<0.01
Fe_2O_3	94.4	95.4	96.7	97.7	59.8	40.6	49.0	58.2
MnO	0.01	<0.01	<0.01	<0.01	0.03	0.27	0.04	0.14
MgO	0.01	<0.01	0.01	0.02	<0.01	1.58	1.27	1.27
CaO	0.01	<0.01	<0.01	<0.01	0.02	4.12	0.16	1.99
Na_2O	<0.01	<0.01	<0.01	<0.01	N.A.	N.A.	N.A.	N.A.
K_2O	<0.01	<0.01	<0.01	<0.01	<0.01	0.22	0.02	<0.01
P_2O_5	0.42	0.15	0.05	0.15	<0.01	0.01	0.03	<0.01
LOI	2.78	1.87	2.85	1.77	0.31	4.86	-0.75	1.08
Sum	100.2	100.1	100.7	100.3	100.2	100.1	100	100.5
Cu	34.3	13.7	8.3	22	4.1	40.0	385	162

N.A. - no available data

5.3 Reliability

The MC-ICP-MS instrument was run in high mass resolution mode to eliminate molecular interferences (see section 5.1). Isobaric interferences of ^{54}Cr on ^{54}Fe were resolved by measuring ^{52}Cr. All measurements were carried out with the standard-sample bracketing method, while simultaneously determining the $^{60}Ni/^{58}Ni$ ratio of a nickel reference solution (NIST SRM 986), in order to correct for mass bias and instrumental drift. The international reference material IRMM-014 was used as standard throughout all measurements. The external reproducibility was determined by repeated measurements of an in-house iron standard Puratronic (Johnson Matthey) over a period of two years, which gave $\delta^{56}Fe = 0.08 \pm 0.06‰$ and $\delta^{57}Fe = 0.12 \pm 0.12‰$ (2σ, n = 47; Table 5.5). This result is in agreement with the analyses of STEINHOEFEL et al. (2009b), who report a composition of $\delta^{56}Fe = 0.08 \pm 0.08‰$ and $\delta^{57}Fe = 0.12 \pm 0.14‰$ (2σ, n = 101). The internal precision during all measurements was generally better than 0.10‰ for $\delta^{56}Fe$ and 0.15‰ for $\delta^{57}Fe$ (2σ). Within analytical uncertainty, all spot analyses plot along the theoretical mass fractionation line of $\delta^{56}Fe$ versus $\delta^{57}Fe$ (Fig. 5.3), i.e. were not influenced by interferences.

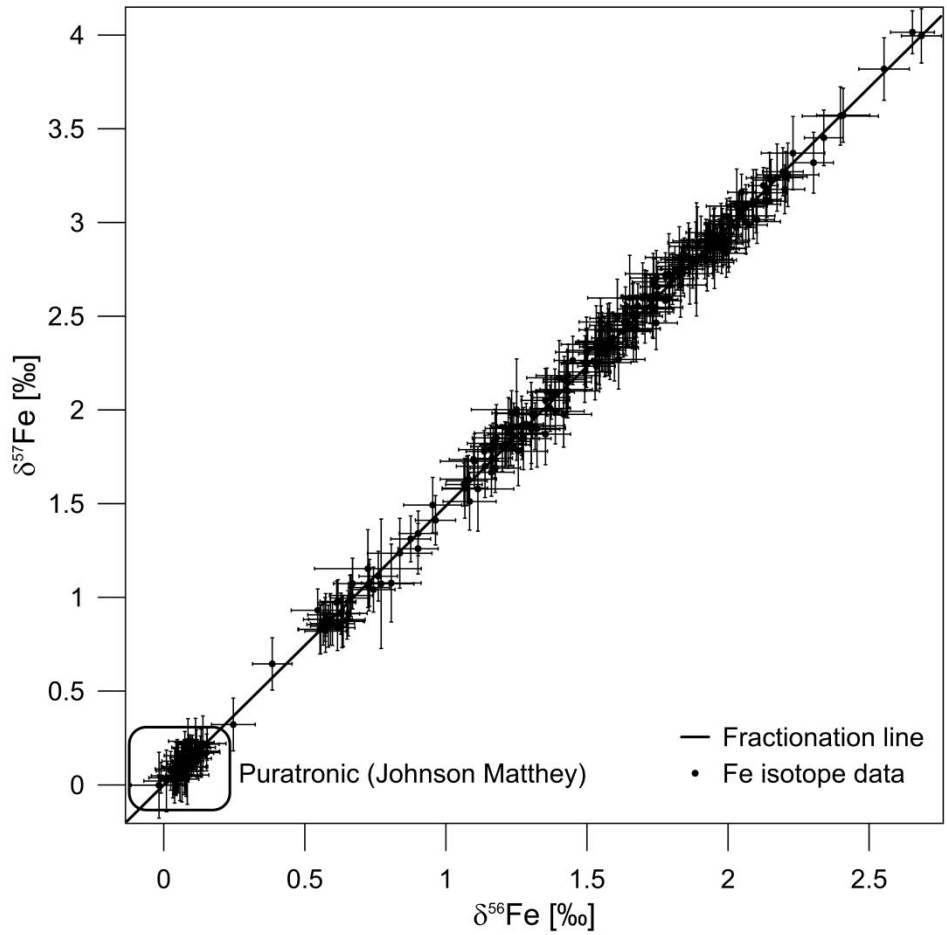

Fig. 5.3 Three-isotope plot of all Fe isotope analyses. The length of the error bars is equivalent to the internal precision (2σ) of the spot analyses. Within analytical uncertainty, all measurements plot on the theoretical mass fractionation line, which has a slope of 1.4881 (STEINHOEFEL et al., 2009a).

Table 5.5 Fe isotope measurements of the iron standard Puratronic (Johnson Matthey).

δ^{56}Fe ± 2σ [‰]	δ^{57}Fe ± 2σ [‰]	δ^{56}Fe ± 2σ [‰]	δ^{57}Fe ± 2σ [‰]
0.08 ± 0.05	0.07 ± 0.09	0.07 ± 0.04	0.08 ± 0.09
0.13 ± 0.06	0.18 ± 0.12	0.15 ± 0.04	0.22 ± 0.09
0.09 ± 0.07	0.23 ± 0.12	0.10 ± 0.05	0.18 ± 0.09
0.14 ± 0.08	0.22 ± 0.15	0.09 ± 0.05	0.16 ± 0.09
0.11 ± 0.07	0.23 ± 0.13	0.07 ± 0.05	0.20 ± 0.09
0.07 ± 0.08	0.10 ± 0.15	0.06 ± 0.05	0.11 ± 0.10
0.04 ± 0.08	0.05 ± 0.15	0.12 ± 0.05	0.14 ± 0.10
0.07 ± 0.08	0.10 ± 0.14	0.13 ± 0.05	0.20 ± 0.11
0.06 ± 0.07	0.05 ± 0.14	0.10 ± 0.05	0.15 ± 0.10
0.08 ± 0.08	0.05 ± 0.16	0.08 ± 0.05	0.13 ± 0.09
0.05 ± 0.06	0.13 ± 0.10	0.10 ± 0.04	0.13 ± 0.07
0.03 ± 0.05	0.04 ± 0.09	0.05 ± 0.04	0.09 ± 0.08
0.04 ± 0.05	0.04 ± 0.09	0.05 ± 0.05	0.16 ± 0.09
0.06 ± 0.04	0.15 ± 0.07	0.05 ± 0.04	0.04 ± 0.08
0.06 ± 0.04	0.07 ± 0.07	0.05 ± 0.05	0.05 ± 0.09
0.04 ± 0.04	0.04 ± 0.08	0.09 ± 0.04	0.18 ± 0.08
0.06 ± 0.04	0.10 ± 0.08	0.11 ± 0.04	0.17 ± 0.07
-0.01 ± 0.04	0.04 ± 0.08	0.08 ± 0.04	0.12 ± 0.08
0.09 ± 0.04	0.12 ± 0.09	0.02 ± 0.05	0.07 ± 0.10
0.08 ± 0.04	0.03 ± 0.09	0.03 ± 0.05	0.03 ± 0.10
0.07 ± 0.05	0.13 ± 0.09	0.13 ± 0.05	0.17 ± 0.09
0.09 ± 0.04	0.2 ± 0.07	0.15 ± 0.05	0.17 ± 0.10
0.08 ± 0.04	0.15 ± 0.08	0.12 ± 0.05	0.20 ± 0.10
0.10 ± 0.04	0.16 ± 0.08		

5.4 Results

In total, 233 spot analyses were carried out to determine the Fe isotope composition of magnetite, martite, microplaty hematite, goethite, pyrite and chalcopyrite (Table 5.6). The position of the ablation points on the polished thin sections is shown in Fig. 5.4. The detected range of δ^{56}Fe values varies from 0.55 to 2.30‰ in magnetite (1.46 ± 0.56‰, 1σ, n = 94), 0.84 to 2.41‰ in martite (1.70 ± 0.32‰, 1σ, n = 59), 1.30 to 1.89‰ in microplaty hematite (1.65 ± 0.16‰, 1σ, n = 9), -0.02 to 2.69‰ in goethite (1.44 ± 0.55‰, 1σ, n = 58), 0.55 to 2.03‰ in pyrite (1.49 ± 0.45‰, 1σ, n = 10) and 0.01 to 0.06‰ in chalcopyrite (0.04 ± 0.02‰, 1σ, n = 3).

Contrary to the overall broad range of δ^{56}Fe values, magnetite reveals a rather narrow and homogeneous Fe isotope composition in individual drill core intervals over several tens of centimeters in thickness, i.e. the BIF samples from the N7 deposit. The comparison of all δ^{56}Fe values obtained from magnetite shows that each sample has a distinct range of δ^{56}Fe values (Fig. 5.5).

Hematite was analyzed in six samples. Similar to magnetite, the variation range of δ^{56}Fe values is rather small in individual samples. The Fe isotope composition of hematite closely resembles the composition of magnetite, regardless of whether hematite is present as martite or microplaty hematite. However, it appears that hematite has a tendency to be slightly more enriched in ^{56}Fe. In a limited number of measurements, martite deviates by a few tenths permil from the homogeneous Fe isotope composition of magnetite, e.g. a single measurement of martite in soft ore from 97 m depth (Table 5.6, Mt 15), gave an anomalously low δ^{56}Fe value of 0.84 ± 0.11‰. In the near-surface soft ore sample at 34 m depth, martite presents a variable Fe isotope pattern, with a significant range of 0.98‰, which distinguishes it from the martite in other samples.

Goethite has a heterogeneous Fe isotope composition in all samples, e.g. in the canga sample, it varies from -0.02 to 2.17‰. Goethite provided both the highest and lowest δ^{56}Fe values in this study.

Both pyrite and chalcopyrite precipitated from hydrothermal solutions, possibly during retrograde greenschist facies metamorphism (see chapter 3, section 3.2). However, while disseminated chalcopyrite in the BIF sample from the N8 deposit is characterized by homogeneous δ^{56}Fe values, pyrite in the magnetite-rich breccia from the S11D deposit has variable δ^{56}Fe values ranging from 0.55 to 2.03‰. Closer examination of the data reveals that the δ^{56}Fe values of disseminated pyrite with grain sizes between 50 to 100 µm vary from 1.57 to 2.03‰, while the measurement of a coarse-grained aggregate generated δ^{56}Fe values ranging from 0.55 to 1.55‰. The pyrite aggregate is isotopically zoned with light values in its core and ^{56}Fe being increasingly enriched toward its rims.

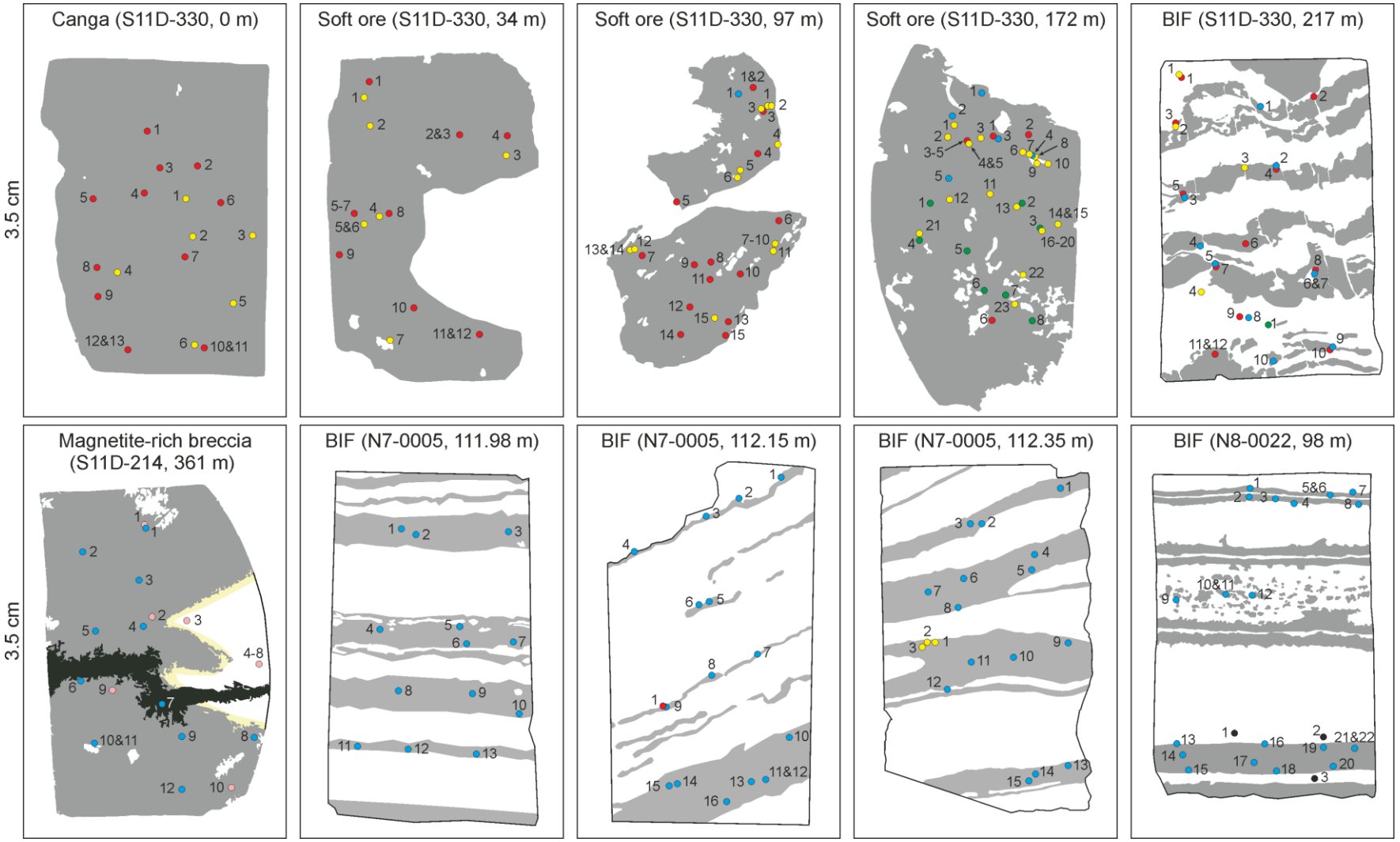

Fig. 5.4 Sketches of the analyzed thin sections. Sample location and sampling depth in brackets. Iron oxide bands are shown in grey and chert bands are white. The stilpnomelane vein in the magnetite-rich breccia is shown in dark grey and the carbonate rim surrounding the chert fragment is light yellow. The positions of the spot analyses, listed in Table 5.6, are indicated as circles (blue = magnetite, red = martite, green = microplaty hematite, yellow = goethite, black = chalcopyrite and pink = pyrite).

Table 5.6 Fe isotope measurements of BIF, soft ore, canga and the magnetite-rich breccia.

Mineral	δ^{56}Fe ± 2σ [‰]	δ^{57}Fe ± 2σ [‰]	Mineral	δ^{56}Fe ± 2σ [‰]	δ^{57}Fe ± 2σ [‰]
Canga (S11D-330, 0 m)			**Soft ore (S11D-330, 97 m)**		
Goe 01	-0.02 ± 0.10	0.00 ± 0.18	Goe 01	1.83 ± 0.09	2.67 ± 0.17
Goe 02	0.81 ± 0.11	1.08 ± 0.21	Goe 02	1.58 ± 0.11	2.36 ± 0.18
Goe 03	1.42 ± 0.10	1.98 ± 0.17	Goe 03	1.95 ± 0.11	2.86 ± 0.21
Goe 04	2.17 ± 0.09	3.24 ± 0.18	Goe 04	1.25 ± 0.16	2.00 ± 0.27
Goe 05	1.71 ± 0.10	2.54 ± 0.18	Goe 05	1.65 ± 0.15	2.60 ± 0.23
Goe 06	1.17 ± 0.10	1.82 ± 0.18	Goe 06	1.89 ± 0.10	2.89 ± 0.19
Mt 01	1.84 ± 0.07	2.75 ± 0.11	Goe 07	1.30 ± 0.12	1.92 ± 0.23
Mt 02	1.78 ± 0.07	2.72 ± 0.12	Goe 08	1.50 ± 0.11	2.31 ± 0.19
Mt 03	1.79 ± 0.06	2.67 ± 0.11	Goe 09	1.89 ± 0.13	2.80 ± 0.30
Mt 04	1.72 ± 0.10	2.59 ± 0.13	Goe 10	1.73 ± 0.11	2.61 ± 0.23
Mt 05	1.95 ± 0.07	2.86 ± 0.13	Goe 11	1.61 ± 0.10	2.49 ± 0.21
Mt 06	1.92 ± 0.07	2.90 ± 0.11	Goe 12	1.58 ± 0.10	2.34 ± 0.17
Mt 07	1.84 ± 0.06	2.80 ± 0.11	Goe 13	1.66 ± 0.11	2.50 ± 0.17
Mt 08	2.03 ± 0.11	3.09 ± 0.20	Goe 14	1.43 ± 0.09	2.15 ± 0.16
Mt 09	1.81 ± 0.07	2.75 ± 0.12	Goe 15	1.67 ± 0.08	2.43 ± 0.18
Mt 10	1.84 ± 0.08	2.75 ± 0.13	Mt 01	1.56 ± 0.09	2.34 ± 0.16
Mt 11	1.74 ± 0.08	2.68 ± 0.12	Mt 02	1.54 ± 0.08	2.36 ± 0.16
Mt 12	2.15 ± 0.08	3.24 ± 0.14	Mt 03	1.89 ± 0.13	2.79 ± 0.22
Mt 13	2.19 ± 0.07	3.27 ± 0.13	Mt 04	1.86 ± 0.12	2.77 ± 0.20
			Mt 05	1.66 ± 0.09	2.51 ± 0.17
Soft ore (S11D-330, 34 m)			Mt 06	1.60 ± 0.09	2.33 ± 0.18
Goe 01	1.14 ± 0.10	1.70 ± 0.17	Mt 07	1.49 ± 0.08	2.25 ± 0.15
Goe 02	1.27 ± 0.10	1.85 ± 0.17	Mt 08	1.66 ± 0.10	2.43 ± 0.18
Goe 03	0.77 ± 0.12	1.07 ± 0.35	Mt 09	1.55 ± 0.09	2.36 ± 0.16
Goe 04	1.40 ± 0.12	2.17 ± 0.20	Mt 10	1.54 ± 0.07	2.30 ± 0.16
Goe 05	0.72 ± 0.19	1.15 ± 0.21	Mt 11	1.22 ± 0.12	1.88 ± 0.19
Goe 06	1.11 ± 0.13	1.58 ± 0.23	Mt 12	1.49 ± 0.09	2.20 ± 0.16
Goe 07	1.53 ± 0.13	2.25 ± 0.20	Mt 13	1.53 ± 0.12	2.35 ± 0.21
Mt 01	1.70 ± 0.09	2.60 ± 0.19	Mt 14	1.39 ± 0.10	1.99 ± 0.17
Mt 02	1.94 ± 0.08	2.95 ± 0.14	Mt 15	0.84 ± 0.11	1.24 ± 0.19
Mt 03	1.43 ± 0.09	2.11 ± 0.15	Mag 01	1.55 ± 0.07	2.26 ± 0.14
Mt 04	1.93 ± 0.10	2.80 ± 0.16			
Mt 05	2.41 ± 0.09	3.57 ± 0.14	**Soft ore (S11D-330, 172 m)**		
Mt 06	1.64 ± 0.08	2.52 ± 0.14	Goe 01	1.31 ± 0.07	1.98 ± 0.12
Mt 07	2.06 ± 0.12	3.01 ± 0.17	Goe 02	1.55 ± 0.08	2.43 ± 0.13
Mt 08	2.21 ± 0.11	3.25 ± 0.17	Goe 03	1.80 ± 0.08	2.70 ± 0.14
Mt 09	2.10 ± 0.11	3.11 ± 0.17	Goe 04	1.90 ± 0.10	2.90 ± 0.13
Mt 10	2.23 ± 0.11	3.37 ± 0.20	Goe 05	1.71 ± 0.09	2.60 ± 0.14
Mt 11	1.79 ± 0.15	2.73 ± 0.21	Goe 06	1.36 ± 0.07	2.10 ± 0.13
Mt 12	2.40 ± 0.14	3.57 ± 0.16	Goe 07	0.38 ± 0.07	0.65 ± 0.14

Table 5.6 (*continued*).

Mineral	δ^{56}Fe ± 2σ [‰]	δ^{57}Fe ± 2σ [‰]	Mineral	δ^{56}Fe ± 2σ [‰]	δ^{57}Fe ± 2σ [‰]
Goe 08	0.25 ± 0.08	0.32 ± 0.14	Mt 03	1.37 ± 0.07	2.01 ± 0.12
Goe 09	1.42 ± 0.07	2.16 ± 0.12	Mt 04	1.35 ± 0.09	1.87 ± 0.16
Goe 10	1.93 ± 0.08	2.85 ± 0.14	Mt 05	1.35 ± 0.09	2.05 ± 0.17
Goe 11	2.21 ± 0.08	3.25 ± 0.13	Mt 06	1.21 ± 0.07	1.82 ± 0.12
Goe 12	2.34 ± 0.07	3.45 ± 0.15	Mt 07	1.16 ± 0.08	1.67 ± 0.13
Goe 13	0.90 ± 0.07	1.26 ± 0.13	Mt 08	1.61 ± 0.09	2.27 ± 0.16
Goe 14	1.06 ± 0.06	1.60 ± 0.12	Mt 09	1.39 ± 0.07	2.10 ± 0.12
Goe 15	1.49 ± 0.08	2.25 ± 0.12	Mt 10	1.75 ± 0.08	2.46 ± 0.14
Goe 16	1.43 ± 0.11	2.18 ± 0.17	Mt 11	1.73 ± 0.11	2.55 ± 0.16
Goe 17	0.62 ± 0.06	0.98 ± 0.12	Mt 12	1.63 ± 0.10	2.42 ± 0.14
Goe 18	0.88 ± 0.07	1.31 ± 0.12	Mag 01	1.14 ± 0.06	1.78 ± 0.11
Goe 19	0.63 ± 0.08	0.87 ± 0.14	Mag 02	1.27 ± 0.08	1.92 ± 0.16
Goe 20	0.96 ± 0.07	1.41 ± 0.13	Mag 03	1.24 ± 0.08	1.91 ± 0.13
Goe 21	1.73 ± 0.08	2.54 ± 0.12	Mag 04	1.07 ± 0.08	1.58 ± 0.16
Goe 22	1.59 ± 0.07	2.38 ± 0.14	Mag 05	1.08 ± 0.09	1.51 ± 0.15
Goe 23	1.58 ± 0.09	2.43 ± 0.14	Mag 06	1.16 ± 0.07	1.74 ± 0.11
H 01	1.70 ± 0.08	2.61 ± 0.14	Mag 07	1.10 ± 0.09	1.74 ± 0.11
H 02	1.73 ± 0.08	2.52 ± 0.14	Mag 08	1.18 ± 0.09	1.69 ± 0.13
H 03	1.83 ± 0.12	2.81 ± 0.16	Mag 09	1.32 ± 0.07	1.91 ± 0.12
H 04	1.89 ± 0.07	2.80 ± 0.13	Mag 10	1.10 ± 0.12	1.73 ± 0.15
H 05	1.68 ± 0.06	2.56 ± 0.12			
H 06	1.57 ± 0.06	2.45 ± 0.12	**Magnetite-rich breccia (S11D-214, 361 m)**		
H 07	1.53 ± 0.07	2.23 ± 0.13	Mag 01	1.25 ± 0.07	1.98 ± 0.12
H 08	1.64 ± 0.08	2.43 ± 0.14	Mag 02	1.27 ± 0.06	1.85 ± 0.11
Mt 01	1.68 ± 0.06	2.50 ± 0.11	Mag 03	1.23 ± 0.07	1.83 ± 0.13
Mt 02	1.67 ± 0.06	2.43 ± 0.10	Mag 04	1.37 ± 0.07	2.07 ± 0.12
Mt 03	1.75 ± 0.06	2.66 ± 0.11	Mag 05	1.28 ± 0.06	1.93 ± 0.11
Mt 04	1.75 ± 0.06	2.62 ± 0.10	Mag 06	1.07 ± 0.07	1.62 ± 0.13
Mt 05	1.63 ± 0.06	2.47 ± 0.10	Mag 07	1.18 ± 0.09	1.85 ± 0.18
Mt 06	1.54 ± 0.07	2.37 ± 0.13	Mag 08	1.21 ± 0.09	1.81 ± 0.12
Mag 01	1.45 ± 0.07	2.26 ± 0.13	Mag 09	1.32 ± 0.10	1.90 ± 0.21
Mag 02	1.56 ± 0.06	2.33 ± 0.12	Mag 10	1.23 ± 0.09	1.87 ± 0.10
Mag 03	1.65 ± 0.06	2.45 ± 0.11	Mag 11	1.20 ± 0.07	1.80 ± 0.12
Mag 04	1.64 ± 0.07	2.47 ± 0.13	Mag 12	1.17 ± 0.08	1.81 ± 0.13
Mag 05	1.57 ± 0.06	2.32 ± 0.12	Py 01	1.92 ± 0.07	2.82 ± 0.12
			Py 02	2.03 ± 0.07	2.97 ± 0.13
BIF (S11D-330, 217 m)			Py 03	1.57 ± 0.06	2.30 ± 0.11
Goe 01	1.08 ± 0.10	1.63 ± 0.13	Py 04	1.23 ± 0.07	1.98 ± 0.12
Goe 02	0.95 ± 0.10	1.49 ± 0.15	Py 05	0.90 ± 0.07	1.34 ± 0.12
Goe 03	1.26 ± 0.10	1.78 ± 0.18	Py 06	0.55 ± 0.08	0.83 ± 0.13
Goe 04	1.43 ± 0.11	2.10 ± 0.14	Py 07	1.50 ± 0.07	2.32 ± 0.12
H 01	1.30 ± 0.10	1.90 ± 0.18	Py 08	1.55 ± 0.08	2.47 ± 0.13
Mt 01	1.16 ± 0.11	1.79 ± 0.13	Py 09	1.87 ± 0.07	2.78 ± 0.13
Mt 02	1.23 ± 0.09	1.90 ± 0.16	Py 10	1.75 ± 0.09	2.70 ± 0.15

Table 5.6 (*continued*).

Mineral	δ^{56}Fe ± 2σ [‰]	δ^{57}Fe ± 2σ [‰]	Mineral	δ^{56}Fe ± 2σ [‰]	δ^{57}Fe ± 2σ [‰]
BIF (N7-0005, 111.98 m)					
Mag 01	2.00 ± 0.06	2.86 ± 0.13	Mag 07	1.92 ± 0.05	2.87 ± 0.09
Mag 02	1.98 ± 0.06	2.99 ± 0.11	Mag 08	2.05 ± 0.05	3.16 ± 0.10
Mag 03	2.09 ± 0.06	3.10 ± 0.11	Mag 09	2.15 ± 0.06	3.23 ± 0.11
Mag 04	1.94 ± 0.07	2.90 ± 0.11	Mag 10	2.04 ± 0.05	3.07 ± 0.09
Mag 05	1.95 ± 0.06	2.87 ± 0.12	Mag 11	2.14 ± 0.07	3.16 ± 0.13
Mag 06	1.95 ± 0.07	2.94 ± 0.13	Mag 12	1.85 ± 0.05	2.83 ± 0.09
Mag 07	2.07 ± 0.07	2.99 ± 0.12	Mag 13	1.96 ± 0.04	2.88 ± 0.09
Mag 08	2.00 ± 0.07	2.91 ± 0.14	Mag 14	2.06 ± 0.06	3.08 ± 0.12
Mag 09	1.88 ± 0.06	2.79 ± 0.12	Mag 15	1.93 ± 0.05	2.93 ± 0.09
Mag 10	2.00 ± 0.07	2.90 ± 0.14			
Mag 11	1.86 ± 0.07	2.87 ± 0.13	**BIF (N8-0022, 98 m)**		
Mag 12	1.98 ± 0.06	2.86 ± 0.13	Mag 01	0.73 ± 0.07	1.08 ± 0.13
Mag 13	1.99 ± 0.07	2.89 ± 0.11	Mag 02	0.62 ± 0.06	0.84 ± 0.12
			Mag 03	0.76 ± 0.07	1.11 ± 0.13
BIF (N7-0005, 112.15 m)			Mag 04	0.64 ± 0.07	0.87 ± 0.14
Mt 01	2.20 ± 0.07	3.18 ± 0.13	Mag 05	0.57 ± 0.06	0.86 ± 0.11
Mag 01	2.13 ± 0.05	3.12 ± 0.11	Mag 06	0.55 ± 0.09	0.93 ± 0.11
Mag 02	2.05 ± 0.11	3.04 ± 0.14	Mag 07	0.65 ± 0.06	0.88 ± 0.10
Mag 03	2.10 ± 0.06	3.02 ± 0.13	Mag 08	0.65 ± 0.07	0.92 ± 0.12
Mag 04	2.09 ± 0.10	3.10 ± 0.18	Mag 09	0.57 ± 0.06	0.91 ± 0.11
Mag 05	2.01 ± 0.06	3.01 ± 0.12	Mag 10	0.66 ± 0.08	1.01 ± 0.11
Mag 06	1.96 ± 0.07	2.86 ± 0.13	Mag 11	0.73 ± 0.07	1.05 ± 0.12
Mag 07	2.30 ± 0.07	3.32 ± 0.16	Mag 12	0.57 ± 0.07	0.82 ± 0.11
Mag 08	2.09 ± 0.07	3.11 ± 0.13	Mag 13	0.66 ± 0.07	1.00 ± 0.12
Mag 09	1.93 ± 0.06	2.88 ± 0.11	Mag 14	0.59 ± 0.08	0.88 ± 0.14
Mag 10	1.98 ± 0.07	2.94 ± 0.14	Mag 15	0.56 ± 0.08	0.83 ± 0.13
Mag 11	1.98 ± 0.06	2.93 ± 0.12	Mag 16	0.67 ± 0.07	1.07 ± 0.14
Mag 12	2.01 ± 0.06	2.99 ± 0.12	Mag 17	0.58 ± 0.06	0.85 ± 0.11
Mag 13	1.95 ± 0.07	2.87 ± 0.17	Mag 18	0.57 ± 0.08	0.88 ± 0.12
Mag 14	1.99 ± 0.07	2.84 ± 0.13	Mag 19	0.61 ± 0.07	0.97 ± 0.11
Mag 15	2.04 ± 0.06	3.03 ± 0.12	Mag 20	0.63 ± 0.07	0.91 ± 0.11
Mag 16	1.97 ± 0.06	2.90 ± 0.12	Mag 21	0.60 ± 0.08	0.86 ± 0.12
			Mag 22	0.74 ± 0.08	1.04 ± 0.12
BIF (N7-0005, 112.35 m)			Ccp 01	0.01 ± 0.08	0.02 ± 0.16
Goe 01	2.69 ± 0.07	4.00 ± 0.14	Ccp 02	0.06 ± 0.08	0.05 ± 0.13
Goe 02	2.65 ± 0.08	4.02 ± 0.11	Ccp 03	0.04 ± 0.07	0.08 ± 0.14
Goe 03	2.55 ± 0.09	3.82 ± 0.17			
Mag 01	2.00 ± 0.05	3.03 ± 0.09			
Mag 02	1.82 ± 0.05	2.73 ± 0.09			
Mag 03	1.86 ± 0.05	2.81 ± 0.10			
Mag 04	1.92 ± 0.05	2.90 ± 0.10			
Mag 05	2.13 ± 0.05	3.20 ± 0.10			
Mag 06	1.78 ± 0.06	2.58 ± 0.11			

Goe	-	Goethite
H	-	Microplaty hematite
Mt	-	Martite
Mag	-	Magnetite
Py	-	Pyrite
Ccp	-	Chalcopyrite

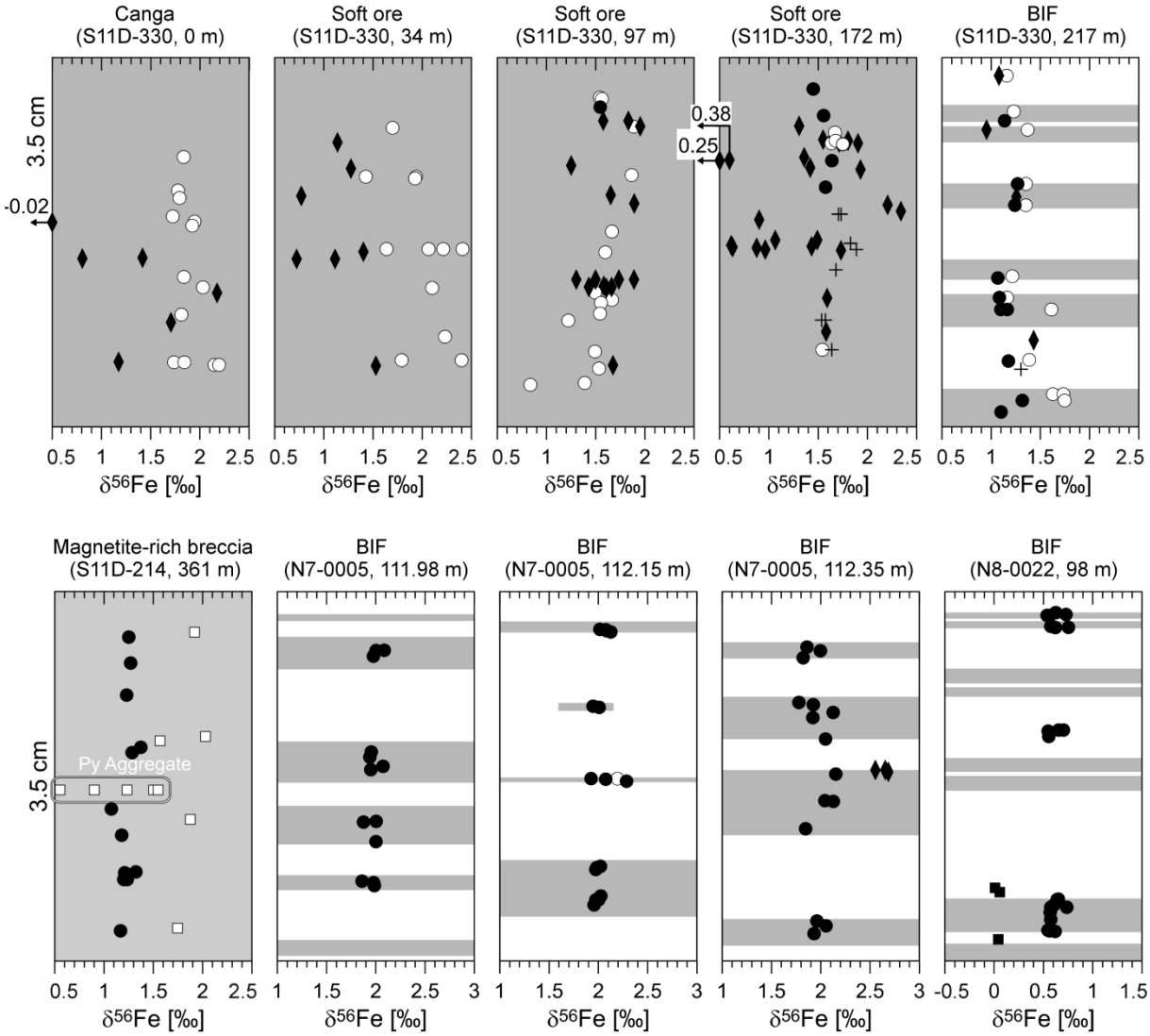

Fig. 5.5 Schematic representation of the analyzed thin sections (filled circles = magnetite, open circles = martite, crosses = microplaty hematite, rhombs = goethite, filled rectangles = chalcopyrite, open rectangles = pyrite). Sample location and sampling depth in brackets. Iron oxide bands are shown in grey and chert bands are white. The δ^{56}Fe values of the spot analyses are shown on the x-axis. The δ^{56}Fe values obtained from a large pyrite aggregate (diameter >500 µm) in the magnetite-rich breccia, are highlighted with an ellipse.

5.5 Discussion

5.5.1 Constraints on biologic activity

MACAMBIRA (2003) and LUZ & CROWLEY (2012) observed spherulitic microstructures in chert bands of BIF samples from the Carajás region, which these researchers interpret as microfossils. Due to the undisturbed lamination of their samples, suggestive of water depths beyond ca. 200 m, LUZ & CROWLEY (2012) proposed that the spherulites represent microfossils of dissimilatory iron-reducing bacteria (DIR). Such depths would represent unfavorable conditions for other potential microorganisms, e.g. cyanobacteria or photoferrotropic bacteria, because of the low ambient light level. Furthermore, the frequent ring-like arrangement of chert spherulites in samples of LUZ & CROWLEY (2012) resembles fruiting bodies of modern bacteria (Fig. 5.6). Thus, if these delicate microstructures are of biogenic origin, they probably formed in-situ and not from allochthonous organic material generated at shallower water depths. Similar spherulitic microstructures occur in two BIF samples studied here (N8, 98 m; N7, 112.35 m), which allows to test this hypothesis.

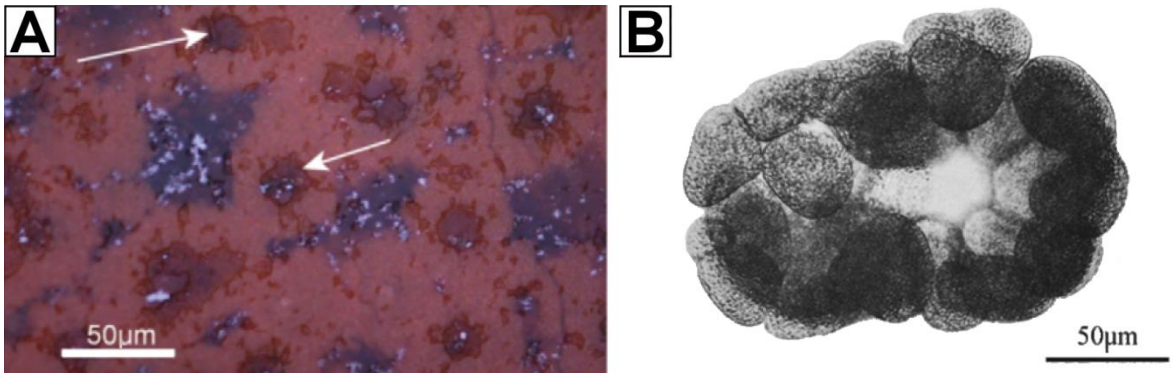

Fig. 5.6 Photomicrographs of (**A**) chert microspherulites making up ring-like structures (arrows; reflected light), bearing resemblance to (**B**) fruiting bodies of modern bacteria (transmitted light; modified after LUZ & CROWLEY, 2012).

DIR bacteria are known to produce ferrous aqueous iron with a distinctly negative Fe isotope signature (BEARD et al., 1999, 2003a; JOHNSON et al., 2005; CROSBY et al., 2007). Therefore, low δ^{56}Fe values of sedimentary rocks, such as those from the 3.8 Ga Isua supracrustal belt (YOSHIYA et al., 2015), shale of the 2.9 Ga Rietkuil Formation (YAMAGUCHI et al., 2005) and BIF of the 2.5 Ga Brockman Iron Formation (JOHNSON et al., 2008), were interpreted as DIR biosignatures.

Consequently, the strictly positive Fe isotope composition of magnetite from the Carajás Formation precludes the presence of DIR bacteria during the formation of the analyzed BIF samples. The absence of magnetite with negative Fe isotope signatures in the two BIF samples hosting abundant chert spherulites (N8, 98 m; N7, 112.35 m), shows that these microstructures do not represent microfossils of bacteria with a DIR type of metabolism, as proposed by LUZ & CROWLEY (2012). This observation, of course, does not completely rule out a biogenic origin for these structures.

5.5.2 Fe isotope homogeneity of magnetite

The measured Fe isotope composition of magnetite (1.46 ± 0.56‰, 1σ, n = 94) is in agreement with previous solution ICP-MS analyses of three BIF samples from the N4 iron ore deposit (1.38 ± 0.21‰, 1σ, n = 9), carried out by FABRE et al. (2011). Similar to the results of FABRE et al. (2011), each of the samples studied here, provides a distinct set of positive δ^{56}Fe values (Figs. 5.5 and 5.7). The BIF samples from the N7 deposit, which were taken from a single 37 cm long drill core interval, even display a rather invariable Fe isotope composition over a thickness of several tens of centimeters. It is interesting to note that similar findings have been reported before, for samples of both Archean and Proterozoic BIFs (CZAJA et al., 2013; LI et al., 2013, 2015; STEINHOEFEL et al., 2009b, 2010), although at lower δ^{56}Fe values. This homogeneity at the sample-scale could result from different processes, e.g. diffusive exchange during metamorphism, precipitation from seawater, whose Fe isotope composition remained constant over long periods of time, or pervasive hydrothermal alteration. The Carajás Formation was affected by lower greenschist metamorphism. Under these conditions, isotopic exchange should occur at a rate of ca. 114 µm/Ma, assuming pure solid diffusion (LI et al., 2013). Therefore, it is likely that the Fe isotope composition of individual magnetite bands was homogenized, but diffusive exchange during metamorphism cannot account for the low variability encountered over several tens of centimeters in the BIF samples from the N7 deposit. Especially since interlayering chert bands would inhibit exchange between magnetite bands. Instead, the homogeneous δ^{56}Fe values of magnetite could reflect fractionation processes during the precipitation and diagenesis of its precursor minerals (CZAJA et al., 2013).

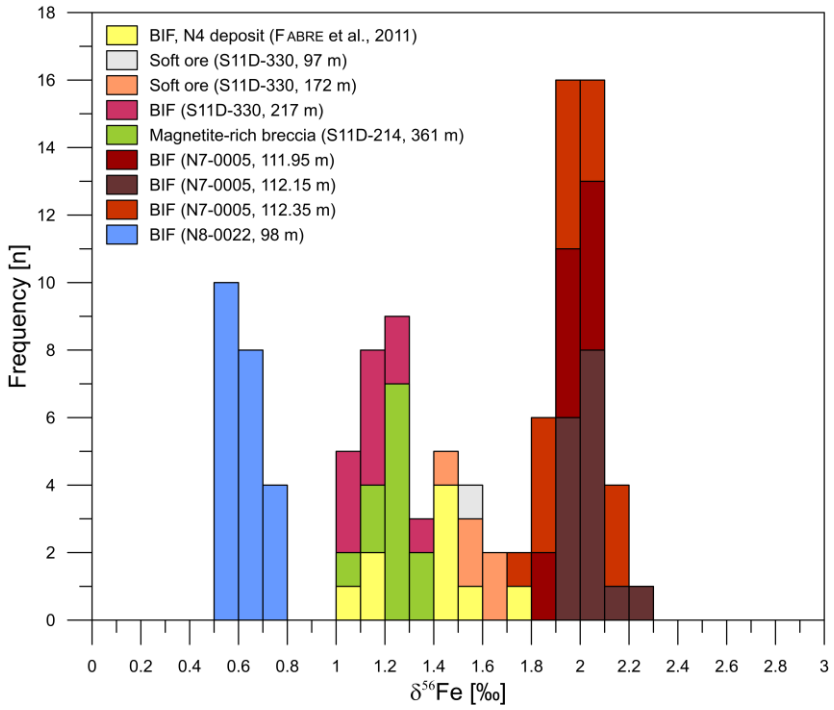

Fig. 5.7 Cumulative histogram plot of the magnetite spot analyses presented in this thesis, shown together with the bulk Fe isotope composition of three BIF samples from the N4 deposit (FABRE et al., 2011).

5.5.3 Deposition of the Carajás Formation

If magnetite preserved the δ^{56}Fe values of its precursor iron-bearing minerals, then the Fe isotope composition of seawater must have remained constant throughout the deposition of the BIF units represented by the analyzed samples. Otherwise, magnetite should exhibit more variable δ^{56}Fe values, due to the strong temperature-dependence of Fe isotope exchange reactions. It is generally assumed that the majority of the dissolved iron in the Precambrian ocean was contributed by hydrothermal vents (e.g. BAU et al., 1997; JACOBSEN & PIMENTEL-KLOSE, 1988). Modern submarine hydrothermal systems exhibit constant δ^{56}Fe values over periods of at least 16 ka (SEVERMANN et al., 2004). If the compacted sedimentation rate of the Carajás Formation is comparable to other BIFs, estimated from 2.2 to 18 cm/ka (PICKARD, 2003; TRENDALL et al., 2004), then the 37 cm long drill core interval from the N7 deposit should account for a timespan of 2 to 17 ka. Consequently, the Fe isotope composition of coeval seawater should not have changed significantly during the deposition of the analyzed BIF units, provided that the Archean submarine hydrothermal systems emitted fluids with constant δ^{56}Fe values over periods similar to modern hydrothermal vent systems. The low variability of δ^{56}Fe values between magnetite bands in individual samples further requires a steady rate of Fe(II) oxidation, since fluctuating oxidation rates would produce precipitates with variable Fe isotope compositions. Constant rates could be the result of limited nutrient supply to oxygen producing bacteria, or the microorganisms might only have been resistant to low oxygen concentrations. If ferric iron was instead produced by anoxygenic phototrophic bacteria, a limited nutrient supply would still be a viable possibility to achieve steady oxidation rates. Similar to abiologic processes, anoxygenic phototrophic bacteria generate ferric iron with positive Fe isotope signatures of $\Delta^{56}Fe_{Precipitate - Fluid}$ = 1.5 ± 0.2‰ (CROAL et al., 2004; SWANNER et al., 2015).

Both scenarios (abiotic partial oxidation and anoxygenic phototropic bacteria) would facilitate the precipitation of similar percentages of dissolved iron, thereby generating ferrihydrite layers with similar Fe isotope compositions. Consequently, the strictly positive δ^{56}Fe values of magnetite could represent partial iron oxidation, since quantitative oxidation would instead record the slightly negative Fe isotope composition of seawater, which was controlled by submarine hydrothermal systems with δ^{56}Fe <0‰. If this interpretation is correct, then the low variation of δ^{56}Fe values of magnetite in the BIF samples from the N7 deposit would suggest that the processes controlling BIF deposition remained stable over periods of several thousand years. This view is supported by recent findings of LI et al. (2015), who report a similar homogeneity of δ^{56}Fe values for BIF samples of the 2.5 Ga Dales Gorge member (Hamersley basin, Australia), representative of 1 to 1000 years of sedimentation.

5.5.4 Fe isotope fractionation model

The sub-millimeter lamination of magnetite and chert bands (microbanding) preserved in the Carajás Formation shows that the oxidation of Fe(II) was not a continuous process, but instead occurred during short pulsed events, e.g. periodic upwelling of iron-rich deep water to shallower ocean basin settings (KLEIN, 2005). These events were interrupted by periods of quiescence and chert formation. Consequently, iron oxidation, followed by precipitation of ferrihydrite from seawater, is a unidirectional process during which the initial Fe(II) reservoir progressively decreases in size. This process can be illustrated by a Rayleigh fractionation model. Since temperature exerts a strong influence on equilibrium fractionation processes, the experimentally determined equilibrium fractionation factors of WELCH et al. (2003) for the reaction of aqueous Fe(II) to Fe(III) were used to assess the effects of Rayleigh fractionation at different temperatures (Fig. 5.8). Estimates for Archean seawater range from ca. 30 to 60°C (BLAKE et al., 2010; ROBERT & CHAUSSIDON, 2006). However, recent findings suggest that temperatures could have been even lower (DE WIT & FURNES, 2016).

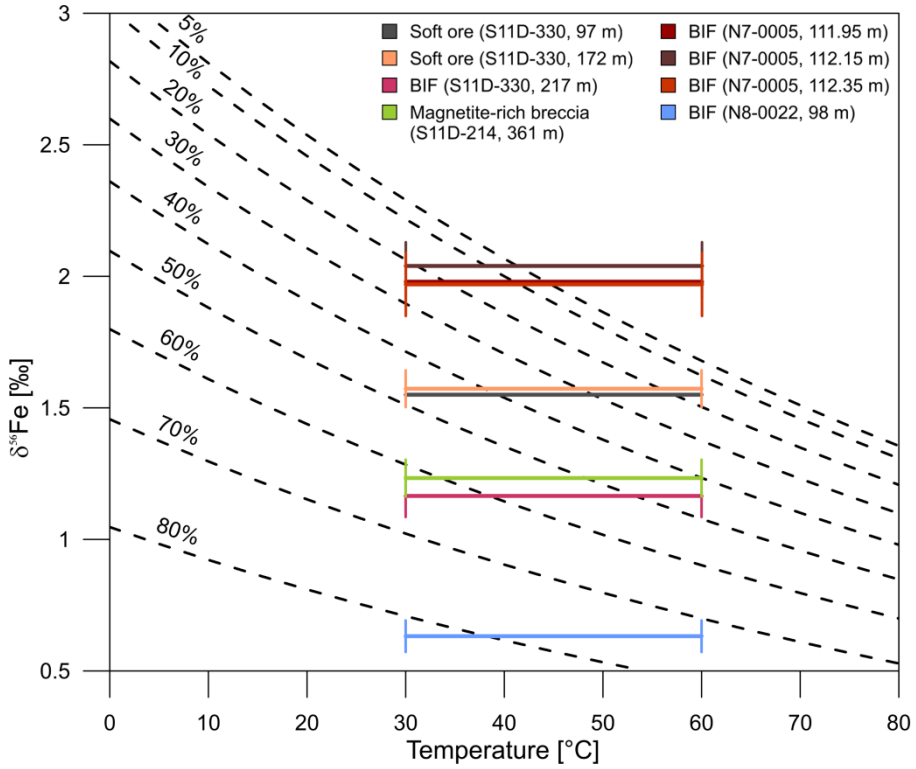

Fig. 5.8 Rayleigh fractionation model for the equilibrium Fe isotope fractionation between aqueous Fe(II) and Fe(III), calculated with α-factors of WELCH et al. (2003). The mean Fe isotope composition of magnetite in individual samples is plotted with 1σ over the estimated temperature range of Archean seawater (BLAKE et al., 2010; ROBERT & CHAUSSIDON, 2006). Dashed lines indicate the Fe isotope composition of different percentages of ferrihydrite, formed by the oxidation of aqueous Fe(II). The initial Fe isotope composition of seawater is assumed to be -0.40‰.

Potential fractionation processes during the transformation of aqueous Fe(III) to particulate ferrihydrite and isotope exchange reactions during the settling of particles are not considered in this model. It is assumed that ferrihydrite is completely transformed to magnetite during diagenesis without the addition of significant amounts of Fe(II) by seawater-derived pore fluids. The Fe isotope composition of magnetite should therefore match the composition of ferrihydrite.

In this model, high estimates for Archean ocean temperatures are barely consistent with the δ^{56}Fe values observed in some of the samples. At 60°C, the measured δ^{56}Fe values of magnetite in the BIF samples from the N7 deposit would require exceedingly low percentages of precipitation (<5%) from seawater with an initial Fe isotope composition of -0.40‰. However, if we assume an Archean ocean temperature similar to modern oceans, as recently suggested (DE WIT & FURNES, 2016), then the measured range of δ^{56}Fe values of magnetite would be equivalent of 40 to 80% precipitation. The observed variations between δ^{56}Fe values of samples from different depths indicates the occurrence of significant long-term changes in the depositional history of the Carajás Formation. A slightly negative δ^{56}Fe value for seawater was utilized for the model, because of the predominantly hydrothermal origin of iron in the Archean ocean (see chapter 1, section 1.5). Equilibrium fractionation experiments by WU et al. (2011, 2012) demonstrate that elevated concentrations of dissolved silica, similar to the conditions in the Archean, affect the fractionation between aqueous Fe(II) and ferrihydrite. However, these experiments were carried out at 20°C only, which prevents the conversion of the factors to other temperatures. Nonetheless, the results of WU et al. (2011, 2012) show that molar ratios of Si:Fe >1 would move the equilibrium fractionation factors towards more positive values (Table 5.1). In regard to the Rayleigh fractionation model, this implies that the Fe isotope data on magnetite could represent higher degrees of precipitation than expected from the utilized equilibrium fractionation factors of WELCH et al. (2003).

5.5.5 Hydrothermal alteration

The presence of trace amounts of pyrite and chalcopyrite in fractures crosscutting BIF banding, and the observed textural evidence of carbonate metasomatism in the periphery of dolerite dikes indicate that the Carajás Formation was affected by minor hydrothermal overprint. Small localized hydrothermal systems likely developed around mafic dikes during their emplacement and later retrograde greenschist facies metamorphism (see chapter 3, section 3.2). It is possible that circulating hydrothermal solutions affected the Fe isotope composition of the surrounding BIF units, e.g. by homogenization of δ^{56}Fe values or introducing a larger scatter.

At present, available literature on iron isotope fractionation during hydrothermal alteration is scarce. A study by ROUXEL et al. (2003) investigating the effects of spilitization on the Fe isotope composition of oceanic crust, shows that hydrothermal leaching of iron leaves behind altered crust with a wide scatter of positive δ^{56}Fe values. The extent of this scatter

appears to depend on the intensity of the alteration. Furthermore, in a recent study carried out by DZIONY et al. (2014), in-situ analyses of titanium rich magnetite from altered basalt yielded δ^{56}Fe values up to 0.64‰, deviating considerably from the homogeneous Fe isotope composition of 0.07 ± 0.02‰ of unaltered igneous rocks (POITRASSON, 2006). These results imply preferential mobilization of ^{54}Fe during hydrothermal alteration, which is in accordance with the strictly negative Fe isotope signature of modern submarine hydrothermal systems, ranging from -0.12 to -0.86‰ (Fig. 5.9; BEARD et al., 2003a; BENNETT et al., 2009; MOELLER et al., 2014; ROUXEL et al., 2008; SHARMA et al., 2001). Magnetite dissolution is significantly enhanced in chloride-rich fluids (CHOU & EUGSTER, 1977), and hydrothermal alteration of oceanic crust is driven mainly by heated seawater, which has a considerable chloride content. In comparison, early-stage fluid inclusions from the Serra Norte iron ore deposits also have high salinities of up to 30 eq. wt.% NaCl (FIGUEIREDO E SILVA et al., 2013).

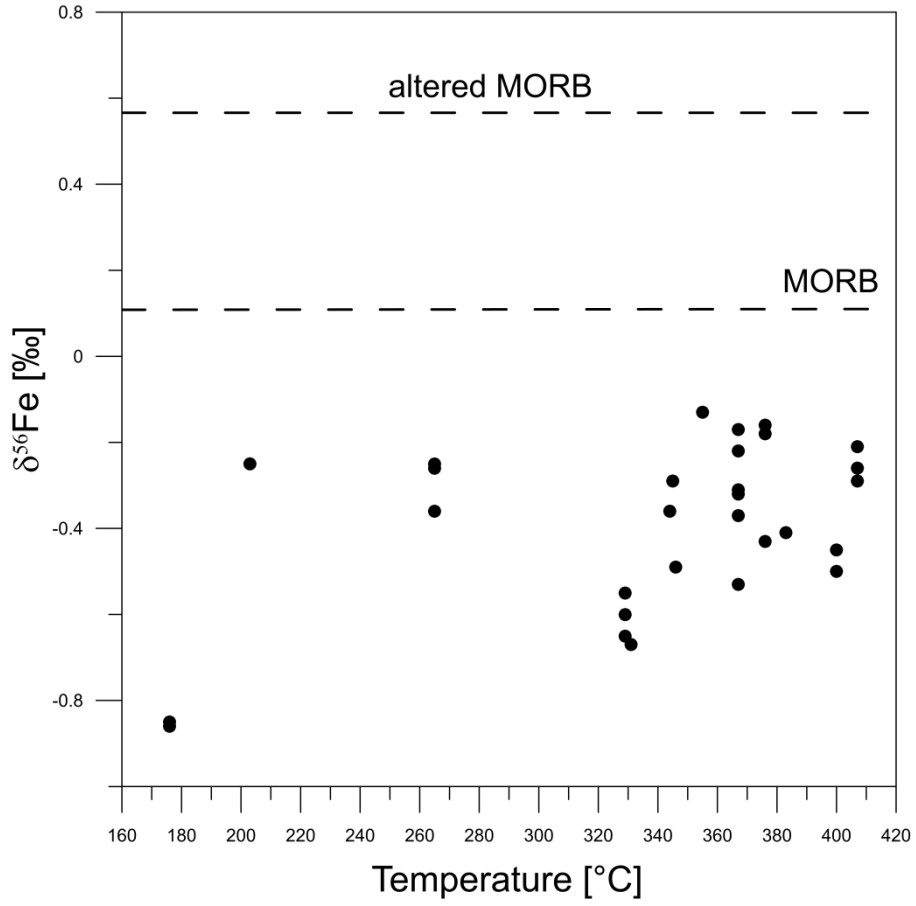

Fig. 5.9 Fe isotope composition of submarine hydrothermal vent fluids (n = 29) vs. measured temperature (data from BENNETT et al., 2009; MOELLER et al., 2014; ROUXEL et al., 2008; SHARMA et al., 2001). For comparison, the mean Fe isotope composition of altered and unaltered oceanic crust (MORB) is shown as dashed lines (BEARD et al., 2003b; ROUXEL et al., 2003; TENG et al., 2013). The δ^{57}Fe values of ROUXEL et al. (2003) were converted to δ^{56}Fe values with $\delta^{56}Fe = \delta^{57}Fe \times 1.4881^{-1}$. All δ^{56}Fe values are reported relative to the IRMM-014 reference material.

The equilibrium fractionation between magnetite and a ferrous chloride-rich fluid can be assessed with the β-factors of $FeCl_4^{2-}$ and magnetite determined by SCHAUBLE et al. (2001) and POLYAKOV et al. (2007), which gives $\Delta^{56}Fe_{Magnetite\ -\ Fluid}$ = 1.19 to 0.79‰, for 210 to 320°C, i.e. the recorded temperature range of fluid inclusions from the Serra Norte (FIGUEIREDO E SILVA et al., 2013). This demonstrates that partial dissolution of magnetite by chloride solutions under hydrothermal conditions preferentially mobilizes ^{54}Fe, if iron is transported in ferrous chloride complexes (HEIMANN et al., 2008). Therefore, it is likely that hydrothermal overprinting of the Carajás Formation did not homogenize the Fe isotope composition of different magnetite bands, but instead introduced a scattered distribution combined with a shift towards more positive $\delta^{56}Fe$ values, similar to the findings of ROUXEL et al. (2003) for altered oceanic crust. The detected 0.20 to 0.37‰ variation of magnetite in individual samples of the Carajás Formation is larger than the 0.06‰ (2σ) range of the external reproducibility for $\delta^{56}Fe$ and might result from a weak hydrothermal overprint.

The isotopic zonation of the pyrite aggregate in the magnetite-rich breccia sample (see section 5.4), provides further evidence for the enhanced mobility of ^{54}Fe during the localized hydrothermal alteration of the Carajás Formation. The Fe isotope composition of the aggregate increases significantly by 1‰ from the core to the rim (Fig. 5.10). It follows that pyrite initially precipitated from a solution with a relatively light Fe isotope composition, which became increasingly heavier over time. Alternatively, the pyrite aggregate could have formed during successive hydrothermal stages that involved fluids with changing Fe isotope compositions. Some studies suggest that the initially low $\delta^{56}Fe$ values of hydrothermally formed minerals may result from kinetic fractionation processes taking place during rapid precipitation (e.g. GAGNEVIN et al., 2012; ROUXEL et al., 2008). These researchers propose that due to the speed of the precipitation process, equilibrium conditions cannot be established. In this case, kinetic fractionation is the controlling process and the precipitate is enriched in ^{54}Fe, while ^{56}Fe accumulates in the evolving fluid phase. Two studies by HORN et al. (2006) and GAGNEVIN et al. (2012) report similarly zoned aggregates of hydrothermal siderite and sphalerite with light $\delta^{56}Fe$ values in their cores and progressively heavier $\delta^{56}Fe$ values towards their rims. Furthermore, an experimental study by SKULAN et al. (2002), investigating the fractionation between $[Fe^{III}(H_2O)_6]^{3+}$ and hematite at 98°C, shows that hematite is significantly enriched in ^{54}Fe if precipitation occurs rapidly (over ca. 12 hours; Fig. 5.11). Therefore, both experimental evidence and findings in natural samples support the idea that reservoir effects, caused by kinetic fractionation, could exist in hydrothermal systems.

The smaller disseminated pyrite grains in the magnetite-rich breccia sample exhibit a much lower variation of 1.57 to 2.03‰, analogous to the low variation of chalcopyrite in the BIF sample from the N8 deposit. It is likely that the small range of $\delta^{56}Fe$ values indicates that these disseminated pyrite crystals formed during a single hydrothermal event. If this observation also applies to iron-bearing minerals in other hydrothermal systems, Fe isotope studies could be used to identify and differentiate separate hydrothermal stages. This hypothesis remains to be tested.

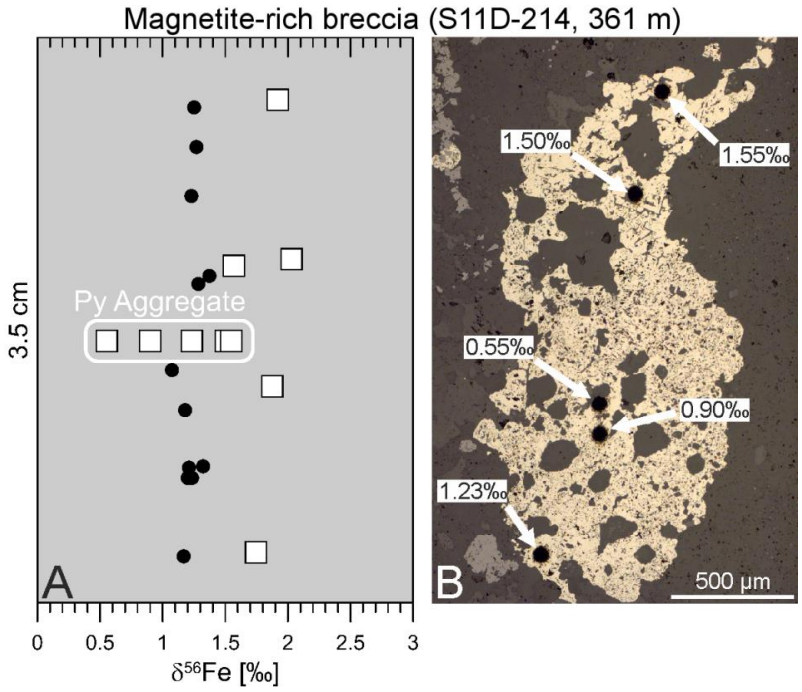

Fig. 5.10 (**A**) Schematic representation of a magnetite-rich breccia sample. With the exception of a single large pyrite aggregate, the δ^{56}Fe values of pyrite (open squares) and magnetite (filled circles), both exhibit only a minor variation over the entire thin section. (**B**) Reflected-light photomicrograph of the pyrite aggregate, showing a zoned Fe isotope composition.

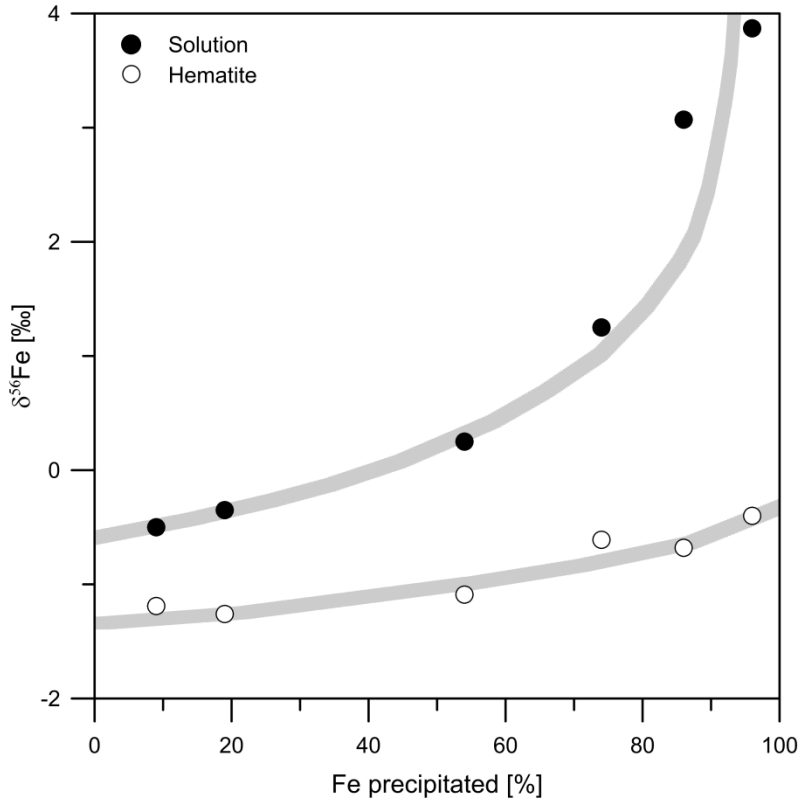

Fig. 5.11 δ^{56}Fe values vs. percentage of precipitated iron, for a kinetic fractionation experiment that was run for 12 hours at 98°C (redrawn from SKULAN et al., 2002).

5.5.6 Martitization

The main constituent of soft ore is martite, i.e. hematite pseudomorphic after magnetite. The martitization reaction represents a redox process that can proceed both during retrograde metamorphism and during near-surface oxidation (RAMDOHR, 1969):

$$2\ Fe_3O_4 + 0.5\ O_2 \rightarrow 3\ Fe_2O_3 \quad (2)$$

An alternative non-redox mechanism for hematite ore formation was proposed by OHMOTO (2003). This approach requires the presence of an acidic fluid phase. The reaction results in the mobilization of one third of the iron initially bound in magnetite:

$$Fe_3O_4 + 2\ H^+ \rightarrow Fe_2O_3 + Fe^{2+} + H_2O \quad (3)$$

The non-redox reaction of OHMOTO (2003) is of particular interest due to the recent popularity of hypogene genetic models for BIF-hosted iron ore deposits. Since $\Delta^{56}Fe_{Magnetite\ -\ Hematite}$ = -0.92 to -0.20‰ (calculated with β-factors of POLYAKOV et al., 2007), in the temperature range of 20 to 320°C (i.e. the relevant range for weathering and hydrothermal overprint of the Carajás deposits), the removal of one third of the iron bound in magnetite during the reaction would produce hematite with a distinctly different Fe isotope composition than magnetite. The analyzed martite in samples of both BIF and soft ore from the Carajás Formation has $\delta^{56}Fe$ values that predominantly lie close to the Fe isotope composition of magnetite (Fig. 5.5). This indicates quantitative transformation of magnetite to martite, which cannot be achieved by the non-redox reaction. These findings imply that martite is the product of the redox process, which is also in accordance with volumetric considerations. The non-redox formation of hematite involves a reduction in volume of 32% (OHMOTO, 2003). However, martite grains usually show no evidence of such shrinkage (MÜCKE & CABRAL, 2005), thus it is more likely that martitization proceeds by reaction (2), which induces only a 2% volume increase.

Although the majority of the analyzed martite grains have $\delta^{56}Fe$ values similar to magnetite, some measurements deviate from this trend. In most of these cases, martite is locally enriched in ^{56}Fe. For example, martite is ca. 0.40‰ heavier than magnetite in the lower part of the BIF sample from the S11D deposit (217 m). This shift could result from the intermediate step of kenomagnetite formation during the redox transformation of magnetite to hematite. In the martitization process, part of the Fe(II) in magnetite diffuses through the crystal structure and reacts with oxygen to hematite (DAVIS et al., 1968). The elevated $\delta^{56}Fe$ values of some martite grains might indicate that minor amounts of ^{54}Fe are released into the fluid phase during this process. Alternatively, these grains may have formed by partial martitization. The calculated $\Delta^{56}Fe_{Magnetite\ -\ Hematite}$ (see above), shows that martite is initially enriched in ^{56}Fe. Thus, martitization only preserves the Fe isotope composition of magnetite if the transformation to martite is quantitative. However, if the process is interrupted, e.g. due to leaching of kenomagnetite by meteoric or hydrothermal fluids, then martite becomes enriched in ^{56}Fe. Since martitization proceeds along the [111]

directions of magnetite (Fig. 5.12A; DAVIS et al., 1968), martite formed by partial replacement should exhibit a skeletal microstructure. In the near-surface soft ore sample at 34 m depth, skeletal martite is the main constituent (Fig. 5.12B), which might explain the anomalously large variation of 0.98‰ for martite in this sample.

Nonetheless, the largely close resemblance between δ^{56}Fe values of magnetite and martite in most of the analyzed samples shows that the loss of Fe(II) during martitization is generally rather negligible and that most martite formed by quantitative replacement of magnetite. Consequently, martite mirrors the Fe isotope composition of magnetite in individual samples. This close relation suggests that soft ore formed predominantly in place without the mobilization of large quantities of iron by hydrothermal or meteoric fluids. Otherwise, the majority of martite grains should exhibit variable Fe isotope compositions, which is not the case.

A single measurement of martite in soft ore from 97 m depth (Table 5.6, Mt 15), gave an anomalously low δ^{56}Fe value of 0.84 ± 0.11‰, which is 0.74‰ lighter compared to the mean δ^{56}Fe value of martite in this sample. During the initial phase of the measurement cycle, a change towards a lighter composition occurred. This anomalous δ^{56}Fe value could result from intergrowth with isotopically lighter goethite (see section 5.5.8), which was not observable prior to ablation.

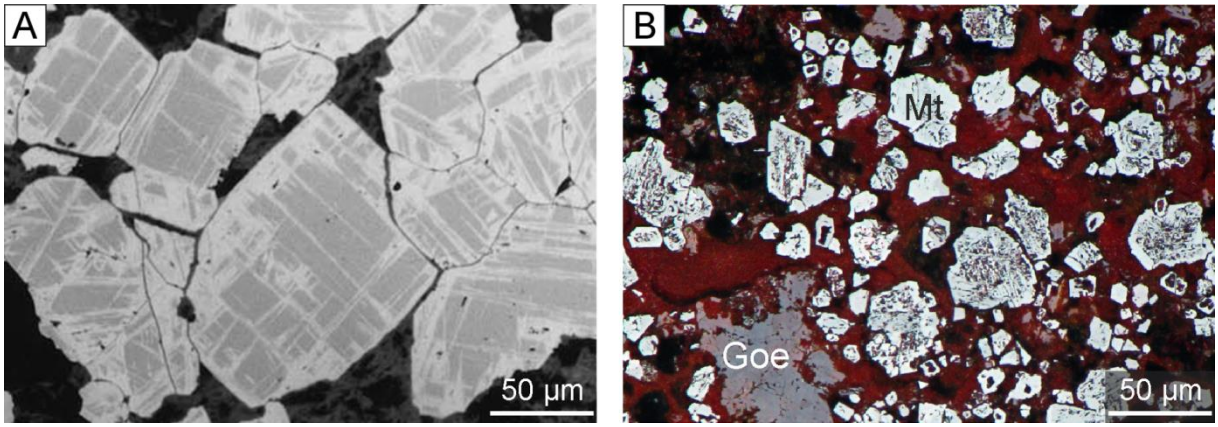

Fig. 5.12 Photomicrographs of (**A**) Martite (light grey) replacing kenomagnetite (dark grey) along the [111] directions of magnetite (BIF, reflected light, oil immersion; modified after MÜCKE & CABRAL, 2005). (**B**) Martite (Mt) with a skeletal microstructure next to interstitial goethite (Goe; soft ore, S11D-330, 34 m, reflected light, oil immersion).

5.5.7 Microplaty hematite formation

Microplaty hematite is a minor constituent of soft ore and BIF. It occurs as finely dispersed platelets and as crystals nucleating on martite (see chapter 3, section 3.2). This indicates that it formed after or contemporaneous with martite. According to the classic supergene-metamorphic model of MORRIS (1980, 1985), microplaty hematite replaces goethite, which requires temperatures in excess of 80°C (LANGMUIR, 1971). The conceptual model of MORRIS (1980, 1985) envisages martite-microplaty hematite ore genesis as a two-step process, consisting of weathering of BIF followed by burial and low-grade metamorphism. During weathering, magnetite is transformed to martite and goethite, while subsequent metamorphism causes goethite to dehydrate to microplaty hematite.

However, the wide range of δ^{56}Fe values obtained for goethite in samples of BIF, soft ore and canga from the Carajás region (Fig. 5.5), shows that weathering generates goethite with an extremely variable Fe isotope composition (see section 5.5.8). If the model of MORRIS (1980, 1985) is correct, microplaty hematite should reflect this variability. Instead, the δ^{56}Fe values of microplaty hematite are homogeneous and closely resemble the Fe isotope composition of martite and magnetite (Fig. 5.13). Microplaty hematite must therefore have formed by a different process. The growth of microplaty hematite on martite suggests that these crystals might have formed by recrystallization of martite, thus inheriting its Fe isotope composition. This is in agreement with the results of HENSLER et al. (2015). In their study, martite and microplaty hematite exhibit almost identical chemical compositions, which suggests that microplaty hematite formed by isochemical recrystallization of martite. The pressure and temperature conditions during weathering should not allow this degree of recrystallization. Thus, martitization and microplaty hematite formation must have occurred earlier, possibly during retrograde metamorphism, when the prevalent P-T conditions shifted the stability of magnetite towards hematite. The finely dispersed microplaty hematite could have precipitated from metamorphic fluids in isotopic equilibrium with the surrounding BIF.

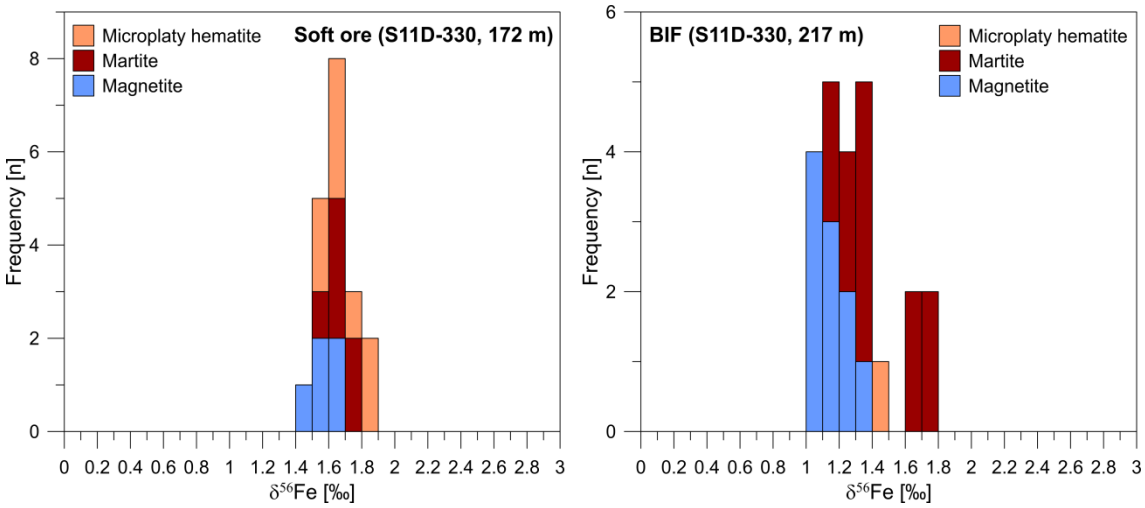

Fig. 5.13 Cumulative histogram plots, illustrating the close resemblance between the Fe isotope composition of microplaty hematite, martite and magnetite in samples from the Carajás region.

5.5.8 Weathering

Goethite is a weathering product, derived mainly from the dissolution of kenomagnetite by meteoric fluids. Its Fe isotope composition is extremely heterogeneous in the analyzed samples and varies considerably even in single aggregates (Fig. 5.14). This heterogeneity probably results from recurring events of precipitation and leaching. Furthermore, the δ^{56}Fe values of goethite will differ greatly, depending on whether it forms in isotopic equilibrium with the fluid phase or not. Rapid precipitation is likely accompanied by kinetic fractionation and would produce goethite with low δ^{56}Fe values. In contrast, newly formed goethite would become enriched in ^{56}Fe under equilibrium conditions, since $\Delta^{56}Fe_{Goethite - Aqueous\ Fe(II)}$ = 1.05‰ at 22°C (BEARD et al., 2010).

In the canga sample and the near-surface soft ore sample at 34 m depth, goethite exhibits a predominantly lighter Fe isotope composition than martite (Fig. 5.15). This implies that precipitation of goethite occurred rapidly and involved kinetic fractionation. Dissolved ^{56}Fe was mostly transported away. This appears to contradict recent findings by CHENG et al. (2015), who report that supergene alteration progressively enriches weathered rocks in ^{56}Fe.

The Fe isotope composition of martite in the canga sample (S11D-330, 0 m) closely resembles the homogeneous composition of soft ore from greater depths (Fig. 5.5). Since canga is the product of weathering of BIF fragments at the surface, the similarity between its Fe isotope pattern and soft ore from greater depths shows that supergene alteration does not affect the Fe isotope composition of martite. Thus, martite, i.e. the main constituent of soft ore, remains mostly immobile during weathering even if large quantities of silica are removed. However, this is not the case for goethite. The extremely heterogeneous Fe isotope composition of goethite, even on small scales of a few tenths of micrometers (Fig. 5.14), shows that goethite formed in an open system, i.e. behaves mobile during weathering. Even though ^{54}Fe is enriched in goethite of the near-surface soft ore sample and the canga sample, the relative proportion of goethite compared to martite, will decrease over time with ongoing weathering. Consequently, supergene alteration progressively enriches the bulk Fe isotope composition of weathered rocks in ^{56}Fe, which is in accordance with the results of CHENG et al. (2015).

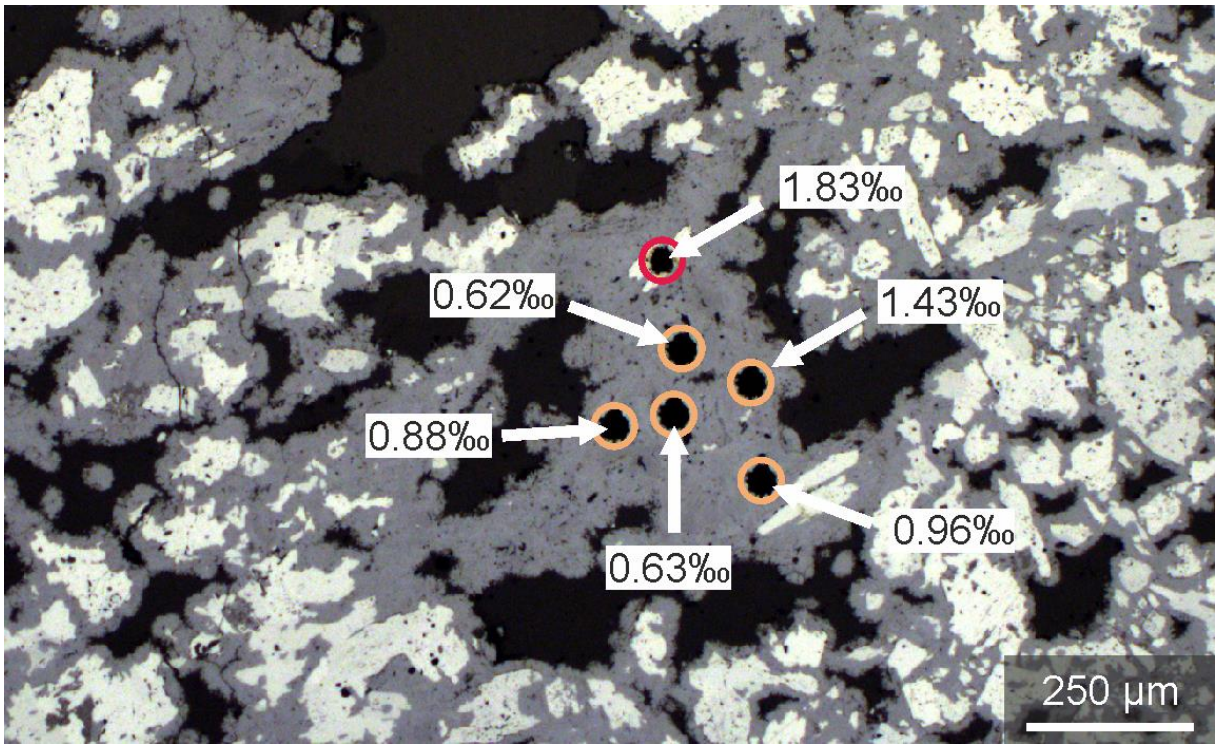

Fig 5.14 Photomicrograph showing the variable Fe isotope composition of goethite (orange circles) obtained from spot analyses that were taken only several tenths of micrometers apart from each other. The red circle indicates a single measurement of microplaty hematite (soft ore, S11D-330, 172 m, reflected light).

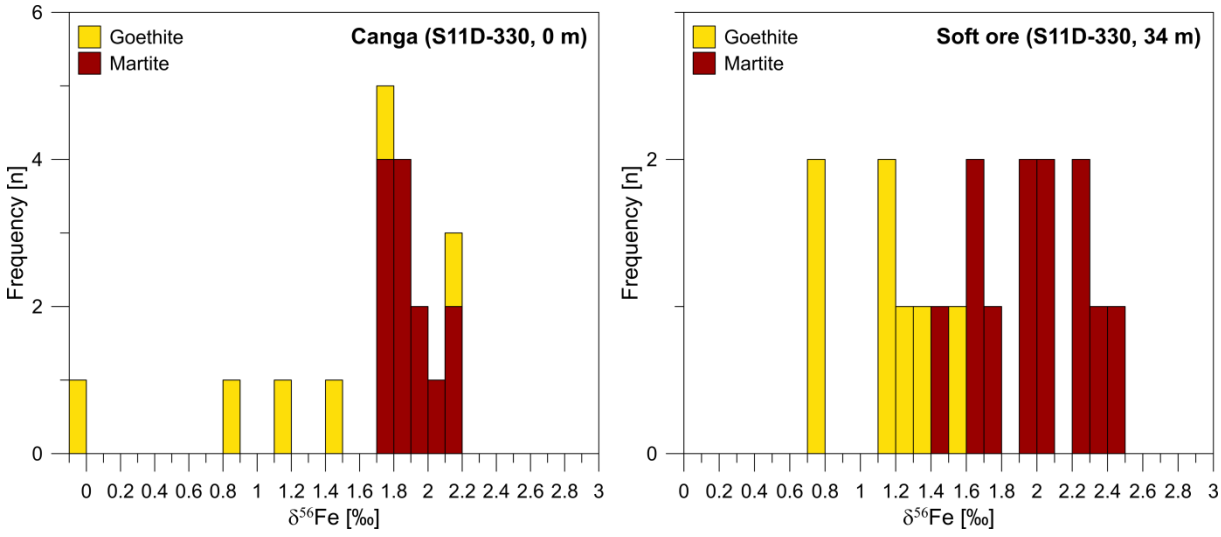

Fig. 5.15 Cumulative histogram plots, illustrating the distribution of δ^{56}Fe values of goethite and martite in a sample of superficial canga and a near-surface soft ore sample, both from the S11D deposit.

References

ALFIMOVA, N.A, NOVOSELOV, A.A., MATRENICHEV, V.A., SOUZA FILHO, C.R. (2014): Conditions of subaerial weathering of basalts in the Neoarchean and Paleoproterozoic. – Precambrian Research, **241**: 1 – 16.

ALMEIDA, J.A.C., DALL'AGNOL, R., OLIVEIRA, M.A., MACAMBIRA, M.J.B., PIMENTEL, M.M., RÄMÖ, O.T., GUIMARÃES, LEITE, A.A.S. (2011): Zircon geochronology, geochemistry and origin of the TTG suites of the Rio Maria granite-greenstone terrane: Implications for the growth of the Archean crust of the Carajás province, Brazil. – Precambrian Research, **187**: 201 – 221.

ANBAR, A.D., JARZECKI, A.A., SPIRO, T.G. (2005): Theoretical investigation of iron isotope fractionation between $Fe(H_2O)_6^{3+}$ and $Fe(H_2O)_6^{2+}$: Implications for iron stable isotope geochemistry. – Geochimica et Cosmochimica Acta, **69**: 825 –837.

ANDERSON, R., GRAHAM, C.M., BOYCE, A.J., FALLICK, A.E. (2004): Metamorphic and basin fluids in quartz-carbonate-sulphide veins in the SW Scottish Highlands: A stable isotope and fluid inclusion study. – Geofluids, **4**: 169 – 185.

ARAÚJO, O.J.B., MAIA, R.G.N. (1991): Programa levantamentos geológicos básicos do Brasil. Projeto especial mapa de recursos minerais, de solos e de vegetação para a área do Programa Grande Carajás. Subprojeto Recursos Minerais. Serra dos Carajás, Folha SB. 22-Z-A. – Departamento Nacional da Produção Mineral/DNPM, Companhia de Recursos Minerais/CPRM, Brasília, Brazil, 152 p.

ARAÚJO, O.J.B., MAIA, R.G.N., XAFI, J.J.S., COSTA, J.B.S. (1988): A megaestruturação arqueana da folha Serra dos Carajás. – VII Congresso Latino-Americano de Geologia, Belém, SBG, **1**: 324 – 338.

ASSIS, L.M. (2013): Geração de Modelo Exploratório para o Minério de Ferro da Província Mineral de Carajás Através da Integração de dados Multifonte. – Master's thesis, Universidade de Brasília, Instituto de Geociências, Brasília, Brazil, 105 p.

AVELAR, V.G., LAFON, J.,M., CORREIA, F.C., MACAMBIRA, E.M.B. (1999): O Magmatismo arqueano da região de Tucumã-Província Mineral de Carajás: Novos resultados geocronológicos. – Revista Brasileira de Geociências, **29**: 453 – 460.

BAO, S.X., ZHOU, H.Y., PENG, X.T., JI, F.W., YAO, H.Q. (2008): Geochemistry of REE and yttrium in hydrothermal fluids from the Endeavour segment, Juan de Fuca Ridge. – Geochemical Journal, **42**: 359 – 370.

BARLEY, M.E., PICKARD, A.L., HAGEMANN, S.G., FOLKERT, S.L. (1999): Hydrothermal origin for the 2 billion year old Mount Tom Price giant iron ore deposit, Hamersley Province, Western Australia. – Mineralium Deposita, **34**: 784 – 789.

BARROS, C.E.M., SARDINHA, A.S., BARBOSA, J.P.O., MACAMBIRA, M.J.B., BARBEY, P., BOUILLER, A.M. (2009): Structure, petrology, geochemistry and zircon U/Pb and Pb/Pb geochronology of the synkinematic Archean (2.7 Ga) A-type granites from the Carajás metallogenic province, northern Brazil. – The Canadian Mineralogist, **47**: 1423 – 1440.

BAU, M. (1996): Controls on the fractionation of isovalent trace elements in magmatic and aqueous systems: evidence from Y/Ho, Zr/Hf, and lanthanide tetrad effect. – Contributions to Mineralogy and Petrology, **123**: 323 – 333.

BAU, M., DULSKI, P. (1996): Distribution of yttrium and rare-earth elements in the Penge and Kuruman iron-formations, Transvaal Supergroup, South Africa. – Precambrian Research, **79**: 37 – 55.

BAU, M., HÖHNDORF, A., DULSKI, P., BEUKES, N.J. (1997): Sources of rare-earth elements and iron in Paleoproterozoic iron-formations from the Transvaal Supergroup, South Africa: Evidence from neodymium isotopes. – The Journal of Geology, **105**: 121 – 129.

BAU, M., MÖLLER, P. (1993): Rare earth element systematics of the chemically precipitated component in Early Precambrian iron formations and the evolution of the terrestrial atmosphere-hydrosphere-lithosphere system. – Geochimica et Cosmochimica Acta, **57**: 2239 – 2249.

BEARD, B.L., HANDLER, R.M., SCHERER, M.M., WU, L., CZAJA, A.D., HEIMANN, A., JOHNSON, C.M. (2010): Iron isotope fractionation between aqueous ferrous iron and goethite. – Earth and Planetary Science Letters, **295**: 241 – 250.

BEARD, B.L., JOHNSON, C.M., COX, L., SUN, H., NEALSON, K.H., AGUILAR, C. (1999): Iron isotope biosignatures. – Science, **285**: 1889 – 1892.

BEARD, B.L., JOHNSON, C.M., SKULAN, J.L, NEALSON, K.H., COX, L., SUN, H. (2003a): Application of Fe isotopes to tracing the geochemical and biological cycling of Fe. – Chemical Geology, **195**: 87 – 117.

BEARD, B.L., JOHNSON, C.M., VON DAMM, K.L., POULSON, R.L. (2003b): Iron isotope constraints on Fe cycling and mass balance in oxygenated Earth oceans. – Geology, **31**: 629 – 632.

BEISIEGEL, V.R., BERNARDELLI, A.L., DRUMMOND, N.F., RUFF, A.W., TREMAINE, J.W. (1973): Geologia e recursos minerais da Serra dos Carajás. – Revista Brasileira de Geociências, **3**: 215 – 242.

BEKKER, A., HOLLAND, H.D., WANG, P.L., RUMBLE III, D., STEIN, H.J., HANNAH, J.L., COETZEE, L.L., BEUKES, N.J. (2004): Dating the rise of atmospheric oxygen. – Nature, **427**: 117 – 120.

BEKKER, A., PLANAVSKY, N.J., KRAPEŽ, B., RASMUSSEN, B., HOFMANN, A., SLACK, J.F., ROUXEL, O.J., KONHAUSER, K.O. (2014): Iron formations: their origins and implications for ancient seawater chemistry. – in: MACKENZIE, F.T. (ed.): Treatise on Geochemistry (Second Edition), **9**: 561 – 628; Amsterdam (Elsevier).

BEKKER, A., SLACK, J.F., PLANAVSKY, N., KRAPEŽ, B., HOFFMANN, A., KONHAUSER, K.O., ROUXEL, O.J. (2010): Iron formation: The sedimentary product of a complex interplay among mantle, tectonic, oceanic, and biospheric processes. – Economic Geology, **105**: 467 – 508.

BELEVTSEV, Y.N. (1973): Genesis of high-grade iron ores of the Krivoyrog type. – in: Genesis of Precambrian iron and manganese deposits, Proceedings of the Kiev Symposium 1970, 167 – 180; Paris (UNESCO).

BENNETT, S.A., ROUXEL, O., SCHMIDT, K., GARBE-SCHÖNBERG, D., STATHAM, P.J., GERMAN, C.R. (2009): Iron isotope fractionation in a buoyant hydrothermal plume, 5°S Mid-Atlantic Ridge. – Geochimica et Cosmochimica Acta, **73**: 5619 – 5634.

BEUKES, N.J., GUTZMER, J., MUKHOPADHYAY, J. (2003): The geology and genesis of high-grade hematite iron ore deposits. – Applied Earth Science (Trans. Inst. Min. Metall. B), **112**: 18 – 25.

BEUKES, N.J., KLEIN, C. (1990): Geochemisty and sedimentology of a facies transition – from microbanded to granular iron-formation – in the early Proterozoic Transvaal Supergroup, South Africa. – Precambrian Research, **47**: 99 – 139.

BICKLE, M.J. (1986): Implications of melting for stabilisation of the lithosphere and heat loss in the Archean. – Earth and Planetary Science Letters, **80**: 314 – 324.

BIGELEISEN, J. (1965): Chemistry of Isotopes. – Science, **147**: 463 – 471.

BLAKE, R.E., CHANG, S.J., LEPLAND, A. (2010): Phosphate oxygen isotopic evidence for a temperate and biologically active Archaean ocean. – Nature, **464**: 1029 – 1032.

BLAKE, T.S., BUICK, R., BROWN, S.J.A., BARLEY, M.E. (2004): Geochronology of a Late Archaean flood basalt province in the Pilbara Craton, Australia: constraints on basin evolution, volcanic and sedimentary accumulation, and continental drift rates. – Precambrian Research, **133**: 143 – 173.

BOLHAR, R., HOFMANN, A., SIAHI, M., FENG, Y.X., DELVIGNE, C. (2015): A trace element and Pb isotopic investigation into the provenance and deposition of stromatolitic carbonates, ironstones and associated shales of the ~3.0 Ga Pongola Supergroup, Kaapvaal Craton. – Geochimica et Cosmochimica Acta, **158**: 57 – 78.

BOLHAR, R., KAMBER, B.S., MOORBATH, S., FEDO, C.M., WHITEHOUSE, M.J. (2004): Characterisation of early Archaean chemical sediments by trace element signatures. – Earth and Planetary Science Letters, **222**: 43 – 60.

BRAUN, J.J., PAGEL, M., MULLER, J.P., BILONG, P., MICHARD, A., GUILLET, B. (1990): Cerium anomalies in lateritic profiles. – Geochimica et Cosmochimica Acta, **54**: 781 – 795.

BREWER, T.S., ATKIN, B.P. (1989): Elemental mobilities produced by low-grade metamorphic events. A case study from the Proterozoic supracrustals of southern Norway. – Precambrian Research, **45**: 143 – 158.

BUCHER, K., FREY, M. (1994): Petrogenesis of metamorphic rocks. – Springer, Berlin, Germany, **6**: 318 p.

BULLEN, T.D., WHITE, A.F., CHILDS, C.W., VIVIT, D.V., SCHULZ, M.S. (2001): Demonstration of significant abiotic iron isotope fractionation in nature. – Geology, **29**: 699 – 702.

BURKE, K., KIDD, W.S.F. (1978): Were Archean continental geothermal gradients much steeper than those of today?. – Nature, **272**: 240 – 241.

CABRAL, A.R., CREASER, R.A., NÄGLER, T., LEHMANN, B. VOEGELIN, A.R., BELYATSKY, B., PAŠAVA, J., GOMES, A.A.S., GALBIATTI, H., BÖTTCHER, M.E., ESCHER, P. (2013): Trace-element and multi-isotope geochemistry of Late-Archean black shales in the Carajás iron-ore district, Brazil. – Chemical Geology, **362**: 91 – 104.

CABRAL, A.R., LEHMANN, B., GOMES, A.A.S., PAŠAVA, J. (2016): Episodic negative anomalies of cerium at the depositional onset of the 2.65-Ga Itabira iron formation, Quadrilátero Ferrífero of Minas Gerais, Brazil. – Precambrian Research, **276**: 101 – 109.

CAIRNS-SMITH, A.G. (1978): Precambrian solution photochemistry, inverse segregation, and banded iron formations. – Nature, **276**: 807 – 808.

CANFIELD, D.E. (1998): A new model for Proterozoic ocean chemistry. – Nature, **396**: 450 – 453.

CHENG, Y., MAO, J., ZHU, X., WANG, Y. (2015): Iron isotope fractionation during supergene weathering process and its application to constrain ore genesis in Gaosong deposit, Gejiu district, SW China. – Gondwana Research, **27**: 1283 – 1291.

CHOU, I.-M., EUGSTER, H.P. (1977): Solubility of magnetite in supercritical chloride solutions. – American Journal of Science, **277**: 1296 – 1314.

CLOUD, P.E. (1968): Atmospheric and hydrospheric evolution on the primitive earth. – Science, **160**: 729 – 736.

CONDIE, K.C. (1993): Chemical composition and evolution of the upper continental crust: Contrasting results from surface samples and shales. – Chemical Geology, **104**: 1 – 37.

COSTA, J.B.S., HASUI, Y., BEMERGUY, R.L., BORGES, M.S., COSTA, A.R., TRAVASSOS, W., MIOTO, J.A., IGREJA, H.L.S. (1993): Aspectos fundamentais da tectônica na Amazônia Brasileira. – Simpósio Internacional do Quaternário da Amazônia, Manaus, **1**: 103 – 106.

COSTA, L.P. (2007): Characterização das Seqüências Metavulcanossedimentares da Porção Leste da Província Mineral Carajás (PA). – Master's thesis, Universidade Federal de Minas Gerais, Instituto de Geociências, Belo Horizonte, Brazil, 120 p.

CROAL, L.R., JOHNSON, C.M., BEARD, B.L., NEWMAN, D.K. (2004): Iron isotope fractionation by Fe(II)-oxidizing photoautotrophic bacteria. – Geochimica et Cosmochimica Acta, **68**: 1227 – 1242.

CROSBY, H.A., RODEN, E.E., JOHNSON, C.M., BEARD, B.L. (2007): The mechanisms of iron isotope fractionation produced during dissimilatory Fe(III) reduction by Shewanella putrefaciens and Geobacter sulfurreducens. – Geobiology, **5**: 169 – 189.

CROWE, S.A., JONES, C.A., KATSEV, S., MAGEN, C., O'NEILL, A.H., STURM, A., CANFIELD, D.E., HAFFNER, G.D., MUCCI, A., SUNDBY, B., FOWLE, D.A. (2008): Photoferrotrophs thrive in an Archean ocean analogue. – Proceedings of the National Academy of Sciences, **105**: 15938 – 15943.

CROWE, S.A., PARIS, G., KATSEV, S., JONES, C.A., KIM, S.T., ZERKLE, A.L., NOMOSATRYO, S., FOWLE, D.A., ADKINS, J.F., SESSIONS, A.L., FARQUHAR, J., CANFIELD, D.E. (2014): Sulfate was a trace constituent of Archean seawater. – Science, **346**: 735 – 739.

CZAJA, A.D., JOHNSON, C.M., BEARD, B.L., RODEN, E.E., LI, W., MOORBATH, S. (2013): Biological Fe oxidation controlled deposition of banded iron formation in the ca. 3770 Ma Isua Supracrustal Belt (West Greenland). – Earth and Planetary Science Letters, **363**: 192 – 203.

DALL'AGNOL, R., TEIXEIRA, N.P., RÄMÖ, O.T., MOURA, C.A.V., MACAMBIRA, M.J.B., OLIVEIRA, D.C. (2005): Petrogenesis of the Paleoproterozoic rapakivi A-type granites of the Archean Carajás metallogenic province, Brazil. – Lithos, **80**: 109 – 129.

DALSTRA, H.J., GUEDES, S. (2004): Giant hydrothermal hematite deposits with Mg-Fe metasomatism: A comparison of the Carajás, Hamersley, and other iron ores. – Economic Geology, **99**: 1793 – 1800.

DARDENNE, M.A., FILHO, C.F.F., MEIRELLES, M.R. (1988): The role of shoshonitic and calc-alkaline suites in the tectonic evolution of the Carajás District, Brazil. – Journal of South American Earth Sciences, **1**: 363 – 372.

DARDENNE, M.A., SCHOBBENHAUS, C. (2001): Metalogénese do Brasil. – Editora Universidade de Brasília, Brasília, Brazil, 392 p.

DAUPHAS, N., JANNEY, P.E., MENDYBAEV, R.A., WADHWA, M., RICHTER, F., DAVIS, A.M., VAN ZUILEN, M., HINES, R., FOLEY, C.N. (2004): Chromatographic separation and multicollection-ICPMS analysis of iron. Investigating mass-dependent and -independent isotope effects. – Analytical Chemistry, **76**: 5855 – 5863.

DAUPHAS, N., ROUXEL, O. (2006): Mass spectrometry and natural variations of iron isotopes. – Mass Spectrometry Reviews, **25**: 515 – 550.

DAVIES, G.F. (2009): Effect of plate bending on the Urey ratio and the thermal evolution of the mantle. – Earth and Planetary Science Letters, **287**: 513 – 518.

DAVIS, A.M., GALLINO, R., LUGARO, M., TRIPA, C.E., SAVINA, M.R., PELLIN, M.J., LEWIS, R.S. (2002): Presolar grains and the nucleosynthesis of iron isotopes. – Lunar and Planetary Science Conference, Houston, **33**: 2018.

DAVIS, B.L., RAPP JR., G., WALAWENDER, M.J. (1968): Fabric and structural characteristics of the martitization process. – American Journal of Science, **266**: 482 – 496.

DELVIGNE, C., CARDINAL, D., HOFMANN, A., ANDRÉ, L. (2012): Stratigraphic changes of Ge/Si, REE+Y and silicon isotopes as insights into the deposition of a Mesoarchaean banded iron formation. – Earth and Planetary Science Letters, **355-356**: 109 – 118.

DELVIGNE, C., OPFERGELT, S., CARDINAL, D., HOFMANN, A., ANDRÉ, L. (2016): Desilication in Archean weathering processes traced by silicon isotopes and Ge/Si ratios. – Chemical Geology, **420**: 139 – 147.

DERRY, L.A., JACOBSEN, S.B. (1990): The chemical evolution of Precambrian seawater: Evidence from REEs in banded iron formations. – Geochimica et Cosmochimica Acta, **54**: 2965 – 2977.

DE WIT, M.J., FURNES, H. (2016): 3.5-Ga hydrothermal fields and diamictites in the Barberton Greenstone Belt - Paleoarchean crust in cold environments. – Science Advances, **2**:e1500368.

DIAS, G.S., MACAMBIRA, M.J.B., DALL'AGNOL, R., SOARES, A.D.V., BARROS, C.E.M. (1996): Datação de zircões de sill de metagabro: comprovação da idade arqueana da Formação Águas Claras, Carajás, Pará. – Simpósio de Geologia da Amazônia, Belém, SBG, **4**: 376 – 379.

DIELLA, V., FERRARIO, A., GIRARDI, V.A.V. (1995): PGE and PGM in the Luanga mafic-ultramafic intrusion in Serra dos Carajás (Pará State, Brazil). – Ore Geology Reviews, **9**: 445 – 453.

DOCEGEO (1988): Revisão litoestratigráfica da Província Mineral de Carajás. – Congresso Brasileiro de Geologia, Belém, Anais, **35**: 11 – 54.

DORR, J.V.N. (1965): Nature and origin of the high-grade hematite ores of Minas Gerais, Brazil. – Economic Geology, **60**: 1 – 46.

DRIESE, S.G., JIRSA, M.A., REN, M., BRANTLEY, S.L., SHELDON, N.D., PARKER, D., SCHMITZ, M. (2011): Neoarchean paleoweathering of tonalite and metabasalt: Implications for reconstructions of 2.69 Ga early terrestrial ecosystems and paleoatmospheric chemistry. – Precambrian Research, **189**: 1 – 17.

DUDLEY, M.A. (2010): Laminated iron formations in the Mesoproterozoic St. Francois Mountains igneous terrane, SE Missouri. Do they represent Algoma-type BIF? – Annual Meeting of the North-Central Section, Branson, GSA, **44**: 55.

DZIONY, W., HORN, I., LATTARD, D., KOEPKE, J., STEINHOEFEL, G., SCHUESSLER, J.A., HOLTZ, F. (2014): In-situ Fe isotope ratio determination in Fe-Ti oxides and sulfides from drilled gabbros and basalt from the IODP Hole 1256D in the eastern equatorial Pacific. – Chemical Geology, **363**: 101 – 113.

EVANS, K.A., MCCUAIG, T.C., LEACH, D., ANGERER, T., HAGEMANN, S.G. (2013): Banded iron formation to iron ore: A record of the evolution of Earth environments. – Geology, **41**: 99 – 102.

FABRE, S., NÉDÉLEC, A., POITRASSON, F., STRAUSS, H., THOMAZO, C., NOGUEIRA, A. (2011): Iron and sulphur isotopes from the Carajás mining province (Pará, Brazil): Implications for the oxidation of the ocean and the atmosphere across the Archaean-Proterozoic transition. – Chemical Geology, **289**: 124 – 139.

FEIO, G.R.L., DALL'AGNOL, R., DANTAS, E.L., MACAMBIRA, M.J.B., SANTOS, J.O.S., ALTHOFF, F.J., SOARES, J.E.B. (2013): Archean granitoid magmatism in the Canaã dos Carajás area: Implications for crustal evolution of the Carajás province, Amazonian craton, Brazil. – Precambrian Research, **227**: 157 – 185.

FIGUEIREDO E SILVA, R.C., HAGEMANN, S., LOBATO, L.M., ROSIÈRE, C.A., BANKS, D.A., DAVIDSON, G.J., VENNEMANN, T., HERGT, J. (2013): Hydrothermal fluid processes and evolution of the giant Serra Norte jaspilite-hosted iron ore deposits, Carajás Mineral Province, Brazil. – Economic Geology, **108**: 739 – 779.

FIGUEIREDO E SILVA, R.C., LOBATO, L.M., ROSIÈRE, C.A., HAGEMANN, S. (2011): Petrographic and geochemical studies at giant Serra Norte iron ore deposits in the Carajás mineral province, Pará State, Brazil. – Geonomos, **19 (2)**: 198 – 223.

FIGUEIREDO E SILVA, R.C., LOBATO, L.M., ROSIÈRE, C.A., HAGEMANN, S., ZUCCHETTI, M., BAARS, F.J., MORAIS, R., ANDRADED, I. (2008): Hydrothermal origin for the jaspilite-hosted, giant Serra Norte iron ore deposits in the Carajás mineral province, Para State, Brazil. – in: HAGEMANN, S., ROSIÈRE, C., GUTZMER, J., BEUKES, N.J. (eds.): Banded iron formation-related high-grade iron ore, **15**: 255 – 290; Littleton (Society of Economic Geologists).

FLAATHEN, T.K., GISLASON, S.R., OELKERS, E.H., SVEINBJÖRNSDÓTTIR, Á.E. (2009): Chemical evolution of the Mt. Hekla, Iceland, groundwaters: A natural analogue for CO_2 sequestration in basaltic rocks. – Applied Geochemistry, **24**: 463 – 474.

FRIDRIKSSON, T., ARNÓRSSON, S., BIRD, D.K. (2009): Processes controlling Sr in surface and ground waters of Tertiary tholeiitic flood basalts in Northern Iceland. – Geochimica et Cosmochimica Acta, **73**: 6727 – 6746.

GAGNEVIN, D., BOYCE, A.J., BARRIE, C.D., MENUGE, J.F., BLAKEMAN, R.J. (2012): Zn, Fe and S isotope fractionation in a large hydrothermal system. – Geochimica et Cosmochimica Acta, **88**: 183 – 198.

GALARZA, M.A.T., MACAMBIRA, M.J.B., MAURITY, C.W., MEIRELES, H.P. (2001): Idade do depósito Igarapé Bahia (Província Mineral de Carajás, Brasil), com base em isótopos de Pb. – Simpósio de Geologia da Amazônia, Belém, SBG, **7**: 116 – 119.

GARRELS, R.M., PERRY, E.A., MACKENZIE, F.T. (1973): Genesis of Precambrian iron-formations and the development of atmospheric oxygen. – Economic Geology, **68**: 1173 – 1179.

GERMAN, C.R., ELDERFIELD, H. (1990): Application of the Ce anomaly as a paleoredox indicator: the ground rules. – Paleoceanography, **5**: 823 – 833.

GISLASON, S.R., EUGSTER, H.P. (1987): Meteoric water-basalt interactions. II: A field study in N.E. Iceland. – Geochimica et Cosmochimica Acta, **51**: 2841 – 2855.

GOLE, M.J., KLEIN, C. (1981): Banded iron-formations through much of Precambrian time. – The Journal of Geology, **89**: 169 – 183.

GRAHAM, C.M., GREIG, K.M., SHEPPARD, S.M.F., TURI, B. (1983): Genesis and mobility of the H_2O-CO_2 fluid phase during regional greenschist and epidote amphibolite facies metamorphism: A petrological and stable isotope study in the Scottish Dalradian. – Geological Society of London Journal, **140**: 577 – 599.

GRAINGER, C.J., GROVES, D.I., TALLARICO, F.H.B., FLETCHER, I.R. (2008): Metallogenesis of the Carajás Mineral Province, Southern Amazon Craton, Brazil: Varying styles of Archean through Paleoproterozoic to Neoproterozoic base- and precious-metal mineralisation. – Ore Geology Reviews, **33**: 451 – 489.

GROMET, L.P., DYMEK, R.F., HASKIN, L.A., KOROTEV, R.L. (1984): The "North American shale composite": Its compilation, major and trace element characteristics. – Geochimica et Cosmochimica Acta, **48**: 2469 – 2482.

GROSS, G.A. (1980): A classification of iron-formation based on depositional environments. – Canadian Mineralogist, **18**: 215 – 222.

GROVE, T.L., PARMAN, S.W. (2004): Thermal evolution of the Earth as recorded by komatiites. – Earth and Planetary Science Letters, **219**: 173 – 187.

GRUNER, J.W. (1937): Hydrothermal leaching of iron ores of the Lake Superior type - a modified theory. – Economic Geology, **32**: 121 – 130.

GUEDES, S.C., ROSIÈRE, C.A., BARLEY, M.E. (2003): The association of carbonate alteration of banded iron formation with the Carajás high-grade hematite deposits. – Applied Earth Science (Trans. Inst. Min. Metall. B), **112**: 26 – 30.

GUTZMER, J., CHISONGA, B.C., BEUKES, N.J., MUKHOPADHYAY, J. (2008): The geochemistry of banded iron formation-hosted high-grade hematite-martite iron ores. – in: HAGEMANN, S., ROSIÈRE, C., GUTZMER, J., BEUKES, N.J. (eds.): Banded iron formation-related high-grade iron ore, **15**: 157 – 183; Littleton (Society of Economic Geologists).

GUTZMER, J., MUKHOPADHYAY, J., BEUKES, N.J., PACK, A., HAYASHI, K., SHARP, Z.D. (2006): Oxygen isotope composition of hematite and genesis of high-grade BIF-hosted iron ores. – Geological Society of America Memoir, **198**: 257 – 268.

HAGEMANN, S.G., ANGERER, T., DUURING, P., ROSIÈRE, C.A., FIGUEIREDO E SILVA, R.C., LOBATO, L., HENSLER, A.S., WALDE, D.H.G. (2016): BIF-hosted iron mineral system: A review. – Ore Geology Reviews, **76**: 317 – 359.

HALLIDAY, A.N., LEE, D.C., CHRISTENSEN, J.N., WALDER, A.J., FREEDMAN, P.A., JONES, C.E., HALL, C.M., YI, W., TEAGLE, D. (1995): Recent developments in inductively coupled plasma magnetic sector multiple collector mass spectrometry. – International Journal of Mass Spectrometry and Ion Processes, **146/147**: 21 – 33.

HALVERSON, G.P., POITRASSON, F., HOFFMAN, P.F., NÉDÉLEC, A., MONTEL, J.M., KIRBY, J. (2011): Fe isotope and trace element geochemistry of the Neoproterozoic syn-glacial Rapitan iron formation. – Earth and Planetary Science Letters, **309**: 100 – 112.

HASKIN, L.A., WILDEMAN, T.R., HASKIN, M.A. (1968): An accurate procedure for the determination of the rare earths by neutron activation. – Journal of Radioanalytical Chemistry, **1**: 337 – 348.

HEANEY, P.J., VEBLEN, D.R. (1991): An examination of spherulitic dubiomicrofossils in Precambrian banded iron formations using the transmission electron microscope. – Precambrian Research, **49**: 355 – 372.

HEIMANN, A., BEARD, B.L., JOHNSON, C.M. (2008): The role of volatile exsolution and sub-solidus fluid/rock interactions in producing high $^{56}Fe/^{54}Fe$ ratios in siliceous igneous rocks. – Geochimica et Cosmochimica Acta, **72**: 4379 – 4396.

HENSLER, A.S., HAGEMANN, S.G., ROSIÈRE, C.A., ANGERER, T., GILBERT, S. (2015): Hydrothermal and metamorphic fluid-rock interaction associated with hypogene "hard" iron ore mineralisation in the Quadrilátero Ferrífero, Brazil: Implications from in-situ laser ablation ICP-MS iron oxide chemistry. – Ore Geology Reviews, **69**: 325 – 351.

HERZBERG, C., CONDIE, K., KORENAGA, J. (2010): Thermal history of the Earth and its petrological expression. – Earth and Planetary Science Letters, **292**: 79 – 88.

HIRATA, T., OHNO, T. (2001): In-situ isotopic ratio analysis of iron using laser ablation-multiple collector-inductively coupled plasma mass spectrometry (LA-MC-ICP-MS). – Journal of Analytical Atomic Spectrometry, **16**: 487 – 491.

HOEFS (1987): Stable isotope geochemistry. – Springer, Berlin, Germany, **3**: 241 p.

HOFFMAN, P.F. (2005): On Cryogenian (Neoproterozoic) ice-sheet dynamics and the limitations of the glacial sedimentary record [28th De Beers Alex. Du Toit Memorial Lecture]. – South African Journal of Geology, **108**: 557 – 576.

HÖINK, T., LENARDIC, A., JELLINEK, A.M. (2013): Earth's thermal evolution with multiple convection modes: A Monte-Carlo approach. – Physics of the Earth and Planetary Interiors, **221**: 22 – 26.

HOLDSWORTH, R.E., PINHEIRO, R.V.L. (2000): The anatomy of shallow-crustal transpressional structures: insights from the Archaean Carajás fault zone, Amazon, Brazil. – Journal of Structural Geology, **22**: 1105 – 1123.

HOLLAND, H.D. (2005): Sedimentary mineral deposits and the evolution of Earth's near-surface environments. – Economic Geology, **100**: 1489 – 1509.

HOLM, N.G. (1989): The $^{13}C/^{12}C$ ratios of siderite and organic matter of a modern metalliferous hydrothermal sediment and their implications for banded iron formations. – Chemical Geology, **77**: 41 – 45.

HORN, I., VON BLANCKENBURG, F. (2007): Investigation on elemental and isotopic fractionation during 196 nm femtosecond laser ablation multiple collector inductively coupled plasma mass spectrometry. – Spectrochimica Acta Part B, **62**: 410 – 422.

HORN, I., VON BLANCKENBURG, F., SCHOENBERG, R., STEINHOEFEL, G., MARKL, G. (2006): In situ iron isotope ratio determination using UV-femtosecond laser ablation with application to hydrothermal ore formation processes. – Geochimica et Cosmochimica Acta, **70**: 3677 – 3688.

HREN, M.T., TICE, M.M., CHAMBERLAIN, C.P. (2009): Oxygen and hydrogen isotope evidence for a temperate climate 3.42 billion years ago. – Nature, **462**: 205 – 208.

HUSTON, D.L., LOGAN, G.A. (2004): Barite, BIFs and bugs: evidence for the evolution of the Earth's early hydrosphere. – Earth and Planetary Science Letters, **220**: 41 – 55.

IRMM (2008): Isotopic reference materials catalogue. –Institute for Reference Materials and Measurements, Brussels, Belgium, 51 p.

ISLEY, A.E., ABBOTT, D.H. (1999): Plume-related mafic volcanism and the deposition of banded iron formation. – Journal of Geophysical Research, **104**: 15,461 – 15,477.

JACOBSEN, S.B, PIMENTEL-KLOSE, M.R. (1988): A Nd isotopic study of the Hamersley and Michipicoten banded iron formations: the source of REE and Fe in Archean oceans. – Earth and Planetary Science Letters, **87**: 29 – 44.

JAMES, H.L. (1954): Sedimentary facies of iron-formation. – Economic Geology, **49**: 235 – 293.

JOHNSON, C.M., BEARD, B.L., KLEIN, C., BEUKES, N.J., RODEN, E.E. (2008): Iron isotopes constrain biologic and abiologic processes in banded iron formation genesis. – Geochimica et Cosmochimica Acta, **72**: 151 – 169.

JOHNSON, C.M., RODEN, E.E., WELCH, S.A., BEARD, B.L. (2005): Experimental constraints on Fe isotope fractionation during magnetite and Fe carbonate formation coupled to dissimilatory hydrous ferric oxide reduction. – Geochimica et Cosmochimica Acta, **69**: 963 – 993.

JOHNSON, C.M., SKULAN, J.L., BEARD, B.L., SUN, H., NEALSON, K.H., BRATERMAN, P.S. (2002): Isotopic fractionation between Fe(III) and Fe(II) in aqueous solutions. – Earth and Planetary Science Letters, **195**: 141 – 153.

KAASALAINEN, H., STEFÁNSSON, A. (2012): The chemistry of trace elements in surface geothermal waters and steam, Iceland. – Chemical Geology, **330–331**: 60 – 85.

KAPPLER, A., PASQUERO, C., KONHAUSER, K.O., NEWMAN, D.K. (2005): Deposition of banded iron formations by anoxygenic phototrophic Fe(II)-oxidizing bacteria. – Geology, **33**: 865 – 868.

KATO, Y., YAMAGUCHI, K.E., OHMOTO, H. (2006): Rare earth elements in Precambrian banded iron formations: Secular changes of Ce and Eu anomalies and evolution of atmospheric oxygen. – in: KESSLER, S.E., OHMOTO, H. (eds.): Evolution of the atmosphere, hydrosphere, and biosphere on early earth: constraints from ore deposits, **198**: 269 – 289; Denver (Geological Society of America).

KLEIN, C. (2005): Some Precambrian banded iron-formations (BIFs) from around the world: Their age, geologic setting, mineralogy, metamorphism, geochemistry, and origin. – American Mineralogist, **90**: 1473 – 1499.

KLEIN, C., BEUKES, N.J. (1989): Geochemistry and sedimentology of a facies transition from limestone to iron-formation deposition in the Early Proterozoic Transvaal Supergroup, South Africa. – Economic Geology, **84**: 1733 – 1774.

KLEIN, E.L., ALMEIDA, M.E., ROSA-COSTA, L.T. (2012): The 1.89-1.87 Ga Uatumã silicic large igneous province, northern South America. – Large Igneous Province of the month, 1 – 14.

KLEINE, B. I. (2015): How do metamorphic fluids move through rocks? An investigation of timescales, infiltration mechanisms and mineralogical controls. – Ph.D. thesis, comprehensive summary, Stockholm University, Department of Geological Sciences, Stockholm, Sweden, 37 p.

KNAUTH, L.P., EPSTEIN, S. (1976): Hydrogen and oxygen isotope ratios in nodular and bedded cherts. – Geochimica et Cosmochimica Acta, **40**: 1095 – 1108.

KNAUTH, L.P., LOWE, D.R (2003): High Archean climatic temperature inferred from oxygen isotope geochemistry of cherts in the 3.5 Ga Swaziland Supergroup, South Africa. – Geological Society of America Bulletin, **115**: 566 – 580.

KONHAUSER, K.O., AMSKOLD, L., LALONDE, S.V., POSTH, N.R., KAPPLER, A., ANBAR, A. (2007): Decoupling photochemical Fe(II) oxidation from shallow-water BIF deposition. – Earth and Planetary Science Letters, **258**: 87 – 100.

KONHAUSER, K.O., HAMADE, T., RAISWELL, R., MORRIS, R.C., FERRIS, F.G., SOUTHAM, G., CANFIELD, D.E. (2002): Could bacteria have formed the Precambrian banded iron formations? – Geology, **30**: 1079 – 1082.

KRAPEŽ, B., BARLEY, M.E., PICKARD, A.L. (2003): Hydrothermal and resedimented origins of the precursor sediments to banded iron formation: sedimentological evidence from the Early Palaeoproterozoic Brockman Supersequence of Western Australia. – Sedimentology, **50**: 979 – 1011.

KRYMSKY, R.S., MACAMBIRA, M.J.B., LAFON, J.M., ESTUMANO, G.S. (2007): Uranium-lead dating method at the Pará-Iso isotope geology laboratory, UFPA, Belém - Brazil. – Anais da Academia Brasileira de Ciências, **79(1)**: 115 – 128.

KULLERUD, G., DONNAY, G., DONNAY, J.D.H. (1969): Omission solid solution in magnetite: Kenotetrahedral magnetite. – Zeitschrift für Kristallographie, **128**: 1 – 17.

KUMP, L.R., SEYFRIED, W.E. (2005): Hydrothermal Fe fluxes during the Precambrian: Effect of low oceanic sulfate concentrations and low hydrostatic pressure on the composition of black smokers. – Earth and Planetary Science Letters, **235**: 654 – 662.

LABERGE, G.L. (1973): Possible biological origin of Precambrian iron-formations. – Economic Geology, **68**: 1098 – 1109.

LAN, T.G., FAN, H.R., SANTOSH, M., HU, F.F., YANG, K.F., LIU, Y. (2014): U-Pb zircon chronology, geochemistry and isotopes of the Changyi banded iron formation in the eastern Shandong Province: Constraints on BIF genesis and implications for Paleoproterozoic tectonic evolution of the North China Craton. – Ore Geology Reviews, **56**: 472 – 486.

LANGMUIR, D. (1971): Particle size effect on the reaction goethite = hematite + water. – American Journal of Science, **271**: 147 – 156.

LASCELLES, D.F. (2002): A new look at old rocks - an alternative model for the origin of in situ iron ore deposits derived from banded iron formation. – Iron Ore Conference, Perth, Australian Institute for Mining and Metallurgy, 107 – 126.

LASCELLES, D.F. (2007): Black smokers and density currents: A uniformitarian model for the genesis of banded iron-formations. – Ore Geology Reviews, **32**: 381 – 411.

LASCELLES, D.F. (2012): Banded iron formation to high-grade iron ore: a critical review of supergene enrichment models. – Australian Journal of Earth Sciences, **59**: 1105 – 1125.

LEITH, C.K. (1903): The Mesabi iron-bearing district of Minnesota. – U.S. Geological Survey Monograph, **43**: 316p.

LENARDIC, A. (1998): On the partitioning of mantle heat loss below oceans and continents over time and its relationship to the Archean Paradox. – Geophysical Journal International, **134**: 706 – 720.

LI, W., BEARD, B.L., JOHNSON, C.M. (2015): Biologically recycled continental iron is a major component in banded iron formations. – Proceedings of the National Academy of Sciences of the United States of America, **112**: 8193 – 8198.

LI, W., HUBERTY, J.M., BEARD, B.L., KITA, N.T., VALLEY, J.W., JOHNSON, C.M. (2013): Contrasting behavior of oxygen and iron isotopes in banded iron formations revealed by in situ isotopic analysis. – Earth and Planetary Science Letters, **384**: 132 – 143.

LLIRÓS, M., GARCÍA-ARMISEN, T., DARCHAMBEAU, F., MORANA, C., TRIADÓ-MARGARIT, X., INCEOĞLU, Ö., BORREGO, C.M., BOUILLON, S., SERVAIS, P., BORGES, A.V., DESCY, J.P., CANFIELD, D.E., CROWE, S.A. (2015): Pelagic photoferrotrophy and iron cycling in a modern ferruginous basin. – Scientific Reports, **5**: 1 – 7.

LOBATO, L.M., FIGUEIREDO E SILVA, R.C., HAGEMANN, S., THORNE, W., ZUCCHETTI, M. (2008): Hypogene alteration associated with high-grade banded iron formation-related iron ore. – in: HAGEMANN, S., ROSIÈRE, C., GUTZMER, J., BEUKES, N.J. (eds.): Banded iron formation-related high-grade iron ore, **15**: 107 – 128; Littleton (Society of Economic Geologists).

LOBATO, L.M., FIGUEIREDO E SILVA, R.C., ROSIÈRE, C.A., ZUCCHETTI, M., BAARS, F.J., SEOANE, J.C.S., RIOS, F.J., MONTEIRO, A.M. (2005): Hydrothermal origin for the iron mineralisation, Carajás Province, Pará State, Brazil. – Iron Ore 2005 Conference, AusIMM, Perth, Proceedings, **8**: 99 – 110.

LUZ, B.R., CROWLEY, J.K. (2012): Morphological and chemical evidence of stromatolitic deposits in the 2.75 Ga Carajás banded iron formation, Brazil. – Earth and Planetary Science Letters, **355–356**: 60 – 72.

MACAMBIRA, J.B. (2003): O ambiente deposicional da Formação Carajás e uma proposta de modelo evolutivo para a Bacia Grão Pará. – Ph.D. thesis, Universidade Estadual de Campinas, Instituto de Geociências, Campinas, Brazil, 212 p.

MACAMBIRA, J.B., RAMOS, J.F.F., ASSIS, J.F.P., FIGUEIRAS, A.J.M. (1990): Projeto Serra Norte e Projeto Pojuca: relatório final. – Convênio Seplan/DOCEGEO/UFPA/DNPM, Belém.

MACHADO, N., LINDENMAYER, Z., KROGH, T.E., LINDENMAYER, D. (1991): U-Pb geochronology of Archean magmatism and basement reactivation in the Carajás area, Amazon shield, Brazil. – Precambrian Research, **49**: 329 – 354.

MACLEOD, W.N. (1966): The geology and iron deposits of the Hamersley Range area, Western Australia. – Western Australian Geological Survey Bulletin, **117**: 170 p.

MANDERNACK, K.W., BAZYLINSKI, D.A., SHANKS, W.C., BULLEN, T.D. (1999): Oxygen and iron isotope studies of magnetite produced by magnetotactic bacteria. – Science, **285**: 1892 – 1896.

MARHAS, K.K., HOPPE, P., BESMEHN, A. (2004): A NanoSIMS study of iron-isotopic compositions in presolar silicon carbide grains. – Lunar and Planetary Science Conference, Houston, **35**: 1834.

McDONOUGH, W.F., SUN, S.S. (1995): The composition of the Earth. – Chemical Geology, **120**: 223 – 253.

MENDES, M., LOBATO, L.M., KUNZMANN, M., HALVERSON, G.P., ROSIÈRE, C.A. (2016): Iron isotope and REE+Y composition of the Cauê banded iron formation and related iron ores of the Quadrilátero Ferrífero, Brazil. – Mineralium Deposita, doi:10.1007/s00126-016-0649-9.

MIDDLETON, G.V. (1973): Johannes Walther's law of the correlation of facies. – Geological Society of America Bulletin, **84**: 979 – 988.

MOELLER, K., SCHOENBERG, R., GRENNE, T., THORSETH, I.H., DROST, K., PEDERSEN, R.B. (2014): Comparison of iron isotope variations in modern and Ordovician siliceous Fe oxyhydroxide deposits. – Geochimica et Cosmochimica Acta, **126**: 422 – 440.

MORRIS, R.C (1980): A textural and mineralogical study of the relationship of iron ore to banded iron-formation in the Hamersley Iron Province of Western Australia. – Economic Geology, **75**: 184 – 209.

MORRIS, R.C. (1985): Genesis of iron ore in banded iron-formation by supergene and supergene–metamorphic processes – A conceptual model. – In: WOLF K.H. (Ed.), Handbook of strata-bound and stratiform ore deposits, **13**: 73 – 235. Amsterdam (Elsevier).

MORRIS, R.C. (2012): Microplaty hematite—its varied nature and genesis. – Australian Journal of Earth Sciences, **59**: 411 – 434.

MORRIS, R.C., KNEESHAW, M. (2011): Genesis modelling for the Hamersley BIF-hosted iron ores of Western Australia: a critical review. – Australian Journal of Earth Sciences, **58**: 417 – 451.

MORRIS, R.C., THORNBER, M.R., EWERS, W.E. (1980): Deep-seated iron ores from banded-iron formation. – Nature, **288**: 250 – 252.

MÜCKE, A., CABRAL, A.R. (2005): Redox and nonredox reactions of magnetite and hematite in rocks. – Chemie der Erde, **65**: 271 – 278.

MUKASA, S.B., WILSON, A.H., YOUNG, K.R. (2013): Geochronological constraints on the magmatic and tectonic development of the Pongola Supergroup (Central Region), South Africa. – Precambrian Research, **224**: 268 – 286.

MULKIDJANIAN, A.Y., GALPERIN, M.Y. (2013): A time to scatter genes and a time to gather them: evolution of photosynthesis genes in bacteria. – in: JACQUOT, J.P., GADAL, P. (eds.): Advances in Botanical Research, **66**: 1 – 35; Amsterdam (Elsevier).

NELSON, B.J., WOOD, S.A., OSIENSKY, J.L. (2003): Partitioning of REE between solution and particulate matter in natural waters: a filtration study. – Journal of Solid State Chemistry, **171**: 51 – 56.

NOZAKI, Y. (1997): A fresh look at element distribution in the North Pacific. – EOS, American Geophysical Union, **78**: 221.

OEHLER, J.H. (1976): Hydrothermal crystallization of silica gel. – Geological Society of America Bulletin, **87**: 1143 – 1152.

OESER, M., WEYER, S., HORN, I., SCHUTH, S. (2014): High-precision Fe and Mg isotope ratios of silicate reference glasses determined in situ by femtosecond LA-MC-ICP-MS and by solution nebulisation MC-ICP-MS. – Geostandards and Geoanalytical Research, **38**: 311 – 328.

OHMOTO, H. (2003): Nonredox transformations of magnetite-hematite in hydrothermal systems. – Economic Geology, **98**: 157 – 161.

OLSZEWSKI, W.J., WIRTH, K.R., GIBBS, A.K., GAUDETTE, H.E. (1989): The age, origin, and tectonics of the Grão Pará Group and associated rocks, Serra dos Carajás, Brazil: Archean continental volcanism and rifting. – Precambrian Research, **42**: 229 – 254.

PEARCE, J.A. (1983): Role of the sub-continental lithosphere in magma genesis at active continental margins. – in: HAWKESWORTH, C.J., NORRY, M.J. (eds.): Continental basalts and mantle xenoliths, **1**: 230 – 250; Nantwich (Shiva).

PEARCE, J.A. (1996): A user's guide to basalt discrimination diagrams. – in: WYMAN, D.A. (ed.): Trace element geochemistry of volcanic rocks: Applications for massive sulphide exploration. Short course notes, **12**: 79 – 113; Winnipeg (Geological Association of Canada).

PICKARD, A.L. (2003): SHRIMP U–Pb zircon ages for the Palaeoproterozoic Kuruman Iron Formation, Northern Cape Province, South Africa: evidence for simultaneous BIF deposition on Kaapvaal and Pilbara Cratons. – Precambrian Research, **125**: 275 – 315.

PIDGEON, R.T., MACAMBIRA, M.J.B., LAFON, J.M. (2000): Th-U-Pb isotopic systems and internal structures of complex zircons from an enderbite from the Pium Complex, Carajás Province, Brazil: evidence for the ages of granulite facies metamorphism and the protolith of the enderbite. – Chemical Geology, **166**: 159 – 171.

PIMENTEL, M.M., LINDENMAYER, Z.G., LAUX, J.H., ARMSTRONG, R., ARAÚJO, J.C. (2003): Geochronology and Nd isotope geochemistry of the Gameleira Cu–Au deposit, Serra dos Carajás, Brazil: 1.8–1.7 Ga hydrothermal alteration and mineralization. – Journal of South American Earth Sciences, **15**: 803 – 813.

PINHEIRO, R.V.L. (1997): Reactivation history of the Carajás and Cinzento strike-slip systems, Amazon, Brazil. – Ph.D. thesis, Durham University, Department of Geological Sciences, Durham, United Kingdom, 408 p.

PINHEIRO, R.V.L., HOLDSWORTH, R.E. (1997): The structure of the Carajás N-4 Ironstone deposit and associated rocks: relationship to Archaean strike-slip tectonics and basement reactivation in the Amazon region, Brazil. – Journal of South American Earth Sciences, **10**: 305 – 319.

PLANAVSKY, N., BEKKER, A., ROUXEL, O.J., KAMBER, B., HOFMANN, A., KNUDSEN, A., LYONS, T.W. (2010): Rare earth element and yttrium compositions of Archean and Paleoproterozoic Fe formations revisited: New perspectives on the significance and mechanisms of deposition. – Geochimica et Cosmochimica Acta, **74**: 6387 – 6405.

PLANAVSKY, N.J., MCGOLDRICK, P., SCOTT, C.T., LI, C., REINHARD, C.T., KELLY, A.E., CHU, X., BEKKER, A., LOVE, G.D., LYONS, T.W. (2011): Widespread iron-rich conditions in the mid-Proterozoic ocean. – Nature, **477**: 448 – 451.

POITRASSON, F. (2006): On the iron isotope homogeneity level of the continental crust. – Chemical Geology, **235**: 195 – 200.

POLYAKOV, V.B., CLAYTON, R.N., HORITA, J., MINEEV, S.D. (2007): Equilibrium iron isotope fractionation factors of minerals: Reevaluation from the data of nuclear inelastic resonant X-ray scattering and Mössbauer spectroscopy. – Geochimica et Cosmochimica Acta, **71**: 3833 – 3846.

POLYAKOV, V.B., MINEEV, S.D. (2000): The use of Mössbauer spectroscopy in stable isotope geochemistry. – Geochimica et Cosmochimica Acta, **64**: 849 – 865.

PONS, M.-L., FUJII, T., ROSING, M., QUITTÉ, G., TÉLOUK, P., ALBARÈDE, F. (2013): A Zn isotope perspective on the rise of continents. – Geobiology, **11**: 201 – 214.

POULTON, S.W., FRALICK, P.W., CANFIELD, D.E. (2004): The transition to a sulphidic ocean ~ 1.84 billion years ago. – Nature, **431**: 173 – 177.

POURMAND, A., DAUPHAS, N., IRELAND, T.J. (2012): A novel extraction chromatography and MC-ICP-MS technique for rapid analysis of REE, Sc and Y: Revising C1-chondrite and Post-Archean Australian Shale (PAAS) abundances. – Chemical Geology, **291**: 38 – 54.

POWELL, C.MCA., OLIVER, N.H.S., LI, Z.X., MARTIN, D.MCB., RONASZEKI, J. (1999): Synorogenic hydrothermal origin for giant Hamersley iron oxide ore bodies. – Geology, **27**: 175 – 178.

RAINBIRD, R.H., JEFFERSON, C.W., YOUNG, G.M. (1996): The early Neoproterozoic sedimentary Succession B of northwestern Laurentia: Correlations and paleogeographic significance. – Geological Society of America Bulletin, **108**: 454 – 470.

RAMANAIDOU, E.R. (2009): Genesis of lateritic iron ore from banded iron-formation in the Capanema mine (Minas Gerais, Brazil). – Australian Journal of Earth Sciences, **56**: 605 – 620.

RAMDOHR, P. (1969): The ore minerals and their intergrowths. – Pergamon Press, Oxford, United Kingdom, **3**: 1174 p.

RIMSTIDT, J.D. (1997): Quartz solubility at low temperatures. – Geochimica et Cosmochimica Acta, **61**: 2553 – 2558.

ROBERT, F., CHAUSSIDON, M. (2006): A paleotemperature curve for the Precambrian oceans based on silicon isotopes in cherts. – Nature, **443**: 969 – 972.

ROSIÈRE, C.A., BAARS, F.J., SEOANE, J.C.S., LOBATO, L.M., DA SILVA, L.L., DE SOUZA, S.R.C., MENDES, G.E. (2006): Structure and iron mineralisation of the Carajás Province. – Applied Earth Science (Trans. Inst. Min. Metall. B), **115**: 126 – 133.

ROUXEL, O., DOBBEK, N., LUDDEN, J., FOUQUET, Y. (2003): Iron isotope fractionation during oceanic crust alteration. – Chemical Geology, **202**: 155 – 182.

ROUXEL, O., SHANKS III, W.C., BACH, W., EDWARDS, K.J. (2008): Integrated Fe- and S-isotope study of seafloor hydrothermal vents at East Pacific Rise 9–10°N. – Chemical Geology, **252**: 214 – 227.

RUFFET, G., INNOCENT, C., MICHARD, A., FÉRAUD, G., BEAUVAIS, A., NAHON, D., HAMELIN, B. (1996): A geochronological $^{40}Ar/^{39}Ar$ and $^{87}Rb/^{87}Sr$ study of K-Mn oxides from the weathering sequence of Azul, Brazil. – Geochimica et Cosmochimica Acta, **60**: 2219 – 2232.

SAUNIER, G., POKROVSKI, G.S., POITRASSON, F. (2011): First experimental determination of iron isotope fractionation between hematite and aqueous solution at hydrothermal conditions. – Geochimica et Cosmochimica Acta, **75**: 6629 – 6654.

SCHAUBLE, E.A., ROSSMAN, G.R., TAYLOR, JR., H.P. (2001): Theoretical estimates of equilibrium Fe-isotope fractionations from vibrational spectroscopy. – Geochimica et Cosmochimica Acta, **65**: 2487 – 2497.

SEVERMANN, S., JOHNSON, C.M., BEARD, B.L., GERMAN, C.R., EDMONDS, H.N., CHIBA, H., GREEN, D.R.H. (2004): The effect of plume processes on the Fe isotope composition of hydrothermally derived Fe in the deep ocean as inferred from the Rainbow vent site, Mid-Atlantic Ridge, 36°14´ N. – Earth and Planetary Science Letters, **225**: 63 – 76.

SEYFRIED, W.E., JANECKY, D.R. (1985): Heavy metal and sulfur transport during subcritical and supercritical hydrothermal alteration of basalt: Influence of fluid pressure and basalt composition and crystallinity. – Geochimica et Cosmochimica Acta, **49**: 2545 – 2560.

SHARMA, M., POLIZZOTTO, M., ANBAR, A.D. (2001): Iron isotopes in hot springs along the Juan de Fuca Ridge. – Earth and Planetary Science Letters, **194**: 39 – 51.

SHIMIZU, H., UMEMOTO, N., MASUDA, A., APPEL, P.W.U. (1990): Sources of iron-formations in the Archean Isua and Malene supracrustals, West Greenland: Evidence from La-Ce and Sm-Nd isotopic data and REE abundances. – Geochimica et Cosmochimica Acta, **54**: 1147 – 1154.

SHUSTER, D.L., FARLEY, K.A., VASCONCELOS, P.M., BALCO, G., MONTEIRO, H.S., WALTENBERG, K., STONE, J.O. (2012): Cosmogenic ^{3}He in hematite and goethite from Brazilian "canga" duricrust demonstrates the extreme stability of these surfaces. – Earth and Planetary Science Letters, **329**: 41 – 50.

SIEPIERSKI, L., FILHO, C.F.F. (2016): Spinifex-textured komatiites in the south border of the Carajas ridge, Selva Greenstone belt, Carajás Province, Brazil. – Journal of South American Earth Sciences, **66**: 41 – 55.

SKELTON, A. (2011): Flux rates for water and carbon during greenschist facies metamorphism. – Geology, **39**: 43 – 46.

SKELTON, A.D.L., GRAHAM, C.M., BICKLE, M. (1995): Lithological and structural controls on regional 3-D fluid flow patterns during greenschist facies metamorphism of the Dalradian of the SW Scottish Highlands. – Journal of Petrology, **36**: 563 – 586.

SKULAN, J.L., BEARD, B.L., JOHNSON, C.M. (2002): Kinetic and equilibrium Fe isotope fractionation between aqueous Fe(III) and hematite. – Geochimica et Cosmochimica Acta, **66**: 2995 – 3015.

SØGAARD, E.G., MEDENWALDT, R., ABRAHAM-PESKIR, J.V. (2000): Conditions and rates of biotic and abiotic iron precipitation in selected Danish freshwater plants and microscopic analysis of precipitate morphology. – Water Research, **34**: 2675 – 2682.

SÓSNICKA, M., BAKKER, R.J., BROMAN, C., PITCAIRN, I., PARANKO, I., BURLINSON, K. (2015): Fluid types and their genetic meaning for the BIF-hosted iron ores, Krivoy Rog, Ukraine. – Ore Geology Reviews, **68**: 171 – 194.

SOUZA, S.R.B., MACAMBIRA, M.J.B., SCHELLER, T. (1996): Novos dados geocronológicos para os granitos deformados do Rio Itacaiúnas (Serra dos Carajás, Pará): implicações estratigráficas. – Simpósio de Geologia da Amazônia, Belém, SBG, **5**: 380 – 383.

SOUZA, Z.S., POTREL, A., LAFON, J.M., ALTHOFF, F.J., PIMENTEL, M.M., DALL'AGNOL, R., OLIVEIRA, C.G. (2001): Nd, Pb and Sr isotopes in the Identidade Belt, an Archaean greenstone belt of the Rio Maria region (Carajás Province, Brazil): implications for the Archaean geodynamic evolution of the Amazonian Craton. – Precambrian Research, **109**: 293 – 315.

SPIER, C.A., VASCONCELOS, P.M., OLIVIERA, S.M.B. (2006): $^{40}Ar/^{39}Ar$ geochronological constraints on the evolution of lateritic iron deposits in the Quadrilátero Ferrífero, Minas Gerais, Brazil. – Chemical Geology, **234**: 79 – 104.

STEINHOEFEL, G., HORN, I., VON BLANCKENBURG, F. (2009a): Matrix-independent Fe isotope ratio determination in silicates using UV femtosecond laser ablation. – Chemical Geology, **268**: 67 – 73.

STEINHOEFEL, G., HORN, I., VON BLANCKENBURG, F. (2009b): Micro-scale tracing of Fe and Si isotope signatures in banded iron formation using femtosecond laser ablation. – Geochimica et Cosmochimica Acta, **73**: 5343 – 5360.

STEINHOEFEL, G., VON BLANCKENBURG, F., HORN, I., KONHAUSER, K.O., BEUKES, N.J., GUTZMER, J. (2010): Deciphering formation processes of banded iron formations from the Transvaal and the Hamersley successions by combined Si and Fe isotope analysis using UV femtosecond laser ablation. – Geochimica et Cosmochimica Acta, **74**: 2677 – 2696.

SWANNER, E.D., WU, W., SCHOENBERG, R., BYRNE, J., MICHEL, F.M., PAN, Y., KAPPLER, A. (2015): Fractionation of Fe isotopes during Fe(II) oxidation by a marine photoferrotroph is controlled by the formation of organic Fe-complexes and colloidal Fe fractions. – Geochimica et Cosmochimica Acta, **165**: 44 – 61.

SYLVESTER, P.J. (1989): Post-collisional alkaline granites – Journal of Geology, **97**: 261 – 280.

TALLARICO, F.H.B., FIGUEIREDO, B.R., GROVES, D.I., KOSITCIN, N., MCNAUGHTON, N.J., FLETCHER, I.R., REGO, J.L. (2005): Geology and SHRIMP U-Pb geochronology of the Igarapé Bahia Deposit, Carajás Copper-Gold Belt, Brazil: An Archean (2.57 Ga) example of iron-oxide Cu-Au-(U-REE) mineralization. – Economic Geology, **100**: 7 – 28.

TALLARICO, F.H.B., MCNAUGHTON, N.J., GROVES, D.I., FLETCHER, I.R., FIGUEIREDO, B.R., CARVALHO, J.B., REGO, J.L., NUNES, A.R. (2004): Geological and SHRIMP II U-Pb constraints on the age and origin of the Breves Cu-Au-(W-Bi-Sn) deposit, Carajás, Brazil. – Mineralium Deposita, **39**: 68 – 86.

TASSINARI, C.C.G., MACAMBIRA, M.J.B. (1999): Geochronological provinces of the Amazonian Craton. – Episodes: Journal of International Geoscience, **22**: 174 – 182.

TAYLOR, D., DALSTRA, H.J., HARDING, A.E., BROADBENT, G.C., BARLEY, M.E. (2001): Genesis of high-grade hematite orebodies of the Hamersley Province, Western Australia. – Economic Geology, **96**: 837 – 873.

TAYLOR, P.D.P., MAECK, R., DE BIÈVRE, P. (1992): Determination of the absolute isotopic composition and atomic weight of a reference sample of natural iron. – International Journal of Mass Spectrometry and Ion Processes, **121**: 111 – 125.

TEIXEIRA, J.B.G., EGGLER, D.H. (1994): Petrology, geochemistry, and tectonic setting of Archean basaltic and dioritic rocks from the N4 iron deposit, Serra dos Carajás, Pará, Brazil. – Acta Geologica Leopoldensia, **17**: 71 – 114.

TENG, F.Z., DAUPHAS, N., HUANG, S., MARTY, B. (2013): Iron isotopic systematics of oceanic basalts. – Geochimica et Cosmochimica Acta, **107**: 12 – 26.

THORNE, W.S., HAGEMANN, S.G., BARLEY, M. (2004): Petrographic and geochemical evidence for hydrothermal evolution of the North Deposit, Mt Tom Price, Western Australia. – Mineralium Deposita, **39**: 766 – 783.

TIPPING, E. (2002): Cation binding by humic substances. – Cambridge University Press, Cambridge, United Kingdom, 434 p.

TOLBERT, G.E., TREMAINE, J.W., MELCHER, G.C., GOMES, C.B. (1971): The recently discovered Serra dos Carajás iron deposits, northern Brazil. – Economic Geology, **66**: 985 – 994.

TRENDALL, A.F., BASEI, M.A.S., DE LAETER, J.R., NELSON, D.R. (1998): SHRIMP zircon U-Pb constraints on the age of the Carajás formation, Grão Pará Group, Amazon Craton. – Journal of South American Earth Sciences, **11**: 265 – 277.

TRENDALL, A.F., COMPSTON, W., NELSON, D.R., DE LAETER, J.R., BENNETT, V.C. (2004): SHRIMP zircon ages constraining the depositional chronology of the Hamersley Group, Western Australia. – Australian Journal of Earth Sciences, **51**: 621 – 644.

TRIPA, C.E., PELLIN, M.J., SAVINA, M.R., DAVIS, A.M., LEWIS, R.S., CLAYTON, R.N. (2002): Fe isotopic compositions of presolar SiC mainstream grains. – Lunar and Planetary Science Conference, Houston, **33**: 1975.

USGS (2016): Mineral commodity summaries 2016. – U.S. Geological Survey, Reston, USA, 202 p.

VALE (2014): Form 20-F annual report pursuant to section 13 or 15 (d) of the securities exchange act of 1934. – United States Securities and Exchange Commission, 1 – 164.

VASCONCELOS, P.M., RENNE, P.R., BRIMHALL, G.H., BECKER, T.A. (1994): Direct dating of weathering phenomena by $^{40}Ar/^{39}Ar$ and K-Ar analysis of supergene K-Mn oxides. – Geochimica et Cosmochimica Acta, **58**: 1635 – 1665.

WANG, C., WU, H., LI, W., PENG, Z., ZHANG, L., ZHAI, M. (2017): Changes of Ge/Si, REE + Y and Sm-Nd isotopes in alternating Fe- and Si-rich mesobands reveal source heterogeneity of the ~2.54 Ga Sijiaying banded iron formation in Eastern Hebei, China. – Ore Geology Reviews, **80**: 363 – 376.

WELCH, S.A., BEARD, B.L., JOHNSON, C.M., BRATERMAN, P.S. (2003): Kinetic and equilibrium Fe isotope fractionation between aqueous Fe(II) and Fe(III). – Geochimica et Cosmochimica Acta, **67**: 4231 – 4250.

WEYER, S., SCHWIETERS, J.B. (2003): High precision Fe isotope measurements with high mass resolution MC-ICPMS. – International Journal of Mass Spectrometry, **226**: 355 – 368.

WHITE, R.W., POWELL, R., PHILLIPS, G.N. (2003): A mineral equilibria study of the hydrothermal alteration in mafic greenschist facies rocks at Kalgoorlie, Western Australia. – Journal of Metamorphic Geology, **21**: 455 – 468.

WIESLI, R.A., BEARD, B.L., JOHNSON, C.M. (2004): Experimental determination of Fe isotope fractionation between aqueous Fe(II), siderite and "green rust" in abiotic systems. – Chemical Geology, **211**: 343 – 362.

WU, L., BEARD, B.L., RODEN, E.E., JOHNSON, C.M. (2011): Stable iron isotope fractionation between aqueous Fe(II) and hydrous ferric oxide. – Environmental Science & Technology, **45**: 1847 – 1852.

WU, L., PERCAK-DENNETT, E.M., BEARD, B.L., RODEN, E.E., JOHNSON, C.M. (2012): Stable iron isotope fractionation between aqueous Fe(II) and model Archean ocean Fe–Si coprecipitates and implications for iron isotope variations in the ancient rock record. – Geochimica et Cosmochimica Acta, **84**: 14 – 28.

XIONG, J. (2006): Photosynthesis: what color was its origin? – Genome Biology, **7**: 1 – 5.

YAMAGUCHI, K.E., JOHNSON, C.M., BEARD, B.L., OHMOTO, H. (2005): Biogeochemical cycling of iron in the Archean–Paleoproterozoic Earth: Constraints from iron isotope variations in sedimentary rocks from the Kaapvaal and Pilbara Cratons. – Chemical Geology, **218**: 135 – 169.

YANG, W., HOLLAND, H.D., RYE, R. (2002): Evidence for low or no oxygen in the late Archean atmosphere from the ~2.76 Ga Mt. Roe #2 paleosol, Western Australia: Part 3. – Geochimica et Cosmochimica Acta, **66**: 3707 – 3718.

YANG, X., ZHANG, Z., GUO, S., CHEN, J., WANG, D. (2016): Geochronological and geochemical studies of the metasedimentary rocks and diabase from the Jingtieshan deposit, North Qilian, NW China: Constraints on the associated banded iron formations. – Ore Geology Reviews, **73**: 42 – 58.

YOSHIYA, K., SAWAKI, Y., HIRATA, T., MARUYAMA, S., KOMIYA, T. (2015): In-situ iron isotope analysis of pyrites in ~ 3.7 Ga sedimentary protoliths from the Isua supracrustal belt, southern West Greenland. – Chemical Geology, **401**: 126 – 139.

YOUNG, G.M. (1976): Iron-formation and glaciogenic rocks of the Rapitan Group, Northwest Territories, Canada. – Precambrian Research, **3**: 137 – 158.

ZUCCHETI, M. (2007): Rochas máficas do Grupo Grão Pará e sua relação com a mineralização de ferro dos depósitos N4 e N5, Carajás, Pará. – Ph.D. thesis, Universidade Federal de Minas Gerais, Instituto de Geociências, Belo Horizonte, Brazil, 125 p.

Appendix

Whole-rock geochemical data for 47 samples from the N7, N8 and S11D high-grade iron ore deposits is presented in the following tables. The sample set includes canga (n=1), soft ore (n=26), BIF (n=11), magnetite-rich breccia (n=6) and intercalated volcanic units (n=3).

Major-element analysis

Major-element contents of canga, soft ore and volcanic material were measured with ICP-ES, after lithium metaborate/tetraborate fusion and dilute nitric digestion. The loss on ignition (LOI) was measured by calculating the weight difference after the ignition of the samples at 1000°C. The total carbon (TOT/C) and total sulfur (TOT/S) contents were determined by burning the samples in an induction furnace and measuring the CO_2 and SO_2 concentrations in the combustion gas with infrared radiation cells (Leco analysis).

Since the reported iron contents for soft ore were too low, i.e. the sum of major elements was routinely between 90 to 95 wt.%. The soft ore samples were reanalyzed with fused disc XRF, which produced correct sums of 99 to 100 wt.%. The major-element abundances of BIF and magnetite-rich breccia samples were only determined via XRF. The disadvantage of this approach is that sodium nitrate is used during the production of the discs for XRF analysis. Because of the addition of sodium to the sample material, Na_2O was not measured by this method; neither was the total carbon content (TOT/C) determined.

The results obtained via ICP-ES and Leco analysis are presented in Table 1. XRF data is presented in Table 2.

Trace-element analysis

Trace-element analysis was carried out with four different methods: (1) The determination of Sc and Cr followed the same procedure used on the major elements, i.e. lithium metaborate/tetraborate fusion and dilute nitric digestion followed by analysis with ICP-ES. (2) 0.5 g of each sample was leached in aqua regia at 95°C and analyzed for Ni, Cu, Zn, As, Se, Mo, Ag, Cd, Sb, Au, Hg, Tl, Pb and Bi with ICP-MS. (3) Be, V, Co, Ga, Rb, Sr, Y, Zr, Nb, Sn, Cs, Ba, La, Ce, Pr, Nd, Sm, Eu, Gd, Tb, Dy, Ho, Er, Tm, Yb, Lu, Hf, Ta, W, Th, U were analyzed with ICP-MS after the same digestion that was used for the major element analysis. (4) Pd and Pt contents were determined via ICP-MS, following lead-collection fire-assay fusion and digestion of the Ag dore bead.

Trace-element abundances of all analyzed samples are presented in Table 3.

Table 1 Major-element contents [wt.%] of the studied samples, obtained by ICP-ES and Leco analysis.

Depth [m]	Type	SiO_2	TiO_2	Al_2O_3	Fe_2O_3	MnO	MgO	CaO	Na_2O	K_2O	P_2O_5	LOI	SUM	TOT/C	TOT/S
Drill hole S11D-330															
0.10 - 0.30	Canga	1.12	0.25	1.01	85.1	0.02	<0.01	<0.01	<0.01	<0.01	0.41	3.80	91.9	0.19	<0.02
06.00 - 06.20	Soft ore	0.03	0.43	2.86	77.9	0.01	<0.01	<0.01	<0.01	<0.01	1.10	11.8	94.4	0.25	<0.02
14.05 - 14.25	Soft ore	0.09	0.27	1.63	84.0	0.01	<0.01	<0.01	<0.01	<0.01	0.50	5.00	91.6	0.13	<0.02
24.40 - 24.60	Soft ore	1.56	0.15	1.14	85.0	0.03	0.01	<0.01	<0.01	<0.01	0.52	5.00	93.5	0.09	<0.02
34.85 - 35.05	Soft ore	0.16	0.15	2.27	87.3	<0.01	<0.01	<0.01	<0.01	<0.01	0.15	2.70	92.8	0.02	<0.02
45.15 - 45.35	Soft ore	0.26	<0.01	0.23	86.1	<0.01	<0.01	<0.01	<0.01	<0.01	0.17	4.30	91.1	0.04	<0.02
55.05 - 55.25	Soft ore	0.53	0.04	0.88	85.7	0.01	<0.01	<0.01	<0.01	0.02	0.12	3.00	90.4	0.07	<0.02
65.35 - 65.55	Soft ore	0.95	<0.01	0.46	82.8	0.04	0.02	<0.01	<0.01	<0.01	0.12	7.10	91.6	0.06	<0.02
76.25 - 76.45	Soft ore	0.51	<0.01	0.48	88.8	0.02	0.02	<0.01	<0.01	<0.01	0.12	2.40	92.4	0.02	<0.02
87.85 - 88.05	Soft ore	0.43	0.02	0.31	88.2	0.02	<0.01	<0.01	<0.01	<0.01	0.13	2.90	92.0	0.03	<0.02
97.50 - 97.70	Soft ore	0.48	0.01	0.61	87.3	0.01	<0.01	<0.01	<0.01	0.02	0.05	3.10	91.6	0.03	<0.02
107.40 - 107.60	Soft ore	0.39	<0.01	0.11	86.3	0.02	0.01	<0.01	<0.01	<0.01	0.02	3.40	90.3	0.03	<0.02
117.55 - 117.75	Soft ore	1.09	0.01	0.70	90.4	0.07	0.14	<0.01	<0.01	<0.01	0.17	7.50	100.1	0.03	<0.02
132.65 - 132.85	Soft ore	0.33	<0.01	0.10	88.5	<0.01	<0.01	<0.01	<0.01	<0.01	0.06	2.60	91.6	<0.02	<0.02
132.85 - 133.05	Soft ore	1.09	0.01	0.68	87.3	0.02	0.04	<0.01	<0.01	<0.01	0.12	2.50	91.8	0.05	<0.02
142.70 - 142.90	Soft ore	0.47	0.01	0.39	90.3	0.02	<0.01	<0.01	<0.01	<0.01	0.11	1.90	93.2	0.02	<0.02
152.50 - 153.00	Soft ore	0.55	0.01	0.33	86.2	0.02	<0.01	<0.01	<0.01	<0.01	0.13	2.10	89.4	0.03	<0.02
162.80 - 163.00	Soft ore	0.61	<0.01	0.36	86.9	0.02	<0.01	<0.01	<0.01	<0.01	0.11	2.60	90.6	0.04	<0.02
172.85 - 173.05	Soft ore	0.49	<0.01	0.24	89.8	0.01	<0.01	<0.01	<0.01	<0.01	0.17	2.30	93.0	0.03	<0.02
182.75 - 182.95	Soft ore	0.54	<0.01	0.11	87.1	0.01	<0.01	<0.01	<0.01	0.01	0.05	1.80	89.6	0.02	<0.02
192.95 - 193.15	Soft ore	0.47	<0.01	0.10	88.7	0.02	<0.01	<0.01	<0.01	<0.01	0.05	1.60	91.0	0.03	<0.02
203.30 - 203.50	Soft ore	0.54	0.03	0.30	87.0	0.02	<0.01	<0.01	<0.01	<0.01	0.07	2.60	90.6	0.04	<0.02

Table 1 (*continued*).

Depth [m]	Type	SiO_2	TiO_2	Al_2O_3	Fe_2O_3	MnO	MgO	CaO	Na_2O	K_2O	P_2O_5	LOI	SUM	TOT/C	TOT/S
Drill hole S11D-330															
213.15 - 213.35	Soft ore	1.02	<0.01	1.76	85.7	0.46	0.02	<0.01	<0.01	<0.01	0.04	1.50	90.5	0.02	<0.02
217.50 - 217.70	Soft ore	28.4	<0.01	0.42	69.6	0.03	0.07	<0.01	<0.01	<0.01	0.03	1.40	100	0.05	<0.02
Drill hole S11D-214															
105.15 - 106.05	Volc	51.7	0.43	16.0	8.19	0.18	8.16	9.79	1.93	1.19	0.05	2.1	99.7	0.02	0.06
Drill hole N7-0005															
391.02 - 391.39	Volc	50.8	1.69	14.0	15.1	0.69	5.92	2.30	3.66	1.07	0.52	3.8	99.6	0.02	<0.02
Drill hole N8-0022															
11.30 - 11.50	Soft ore	0.40	0.56	1.80	87.5	0.04	<0.01	<0.01	<0.01	0.01	0.33	3.10	93.8	0.09	<0.02
29.60 - 29.80	Soft ore	0.49	0.01	0.14	91.4	0.02	0.02	<0.01	<0.01	<0.01	0.03	1.90	94.0	<0.02	<0.02
48.46 - 48.66	Soft ore	0.76	<0.01	0.09	90.0	0.05	0.02	<0.01	<0.01	<0.01	0.02	2.20	93.1	<0.02	<0.02
127.73 - 128.19	Volc	49.6	0.36	14.0	23.0	0.21	6.70	0.02	0.01	0.24	0.04	5.6	99.8	<0.02	<0.02

Volc - Volcanic material

Table 2 Major-element contents [wt.%] of the studied samples, obtained by XRF analysis.

Depth [m]	Type	SiO_2	TiO_2	Al_2O_3	Fe_2O_3	MnO	MgO	CaO	K_2O	P_2O_5	LOI	SUM	S
Drill hole S11D-330													
0.10 - 0.30	Canga	1.27	0.25	1.00	94.4	0.01	0.01	0.01	<0.01	0.42	2.78	100.2	0.004
06.00 - 06.20	Soft ore	0.08	0.46	2.99	85.7	<0.01	<0.01	<0.01	<0.01	1.14	9.90	100.3	0.008
14.05 - 14.25	Soft ore	0.18	0.28	1.68	93.4	<0.01	<0.01	0.01	<0.01	0.53	3.77	99.9	0.007
24.40 - 24.60	Soft ore	0.74	0.15	1.18	94.3	0.03	0.03	<0.01	<0.01	0.57	3.35	100.4	0.006
34.85 - 35.05	Soft ore	0.22	0.16	2.29	95.4	<0.01	<0.01	<0.01	<0.01	0.15	1.87	100.1	<0.001
45.15 - 45.35	Soft ore	0.35	<0.01	0.20	94.9	<0.01	<0.01	0.01	<0.01	0.18	4.06	99.7	<0.001
55.05 - 55.25	Soft ore	0.65	0.04	0.91	95.5	<0.01	0.01	<0.01	0.02	0.13	2.89	100.2	<0.001
65.35 - 65.55	Soft ore	0.90	<0.01	0.46	92.4	0.04	0.04	<0.01	<0.01	0.13	6.69	100.7	0.004
76.25 - 76.45	Soft ore	0.62	<0.01	0.46	97.0	0.02	0.03	<0.01	<0.01	0.12	2.23	100.5	<0.001
87.85 - 88.05	Soft ore	0.45	<0.01	0.29	97.0	<0.01	<0.01	<0.01	<0.01	0.11	2.34	100.2	0.001
97.50 - 97.70	Soft ore	0.53	<0.01	0.60	96.7	<0.01	0.01	<0.01	<0.01	0.05	2.85	100.7	<0.001
107.40 - 107.60	Soft ore	0.46	<0.01	0.08	96.5	0.01	0.01	<0.01	<0.01	0.03	3.15	100.2	<0.001
117.55 - 117.75	Soft ore	1.10	<0.01	0.64	91.5	0.07	0.14	0.01	<0.01	0.17	6.95	100.6	<0.001
132.65 - 132.85	Soft ore	0.43	<0.01	0.06	98.3	<0.01	0.02	<0.01	<0.01	0.04	2.29	101	0.002
132.85 - 133.05	Soft ore	1.16	<0.01	0.69	96.63	0.02	0.04	0.01	0.01	0.09	1.98	100.6	<0.001
142.70 - 142.90	Soft ore	0.50	<0.01	0.38	98.1	0.01	<0.01	0.01	<0.01	0.10	1.26	100.4	<0.001
152.50 - 153.00	Soft ore	0.68	<0.01	0.33	98.1	0.02	<0.01	0.01	<0.01	0.13	1.44	100.7	<0.001
162.80 - 163.00	Soft ore	0.73	<0.01	0.35	96.4	0.02	0.02	<0.01	<0.01	0.11	2.35	100	0.005
172.85 - 173.05	Soft ore	0.45	<0.01	0.20	97.7	<0.01	0.02	<0.01	<0.01	0.15	1.77	100.3	<0.001
182.75 - 182.95	Soft ore	0.59	<0.01	0.09	98.4	0.01	0.02	<0.01	<0.01	0.04	1.44	100.6	<0.001
192.95 - 193.15	Soft ore	0.46	<0.01	0.08	98.0	0.01	0.02	<0.01	<0.01	0.05	1.37	100	<0.001
203.30 - 203.50	Soft ore	0.66	0.02	0.29	97.2	0.02	0.02	<0.01	<0.01	0.10	2.02	100.3	<0.001

Table 2 (*continued*).

Depth [m]	Type	SiO_2	TiO_2	Al_2O_3	Fe_2O_3	MnO	MgO	CaO	K_2O	P_2O_5	LOI	SUM	S
Drill hole S11D-330													
213.15 - 213.35	Soft ore	1.14	<0.01	1.83	95.5	0.48	0.03	0.02	0.01	0.04	1.28	100.3	<0.001
217.50 - 217.70	Soft ore	27.6	<0.01	0.37	71.1	0.02	0.02	<0.01	<0.01	<0.01	0.79	99.9	<0.001
217.70 - 217.90	BIF	40.0	<0.01	<0.01	59.8	0.03	<0.01	0.02	<0.01	<0.01	0.31	100.2	<0.001
219.61 - 219.70	BIF	51.4	<0.01	<0.01	48.3	0.04	<0.01	0.01	<0.01	<0.01	0.17	99.9	<0.001
234.18 - 234.49	BIF	62.5	<0.01	0.09	37.4	0.03	0.13	0.02	<0.01	<0.01	-0.37	99.8	0.004
Drill hole S11D-191													
219.38 - 219.62	BIF	49.2	<0.01	0.10	37.9	0.18	3.03	4.21	0.04	<0.01	5.68	100.3	0.002
251.41 - 251.83	BIF	49.0	<0.01	0.15	41.9	0.08	2.28	3.10	0.03	<0.01	3.66	100.2	<0.001
281.45 - 281.92	Breccia	44.6	0.27	4.03	36.4	0.36	3.99	3.53	0.56	0.02	5.89	100.0	0.310
Drill hole S11D-214													
361.36 -361.61	Breccia	47.8	0.02	0.57	40.6	0.27	1.58	4.12	0.22	0.01	4.86	100.2	0.143
397.11 - 397.36	Breccia	48.3	0.05	1.86	35.7	0.31	1.93	4.40	0.68	0.02	6.34	100.0	0.417
428.07 - 428.27	Breccia	44.1	0.05	1.26	39.6	0.23	2.73	4.96	0.42	0.02	6.09	99.8	0.330
434.52 -434.74	Breccia	45.9	0.02	0.68	37.1	0.34	2.32	5.72	0.29	<0.01	7.56	100.0	0.040
495.40 - 495.55	Breccia	49.8	0.03	0.68	42.0	0.29	2.04	1.23	0.18	0.01	3.59	100.1	0.213
Drill hole N7-0005													
111.98 - 112.35	BIF	50.0	<0.01	0.19	49.0	0.04	1.27	0.16	0.02	0.03	-0.75	100	0.027
111.98 - 112.35	BIF	33.6	<0.01	0.04	66.3	0.13	0.45	0.11	0.01	0.02	-0.54	100.1	0.003

Table 2 (*continued*).

Depth [m]	Type	SiO_2	TiO_2	Al_2O_3	Fe_2O_3	MnO	MgO	CaO	K_2O	P_2O_5	LOI	SUM	S
Drill hole N8-0022													
11.30 - 11.50	Soft ore	0.47	0.53	1.76	94.7	0.04	0.01	0.01	<0.01	0.35	1.94	99.8	0.014
29.60 - 29.80	Soft ore	0.61	<0.01	0.12	97.9	0.02	0.04	0.01	<0.01	0.04	1.35	100.1	0.007
48.46 - 48.66	Soft ore	0.88	<0.01	0.06	97.8	0.05	0.03	<0.01	<0.01	0.02	1.88	100.7	<0.001
50.80 - 50.99	BIF	41.3	<0.01	<0.01	56.5	0.01	<0.01	0.02	<0.01	<0.01	2.45	100.3	<0.001
84.36 - 84.52	BIF	37.0	<0.01	<0.01	61.1	0.16	0.02	0.03	<0.01	<0.01	1.38	99.7	<0.001
98.59 - 98.75	BIF	37.8	<0.01	<0.01	58.2	0.14	1.27	1.99	<0.01	<0.01	1.08	100.5	0.004
135.50 - 135.60	BIF	42.1	<0.01	0.03	57.9	0.04	0.02	0.03	0.01	<0.01	-0.14	100	<0.001

Breccia - Magnetite-rich breccia

Table 3 Trace-element contents [ppm] of the studied samples. Pd, Pt and Au in [ppb].

Drill hole	S11D-330	S11D-330	S11D-330	S11D-330	S11D-330	S11D-330
Type	Canga	Soft ore	Soft ore	Soft ore	Soft ore	Soft ore
Depth [m]	0.10 - 0.30	06.00 - 06.20	14.05 - 14.25	24.40 - 24.60	34.85 - 35.05	45.15 - 45.35
Be	<1	1	<1	2	<1	2
Sc	2	4	5	7	6	1
V	40	61	38	16	13	<8
Cr	48	55	48	34	41	27
Co	0.5	0.7	0.8	3.9	1	<0.2
Ni	1.0	1.4	0.8	2.7	2.5	0.6
Cu	34.3	18.1	18.4	22.6	13.7	7.0
Zn	36	14	11	27	16	16
Ga	6.5	10.2	6.5	3.3	2.1	<0.5
As	4.0	3.1	2.6	6.5	3.0	2.4
Se	1.6	<0.5	<0.5	<0.5	<0.5	<0.5
Rb	0.4	0.1	0.3	0.6	<0.1	0.4
Sr	5.4	4.8	10.7	5.9	3.9	0.6
Y	4.5	6.5	11.9	6.3	12.1	3.4
Zr	63.3	90.2	59.6	50.4	51.7	1.5
Nb	4.1	6.5	4.2	3.4	1.7	0.6
Mo	1.4	1.0	0.5	0.8	0.4	0.2
Pd	0.5	0.8	0.6	0.7	<0.5	0.5
Ag	23.2	<0.1	<0.1	<0.1	<0.1	<0.1
Cd	6.9	<0.1	<0.1	<0.1	<0.1	<0.1
Sn	<1	<1	1	<1	<1	<1
Sb	0.2	0.2	0.2	0.3	0.3	<0.1
Cs	<0.1	<0.1	<0.1	<0.1	<0.1	<0.1
Ba	14	3	8	9	4	6
La	7.3	8.7	21.1	9.6	6.3	1.5
Ce	11.2	14.5	30.3	14.4	20.8	2.5
Pr	1.30	1.44	3.26	1.63	0.97	0.23
Nd	4.7	3.9	10.3	6.2	3.1	1.0
Sm	0.60	0.73	1.80	1.11	0.50	0.24
Eu	0.21	0.25	0.63	0.35	0.35	0.19
Gd	0.59	0.61	1.42	0.91	1.03	0.25
Tb	0.09	0.11	0.18	0.12	0.16	0.04
Dy	0.59	0.77	0.99	0.70	1.10	0.13
Ho	0.09	0.18	0.22	0.12	0.28	0.07
Er	0.29	0.41	0.73	0.45	0.82	0.23
Tm	0.05	0.06	0.09	0.05	0.13	0.02
Yb	0.27	0.51	0.68	0.60	0.85	0.19
Lu	0.06	0.10	0.12	0.07	0.14	0.05
Hf	1.7	2.2	1.3	1.4	1.3	0.1
Ta	0.2	0.4	0.3	0.2	0.2	<0.1
W	2.0	2.1	2.1	1.3	<0.5	4.6
Pt	0.3	0.2	0.2	0.5	0.2	<0.1
Au	1.2	1.7	<0.5	1.4	1.3	<0.5
Hg	0.06	0.10	0.10	0.06	<0.01	<0.01
Tl	<0.1	<0.1	<0.1	<0.1	<0.1	<0.1
Pb	4.0	2.7	1.4	2.5	3.7	2.4
Bi	0.3	0.4	<0.1	<0.1	0.1	<0.1
Th	4.1	4.9	5.4	3.6	4.7	<0.2
U	0.2	0.6	0.5	0.8	1.3	<0.1
∑REE+Y	31.8	38.8	83.7	42.6	48.6	10.0
$(Ce/Ce^*)_{PAAS}$	0.87	0.97	0.86	0.87	1.99	1.01
$(Eu/Eu^*)_{PAAS}$	1.88	1.84	2.14	1.89	2.67	4.10

Table 3 (*continued*).

Drill hole	S11D-330	S11D-330	S11D-330	S11D-330	S11D-330	S11D-330
Type	Soft ore	Soft ore	Soft ore	Soft ore	Soft ore	Soft ore
Depth [m]	55.05 - 55.25	65.35 - 65.55	76.25 - 76.45	87.85 - 88.05	97.50 - 97.70	107.40 - 107.60
Be	<1	2	<1	<1	<1	<1
Sc	2	<1	1	1	1	<1
V	<8	<8	<8	<8	<8	<8
Cr	<14	21	34	34	14	27
Co	0.5	0.5	0.2	0.6	<0.2	0.2
Ni	1.0	0.5	0.5	1.3	0.6	0.3
Cu	10.9	14.0	11.1	4.6	8.3	4.5
Zn	33	15	24	9	18	13
Ga	0.8	<0.5	<0.5	<0.5	<0.5	<0.5
As	1.3	1.5	3.7	2.6	1.6	1.3
Se	<0.5	<0.5	<0.5	<0.5	<0.5	<0.5
Rb	0.8	0.2	0.4	0.2	0.8	0.5
Sr	4.9	<0.5	7.3	2.0	5.2	<0.5
Y	11.7	5.8	4.1	4.0	6.9	5.6
Zr	6.4	1.3	1.2	2.8	0.4	<0.1
Nb	0.9	0.6	0.8	1.0	0.7	0.7
Mo	0.2	0.2	0.5	0.4	0.2	<0.1
Pd	0.5	0.7	<0.5	0.5	0.6	<0.5
Ag	<0.1	<0.1	<0.1	<0.1	<0.1	<0.1
Cd	<0.1	<0.1	<0.1	<0.1	<0.1	<0.1
Sn	<1	<1	<1	<1	<1	<1
Sb	<0.1	<0.1	0.1	0.1	0.1	<0.1
Cs	<0.1	<0.1	<0.1	<0.1	<0.1	0.1
Ba	19	11	38	8	9	10
La	10.4	0.8	16.6	4.9	12.0	0.8
Ce	14.6	1.2	37.5	15.7	15.5	0.8
Pr	1.31	0.10	2.58	0.67	1.26	0.08
Nd	5.6	0.3	10.3	2.1	3.9	<0.3
Sm	0.92	<0.05	1.61	0.45	0.61	<0.05
Eu	0.56	0.14	0.69	0.28	0.42	0.06
Gd	0.88	0.13	1.10	0.73	0.70	0.15
Tb	0.12	0.01	0.10	0.07	0.08	0.02
Dy	0.82	0.06	0.43	0.25	0.48	0.14
Ho	0.14	0.04	0.08	0.05	0.09	0.04
Er	0.47	0.16	0.20	0.20	0.34	0.17
Tm	0.07	0.03	0.04	0.02	0.04	0.02
Yb	0.49	0.20	0.19	0.21	0.17	0.18
Lu	0.09	0.04	0.03	0.04	0.04	0.03
Hf	<0.1	<0.1	<0.1	0.1	<0.1	<0.1
Ta	<0.1	<0.1	<0.1	<0.1	<0.1	<0.1
W	1.4	0.6	<0.5	0.6	1.1	0.8
Pt	0.1	0.1	<0.1	<0.1	<0.1	0.1
Au	<0.5	<0.5	<0.5	<0.5	<0.5	<0.5
Hg	<0.01	0.02	0.01	<0.01	<0.01	<0.01
Tl	<0.1	<0.1	<0.1	<0.1	<0.1	<0.1
Pb	2.9	0.9	1.7	3.9	3.6	1.1
Bi	<0.1	<0.1	<0.1	<0.1	<0.1	<0.1
Th	0.5	<0.2	<0.2	0.4	0.2	<0.2
U	<0.1	<0.1	1.1	<0.1	<0.1	<0.1
∑REE+Y	48.2	9.01	75.6	29.7	42.5	8.09
$(Ce/Ce^*)_{PAAS}$	0.91	0.98	1.36	2.02	0.89	0.70
$(Eu/Eu^*)_{PAAS}$	3.44	D.L.	2.93	3.31	3.88	D.L.

Table 3 (*continued*).

Drill hole	S11D-330	S11D-330	S11D-330	S11D-330	S11D-330	S11D-330
Type	Soft ore	Soft ore	Soft ore	Soft ore	Soft ore	Soft ore
Depth [m]	117.55 - 117.75	132.65 - 132.85	132.85 - 133.05	142.70 - 142.90	152.50 - 153.00	162.80 - 163.00
Be	<1	<1	<1	<1	2	2
Sc	<1	<1	<1	<1	<1	<1
V	<8	<8	<8	<8	<8	<8
Cr	21	14	21	<14	41	21
Co	<0.2	0.8	0.3	<0.2	0.8	<0.2
Ni	1.3	0.4	1.8	1.0	0.7	0.7
Cu	102	8.5	27.5	34.8	45.1	71.8
Zn	17	10	24	11	12	19
Ga	<0.5	<0.5	<0.5	<0.5	<0.5	<0.5
As	2.0	2.8	6.2	5.4	10.5	6.2
Se	<0.5	<0.5	<0.5	<0.5	<0.5	<0.5
Rb	<0.1	0.5	0.7	0.6	<0.1	0.2
Sr	1.1	<0.5	<0.5	2.0	1.1	1.0
Y	8.1	3.3	5.3	2.3	2.2	5.4
Zr	1.1	<0.1	1.7	4.1	<0.1	<0.1
Nb	0.8	0.5	0.6	1.1	0.4	0.6
Mo	0.1	0.3	1.4	0.5	1.1	0.4
Pd	<0.5	0.5	1.6	0.6	0.6	<0.5
Ag	<0.1	<0.1	<0.1	<0.1	<0.1	<0.1
Cd	<0.1	<0.1	<0.1	<0.1	<0.1	<0.1
Sn	<1	<1	<1	<1	<1	<1
Sb	<0.1	<0.1	<0.1	<0.1	<0.1	<0.1
Cs	<0.1	0.2	<0.1	<0.1	<0.1	0.1
Ba	14	11	15	9	9	6
La	2.5	0.8	2.9	4.5	2.5	3.0
Ce	3.7	1.2	3.1	6.3	4.0	3.8
Pr	0.28	0.09	0.30	0.60	0.29	0.29
Nd	0.8	<0.3	0.7	2.5	1.8	1.1
Sm	0.22	0.05	0.21	0.43	0.19	0.15
Eu	0.28	0.14	0.21	0.25	0.19	0.21
Gd	0.47	0.19	0.24	0.38	0.19	0.18
Tb	0.05	0.02	0.03	0.04	0.02	0.03
Dy	0.34	0.08	0.32	0.34	0.23	0.23
Ho	0.08	0.03	0.06	0.04	<0.02	0.04
Er	0.35	0.18	0.15	0.11	0.08	0.27
Tm	0.04	0.02	0.02	<0.01	0.02	0.03
Yb	0.31	0.13	0.22	0.07	0.14	0.22
Lu	0.07	0.03	0.02	0.02	0.02	0.05
Hf	<0.1	<0.1	0.1	0.2	0.1	<0.1
Ta	<0.1	<0.1	<0.1	<0.1	<0.1	<0.1
W	0.6	1.6	6.3	1.3	0.7	<0.5
Pt	<0.1	0.2	0.8	0.1	<0.1	0.1
Au	3.0	<0.5	1.0	<0.5	<0.5	<0.5
Hg	0.03	<0.01	<0.01	<0.01	0.02	0.01
Tl	0.1	<0.1	<0.1	<0.1	<0.1	<0.1
Pb	3.3	2.6	3.2	2.2	4.4	1.8
Bi	0.3	<0.1	<0.1	<0.1	<0.1	<0.1
Th	0.3	<0.2	<0.2	0.4	<0.2	<0.2
U	0.1	0.1	0.4	0.3	0.1	<0.1
∑REE+Y	17.6	6.26	13.8	17.9	11.9	15.0
$(Ce/Ce^*)_{PAAS}$	1.00	1.01	0.74	0.89	1.07	0.90
$(Eu/Eu^*)_{PAAS}$	5.77	9.39	5.48	3.63	6.04	6.72

Table 3 (*continued*).

Drill hole	S11D-330	S11D-330	S11D-330	S11D-330	S11D-330	S11D-330
Type	Soft ore	Soft ore	Soft ore	Soft ore	Soft ore	Soft ore
Depth [m]	172.85 - 173.05	182.75 - 182.95	192.95 - 193.15	203.30 - 203.50	213.15 - 213.35	217.50 - 217.70
Be	2	<1	<1	2	3	<1
Sc	<1	<1	<1	<1	<1	<1
V	<8	<8	<8	<8	<8	<8
Cr	21	<14	<14	27	14	<14
Co	0.2	<0.2	0.3	4.5	4.9	0.4
Ni	0.5	0.4	0.5	1.1	0.8	0.9
Cu	22.0	24.6	18.3	61.0	36.9	37.9
Zn	9	10	12	4	6	4
Ga	<0.5	<0.5	<0.5	<0.5	<0.5	1.5
As	5.1	8.9	3.3	4.8	4.5	0.9
Se	<0.5	<0.5	<0.5	<0.5	<0.5	<0.5
Rb	0.6	1.2	0.8	0.5	0.5	0.5
Sr	<0.5	<0.5	1.1	<0.5	12.9	<0.5
Y	4.9	3.4	6.5	4.2	3.3	2.9
Zr	0.5	0.2	<0.1	2.7	1.7	0.3
Nb	0.5	0.5	0.6	0.7	0.4	0.3
Mo	0.4	0.5	0.2	0.4	0.5	0.2
Pd	0.9	0.8	0.5	0.6	0.7	<0.5
Ag	<0.1	<0.1	<0.1	<0.1	0.1	<0.1
Cd	<0.1	<0.1	<0.1	<0.1	<0.1	<0.1
Sn	<1	<1	<1	<1	<1	<1
Sb	0.1	<0.1	<0.1	<0.1	<0.1	0.2
Cs	<0.1	<0.1	0.1	<0.1	<0.1	<0.1
Ba	7	17	13	5	136	10
La	1.5	0.9	4.0	1.8	1.3	2.8
Ce	1.3	1.2	3.6	1.1	2.4	3.5
Pr	0.14	0.07	0.33	0.15	0.12	0.51
Nd	0.6	<0.3	1.0	<0.3	<0.3	2.7
Sm	0.09	<0.05	0.21	0.09	0.15	0.28
Eu	0.15	0.07	0.26	0.15	0.11	0.22
Gd	0.19	0.12	0.26	0.18	0.19	0.24
Tb	0.02	0.01	0.03	0.03	0.02	0.04
Dy	0.16	0.13	0.24	0.21	0.22	0.34
Ho	0.05	0.05	0.07	0.06	0.03	0.07
Er	0.20	0.17	0.23	0.22	0.14	0.12
Tm	0.02	0.02	0.04	0.02	0.02	0.03
Yb	0.28	0.09	0.27	0.10	0.17	0.18
Lu	0.04	0.04	0.04	0.05	0.03	0.04
Hf	<0.1	<0.1	<0.1	<0.1	<0.1	<0.1
Ta	<0.1	<0.1	<0.1	<0.1	<0.1	<0.1
W	0.7	<0.5	0.6	0.6	<0.5	3.7
Pt	<0.1	<0.1	0.1	0.1	1.1	<0.1
Au	<0.5	<0.5	<0.5	<0.5	<0.5	<0.5
Hg	<0.01	<0.01	<0.01	<0.01	0.08	<0.01
Tl	<0.1	<0.1	<0.1	<0.1	0.1	<0.1
Pb	2.3	1.2	1.2	0.6	3.9	1.7
Bi	<0.1	<0.1	<0.1	<0.1	<0.1	<0.1
Th	<0.2	<0.2	<0.2	<0.2	<0.2	<0.2
U	<0.1	<0.1	<0.1	<0.1	1.5	0.4
∑REE+Y	9.64	6.27	17.1	8.36	8.20	14.0
$(Ce/Ce^*)_{PAAS}$	0.62	1.00	0.67	0.45	1.33	0.70
$(Eu/Eu^*)_{PAAS}$	7.64	D.L.	6.78	6.21	4.11	4.31

Table 3 (*continued*).

Drill hole	S11D-330	S11D-330	S11D-330	S11D-191	S11D-191	S11D-191
Type	BIF	BIF	BIF	BIF	BIF	Breccia
Depth [m]	217.70 - 217.90	219.61 - 219.70	234.18 - 234.49	219.38 - 219.62	251.41 - 251.83	281.45 - 281.92
Be	<1	<1	<1	<1	<1	2
Sc	N.A.	N.A.	N.A.	N.A.	N.A.	N.A.
V	<8	<8	<8	<8	<8	40
Cr	<27	<27	<27	<27	<27	<27
Co	1.8	0.3	1.1	0.3	0.3	7.2
Ni	2.7	2.8	5.1	4.4	3.2	17.2
Cu	4.1	2.9	14.8	93.3	44.1	29.3
Zn	2	1	2	4	4	69
Ga	0.6	<0.5	<0.5	<0.5	<0.5	5.9
As	0.6	<0.5	0.5	0.7	1.1	1.9
Se	<0.5	<0.5	<0.5	<0.5	<0.5	<0.5
Rb	0.3	0.5	0.8	5.9	3.3	60.4
Sr	<0.5	<0.5	<0.5	34.1	19.5	11.1
Y	2.6	1.8	3.9	5.7	4.8	8.9
Zr	0.5	0.4	2.3	1.5	2.2	35.7
Nb	<0.1	0.2	0.2	<0.1	0.1	1.8
Mo	0.2	0.2	0.2	0.3	<0.1	1.3
Pd	N.A.	N.A.	N.A.	N.A.	N.A.	N.A.
Ag	<0.1	<0.1	0.1	<0.1	0.1	0.1
Cd	<0.1	<0.1	<0.1	<0.1	<0.1	<0.1
Sn	6	<1	3	2	3	1
Sb	0.2	0.1	0.1	<0.1	0.1	<0.1
Cs	<0.1	<0.1	<0.1	<0.1	0.1	2.1
Ba	3	6	7	4	9	203
La	1.7	1.1	2.7	0.8	1.8	3.7
Ce	1.3	1.3	3.3	1.4	2.3	7.1
Pr	0.22	0.12	0.28	0.11	0.19	0.84
Nd	0.8	0.4	0.8	0.4	0.7	3.1
Sm	0.17	<0.05	0.11	0.06	0.06	0.67
Eu	0.14	0.10	0.13	0.17	0.19	0.70
Gd	0.21	0.11	0.17	0.13	0.13	1.00
Tb	0.02	0.01	0.02	0.02	0.02	0.17
Dy	0.24	0.07	0.12	0.14	0.18	1.05
Ho	0.04	<0.02	0.04	0.05	0.05	0.21
Er	0.17	0.05	0.14	0.19	0.23	0.60
Tm	0.02	<0.01	0.02	0.03	0.03	0.09
Yb	0.11	0.06	0.14	0.18	0.17	0.48
Lu	0.02	0.01	0.03	0.04	0.03	0.08
Hf	<0.1	<0.1	<0.1	<0.1	<0.1	1.0
Ta	<0.1	<0.1	<0.1	<0.1	<0.1	<0.1
W	0.7	2.2	1.3	<0.5	2.0	1.3
Pt	N.A.	N.A.	N.A.	N.A.	N.A.	N.A.
Au	0.7	<0.5	1.6	<0.5	0.6	<0.5
Hg	<0.01	<0.01	<0.01	<0.01	<0.01	<0.01
Tl	<0.1	<0.1	<0.1	<0.1	<0.1	0.3
Pb	1.2	1.0	0.5	0.4	1.7	1.8
Bi	<0.1	<0.1	<0.1	<0.1	<0.1	0.2
Th	<0.2	<0.2	<0.2	<0.2	0.2	1.6
U	0.7	0.3	0.2	<0.1	<0.1	0.7
∑REE+Y	7.76	5.13	11.9	9.42	10.9	28.7
$(Ce/Ce^*)_{PAAS}$	0.49	0.81	0.85	1.10	0.88	0.97
$(Eu/Eu^*)_{PAAS}$	4.81	D.L.	5.91	10.6	11.8	4.50

Table 3 (*continued*).

Drill hole	S11D-214	S11D-214	S11D-214	S11D-214	S11D-214	S11D-214
Type	Volc	Breccia	Breccia	Breccia	Breccia	Breccia
Depth [m]	105.15 - 106.05	361.36 -361.61	397.11 - 397.36	428.07 - 428.27	434.52 -434.74	495.40 - 495.55
Be	<1	<1	1	<1	<1	1
Sc	28	N.A.	N.A.	N.A.	N.A.	N.A.
V	152	<8	9	<8	<8	<8
Cr	335	<27	<27	<27	55	27
Co	39.2	5.3	10.2	8.7	2.3	5.9
Ni	62.2	5.2	5.6	5.1	4.3	4.9
Cu	46.5	40.0	7.7	8.9	1.3	53.6
Zn	30	3	3	4	4	5
Ga	10.9	0.8	2.4	1.5	0.6	0.9
As	0.9	0.6	1.9	1.1	<0.5	1.5
Se	<0.5	<0.5	<0.5	<0.5	<0.5	<0.5
Rb	29.5	28.4	35.1	35.5	16.9	12.7
Sr	172	4.4	7.2	17.5	15.2	8.5
Y	8.8	2.8	3.9	4.7	4.4	4.1
Zr	47.0	9.5	30.0	15.9	10.1	10.8
Nb	2.3	0.5	1.4	0.6	0.4	0.7
Mo	0.3	0.6	0.4	0.6	0.4	0.4
Pd	N.A.	N.A.	N.A.	N.A.	N.A.	N.A.
Ag	<0.1	<0.1	<0.1	<0.1	<0.1	<0.1
Cd	<0.1	<0.1	<0.1	<0.1	<0.1	<0.1
Sn	<1	2	<1	<1	1	1
Sb	<0.1	0.2	0.2	0.4	0.2	0.4
Cs	0.1	0.5	0.1	0.3	<0.1	0.1
Ba	401	10	53	42	36	51
La	8.5	2.7	5.0	4.2	4.1	2.9
Ce	13.9	4.5	8.5	6.4	6.4	4.1
Pr	1.80	0.44	0.94	0.67	0.62	0.40
Nd	6.2	1.7	3.6	2.3	2.2	1.4
Sm	1.34	0.31	0.59	0.45	0.43	0.29
Eu	0.57	0.23	0.28	0.41	0.40	0.21
Gd	1.39	0.38	0.61	0.54	0.50	0.30
Tb	0.26	0.05	0.11	0.09	0.07	0.05
Dy	1.58	0.28	0.56	0.46	0.39	0.27
Ho	0.38	0.05	0.12	0.10	0.07	0.08
Er	0.98	0.19	0.41	0.34	0.22	0.29
Tm	0.15	0.03	0.05	0.05	0.04	0.04
Yb	1.05	0.17	0.41	0.30	0.25	0.26
Lu	0.17	0.03	0.06	0.05	0.03	0.04
Hf	1.2	0.3	0.8	0.4	0.3	0.3
Ta	0.2	<0.1	0.1	<0.1	<0.1	<0.1
W	<0.5	1.3	0.8	1.2	2.9	0.6
Pt	N.A.	N.A.	N.A.	N.A.	N.A.	N.A.
Au	<0.5	2.6	<0.5	<0.5	<0.5	<0.5
Hg	<0.01	<0.01	<0.01	<0.01	<0.01	<0.01
Tl	<0.1	0.1	<0.1	<0.1	<0.1	<0.1
Pb	0.7	0.6	0.6	0.6	0.4	1.0
Bi	0.1	0.2	0.9	1.1	0.2	0.6
Th	1.5	0.5	2.3	1.0	0.7	0.6
U	0.5	0.2	0.8	0.3	0.2	0.1
∑REE+Y	47.1	13.9	25.1	21.1	20.1	14.7
$(Ce/Ce^*)_{PAAS}$	0.86	0.98	0.94	0.91	0.95	0.89
$(Eu/Eu^*)_{PAAS}$	2.07	3.89	2.35	4.38	4.86	3.70

Table 3 (*continued*).

Drill hole	N7-0005	N7-0005	N7-0005	N8-0022	N8-0022	N8-0022
Type	BIF	BIF	Volc	Soft ore	Soft ore	Soft ore
Depth [m]	111.98 - 112.35	111.98 - 112.35	391.02 - 391.39	11.30 - 11.50	29.60 - 29.80	48.46 - 48.66
Be	1	1	<1	<1	2	1
Sc	N.A.	N.A.	29	12	1	<1
V	<8	<8	242	154	<8	<8
Cr	<27	<27	137	82	<14	34
Co	3.2	3.4	41.4	3.9	3.0	3.7
Ni	3.2	2.8	117	6.4	2.0	0.7
Cu	385	215	1.4	25.6	53.7	28.7
Zn	58	106	1343	7	6	2
Ga	0.9	0.7	14.9	9.4	<0.5	<0.5
As	1.7	0.8	<0.5	4.8	2.1	1.4
Se	<0.5	<0.5	<0.5	0.6	<0.5	<0.5
Rb	0.9	1.2	30.4	0.9	0.8	1.0
Sr	1.9	2.6	73.8	3.4	2.3	0.8
Y	4.3	8.5	18.2	2.2	2.8	2.3
Zr	1.7	0.7	137	101	0.8	1.5
Nb	3.3	2.0	7.2	4.3	0.6	0.8
Mo	0.4	0.5	0.5	1.7	0.2	0.2
Pd	N.A.	N.A.	N.A.	0.7	<0.5	0.7
Ag	0.2	0.2	<0.1	0.8	0.1	0.3
Cd	<0.1	<0.1	0.5	0.3	<0.1	<0.1
Sn	3	<1	1	<1	<1	<1
Sb	<0.1	<0.1	<0.1	0.2	<0.1	0.2
Cs	0.3	0.5	1.0	<0.1	0.1	<0.1
Ba	6	9	867	18	10	11
La	1.7	4.5	26.9	11.2	9.8	3.0
Ce	2.8	6.6	50.1	15.3	9.2	3.1
Pr	0.26	0.60	6.30	1.82	1.80	0.35
Nd	0.9	2.0	25.3	7.6	6.0	1.2
Sm	0.11	0.24	4.88	0.76	0.88	0.13
Eu	0.34	0.57	1.46	0.22	0.31	0.13
Gd	0.17	0.43	4.09	0.41	0.41	0.20
Tb	0.02	0.05	0.68	0.07	0.05	0.02
Dy	0.18	0.34	4.04	0.39	0.34	0.22
Ho	0.05	0.10	0.76	0.08	0.04	0.02
Er	0.21	0.32	2.08	0.33	0.13	0.12
Tm	0.03	0.05	0.33	0.06	0.01	0.02
Yb	0.23	0.28	2.10	0.42	0.17	0.15
Lu	0.04	0.05	0.32	0.07	0.02	0.01
Hf	<0.1	<0.1	3.3	2.2	<0.1	<0.1
Ta	0.1	<0.1	0.4	0.3	<0.1	<0.1
W	0.9	0.7	<0.5	1.1	0.7	2.5
Pt	N.A.	N.A.	N.A.	1.2	0.2	<0.1
Au	2.5	3.0	<0.5	1.1	2.5	1.6
Hg	<0.01	<0.01	<0.01	0.16	<0.01	<0.01
Tl	<0.1	<0.1	<0.1	<0.1	<0.1	<0.1
Pb	2.6	3.1	2.2	4.0	0.6	0.8
Bi	0.1	<0.1	<0.1	0.4	0.2	0.2
Th	<0.2	<0.2	3.5	7.3	<0.2	<0.2
U	<0.1	<0.1	0.6	0.7	<0.1	<0.1
∑REE+Y	11.3	24.6	147	40.9	32.0	11.0
$(Ce/Ce^*)_{PAAS}$	1.00	0.93	0.93	0.81	0.52	0.69
$(Eu/Eu^*)_{PAAS}$	15.5	11.2	1.65	1.81	2.45	5.33

Table 3 (*continued*).

Drill hole	N8-0022	N8-0022	N8-0022	N8-0022	N8-0022
Type	BIF	BIF	BIF	Volc	BIF
Depth [m]	50.80 - 50.99	84.36 - 84.52	98.59 - 98.75	127.73 - 128.19	135.50 - 135.60
Be	<1	<1	<1	<1	<1
Sc	N.A.	N.A.	N.A.	5	N.A.
V	<8	<8	<8	<8	<8
Cr	<27	<27	<27	<14	34
Co	1.4	7.3	7.1	30.4	5.2
Ni	4.0	4.6	2.9	3.7	4.0
Cu	6.4	52.8	162	1.2	21.2
Zn	2	2	3	38	3
Ga	0.6	0.8	0.6	16.9	0.7
As	<0.5	<0.5	0.7	<0.5	1.0
Se	<0.5	<0.5	<0.5	<0.5	<0.5
Rb	0.2	0.4	<0.1	5.7	0.5
Sr	0.6	1.3	1.9	3.5	1.3
Y	1.8	1.0	1.3	69.3	2.1
Zr	0.4	0.2	0.2	588	0.4
Nb	0.7	0.3	0.3	23.4	0.3
Mo	0.1	0.1	0.4	0.6	0.2
Pd	N.A.	N.A.	N.A.	N.A.	N.A.
Ag	<0.1	<0.1	<0.1	<0.1	<0.1
Cd	<0.1	<0.1	<0.1	<0.1	<0.1
Sn	1	1	1	1	5
Sb	<0.1	<0.1	<0.1	<0.1	<0.1
Cs	0.1	<0.1	<0.1	<0.1	<0.1
Ba	5	10	4	35	14
La	1.3	2.1	1.9	82.4	1.6
Ce	1.5	2.6	2.6	142	1.2
Pr	0.13	0.20	0.20	16.2	0.11
Nd	0.4	0.7	0.5	57.0	0.5
Sm	0.07	0.10	<0.05	9.19	0.06
Eu	0.07	0.14	0.13	1.01	0.08
Gd	0.07	0.06	0.06	7.75	0.09
Tb	0.01	<0.01	<0.01	1.41	<0.01
Dy	0.10	<0.05	<0.05	9.38	0.09
Ho	<0.02	<0.02	<0.02	2.33	0.02
Er	0.07	0.03	0.03	7.58	0.08
Tm	<0.01	<0.01	<0.01	1.15	0.01
Yb	0.06	<0.05	<0.05	7.38	0.10
Lu	<0.01	<0.01	<0.01	1.25	0.02
Hf	<0.1	<0.1	<0.1	14.7	<0.1
Ta	<0.1	<0.1	<0.1	1.3	<0.1
W	<0.5	0.5	<0.5	<0.5	0.8
Pt	N.A.	N.A.	N.A.	N.A.	N.A.
Au	1.8	10.8	2.6	2.5	1.1
Hg	<0.01	<0.01	<0.01	<0.01	<0.01
Tl	<0.1	<0.1	<0.1	<0.1	<0.1
Pb	0.5	0.3	0.3	2.8	0.3
Bi	<0.1	<0.1	<0.1	<0.1	<0.1
Th	<0.2	<0.2	<0.2	25.0	<0.2
U	<0.1	0.2	<0.1	6.6	0.1
∑REE+Y	5.58	6.93	6.72	415	6.06
$(Ce/Ce^*)_{PAAS}$	0.81	0.88	0.95	0.93	0.58
$(Eu/Eu^*)_{PAAS}$	5.48	D.L.	D.L.	0.59	D.L.

Table 3 (*continued*).

$(Ce/Ce^*)_{PAAS}$	=	$[2 \times Ce/(La + Pr)]_{PAAS}$
$(Eu/Eu^*)_{PAAS}$	=	$[Eu/(0.67 \times Sm + 0.33 \times Tb)]_{PAAS}$
N.A.	-	No available data
D.L.	-	The values needed for calculation are below the detection limit
PAAS	-	Shale-normalized ratios; shale data from POURMAND et al. (2012)